Specific and Non-Specific Effective Interactions of Proteins in Solution

Dissertation

der Mathematisch-Naturwissenschaftlichen Fakultät

der Eberhard Karls Universität Tübingen

zur Erlangung des Grades eines

Doktors der Naturwissenschaften

(Dr. rer. nat.)

vorgelegt von

Maximilian Darius Senft

aus Neuwied am Rhein

Tübingen

2024

Gedruckt mit Genehmigung der Mathematisch-Naturwissenschaftlichen Fakultät der Eberhard Karls Universität Tübingen

Tag der mündlichen Qualifikation:	23.06.2025
Dekan:	Prof. Dr. Thilo Stehle
1. Berichterstatter:	PD. Dr. Fajun Zhang
2. Berichterstatter:	Prof. Dr. Monika Fleischer

Für Susanne und Ulrich

Contents

Abstract

Proteins are organic macromolecules consisting of a sequence that is composed of a series of amino acids (primary structure) joined together through peptide bonds. Their functionality is obtained through suitable folding (secondary structure) and assembly in three-dimensional space. Proteins are an essential component for every kind of life on earth. The functions of proteins are diverse and extensive. For example, enzymes catalyze chemical reactions which are of vitaly importance for metabolic processes of an organism. Other tasks include the transportation of various molecules as well as structure-forming functions such as the development of muscular tissue(s). Among other criteria, proteins can be divided into different subgroups based on their structural properties. This results in four subgroups, namely disordered proteins, fiber proteins, membrane proteins and globular proteins, the latter being especially relevant for this dissertation.
The water-soluble globular proteins exhibit a rich and diverse phase behavior in the presence of polymers or polyvalent salts. The observed phenomena range from liquid-liquid phase separation (LLPS) to aggregation and crystallization. In addition, "reentrant condensation" (RC) and "reentrant interaction" (RI) are particularly noteworthy. RC describes a phase behavior that is triggered by successively increasing a polyvalent salt concentration at a constant protein concentration. If a certain salt concentration is exceeded, aggregates or condensates form. A further increase beyond another defined salt concentration causes the previously formed aggregates or condensates to dissolve. The greater details of RI will be expanded upon in due course. Understanding and specifically manipulating the phase behavior of proteins is of fundamental importance for medicine, pharmacy and basic research. Protein crystals offer important information about the structure of a protein, which in turn allows for conclusions regarding its function. This information would further our understanding to improve the understanding and potentially aid to treat unwanted aggregations or amyloid fibril formation, commonly seen in Alzheimer's disease patients.
Chapter 7 addresses the effective interactions of four different globular proteins: β-lactoglobulin, bovine serum albumin, human serum albumin and ovalbumin (BLG, BSA, HSA and OVA) admixed with the trivalent salt hexamine cobalt (III) chloride (Hac). In previous studies, this salt has already been shown to induce a phase behavior known as reentrant condensation (RC) in Desoxyribonucleic acid (DNA) and Ribonucleic acid (RNA). This phase behavior is known to be an important concept in DNA packing and folding. Net negatively charged globular proteins such as BSA or HSA exhibit a similar phase behavior in the presence of trivalent salts such as YCl_3 or $LaCl_3$. The phase behavior is predominantly determined

by a charge reversal, which is triggered by an increasing salt concentration at a constant protein concentration (c_p). Within the scope of this work, it was then investigated whether the trivalent cobalt salt Hac can trigger the RC phase behavior despite its structural differences to e.g. YCl3 or LaCl3. From a structural perspective, the Hac cation differs from other polyvalent metal cations by the fact that six ammonia ligands (NH3) are covalently bonded to the central cobalt atom (Co) thereby shielding the present (3^+) charge. It transpired that the effective interactions induced by Hac are not sufficient to trigger RC. Instead, small-angle X-ray scattering experiments (SAXS) revealed that the BLG-Hac system induces a new phenomenon, called reentrant interaction (RI). Characteristically for protein systems with RI, the SAXS profiles are similar to that of protein systems with RC phase behaviour; however, there is an absence of visible or measurable phase transitions occurring in RI. In parallel to the SAXS experiments, static and dynamic light scattering experiments (SLS, DLS) as well as visual investigations were carried out.
Secondly (see Chapter 8), the effect of the polymer polyethylene glycol (PEG) on the protein systems BSA and HSA was investigated. Initially, a rich phase behavior was observed both visually and microscopically, which is characterized by liquid-liquid phase separation (LLPS), aggregate formation and, in the case of BSA, crystallization. The depletion effect, which is commonly known in the context of colloid theory, acts as the initiating effect. This unspecific, yet subtly equilibrium-based attractive interaction potential, which contrary to expectations is caused exclusively by repulsive interactions, can be manipulated and adjusted by tuning the polymer size and concentration. Systematic SAXS measurements of BSA and HSA-PEG systems in combination with quantitative modeling allow a better understanding of the protein phase behavior induced by the depletion effect. Furthermore, the differences between the two related proteins are emphasized and further elaborated. Thus, HSA crystals offer a variety of different symmetry groups, whereas BSA has only been found to crystallize in the symmetry group C121. Furthermore, HSA can crystallize under unspecific (e.g. depletion effect) as well as specific (e.g. trivalent metal cations such as CeCl3) conditions, whereas BSA cannot. This is supported by surface analysis of the contact surfaces within a protein crystal. It transpired that HSA forms more contact surfaces and can therefore also crystallize in more, different symmetry groups compared to BSA.
Chapter 9 examines the effects of temperature and effective interactions of BSA-LaCl3 solutions exposed to sodium-based Co salts (Na_2SO_4, NaCl, NaBr, NaNO3 and NaSCN) belonging to the Hofmeister series, alongside the phase behavior. The Hofmeister series divides anions into two groups: Cosmotropes and chaotropes. This classification is based on whether or not the anions percipitate proteins from a solution (cosmotropes ${SO_4}^{2-}$ and chaotropes SCN^- respectively). Similar to BSA-LaCl3, the BSA-LaCl3 co-salt systems exhibit a rich phase behavior which, in addition to RC, also features LLPS, as well as a lower critical solution temperature (LCST). The phase separation thus takes place during heating. Using

temperature-controlled UV/vis measurements, it was shown that even the addition of low concentrations (mM) of the Co salts to 80 mg/ml BSA with 10 mM-LaCl3 leads to a reduction of the LCST. The reduction of the LCST follows an inverse Hofmeister series, according to which chaotropic anions lower the LCST more strongly than cosmotropic anions. By approximating a Langmuir binding isotherm, it is possible to quantify and describe the association of the investigated anions with the protein surface more precisely. Complementarily performed systematic SAXS experiments combined with model approximation provide further insights about the prevailing effective interactions, however, these only partially support the results from previous UV/vis measurements.

Zusammenfassung in deutscher Sprache

Proteine sind biologische Makromoleküle, die durch eine Abfolge von Aminosäuren (Primärstruktur) aufgebaut und durch Peptidbindungen miteinander verbunden sind. Durch entsprechende Faltungen (Sekundärstruktur) und Anordnung im dreidimensionalem Raum (Tertiärstrucktur) erhalten sie ihre Funktionalität. Sie stellen einen fundamentalen Bestandteil für jede Art von Leben auf der Welt dar. Die Funktionen von Proteinen sind vielfältig und weitreichend. So katalysieren Enzyme chemische Reaktionen, die eine große Relevanz für den Stoffwechsel eines Organismus haben. Weitere Aufgaben reichen vom Transport von Molekülen hin zu strukturbildenden Funktionen wie beispielsweise die Ausbildung von Muskulatur. Eine Unterteilung der Proteine in Untergruppen kann unter anderem anhand ihrer strukturellen Merkmale erfolgen. Dadurch ergeben sich die Untergruppen der ungeordneten Proteine, faserförmigen Proteine, Membranproteine und globulären Proteine, letztere sind für die vorliegende Dissertation von Relevanz.
Die in Wasser löslichen globulären Proteine weisen ein reichhaltiges Phasenverhalten in der Gegenwart von mehrwertigen Salzen oder auch Polymeren auf. So reichen die zu beobachtenden Phänomene von Flüssig-Flüssig Phasentrennung (LLPS) über Aggregation zu Kristallisation. Weiterhin sind vor allem "reentrand condensation" (RC) sowie "reentrand interaktion" (RI) zu nennen. RC beschreibt ein Phasenverhalten, welches durch sukzessives Erhöhen einer multivalenten Salzkonzentration bei konstanter Proteinkonzentration ausgelöst wird. Bei Überschreiten einer gewissen Salzkonzentration, bilden sich Aggregate oder auch Kondensate. Ein weiteres Erhöhen der Salzkonzentration bedingt ab einer weiteren gewissen Salzkonzentration das Auflösen der zuvor gebildeten Aggregate oder Kondensate. RI ist ein Phänomen welches im nachfolgenden Abschnitt dieser Zusammenfassung genauer erläutert wird. Verständnis sowie zielführende Manipulation des Phasenverhaltens von Proteinen ist fundamental für Medizin, Pharma- oder Grundlagenforschung. So liefert ein Proteinkristall wichtige Informationen zur Proteinstrukturaufklärung, die wiederum Rückschlüsse auf die Funktion des Proteins erlauben. Diese gewonnen Informationen können dann dazu beitragen beispielsweise ungewollte Aggregation oder die Ausbildung von Amyloidfibrillen, wie sei bei Alzheimer vorkommen, zu verstehen und somit Möglichkeiten zu finden diese zu bekämpfen.
Das erste Ergebniskapitel (siehe Kapitel 7) handelt von effektiven Wechselwirkungen der vier verschiedenen globulären Proteine β-lactoglobulin, Bovine serum albumin, Human serum albumin und Ovalbumin (BLG, BSA, HSA und OVA)

mit dem trivalenten Salz hexamin cobalt(III) chlorid (Hac). Es ist bereits erwiesen, dass dieses Salz bei Desoxyribonuclein säure (DNA) sowie Ribonucleinsäure (RNA) ein Phasenverhalten bekannt als reentrant condensation (RC) hervorruft, welches ein wichtiges Konzept der DNA-Packung und Faltung darstellt. Ein ähnliches Phasenverhalten zeigen netto negativ geladene globuläre Proteine wie BSA oder HSA in der Gegenwart trivalenter Salze wie YCl3 oder LaCl3. Dabei wird das Phasenverhalten maßgeblich durch eine Ladungsumkehr bestimmt, die durch eine steigende Salzkonzentration bei gleichbleibender Proteinkonzentration (c_p) ausgelöst wird. Im Rahmen dieser Dissertation wurde nun untersucht, ob das trivalente Cobalt-Salz Hac trotz seiner strukturellen Unterschiede zu bspw. YCl3 oder LaCl3, das RC-Phasenverhalten auslösen kann. Strukturell unterscheidet sich das Hac Kation von anderen mehrwertigen Metall Kationen dadurch, das sechs Ammoniakliganden (NH_3) kovalent an das zentrale Kobaltatom (Co) gebunden sind und die vorliegende (3^+) Ladung abgeschirmt wird. Es stellte sich heraus, dass die durch Hac induzierten effektiven Wechselwirkungen nicht ausreichen um RC auszulösen. Stattdessen zeigte sich durch Röntgenkleinwinkelstreuexperimente (SAXS), dass das BLG-Hac System ein neues Phänomen, reentrant interaction (RI), hervorruft. Kennzeichnend für RI ist dabei, dass sich die SAXS-Profile für Proteinsysteme mit RC-Phasenverhalten und Proteinsysteme mit RI ähneln, es bei RI jedoch zu keinem visuell sichtbaren sowie messbaren Phasenübergang kommt. Begleitend zu den bereits angesprochenen SAXS-Experimenten wurden statische und dynamische Lichtstreuungsexperimente (SLS, DLS) sowie visuelle Untersuchungen durchgeführt.
Der zweite Teil der Arbeit (siehe Kapitel 8) untersucht, welche Auswirkung das Polymer Polyethylenglycol (PEG) auf die Proteinsysteme BSA und HSA hat. Dabei wurde zunächst visuell als auch mikroskopisch ein reichhaltiges Phasenverhalten festgestellt, welches durch Flüssig-Flüssig Phasentrennung (LLPS), Aggregatbildung und bei BSA auch Kristallisation geprägt ist. Als auslösender Effekt ist hier der Depletion Effekt anzuführen, welcher im Rahmen der Kolloidtheorie landläufig bekannt ist. Dieses unspezifische und zugleich auf einem subtilen Gleichgewicht basierende anziehende Wechselwirkungspotenzial, welches entgegen der Erwartung ausschließlich durch repulsive Interaktionen hervorgerufen wird, kann durch das Abstimmen von Polymergröße und Konzentration maßgeblich beeinflusst und auch eingestellt werden. Systematische SAXS-Messungen von BSA und HSA-PEG Systemen in Kombination mit quantitativer Modellierung ermöglichen ein besseres Verständnis des durch den Depletion Effekt induzierten Phasenverhalten von Proteinen. Weiterhin werden auch die Unterschiede der beiden verwandten Proteine ersichtlich und weiter herausgearbeitet. So kristallisiert HSA beispielsweise in viele verschiedene Symmetriegruppen während bei BSA bisher ausschließlich die Symmetriegruppe C121 festgestellt wurde. Weiterhin zeigt sich, dass HSA sowohl unter unspezifischen (bspw. Depletion Effekt) als auch spezifischen (bspw. trivalente Metallkationen wie CeCl3) Bedingungen kristallisieren kann, BSA jedoch nicht. Unterstützt wird dies durch die gezeigte Oberflächenanalyse der Kontaktflächen innerhalb eines Proteinkristalls. Es stellt sich heraus,

dass HSA mehr Kontaktflächen ausbildet und somit auch in mehr unterschiedliche Symmetriegruppen kristallisieren kann, verglichen mit BSA.
Das dritte Ergebniskapitel (siehe Kapitel 9) untersucht neben dem Phasenverhalten, die Auswirkungen von Temperatur sowie die effektiven Wechselwirkungen von BSA-LaCl3 Lösungen unter dem Einfluss von natriumbasierten Co-Salzen (Na_2SO_4, NaCl, NaBr, $NaNO_3$ und NaSCN) der Hofmeisterserie. Die Hofmeisterserie unterteilt Anionen in zwei Gruppen: Kosmotrope und Chaotrope. Diese Einteilung basiert auf der Eigenschaft, ob die Anionen Proteine aus einer Lösung fällen (Kosmotrop SO_4^{2-}) oder eben nicht (Chaotrop SCN^-). Ähnlich zu BSA-LaCl3 weisen die BSA-LaCl3 Co-Salz Systeme ein reichhaltiges Phasenverhalten auf, welches jeweils nebst RC auch über LLPS und eine untere kritische Lösungstemperatur (LCST) verfügt. Die Phasentrennung erfolgt somit bei Erwärmung. Mittels Temperatur gesteuerten UV-Vis Messungen wurde nachgewiesen, dass bereits die Addition von geringen Konzentrationen (mM) der Co-Salze zu 80 mg/ml BSA mit 10 mM-LaCl3 eine Reduktion der LCST herbeiführt. Die Reduktion der LCST folgt dabei einer inversen Hofmeisterserie, wonach chaotrope Anionen die LCST stärker senken als kosmotrope Anionen. Durch Annäherung von einer Langmuir-Bindungsisotherme ist es möglich, die Assoziation der untersuchten Anionen mit der Proteinoberfläche genauer zu quantifizieren und zu beschreiben. Zusätzlich durchgeführte systematische SAXS Messungen kombiniert mit Modellannäherung liefern weitere Einblicke in die vorherrschenden effektiven Wechselwirkungen, diese unterstützen jedoch nur bedingt die Ergebnisse aus den vorausgegangenen UV/vis Messungen.

Part I

Introduction and Theory

Chapter 1

Introduction

Proteins can be classified as biological macromolecules, more precisely as biopolymers, which fulfill a variety of biologically relevant tasks [1]. Alongside their molecular, chemical, physical and functional properties [2–5], proteins also serve as an important source of nutrients [6–8]. In general, protein formation is based upon the folding of polypeptides in unique configurations with micron (μm) to nanometer (nm) dimensions [9–11]. Owing to their spatial arrangement, proteins are capable of interacting with all kinds of matter - be it organic or inorganic; likewise, proteins can respond to external stimuli [2–5]. Moreover, most functional proteins are arranged in so-called complexes, which either consist of several replicates, subunits or include other proteins [11–14]. On the basis of protein complexes, an organism succeeds in catalyzing biochemical reactions as well as obtaining structuring elements which facilitate interactions between the organism and its immediate surroundings [10, 15, 16]. Consequently, the basic functions of an organism are realized by proteins, but only the interaction of different proteins, for example in a cluster, will provide an organism with sufficient functional complexity [11, 12, 17]. To provide an overview on the relevance of proteins in the organization of a biological organism, an estimated 13% = 9 kg of a 70 kg person is made up of proteins [18]. Currently, the UniProt protein database lists over 245 million different proteins, of which around 570 thousand have already been manually reviewed. These two numbers will most likely grow in the near future [19].

Apart from their aforementioned complex and versatile functions, especially crystalline proteins are key to the purification and production of pharmaceuticals for medical therapy [20–22]. Protein crystals can be used to treat shortages of endogenous proteins or to suppress an immunoreaction triggered by medication [20, 22–24]. Besides the purification of medically relevant proteins, a multitude of other proteins were purified employing protein crystallization, ranging from Serum albumins to enzymes [23].

Furthermore, *in vivo* crystallization or aggregation of proteins is a clinical finding that represents a downside. On the one hand, proteins and their respective crystals have great potential to help cure diseases; on the other hand, many undesirable protein aggregation and crystallization processes or pathways are associated with diseases. For example, sickle cell anemia describes a defect which, in addition to the structure, also significantly deteriorates the hemoglobin synthesis [25–27]. The mutated S-hemoglobin undergoes a polymerization reaction, which leads to

the formation of linear fiber bundles, causing increased intracellular viscosity and entails an obturation of blood vessels. Patients diagnosed with sickle cell anemia are also susceptible to a variety of complications which includes stroke, lung diseases and organ damage [25–27]. Other examples include eye cataract, Parkinson, Alzheimer's, Huntington's and Creutzfeldt-Jakob's disease [28–34]. In general, *in vivo* protein crystallization and aggregation usually restricts the viability of cells, as demonstrated by the above mentioned diseases, thus providing an evolutionary disadvantage [35]. In rare cases, however, protein crystallization offers an evolutionary advantage, as it is evident in *Bacillus* bacteria, which use protein crystals to preserve toxins [35].

Structural biology represents the main beneficiary of protein crystallization. The importance of this science branch was demonstrated during the pandemic of SARS-CoV-2 commonly known as COVID-19, which caused a severe acute respiratory syndrome (SARS) in humans [36, 37]. SARS-CoV-2 is a single stranded RNA virus, representing a member of *Coronaviridae*, a sub group of the *betacoronaviruses* [36]. Various approaches have been pursued to identify effective virus inhibitors with the ultimate aim of developing a universally applicable vaccine. Therefore, antibody-virus-complexes, as well as [38–41] the NsP5 protease [42], which is responsible for RNA cleavage and thus for the replication of the virus [43], were crystallized. This demonstrates the intimate connection between protein structure and function. Only with extensive information about the protein structure it is possible to deduce the function of a protein [44, 45]. The crystallization of proteins remains a sophisticated venture, as crystallization requires profound structural knowledge, although important structural information remains unknown unless quality crystals are available [46]. Additionally, most protein crystals are the result of trial and error driven experiments [44], which confirms the presence of a vicious circle [46].

Varying parameters such as temperature (T), protein concentration, pH value, ion concentration, the valence of ions [47] or polymer concentration and polymer size exert a major influence on the complex effective interactions of proteins [48, 49], triggering a multitude of different phenomena in response. These include denaturation [50, 51] fibrillation [52] and aggregation [52, 53]. In addition, it was previously found that effective protein interactions in aqueous solutions can be adjusted using trivalent salts, thus obtaining a reentrant condensation (RC) phase behavior, which may be accompanied by LLPS or crystallization [47, 54–67]. As far as crystallization is concerned, polymers in particular are becoming increasingly popular as additives to obtain good quality crystals [68–71]. Although this diverse and rich phase behavior is advantageous for structural biology, the purification and production of drugs presents a disadvantage for the storage and transportation of drugs [20–22, 72–74].

This thesis is divided into three results Chapters (see Chapters 7, 8 and 9), focusing on the examination of effective protein interactions. In Chapter 7, the effective interactions of four different protein systems (BLG, BSA, HSA and OVA) induced by the addition of hexamine cobalt(III) chloride were examined. Emphasis was

primarily placed on the evaluation and quantification of the effective interactions utilizing X-ray and light scattering methods.
In Chapter 8, the phase behavior and the effective interaction of BSA and HSA protein solutions caused by the depletion effect due to the addition of the polymer polyethylene glycol (PEG) were investigated. Systematic SAXS measurements of the two protein-PEG systems in combination with quantitative modeling allow for a better understanding. In addition, the differences between the two related proteins are highlighted and differences in crystallization are elaborated on the basis of a surface contact analysis.
In the final results Chapter, the phase behavior, temperature effects and effective interactions of BSA-LaCl3 solutions under the influence of sodium-based co-salts (Na2SO4, NaCl, NaBr, NaNO3 and NaSCN) of the Hofmeister series were investigated. The BSA-LaCl3 co-salt systems exhibit a rich phase behavior comprising RC, LLPS and a lower critical solution temperature (LCST). To offer a better understanding of this BSA LaCl3 co-salt system, temperature-controlled UV/vis measurements were complemented by systematic SAXS measurements.

1.1 Van der Waals Equation of State

Generally, volume (V), pressure (P) and temperature (T) are required to express the physical state of a liquid or gas. Provided a thermodynamic equilibrium, the relation between V, P and T is termed equation of state. In the case of an ideal gas, the following well known equation is obtained [75–78]:

$$PV = nN_A kT = nRT. \tag{1.1}$$

Here, N_A denotes the Avogadro constant, n the number of moles and the relation $R = N_A k$ gives the ideal gas constant. The variable k is used for the Boltzmann constant. Due to the ideal behavior of the individual particles of the ideal gas, interactions between the particles are excluded. Consequently, the ideal gas is unable to undergo a phase transition such as the condensation of a gas phase to a liquid phase. Therefore, the description of a permanent gas applies to an ideal gas [76]. Including attractive interactions $(n/V)^2 \cdot a$ and considering the excluded volume b per mole n with $(V - nb)$ in Equation 1.1, yields the Van der Waals (vdW) equation of state:

$$\left[P + \left(\frac{n}{V}\right)^2 a\right](V - nb) = nN_A kT. \tag{1.2}$$

Here, a denotes the strength of the attraction [75–78]. Both vdW coefficients a and b are temperature independent and individual for each gas [77].
Illustrating the vdW isotherms in a pressure-volume diagram (see Figure 1.1), reveals that above a critical temperature T_c only a gas can be realized, independent of the pressure. Accordingly, the pressure required to induce condensation

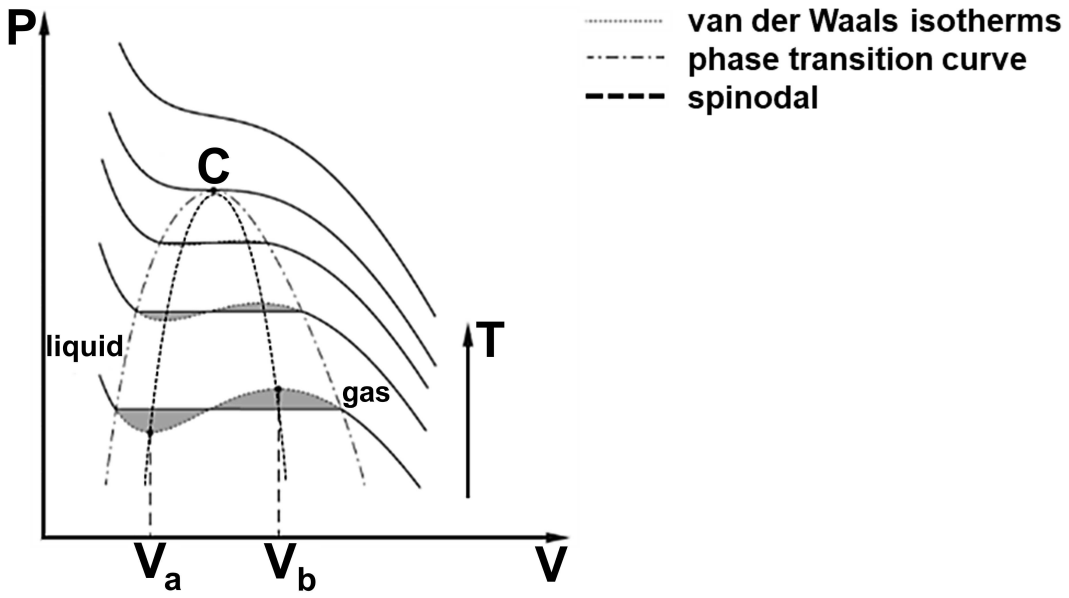

Figure 1.1: *Schematic illustration of the van der Waals isotherms for different temperatures T close to the critical point (C) in a P/V diagram. The van der Waals isotherms are shown in solid/dotted lines for an increasing temperature T. The grayish areas correspond to the Maxwell-construction. This Figure has been adapted from Reference [76].*

of a gas to a liquid is referred to as the critical pressure P_c and consequently the required volume as critical volume V_c [76]. Looking at the critical isotherm, a saddle point (C) can be ascertained. This point satisfies the condition under which both pressure-volume derivatives are equal to zero at constant T (see Figure 1.1) [76, 79]. In the realm above C, the ideal gas is approximated (small values for the term n/V in Equation1.2 for increasing T [76]). The other isotherms that run through the two-phase region located below point C are to be replaced by horizontal lines using the Maxwell's construction. Thus, two equally sized areas $A1 = A2$ are enclosed by the horizontal and isothermal lines (see grayish areas in Figure 1.1) [79]. A phase equilibrium exists, when the chemical potential of the gas (g) and liquid (l) phases is constant $\mu_l = \mu_g$ [75, 78]. Considering the molar Helmholtz free energy $\bar{F}$, the following relationship is obtained:

$$\bar{F}_l - \bar{F}_g = P\left(\bar{V}_g - \bar{V}_l\right). \tag{1.3}$$

Under consideration of

$$\left(\frac{\partial \bar{F}}{\partial \bar{V}}\right)_T = -P \tag{1.4}$$

together with the molar volume $\bar{V} = V/n$ and the relationship $(n_l - n_g)\bar{V} = V$ provides the Maxwell construct

$$P\left(\bar{V}_g - \bar{V}_l\right) = + \int_{\bar{V}_l}^{\bar{V}_g} P\left(\bar{V}\right) \cdot d\bar{V}, \tag{1.5}$$

which explains the equality of the two areas $A1 = A2$ (see gray areas in Figure 1.1 [78]).
Connecting the extreme points of the vdW isotherm within the two phase regions yields the spinodal (illustrated by the two points V_a and V_b). The area enclosed by the spinodal is not realized, as the system splits into two phases: a gas phase and a liquid phase. The area in between spinodal and binodal (phase transition curve) is characterized by metastability. Metastability, that is, the process of heating a liquid above its boiling point or cooling a gas below its condensation temperature, to provide a practical example [79]. Generally, these states posses a limited lifetime and transition to a two phase system as a result of a more favorable chemical potential μ [80].

1.2 Binary Mixtures a Thermodynamic View

Typically, a protein solution can be regarded as a binary mixture. As the name already implies, the mixture is comprised of two components, A and B, together with their respective molar fractions, χ_A and χ_B ($\chi_A + \chi_B = 1$). Moreover, each constituent features an individual Gibbs free energy labeled G_A^0 and G_B^0 respectively [75]. The concept of Gibbs free energy (G) can be used to describe a binary system of dissolved proteins in the context of thermodynamics [28]. For a constant pressure P and fixed temperature T the Gibbs free energy reads as follows:

$$G = U - TS + PV = H - TS. \tag{1.6}$$

Here U denotes the internal energy, S the entropy, V the volume and H the enthalpy [28, 81, 82].
Stability in a thermodynamic context provides a valuable framework to predict the behavior of a system in response to encountered disturbances. In other words, a stable system can be characterized by a global minimum in the energy landscape, causing the system to maintain its current state. In the opposite case, an unstable state is characterized by the transition to another, more stable state, which is initiated in response to minor disturbances. Minor disturbances involve deviations in the thermodynamic variables P, T, S, H or U. A third state, referred to as metastable, is characterized by the presence of a local energy minimum. In order to achieve a transition to a more stable state, energy must first be added to the system [83].
Based on the context provided, the Gibbs free energy of a binary solution can be calculated by use of the following formalism:

$$G = \chi_A G_A^0 + \chi_B G_B^0 + u\,\chi_A \chi_B + RT[c_A ln(\chi_A) + c_B ln(\chi_B)]. \tag{1.7}$$

Here, the ideal gas constant is denoted with a R [75]. This formalism is based on the assumption that the interaction energy between the two components A and B in the mixture can be approximated by the term $u\,c_A c_B$. Here, u denotes the internal energy per unit of volume or mass [75]. The last two terms on the right-hand side of the equation 1.7 denote the entropy contribution of the mixture [75, 84]. The limit of metastability

$$\frac{\partial^2 G}{\partial \chi_B^2} = 0 \tag{1.8}$$

can be converted to

$$-2\,u\chi_a(1-\chi_a) + RT = 0. \tag{1.9}$$

Equation 1.9 yields the spinodal curve, which is depicted in Figure 1.2 (red line) [75].

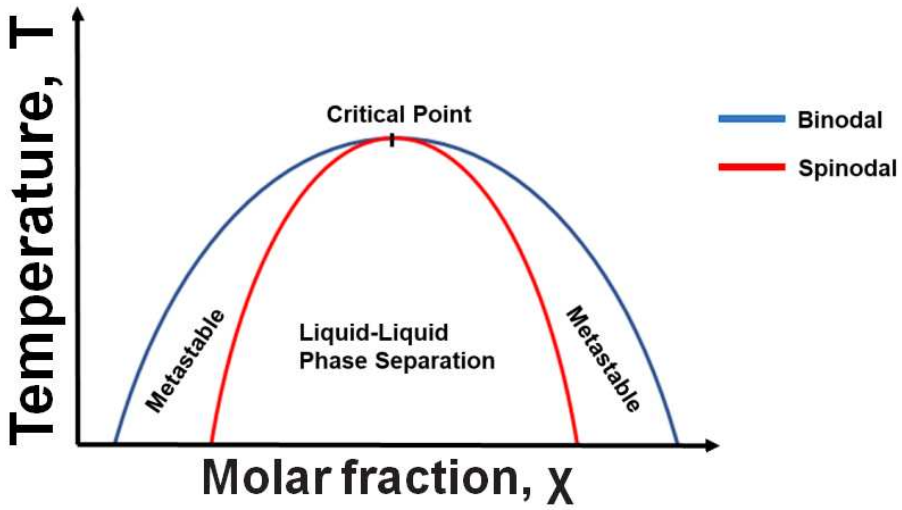

Figure 1.2: *Schematic illustration of the binodal (blue) and spinodal curve (red) for a binary mixture consisting of two substances: A and B. The volume fraction for the substance A (ϕ) is displayed on the X-Axis, whereas the temperature is shown on the Y-Axis. Metastability characterizes the condition of the binary solution in between binodal and spinodal curve. Inside the Spinodal curve, the solution is unstable, resulting in Liquid-Liquid phase separation (LLPS). This Figure has been adapted from Reference [75].*

The critical point marks the transition from a stable homogeneous solution, which is fully miscible for all kinds of concentrations, to an unstable solution (inside the Spinodal see Figure 1.2). Besides the Spinodal, the coexistence curve, known as binodal, is given by the following equation [75]:

$$\frac{1-\chi_A}{\chi_A} = \exp\left(\frac{(1-2\chi_A)\,u}{RT}\right). \tag{1.10}$$

This equation applies, if the chemical potential of a given component remains constant, despite the mixed or demixed condition of the binary solution. The area enclosed by binodal and spinodal is characterized by metastability (see Figure 1.2). A solution located precisely in this metastable area will form droplets as a result of inflicted perturbations. These disturbances are to be equated with a transfer of energy. The droplets mature and eventually the solution separates in two phases [75, 85].

1.3 Phase Diagrams of Collodial Solutions

The colloid theory is a useful concept for the description of protein phase behavior. The particles in solution (e.g. proteins) are visualizds as colloidal particles of diameter σ. In accordance with the picture of atomic liquids, the solvent is neglected and considered only as a background, which allows one to relate the behavior of the colloidal solution to an equivalent interaction potential of atoms [49]. Based on the range of interaction, various kinds of phase diagrams emerge [48, 86]. The phase diagram for a system which exhibits exclusively hard sphere interactions is depicted in Figure 1.3 a. From this, it is evident that only fluid (F) and crystalline (C) phases exist. Given the volume fraction of $\phi = 0.494$, a few colloids are found in a crystalline form. This behavior is entropically favored (see F+C area in Figure 1.3 a). Exceeding the so-called volume fraction of melting $\phi = 0.545$ implies that all colloids are present in crystalline (C) form (see Figure 1.3 a). When a long-range interaction is introduced, the phase behavior alters and a three-phase equilibrium becomes visible (see Figure 1.3 b). Here a stable coexistence between gas (G) and liquid (L) is established. This behavior is commonly found for atomic liquids such as argon [86]. The introduction of short ranged attractions gives rise to a different type of phase diagram. These short ranged attractions are commonly found in protein solutions. Here, the liquid-liquid transition (highlighted by L+L) turns out to be metasatable (see Figure 1.3 c) [86]. Metastable indicates a separation into two distinct liquid phases, one phase being protein-rich, known as the dense phase, and the other phase being protein-poor, known as the dilute phase [87]. Typically, the phase behavior of proteins can be divided into different phases: the solidus line (which separates C from G+C), the solubility line (which separates G from G+C) and the liquid-liquid coexistence line (which separates G+C from L+L), also known as binodal (see Figure 1.3 c and Figure 1.2) [86, 88]. Depending on the course of the solidus or solubility line, the corresponding temperatures and volume fractions are indicated, above which a crystalline or a gaseous phase occurs. The gaseous-crystalline phase is enclosed by these two lines (see Figure 1.3 c). Not far from the solubility line, but within the area of the G+C phase, runs the so-called gas-crystal spinodal. The gas-crystal spinodal describes the metastable decomposition for a coexisting crystal and gas phase [87]. In the case of colloid-polymer solutions, similar phase diagrams emerge (see Figure 1.9) [48].

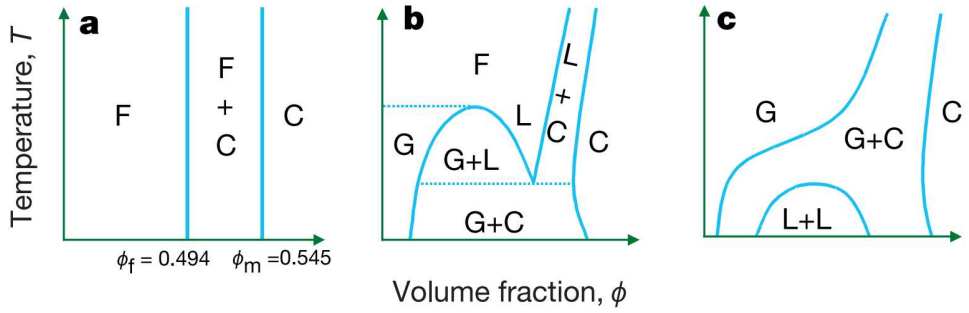

Figure 1.3: *Schematic illustration of different Phase diagrams for colloidal systems. The Y-Axis displays the temperature whereas the X-axis displays the volume fraction (ϕ). Graph a) displays the phase diagram for a hard sphere sytem only showcasing fluid (F) and crystal phases (C). Graph b) depicts the phase diagram for hard spheres accompanied by long-ranged attractions as to be found in atomic systems e.g. argon. Here a stable coexistence between gas (G) and liquid (L) is to be seen. Graph c) depicts the phase diagram for hard spheres with short ranged attractions, common for protein solutions. An equilibrium is established between gas and crystal, but the liquid-liquid transition (L+L) turns out to be metastable. This illustration has been adapted from Reference [86].*

1.4 Specific Interactions between Proteins and Salts

Proteins are comprised of amino acids, which are connected by a peptide bond. Generally, amino acids can be distinguished on the basis of the physical properties of their respective side chains. These include: size, aliphatic or aromatic character, the respective charge, hydrophobicity or hydrophilicity, and polarity [89]. Considering the previously enumerated properties in the context of an extended amino acid chain, along with the associated three-dimensional folding, one yields a functional protein. A protein can thus possess either a positive, neutral or negative net surface charge. The surface charge and ultimately the isoelectric point are dependent on ambient conditions such as the pH value [89].
By suspending a protein in an aqueous electrolyte-containing solution, the electrostatic potential is altered [90]. In this regard, water is viewed as a non-conducting, yet structureless environment. The dissolved protein molecules can be envisioned as charged colloidal particles surrounded by irregularly distributed cations and anions [48, 49]. Generally, charged particles in solution are known to repel particles with the same charge and attract particles with the opposite charge. This type of interaction is commonly referred to as Coulomb interaction [48, 49]. The Coulomb interaction can be used to describe the accumulation of oppositely charged ions at the protein surface. Moving away from the colloidal surface, an equilibrium between cations and anions emerges. This equilibrium oscillates around a constant value, a process that results in the formation of an ionic double layer. A

change in the ambient ion concentration alters the width of this double layer: if the concentration of ions is increased, the screening of the colloidal charge is intensified, which leads to a narrower double layer. In the opposite case, i.e. with decreasing ion concentration, the double layer screening is weakened and the double layer expands. An approach of two double layers from two colloids carrying identical charges causes the double layers to overlap, and leads to mutual repulsion [48, 49]. Yet this repellent force is only effective across a limited range (approximately 3 nm), defined as the Debye screening length λ_D:

$$\frac{1}{\lambda_D} = \kappa = \sqrt{\frac{\sum_i n_i z_i^2}{\epsilon \epsilon_0 k_B T}}. \tag{1.11}$$

Here, κ denotes the inverse Debye length, z denotes the charge carried by the ions, n_i represents the concentration of the i-th component, ϵ denotes the dielectric constant of the solvent, ϵ_0 denotes the permittivity of the free space, k_B denotes the Boltzmann constant and T denotes the temperature [48, 49, 91, 92].

1.4.1 DLVO-Theory

The DLVO theory developed by Derjaguin-Landau-Verwey-Overbeek describes emerging attractive, and repulsive interactions between two polarizeable colloids (proteins) suspended in an aqueous electrolyte solution. Due to Coulomb repulsion, ions of opposing charge accumulate on the surface of the proteins and yield a double layer formation. The overlap of two individual yet similarly comprised double layers culminates in mutual repulsion [48, 49, 90], as described on the previous page. Apart from repulsion, an attractive van der Wals force (vdW) emerges, evoked by fluctuating dipole moments of the colloids [93]. Ultimately, the total energy of interaction corresponds to the sum of the attractive van der Waals forces along with the repellent electric double layer [94]. Figure 1.4 a illustrates the DLVO theory graphically by showing the energy of interaction E as a function of particle spacing r. The repelling electrostatic interactions are emphasized by r^{-3}, while the long-range attractive vdW force is denoted by r^{-1} and the short-range attractive vdW force by r^{-6}. At particle distances where r approaches r_{min}, the long-range vdW forces exert an attractive interaction that leads to weakly bound aggregates. Beyond the secondary minimum, the repulsive electrostatic interactions repel stronger than the long-range attractive vdW force attracts (see Figure 1.4 a). At even shorter distances, the resulting repulsive barrier could be overcome and aggregate formation occurs, (primary minimum) [48, 49, 90]. However, in this regard it is important that these colloids can make contact but not interpenetrate one another.

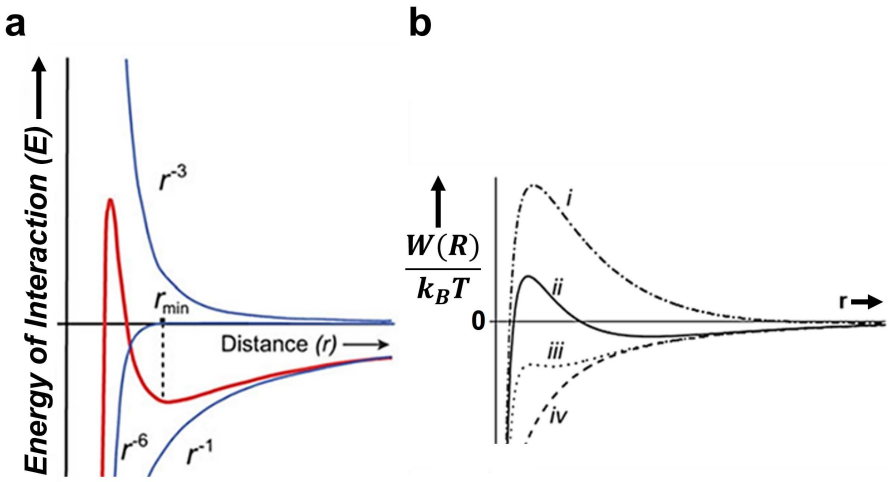

Figure 1.4: *Exemplary visualization of the DLVO theory (Derjaguin-Landau-Verwey-Overbeek) (a) and the effects of an increasing salt concentration on the DLVO theory (b). Graph (a) depicts the interaction between two colloidal particles as they approach each other. The total energy of the interaction E (highlighted by the red line) represents the sum of all interactions (highlighted by the blue lines) as a function of the respective inter particle distance r. The interactions (blue lines) are subdivided as follows: the electrostatic repulsion is highlighted by r^{-3}, the short-range van der Waals (vdW) attraction by r^{-6} and the long-range vdW attraction by r^{-1}. The secondary minimum r_{min} is indicated by a dashed line. Graph (b) illustrates the interactions between two approaching colloids under the perquisite of an increasing salt concentration (from i to iv). The interaction potential W, normalized to thermal energy k_BT, is depicted as function of r. Illustration (a) has been adapted from Reference [90], illustration (b) has been adapted from Reference [48].*

For this reason, the distance between the particles cannot become zero (see Figure 1.4 a). Figure 1.4 b illustrates the behavior of the DLVO theory in response to an increasing salt and, thus, associated ion-concentration. Instead of the energy of interaction, the interaction potential W as a function of r is plotted [48, 49]. At low salt concentrations i, the double layer repulsion is the dominant factor. As a result, the solution is initially stable. Raising the salt concentration from i to ii leads to the development of a secondary minimum at intermediate particle spacing along with the associated weak aggregation. This weak aggregation is reversible, which can be accomplished by means of mechanical actions such as shaking. The curves for (iii) and (iv) depict the situation for even higher salt concentrations. This increase in salt concentration significantly reduces the repulsive potential barrier and leads to a primary minimum which is associated with irreversible ag-

gregates. At this primary minimum, the attractive vdW forces dominate.
However, the applicability of DLVO theory is limited as it neglects ion-ion interactions, interactions beyond electrostatics like hydrophobic interactions and heterogeneity in charge distribution. Yet, experiments have shown to deviate from the concept of DLVO theory, [90, 95, 96], but still the DLVO theory provides acceptable descriptions for many systems under investigation.

1.4.2 Reentrant Phase Behavior

RC phase behavior can be observed in a variety of different systems such as charged colloids [97–99], DNA [100–102], or polyelectrolytes [103–105]. A similar behavior was observed for aqueous solutions of net negatively charged globular proteins (e.g. BSA, HSA, OVA and BLG) in the presence of multivalent metal salts (e.g.YCl_3 or $LaCl_3$) [47, 56, 58, 106]. An exemplary RC phase diagram for globular net negatively charged proteins in the presence of multivalent metal salts (e.g.YCl_3) is shown in Figure 1.5. Starting from a fixed protein concentration ($c_{protein}$ mg/ml) accompanied by a continuous increase of the salt concentration (c_{salt} mM), the globular protein molecules initially repel each other, owing to their net negative surface charge (see regime I in Figure 1.5). Exceeding the first critical salt concentration t^* yields a phase transition, resulting in opacification (regime II) of the formerly clear solution (regime I). This opacification is attributable to the formation of aggregates or condensates, some of which may also precipitate [47, 56, 58, 107]. The aggregate and condensate formation can be traced back to the binding between the carboxy groups on the protein surface with the cations in solution. As a result, bridging contacts are formed, the surface charge of the proteins is reduced and condensation starts at an almost neutral protein charge (regime II). A further increase of the salt concentration (c_{salt}) beyond the second critical concentration t^{**} results in redissolution of the previously formed condensates, the solution becomes stable again and turns clear (regime III). This phase behavior is commonly referred to as reentrand condensation (RC). Fundamental to this phase behavior is the cation-mediated charge reversal of the proteins, which is confirmed by zeta potential measurements [47, 59, 62, 108]. Within regime II, it is possible for a liquid-liquid phase separation (LLPS) to occur (see LLPS area in Figure 1.5). The samples that qualify for LLPS, separate into a two-phase mixture consisting of a dilute and a dense liquid phase. This behavior is illustrated by the dashed lines, which indicate a tie-line pair within the LLPS area shown in Figure 1.5 [56, 108]. The ion-activated patchy particle model [107] enables a detailed description of the RC phase behavior. According to this model, each protein possesses a limited number of patches. The binding of a multivalent cation to a patch occupies and thus activates this patch [107, 109].

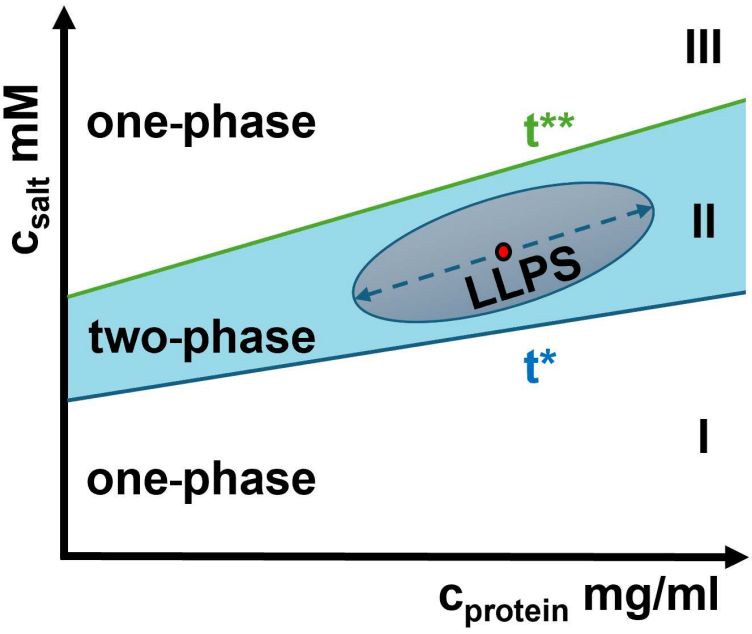

Figure 1.5: *Exemplary illustration of a reentrant condensation (RC) phase diagram for net negatively charged globular proteins in the presence of multivalent cations in aqueous solution. The bulk phase diagram is divided into three regimes I, II, and III and features liquid-liquid phase separation (LLPS). Dashed lines within the LLPS area emphasize a pair of tie-lines indicating the dissociation into a dense and dilute phase. The two critical salt concentrations are highlighted in blue (t^*) and green (t^{**}).*

Only the interaction of an unoccupied (non-activated) patch with an occupied (activated) patch of a second protein molecule leads to a short-range attraction culminating in an ionic bridge. Consequently, as the salt concentration increases, more and more patches become occupied, which results in an increasing number of ion salt bridges. On the other hand, the encounter of two unoccupied or two occupied patches results in repulsion [107, 109].
Minor changes in this model reveal considerable effects. For example, an increase in repulsion between two unoccupied patches or between two occupied patches yields a shift in the interaction energy which in turn affects the distribution of patches. An increase of the attraction between an occupied and an unoccupied patch modifies the ensemble distribution at the critical point. Raising the number of patches moves the interaction energy towards higher values. This is important because interaction energy is required to achieve phase separation [109]. In addition to the number of patches, their distribution on the particle itself is also relevant, which can be recognized by different critical points present in the phase diagram [110, 111]. Another parameter that influences this model is the radius of the hard sphere. For example, the interaction energy required to reach the critical point decreases as the radius increases [109].

1.4.3 Hofmeister Series

The Hofmeister series, named after Franz Hofmeister, classifies anions and cations on the basis of their salting-out and salting-in properties of proteins in aqueous solution [112]. A representative sequence of the Hofmeister series for anions reads as follows [113]: $\mathbf{CO_3^{2-} > SO_4^{2-} > S_2O_3^{2-} > H_2PO_4^- > F^- > Cl^- > Br^- \sim NO_3^- > I^- > ClO_4^- > SCN^-}$.
In this representation of the anionic Hofmeister series the anions to the left (CO_3^{2-}), which are commonly referred to as cosmotropes, precipitate proteins from aqueous solutions (salting out). In contrast, the anions on the right (SCN^-), which are commonly referred to as chaotropes, cause the opposite effect of salting in. Cosmotropic anions are well hydrated, which increases the protein's surface tension and exert a stabilizing effect on the proteins in solution. On the other hand, chaotrope anions exert a destabilizing effect, reducing the proteins surface tension and in turn increasing the probability of proteins to denature [114–116]. The concept of salting out describes a phenomenon in which an increase in anion concentration is accompanied by a slight improvement in the solubility of a protein [114, 116]. Although it may sound simple, the solubility of proteins is rather complex and depends not only on the protein's chemical or physical constitution, but also on temperature, pH-value and, of course, concentration and nature of the admixed salt [114]. Even though the behavior of proteins in the presence of anions which belong to the Hofmeister series has been extensively characterized, it turns out that a consistent ordering of the anions is still lacking [113, 116–118]. The rule of matching water affinities was developed, which is based on the hydration enthalpy of the ions [119, 120]. This rule suggests that ion pairing between two oppositely charged ions is more likely to occur if the respective hydration enthalpies are approximately equal or match [121]. In other words, small ions carry a higher charge density, which means that water is bound more strongly; the opposite is true for larger ions. Thus, a pairing of large cations (chaotrope) with large anions (chaotrope), and small cations (cosmotrope) with small anions (cosmotrope) is favored, but pairing between large and small ions is rather unlikely to form. Looking at proteins, the functional groups on the protein's surface can be categorized as chaotropic or cosmotropic based on the side chain residues, the predominant charge, the respective hydration enthalpy and the similarity to cosmotropic or chaotropic ions [119, 120, 122–124]. It has been shown that the bond between a protein and an anion is characterized by an increase in entropy as the Hofmeister series progresses. However, this increase in entropy is compensated for by a gain in enthalpy. As a result, the binding free energy also gradually decreases as the Hofmeister series progresses, a mechanism which can be explained by the law of matching water affinities [125].
Conversely, it has been observed that a multitude of different factors like the concentration of protein or salt, the pH-value or specific protein attributes affect or even invert the Hofmeister series [126, 127]. This reversal of the Hofmeister series can be observed at low salt concentrations, yet salt concentrations above 200 or

300 mM cause a return to the direct Hofmeister series [127–131].
This demonstrates how multifaceted the phase behavior of proteins can be. Only with extensive knowledge of the various influencing factors can one provide a certain degree of predictability of the protein phase behavior.

1.4.4 UCST-and LCST-Behavior

Temperature is a crucial factor that influences the phase behavior of proteins. A slight change in temperature, both increasing and decreasing, is able to trigger a displacement of a protein's phase diagram [108]. In addition, temperature can be considered as a general control parameter for LLPS, thus offering two conditions for which LLPS emerges: below a critical solution temperature, known as upper critical solution temperature (UCST) [132] or above a critical solution temperature, referred to as lower critical solution temperature (LCST) [62].
In other words, the UCST behavior describes a system which is fully miscible at higher temperatures but phase separates at lower temperatures. Proteins that exhibit this type of phase behavior include, amongst others, BLG [59] and lysozyme [133]. A similar kind of behavior can be observed for synthetic polymers [134–137].
In contrast, the LCST behavior describes a system which is completely miscible at higher temperatures and phase separates at lower temperatures. This behavior can be observed in a variety of systems such as polymers [138–140], elastin like peptides [141–143] or BSA admixed with different trivalent salts [64, 65, 144]. Closer examination of the LCST behavior of polymers reveals a more pronounced interaction and contraction in response to a rise in temperature. As a secondary phenomenon the release of water, previously bound to hydrophobic polymer domains can be observed [145]. Interestingly, a few polymers feature both UCST and LCST behavior [146, 147].
Refocusing on proteins, investigations on BSA and HSA admixed with YCl_3 showed that the observed LCST-LLPS can not be attributed to a strengthening of attraction but rather to an entropy gain [148]. This gain in entropy is caused by the release of water molecules which surround both the cation and the carboxyl groups present on the proteins surface. It was found that establishing a bond between the protein surface and a cation is characterized by endothermicity, which is an indication of an entropic process [148]. In addition, the exchange of the solvent water (H_2O) for deuterium (D_2O) has a major impact on the phase behavior of the protein system. The critical point of the LCST is thereby shifted to lower values and the second condensed regime (Regime (II)) expands, highlighting an entropic regulatory effect of water on the effective protein-protein interactions [148]. Generally, LCST-LLPS is triggered by an entropy increase initiated by the release of bound water molecules and ultimately gives rise to a negative enthalpy of mixing. UCST-LLPS on the other hand is characterized by a positive enthalpy of mixing and demixing [149].

1.5 Depletion Effect

According to the DLVO theory, the interactions between two colloidal particles are the result of both electrostatic and van der Waals interactions. Considering colloids in the presence of polymers or other smaller solutes, different forces are of relevance. Two scientists from Japan, Sho Asakura and Fumio Osawa, developed a physical model (AO) which accounts for these conditions. The AO model is valid within the colloidal limit (CL) [150, 151]. In the following, the fundamentals of the depletion interaction contained by the AO model are covered.
Given the context of colloid theory, proteins (colloids) dissolved in a polymer solution are considered hard spheres of diameter σ. The polymers, on the other hand, are considered penetrable hard spheres with a diameter of 2δ. The special property of the penetrable hard spheres is already evident from the name: these spheres enable for mutual interpenetration, although no interaction occurs among them. Examining the interaction between proteins and polymers in solution reveals a hard sphere interaction between the two [48, 49, 152, 153].
In aqueous solution, each colloid (protein) is individually encapsulated by a so-called depletion layer of width δ, which is characterized by an inversely proportional polymer concentration in comparison to the bulk concentration, outside of the depletion layer (see Figure 1.6). In other words, the depletion layer δ is characterized by a polymer concentration of zero. This situation gives rise to an isotropic osmotic pressure gradient for an individual colloid [48, 49, 152, 153]. If two colloids separated by a distance of $< 2\delta$ approach each other, the respective depletion layers overlap and the formerly inaccessible volume is thus accessible for the polymers. This volume is termed overlap volume $V_0(r)$ (see Figure 1.6). Associated with this is a gain in entropy. Consequently, the overlap volume is filled by pure solvent. In addition, the overlapping of two depletion layers eliminates retention or penetration of polymers inside the overlapping area, thereby giving rise to an attractive anisotropic osmotic force shoving the colloids together (see black arrows in Figure 1.6). Although, this force is attractive, it originates from purely repulsive interactions [48, 49, 150, 151, 153, 154]. Figure 1.6 shows a schematic representation of this situation, in which two depletion layers of two different colloidal particles superimpose.
The depletion interaction enables for easy optimization via an appropriate choice of the penetrable hard spheres. For example, the range of the depletion attraction is significantly influenced by the size 2δ of the depletion agent. Commonly, the thickness or width of the depletion layer is denoted as the radius of gyration R_g, which is an appropriate estimation of δ for dilute polymer solutions. On the other hand, the strength of the depletion interaction scales with the osmotic pressure, which in turn is dependent on the concentration of the depleting agent. However, it should be emphasized that both, i.e. range and strength, can be altered independently of each other [48, 49, 155].

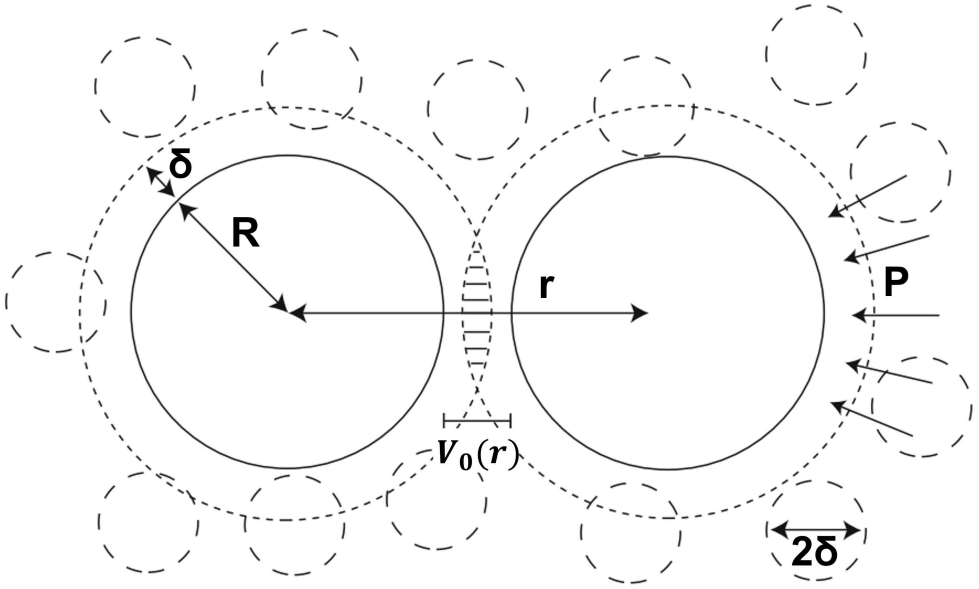

Figure 1.6: *Schematic illustration of the depletion interaction occurring between hard spheres, suspended in a polymer blend. The hard sphere particle diameter is denoted as σ and the corresponding radius R is given by $R = \frac{\sigma}{2}$. The polymers are considered as penetrable hard spheres with a diameter of 2δ. Due to an unbalanced osmotic pressure P between the two hard spheres, indicated by the arrows, a net attractive force emerges. The dashed circles indicate the depletion thickness δ. The dashed area indicates the overlap volume $V_0(r)$. The inter particle spacing is denoted r. This illustration has been adapted from Reference [48].*

The AO model, which was later improved and refined by Vrij [154], understands that the emerging attraction between the two colloids is a result of an anisotropic pressure. The interpretation follows a mechanical approach which yields the depletion interaction potential [48, 154, 156]

$$V(r) = \begin{cases} +\infty & r \leq \sigma, \\ -\Pi_p V_0(r) & \sigma < r \leq \sigma + 2R_g. \\ 0 & r > \sigma + 2R_g \end{cases} \tag{1.12}$$

Here, the depletion interaction potential is expressed as the product of the ideal osmotic pressure Π_p together with the overlap volume $V_0(r)$. The osmotic pressure can be expressed by $\Pi_p = n_b k_B T$ with n_b denoting the number density of the polymer bulk [48, 154, 156].

The overlap volume $V_0(r)$ is given by:

$$V_0(r) = \upsilon_p \left(\frac{J}{J-1}\right)^3 \left[1 - \frac{3}{2}\left(\frac{r}{\sigma J}\right) + \frac{1}{2}\left(\frac{r}{\sigma J}\right)^3\right] \tag{1.13}$$

with υ_p denoting the volume of a penetrable hard sphere (polymer) and $J = \frac{2R_g}{\sigma}$ [48, 154]. Figure 1.7 provides a graphical representation of the depletion interaction potential as a function of the particle spacing r in accordance to the model developed by Asakura, Osawa and Vrij [48, 150, 151, 154]

By relating the polymer radius of gyration R_g (estimation for the width of the depletion layer δ) to the size of the colloid σ, the size ratio q can be determined. The size ratio

$$q = \frac{2\,R_g}{\sigma}, \tag{1.14}$$

is an important measure which enables classification of polymer solutions into different scenarios. Typically, a size ratio of $q < 1$ is refereed to as "colloid limit" whereas a size ratio of $q > 1$ is termed "protein limit". In the colloid limit (see regime I. Figure 1.8), the diameter of the colloid is larger than that of the polymers; in the protein limit the opposite applies (see regime II. Figure 1.8) [48, 49, 157–159].

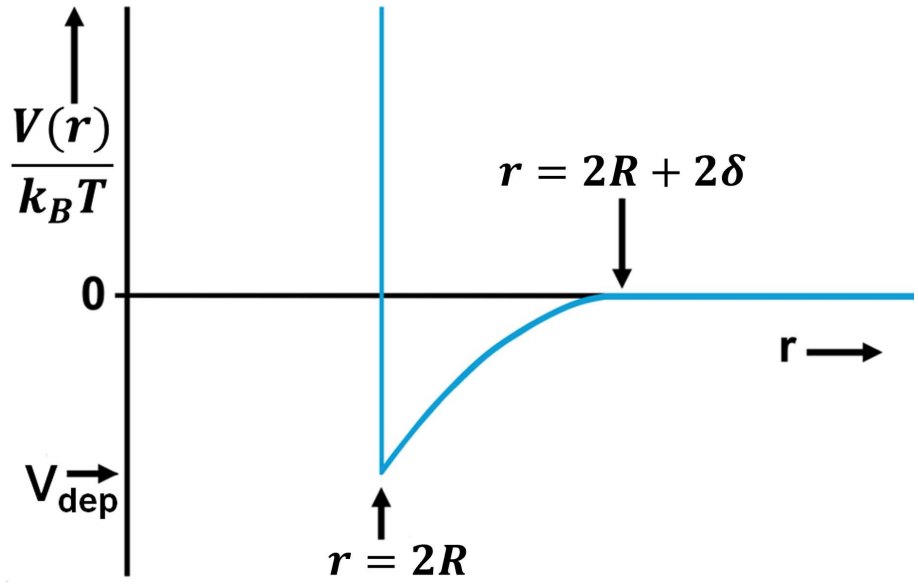

Figure 1.7: *Schematic illustration of the depletion interaction potential $V(r)/k_BT$, emerging between two colloids as a function of the particle spacing r. This illustration was adapted with changes from Reference [48].*

1.5.1 Characteristic Length Scales of Polymers and Interacting Polymer Mixtures

The polymer's radius of gyration R_g can be estimated using of the following Equation:

$$R_g = 0.0215\, M_w{}^{(0.583\pm0.031)}, \tag{1.15}$$

which utilizes the polymers molecular weight M_w [160]. Experiments with polymers in solution have shown that, for higher polymer concentrations, the excluded volume for each polymer molecule decreases. This decrease in excluded volume is attributable to a shrinkage coupled with an increase in compactness [161]. Therefore, the radius of gyration requires modification [161]:

$$R_G = R_g(c_{PEG}/c^*_{PEG})^{-1/8}. \tag{1.16}$$

This is reflected in a 6 % decrease in the polymer's radius of gyration coupled with an concomitant increase of the polymer concentration (1 − 30 wt %) for PEG 3400. The abbreviation wt indicates weight percent [162]. If the polymer concentration is sufficiently high, the overlap concentration denoted c^* is exceeded. c^* marks the transition from a dilute regime to a semidilute one (see Figure 1.8) [48, 49, 68, 158, 163–165]. The overlap concentration can be determined experimentally and is for PEG 3350, located at 10 w/V % [68]. In addition, the following formalism provides a good estimate for a calculation based approach [158]:

$$c^* = M_w/(4/3\pi R_G^3\, N_A)/\mathrm{mg\,ml^{-1}}, \tag{1.17}$$

with N_A denoting the Avogadro number. Alternatively, the overlap concentration can be calculated by use of the following formalism [163]:

$$c^* = M_w/(4/3\pi R_G^3\, N_A) \propto P^{-0.749}, \tag{1.18}$$

with P denoting the degree of polymerization. Similarly, the units for this Equation are mg/ml [163]. Within the semidilute regime, i.e. when $c > c^*$ or $c \gg c^*$ (see Figure 1.8 regime II. and regime IV.), a different type of length scale estimation is required. Here, the polymers disentangle and create a polymer mesh [164]. Therefore, it is appropriate to estimate the length scale based on the mesh or "blob" size of the polymer ζ_b [160, 166]. The following Equation provides a suitable approach when estimating the "blob" size [161]:

$$\zeta_b \approx R_{G,PEG,}(c_{PEG}/c^*_{PEG})^{-3/4}. \tag{1.19}$$

Combining Equations 1.14, 1.15, 1.16, 1.17 and 1.19 allows to adequately estimate the size ratio q:

$$q = \frac{2\,\zeta_b}{\sigma}. \tag{1.20}$$

Figure 1.8 shows schematically the division between the dilute and semidilute regime for different size ratios (R_g/R) as a function of the polymer concentration, normalized to the overlap concentration (c^*/c).
As previously discussed, within the semi-diluted regime, the bulk liquid is to be understood as a polymer network with a characteristic length scale of ζ_b. A closer look at a blob reveals that monomers belonging to one chain do not overlap with another one. At length scales exceeding the characteristic size of a mesh, the emerging interactions between protein and polymer may be screened by the overlapping of other chains. Especially, if the range of observation (r) is sufficiently large [158]. The characteristic length scale ζ_b is independent from the degree of polimerization P but rapidly decreases with increasing concentration of the polymer [48, 158].

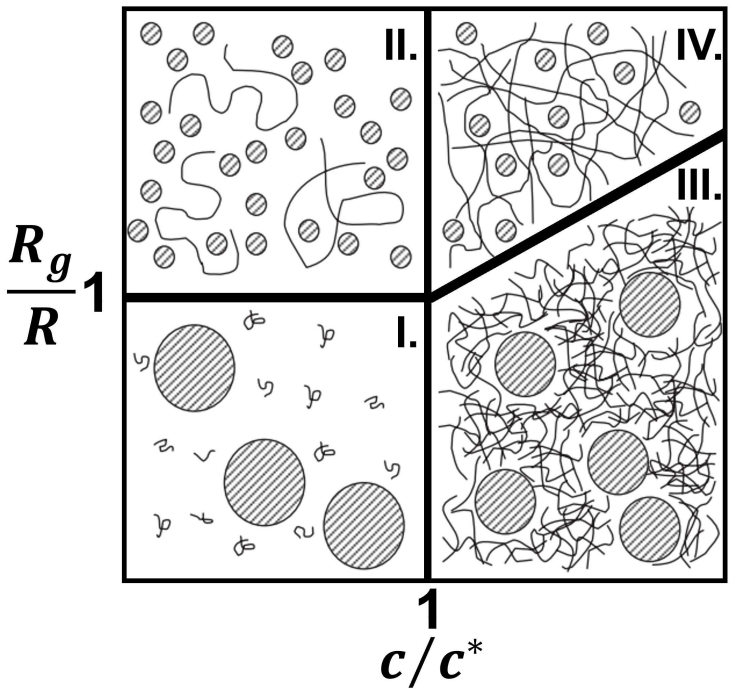

Figure 1.8: *Schematic illustration for the different possible regimes in a colloid (protein)-polymer mixture. Dilute regimes are indicated by I. and II.. Semidilute regimes are indicated by III. and IV.. In regime I., the dilute situation for $R_g \ll R$ is shown. In Regime II., the dilute situation for $R_g \gg R$ is shown. In regime III., the situation for $\zeta \ll R$ is depicted. In regime IV., the situation for $\zeta \gg R$ is illustrated. Note that the scale for both axes increases in the usual manner for a Cartesian coordinate cross. This illustration was adapted with changes from Reference [165].*

1.5.2 Phase Behavior of Protein Solutions Admixed with Polymers

Admixing polymers to a colloidal solution results in an effective osmotic pressure, that pushes the colloids together. Every colloid features a depletion layer of width δ, which can not be entered by the polymer molecules. Upon overlap of these so-called excluded volumes $V_0(r)$, the overlap volume is thus available again to the polymers which yields an entropy gain [48]. As already explained in Chapter 1.5, the polymer concentration (or volume fraction ϕ) and size (and thereby the M_w) control the depletion strength and range respectively. In addition, both variables can be adjusted independently from one another, allowing for a considerable diversity among possible phase diagrams (see Figure 1.9) [48]. Further information on depletion interaction is provided in Chapter 1.5.

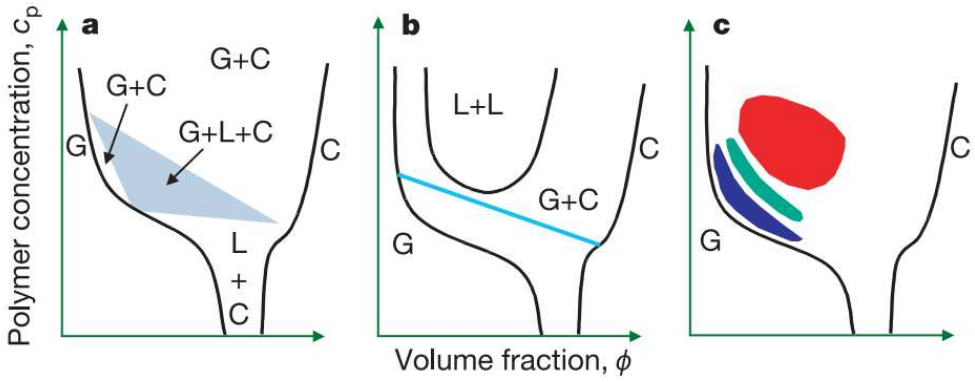

Figure 1.9: *Schematic illustration of different phase diagrams in the context of depletion interaction. a) shows the phase diagram for large polymers. b) depicts the diagram for small polymers. Here different phases can coexist as indicated by the blue line. c) illustrates the phase diagram for proteins in the presence of short polymers. The polymer concentration c_p can be equated to an inverse temperature $1/T$. The gray area in diagram a) illustrates a three phase equilibrium (G+L+C) between gas (G), liquid (L) and crystal (C). In graph c), the blue shaded area highlights crystal nucleation, the green area highlights aggregation and the red area highlights gel-formation. This illustration was adapted from Reference [86].*

By applying statistical mechanics, the separation into colloid-rich and polymer-rich phases is expected. Similar to the phase diagrams of colloidal solutions shown above, the addition of polymers to colloidal solutions gives rise to a rich and diverse phase behavior. The size of the polymers and colloids exerts a considerable influence on the coexisting phases (see Figure 1.9 a for large polymers and Figure 1.9 b for short polymers). Not only can gas (G) and crystal (C) coexist, but liquids (L) too (see Figure 1.9). The polymer concentration can be equated to an inverse temperature behavior, therefore yielding an inverted phase diagram when compared to the diagrams shown in Figure 1.3 [86]. A typical phase diagram for

proteins in the presence of short polymers is given in Figure 1.9 c. Here, different areas are discernible besides crystalline and gaseous phases. The blue shaded area indicates crystal nucleation. Above the crystal nucleation aggregation is to be found (green area). In red, the gelation is highlighted (see Figure 1.9 c). Interestingly, the equilibrium state is reached in close proximity to the phase borders [86].

1.6 Protein Crystallization

In addition to polymers [167, 168], multivalent cations likewise promote crystallization of globular, net-negatively charged proteins in solution [59, 60, 108, 169]. In the following, the classical nucleation theory (CNT) and the non-classical nucleation theory are discussed. Both theories refer to different types of nucleation leading to protein crystals or crystals in general. However, nucleation and crystal growth are two distinct (yet inextricably linked) processes that contribute to crystallization, both of which are equally important [44, 170].
Forming a crystal from solution requires a solution of dissolved molecules, ions or atoms [46]. For example, smaller organic molecules tend to form crystals with an emphasis on the simplest way to occupy space, whereas macromolecules such as proteins prioritize connectivity within a crystalline structure [171]. In addition, the crystallization of proteins is sophisticated, as various different physiochemical parameters such as temperature or pH need to be considered; this means that, proteins posses flexibility in terms of their spatial conformation and the number of different chemical reactions that involve them. Therefore, proteins are much more susceptible to variations in their environment when compared to small molecules or even atoms [171, 172]. In addition, each protein is unique and the diversity of chemical groups involved in the crystal contacts clearly illustrates that only the slightest changes in the prevailing surrounding conditions exerts a profound influence on the process of crystallization. [172].
For the process of crystal nucleation, supersaturation of the solution has proven to be advantageous. [44, 46]. Supersaturation refers to a situation in which the concentration of the dissolved substance exceeds the equilibrium solubility [173]. Crystal growth on the other hand does not require a supersaturated solution [44]. Generally, classical- and non-classical nucleation pathways have in common, that the process of nucleation is connected with a simultaneous formation of a new bulk phase and a new interface. Another common feature of nucleation pathways is that an initial clear, yet supersaturated solution ultimately forms one or more crystals, which can attain macroscopic dimensions [174]. The CNT approach assumes simultaneous fluctuations of density and order, resulting in clusters formation from a supersaturated solution. The dissolved molecules can now either gradually attach or detach from a cluster [174]. The non-classical nucleation theory, on the other hand, assumes independent density and structural development of the new emerging phase. Density fluctuations give rise to disorganized liquid-like clusters, sometimes referred to as droplets, which have an increased density compared to

the initial solution. The next step then involves a reconstruction of the cluster, which yields the crystal. These nucleation processes do not exclude one another; on the contrary both nucleation processes can occur simultaneously [174]. In the following, CNT and non-classical nucleation theory are briefly summarized, followed by an overview of protein nucleation with respect to the osmotic second virial coefficient.

1.6.1 Classical Nucleation Theory

Established almost 100 years ago [175–177], the CNT is a success story. The theory has been used on various systems for the description of nucleation [148, 178–181]. According to CNT, the process of nucleation involves only a single step in which the parameters of order such as density and structure, develop concurrently, resulting in the growth of a cluster [148]. In addition, CNT assumes that the clusters are stationary, therefore disregarding rotational, translational or vibrational movements [182]. Cluster growth can be measured by use of the radius r. The growth of a cluster is favored as soon as it reaches a critical number of molecules. This is expressed by the critical cluster size r^*. If a cluster meets the condition of $r > r^*$, the total free energy ΔG decreases, favoring the growth of a cluster [183]. In the opposite case $r < r^*$, the free energy increases, which indicates the dissolution of a cluster. The change in free energy can be expressed as a function of the radius

$$\Delta G = 4\pi r^2 \gamma - \frac{4}{3}\pi r^3 \, \frac{k_B T \ln(s)}{\nu}, \tag{1.21}$$

where γ denotes the interfacial free energy, k_B the Boltzmann constant, T the temperature, s the solubility and ν the molar volume of the particles within an emerging cluster [184–186].

1.6.2 Nonclassical Nucleation Theory

Experimentally, several studies have shown nucleation pathways involving intermediate precursor structures, not only for proteins in solution [61, 66, 67, 148, 187], but also for polymers [148] or water [188, 189]. This observed behavior is in contrast to direct nucleation from solution, as assumed by CNT [190], thus establishing the non-classical nucleation theory [182, 191, 192].
Provided a solution, $\Delta G = 0$, the formation of a crystal necessitates the change of concentration and structure. In contrast to CNT, non-classical nucleation is characterized by a sequential progression of density and structural fluctuations leading to the final crystalline state [193].
Non-classical nucleation essentially consists of two successive steps, which are shown in Figure 1.10. First, a dense drop of liquid is formed by overcoming an energy barrier ΔG_1^*, which matures into a crystal in the second step. In this process, another second energy barrier ΔG_2^* is overcome [187]. Provided that the dense

liquid is stable compared to the diluted liquid, i.e. $\Delta G^0_{LL} < 0$, the nucleation of the resulting crystals takes place within the dense liquid droplets (see lower, blue curve in Figure 1.10). However, if the dense liquid is unstable, $\Delta G^0_C > 0$, clusters are formed enabling the formation of a crystal from its interior (see upper, red curve in Figure 1.10) [173, 193]. It should be emphasized that liquid-liquid separation proceeds rapidly, whereas nucleation proceeds at a slower rate. Thus, nucleation is ultimately the rate-determining step [192].

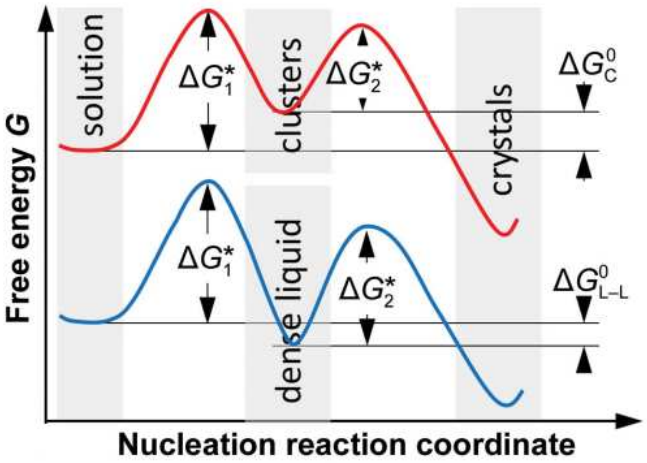

Figure 1.10: *Schematic visualization of non-classical nucleation pathways. The free energy G is depicted as a function of the nucleation reaction coordinate.* ΔG^*_1 *corresponds to the energy barrier for the formation of a cluster (red curve, top) or dense liquid droplets (blue curve, bottom), whereas* ΔG^*_2 *corresponds to the energy barrier for the formation of a crystal nucleus within the cluster or dense liquid, respectively. An unstable dense liquid yields mesoscopic clusters with* $\Delta G^0_C > 0$ *(red curve, top). In the case of a stable macroscopic dense liquid,* $\Delta G^0_{LL} < 0$*, the bottom (blue) curve applies.* ΔG^0_C *denotes the standard free energy for the formation of clusters, whereas* ΔG^0_{LL} *denotes the standard free energy for the formation of the dense liquid phase [187]. This graph was adapted with changes from reference [194].*

1.6.3 Protein Crystallization in the Context of the Second Osmotic Virial Coefficient

The reduced second osmotic virial coefficient B_2/B_2^{HS} serves as a measure to identify the predominant pair interactions between particles or proteins in solution [28]. In order to obtain B_2/B_2^{HS}, the second virial coefficient B_2 is divided by the second virial coefficient for hard spheres B_2^{HS} of radius R. $B_2/B_2^{HS} < 0$ corresponds to attraction whereas $B_2/B_2^{HS} > 0$ corresponds to repulsion.
Empirical studies have shown that attractive interactions between the dissolved proteins are advantageous for crystallization. However, if the attractions are too

strong, arrested aggregates or gels are rapidly formed, which are obstructive for protein crystallization (red area Figure 1.11) [46, 195–197]. Although gelation and aggregation are metastable with respect to the crystalline phase, their longevity negatively impacts the crystallization behavior [46]. On the other hand, weak interactions or even repulsion may be insufficient to induce nucleation (yellow area in Figure 1.11) [46, 195]. George and Wilson discovered a so-called nucleation slot or gap. Within this slot, the B_2 values are usually within a relatively confined range, which indicates favorable conditions for the crystallization of proteins [195]. An extension of this work by Vliegenthart and Lekkerkerker showed, that this crystallization slot is located near the metasatable critical point of LLPS to below this critical point (green area in Figure 1.11) [198]. Typically, this critical point is to be found at reduced second osmotic virial coefficient B_2/B_2^{HS} values of ≈ -1.5 [190, 198].
The presence of metastable LLPS (see area between dashed and solid line in Figure 1.11) within the phase diagram of a protein suggests a two-step process for the crystal formation (see Chapter 1.6.2) [198]. Initially, droplets with an increased protein concentration are formed. These emerging droplets are either linked to density fluctuations or the metastable LLPS [198]. Here, the density fluctuations are beneficial for an increase in nucleation rate [190].

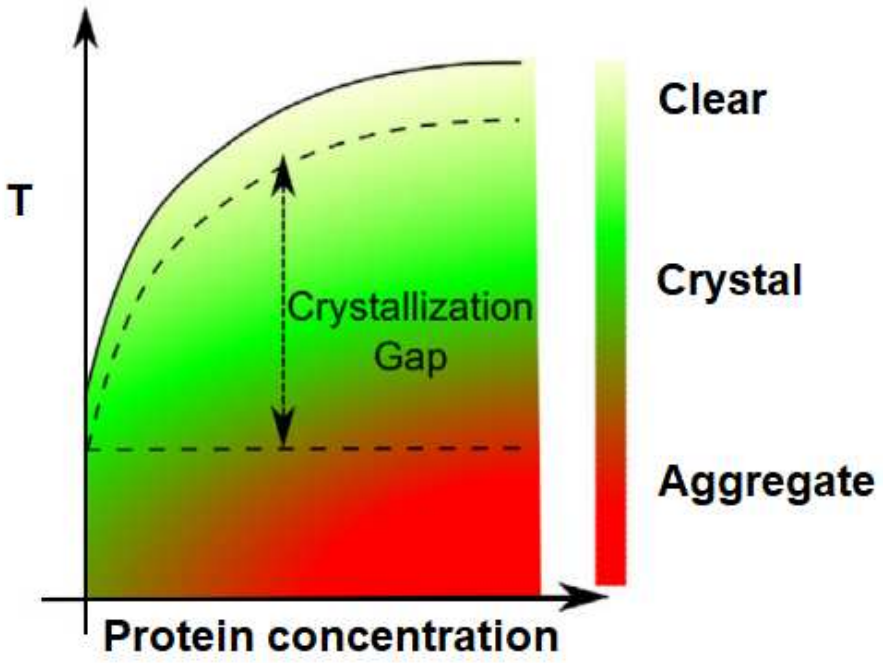

Figure 1.11: *Schematically visualization of the crystal nucleation gap in a typical temperature (T) against protein concentration phase diagram, located to the left of the critical point. The red to green discoloration indicates formation of aggregates (red), crystal formation (green) or a clear phase (greenish to yellow). This graphic was adapted with changes from reference [46].*

In a final step, the protein crystals are formed from these highly concentrated droplets [198]. Therefore, it can be deduced that the proteins require a subtle balance of large enough but not too strong attractions [46, 186]. Currently, it is assumed that the effective attractive forces in between $-10 < B_2/B_2^{HS} < -1$ are optimal for crystallization [196, 197]. Hence, the reduced second osmotic virial coefficient can be used to estimate protein crystallization [106], even though crystallization is not guaranteed to occur [199]. Both specific (salt-induced) and non-specific (polymer-induced) interactions can induce comparable strong effective interactions (B_2) sufficient for protein crystallization. Thus, it is advisable to investigate both conditions (specific and non-specific), as sometimes the opposite effect corresponds to the proteins preferences [199]. The results depicted in Chapter 8 provide a practical example for this behavior.
However, various crystallization processes have been observed depending on the location of the critical point and the phase diagram in general [59, 61, 66, 200]. A detailed description of the reduced second osmotic virial coefficient can be found in Chapter 5.1.7.

Part II

Materials

Chapter 2

Proteins

To provide a better overview, the Materials part is divided into three Chapters. First, the main properties of the proteins investigated are described. This is followed by a description of the additives used, which exert a significant influence on the phase behavior of proteins when added to aqueous protein solutions (see Chapter 3). The last Chapter 4 focuses on a description of the sample preparation procedures. This chapter introduces the various proteins, which were the main subject of the investigations shown in this dissertation. Apart from the protein's basic functions, their biophysical properties, their photophysical properties and relevance are described below. Based on their structure and functions, proteins can be categorized into four different subgroups: fibrous, disordered, membrane and globular proteins [201, 202]. The latter, globular proteins, are investigated in the present work.

2.1 Beta-Lactoglobulin

In bovine milk and many other mammalian species [203], the extracellular protein β-lactoglobulin (BLG) is the major component of whey and belongs to the lipocalin family [203–205]. Apart from its nutritional significance [206–208], it is thought to transport various hydrophobic molecules, such as long-chain fatty acids, cholesterol or vitamin D, across the intestinal membrane [204, 209–211]. Under physiological conditions, BLG typically exists in its dimeric form (see Figure 2.1 a) [204]. The dimer exhibits a molecular weight of 36.8 kDa [205] and consists of the genetic monomer variants A and B, which solely differ in two of the 162 long amino acid sequences [204, 206, 212, 213]. At position 64 out of the 162 long amino acid sequences, asparagine is exchanged for glycine and at position 118 valine is exchanged for alanine [206, 212]. BLG has an Isoelectric Point (pI) of 5.2 [213, 214]. The pI defines the pH value at which the protein exhibits a neutral net charge. A value below the pI indicates a positive charge, whereas a value above the pI indicates a negative charge. At physiological conditions, BLG exhibits a net surface charge of -10 e [204]. Given acidic (pH ≈ 2) or alkaline (pH $\approx > 9$) pH values, a dissociation of the dimers into monomers has been reported [204]. BLG from bovine milk (product no. L3908) with a purity of $\geq 90\%$ was purchased from Sigma Aldrich, now Merck, and used in the experiments without additional purification.

2.2 Serum Albumins

The next type of globular proteins investigated in the present work are serum albumins. In terms of occurrence, serum albumin is the most abundant protein found in the bloodstream [215–217]. With a concentration of around 40 mg/ml, it accounts for around 60 % of the total amount. A sufficient supply of serum albumin is ensured by the liver [217]. The functions of serum albumin are diverse and range from the regulation of blood pressure and pH (pH) [216] to the maintenance of fluid balance due to colloid osmotic pressure [167, 218] to the transportation of fatty acids, ligands, amino acids, hormones, dyes or biopharmaceuticals [167, 217, 219]. In this thesis the proteins Bovine serum albumin (BSA) and Human serum albumin (HSA) are of relevance, which are respectively described in further detail below (see Figures 2.1 b, c respectively). Owing to evolution, distinct variants developed among mammals which differ in their respective primary and tertiary structures. Despite their evolutionary differences, both proteins share a sequence identity of 75.6%. Additionally, both have preserved a highly helical structure along with 17 disulfide bridges [167]. Consisting of three homologous subunits (I, II, III), the form of serum albumin is generally described as heart-shaped. The subunits in turn consist of three secondary subunits, with IIA and IIIA being particularly noteworthy as they possess hydrophobic pockets, responsible for ligand interaction [167].

2.2.1 Bovine Serum Albumin

With a molecular weight of 66.4 kDa, the heart-shaped BSA molecule is comprised of 583 amino acids, without carbohydrate residues, and is predominantly (67 %) alpha-helically folded (see Figure 2.1 b) [167, 217, 220, 221]. Both negative and positive charged residues can be found on the surface of BSA. Nevertheless, its net charge is negative (−11 e) at neutral pH. Its isoelectric point is 4.6 [58]. The protein BSA (product no. A3733, purity of $\leq 98\,\%$), was purchased from Merck and used in the experiments without additional purification.

2.2.2 Human Serum Albumin

Based on its increased availability and accessibility, BSA is frequently used in scientific studies instead of HSA and the resulting findings are then transferred to HSA [167]. Despite its similarity to BSA, HSA has a few distinctive features.
Instead of 583, HSA consists of 585 consecutive amino acids and features a molecular weight between 66.44 kDa [222] and 66.5 kDa [223]. At neutral pH, its net negative surface charge of −9 e is slightly lower than that of BSA, while the pI is slightly higher with a value between pH 4.6 [58] and 4.7 [222].
HSA (product no. A9511, purity of $\leq 97\,\%$) was purchased from Merck and used

in the experiments without additional purification. A schematic illustration of the secondary structure of HSA is provided in Figure 2.1 c)

2.3 Ovalbumin

The fourth globular protein investigated is Ovalbumin (OVA)(see Figure 2.1 d) The glycoprotein OVA, which is the most abundant protein in chicken hen's egg white [224–228], belongs to the protein family of serpins [224]. Depending on the reference, percentages of ovalbumin found in chicken eggs can range from 54 % up to 65 % [224–228]. In general, the primary task of serpins is the inhibition of proteases. Interestingly, OVA shares about 30 % of its sequence identity with serpins, such as antitrypsin, is however devoid of any protease inhibitory activity [224]. The exact function of OVA in chicken egg white has yet to be elucidated [225], but it is believed that it contributes to the embryonic development [224]. Apart from its biological function, the glycoprotein OVA is also of medical relevance, as it is a known food allergen [225].
OVA from chicken egg white has a molecular mass of 44 kDa, is comprised of 385 amino acids and features a pI of 4.54 [224, 225, 229]. This protein (product no. A5503, purity of $\geq$ 98%) was purchased from Merck and used in the experiments without additional purification.

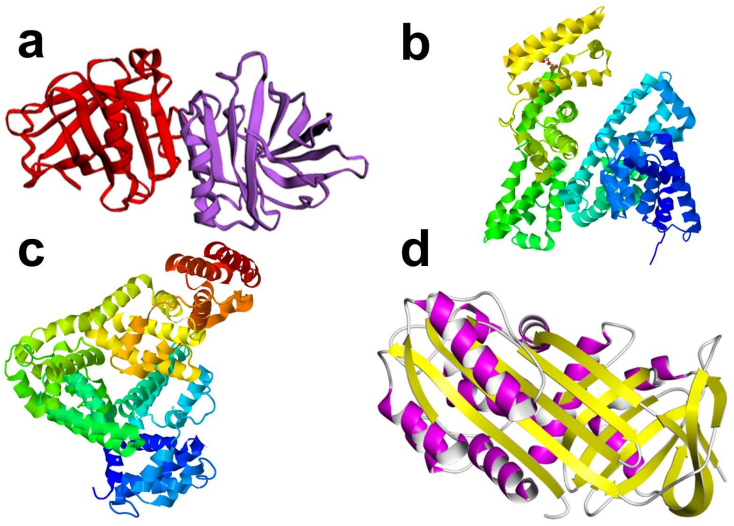

Figure 2.1: *Schematic illustrations of (a) BLG (pdb entry 1beb) [207], (b) BSA (pdb entry 4F5S) [167], (c) HSA (pdb entry 7A9C) [60] and (d) OVA (pdb entry 1JTI) [230]. All illustrations display secondary structures. In (a), the respective subunits of BLG (A and B) are emphasized (red and purple respectively). In (b) and (c) the different colors are guides to the eye. In (d) the spirals (purple) correspond to an alpha helical whereas the thick bars (yellow) represent beta sheets.*

Chapter 3

Additives

The following Chapter presents all the additives used (salts and polymer) and their most important properties. These additives can essentially influence the phase behavior of proteins and thus their effective interactions. Similarly to the proteins, the additives shown here were also used in aqueous solutions. For detailed descriptions on the preparation of stock solutions (protein and additives), and sample preparation, please refer to chapter 4.

3.1 Hexamine Cobalt(III) Chloride

The trivalent salt hexamine cobalt(III) chloride ($[Co(NH_3)_6]Cl_3$; Hac) [231] is commonly synthesized by oxidizing the cobalt (II) ion in an ammoniacal solution either with oxygen or hydrogen peroxide. Alternatively, oxidation at ambient pressure and room temperature (RT) can be mediated by a catalyst such as activated carbon. In both cases, the intermediate product is a pentaamine ion, which is subsequently converted to Hac either by ammonia mediation or by an equilibrium reaction (also mediated by the activated carbon) [232]. Its six ammonia ligands are arranged in octhahedral shape around the central cobalt ion, resulting in a chemically and thermally stable chemical compound in aqueous solution [233, 234].
This salt was purchased from Sigma Aldrich, now Merck (H7891, for use in transformations and X-ray crystallography), and used in the experiments without further treatment. It features a density of 1.17 g/ml and a molecular weight of 264.48 g/mol [231].

3.2 Poly Ethylene Glycol

Due to its biocompatibility and water solubility, polyethylene glycol (PEGs) represent a popular chemical compound for pharmaceuticals. Apart from pharmaceutical [235] and medical applications, PEGs are also frequently used as cleaning agents or materials for colloidal particles. A common method for the production of PEGs is the ether synthesis. Alongside this method, other, less established and more experimental approaches can be used as well [236]. The unbranched, non-ionic and non-adsorbing polymer PEG [237] $H(OCH_2CH_2)nOH$, with an average size of $M_n 3\,350$ was purchased from Sigma Aldrich, now Merck (product

No. 202444), and used in the executed experiments without further purification. According to the manufacturer, the density at 25 °C is 1.204 g/ml [238]. Based on the induced depletion effect, it is possible to use PEG to separate molecules of different shapes and sizes. The size of PEG (molecular weight) and thus the interaction range and the strength of the interaction (PEG concentration) can be freely selected and adapted accordingly [48].

3.3 Lanthanum(III) Chloride

Lanthanum belongs to the group of so-called rare earth elements, that occur in the terrestrial crust in comparable quantities to copper [239]. To produce $LaCl_3$, lanthanum(III) oxide (La_2O_3) and ammonium chloride (NH_4Cl) are heated up to $200 - 250$ °C and react to form $LaCl_3$, releasing H_2O and NH_3. Another established $LaCl_3$ production method involves the reaction of lanthanum(III) oxide (La_2O_3) with hydrogen chloride (HCl) which includes the release of water [240]. Working with $LaCl_3$ is not without a risk; for example, exposure of rats to even low levels of $LaCl_3$ have effects on the individual animals' cognitive abilities. This leads to apoptosis, the programmed cell death, affecting cells of the endoplasmic reticulum and mitochondria, which ultimately results in damage to the nerve cells in the brain [241]. Handling of solid $LaCl_3$ was carried out under a fume hood whilst accurate personal protection was worn at all times.
The inorganic halide $LaCl_3$ was purchased from sigma Aldrich, now Merck (product No. 449830) as anhydrous beads with a purity of ≥ 99.99 %. This multivalent metal salt was then used in the experiments without further treatment. According to a conducted trace element and rare earth analysis, the contamination is below ≤ 100 ppm. Given the condition of RT, $LaCl_3$ features a density of 3.84 g/ml [242].

3.4 Sodium Chloride

To obtain sodium chloride, rock salt is usually mined from halite deposits or brine is extracted. Alternatively, salt can also be obtained by evaporating water from the sea or from salt lakes, taking advantage of the fact that salt is the most abundant dissolved solute. Also known as table salt, NaCl is very popular among the world's population due to its frequent consumption [243].
The electrolyte NaCl was purchased from sigma Aldrich, now Merck (product No. 450014) as anhydrous beads with a purity of 99.99 % based on trace metal analysis.

3.5 Sodium Thiocyanate

Sodium thiocyanate NaSCN is a white powder consisting of orthorhombic crystals, which can be dissolved in water as well as ethanol and acetone. NaSCNis commonly used as base material for the manufacturing of fine chemicals and pharmaceuticals. Owing to its tendency to have a strong chemical reaction, exposure to strong bases, acids or even strong oxidants should be avoided [244, 245].
The monovalent salt sodium thiocyanate NaSCN was purchased from sigma Aldrich, now Merck (product No. 467871) and used without further purification. According to the manufacturer, the purity of the salt is $\geq$ 99.99 % based on trace metal analysis. Impurities include $\geq$ 0.2 % Na_2CO_3 as well as in-solubles $\geq$ 0.005 % and metallic impurities $\geq$ 100 ppm. It features a molecular weight of 81.07 g/mol [246].

3.6 Sodium Sulfate

Apart from sodium chloride, sodium sulfate accounts for the second largest occurrence of dissolved solids/minerals in water. Sodium sulfate, which naturally accumulates in small halite deposits, occurs as a comparatively pure mineral, but can also be found in almost all freshwater springs, drinking water sources or salt lakes. Na_2SO_4 is quite easy to recover, as it often accompanies the extraction of other minerals or it can be recovered from brine [247]. A large proportion of sodium sulfate is primarily used as a filler for detergent production [248].
Sodium sulfate Na_2SO_4 was purchased from sigma Aldrich, now Merck (product No. 239313) as anhydrous granular with a purity of $\geq$ 99.0 % and used without any further purification. The impurities are indicated with $\geq$ 0.01 % of in-solubles and $\geq$ 5 ppm of so-called N containing compounds. Moreover, Na_2SO_4 features a molecular weight of 142.04 g/mol and density of 2.68 g/mL at 25 °C, according to the manufacturer [249].

3.7 Sodium azide

In the context of this work, sodium azide is of particular interest due to its bacteriocidal effect. At low levels, it inhibits the ATPase activity of SecA, an enzyme required for the transport of proteins through the cytoplasmic membrane, by use of the SecYEG channel. After administration, the inhibitory effect develops quickly, yielding almost a full blockage of the SecA mediated SecYEG channel, and restricting the growth of living cells [250]. Apart from its bacteriocidal use in biological wet lab, it is frequently used in airbag charges. However, working with NaN_3 is not without any risk, as it has been demonstrated to be toxic or even lethal at comparatively low dosages [251].
The crystalline powder sodium azide NaN_3 (S8032-25G) was purchased from sigma Aldrich now Merck, and used without further purification. The supplier states the molecular weight as 65.01 g/mol and the purity as $\geq$ 99.8 % [252].

3.8 Sodium bromide

This visually colorless to white appearing solid has a density of 3.20 g/cm^3 and is soluble in water and ethanol. It is manufactured using a so-called neutralization reaction in which hydrobromic (HBr) acid reacts with sodium hydroxide (NaOH) to produce water and sodium bromide (NaBr). Formerly, it was an important resource for the production of silver bromide, which was used to manufacture light-sensitive analog photographic film. At present, it is used as a biocide in swimming pools. Industrially, it is mainly used as a detergent for purifying rocks with a high carbonate ($CO3^{2-}$) content. This prevents the formation of poorly soluble calcium carbonate ($CaCO3$) [253].
The crystalline powder sodium bromide NaBr was purchased from sigma Aldrich, now Merck (product No. 310506) and used without further purification. The supplier states the molecular weight to be 102.89 g/mol with a purity of $\geq$ 99.0 %. Moreover, the impurities account for approximately $\geq$ 0.005 % [254].

3.9 Sodium nitrate

Sodium nitrate ($NaNO3$) is the most important nitrate in nature. Deposits can be found in Egypt, Colombia, California, and Chile, with the most significant deposit being located in Chile. Contaminants such as sand, clay, and other minerals like sodium chloride, various sulfate salts ($NaSO4$, $CaSO4$, $MgSO4$), or potassium perchlorate ($KClO4$) must be removed from the extracted rock mass. This is done using hot water. Subsequently, this leach is then filtered to remove sand, clay, and NaCl. Finally, the leach is cooled down to obtain pure $NaNO3$ crystals [255]. $NaNO3$ was used in the past as a fertilizer, but nowadays this application is negligible. Moreover, sodium nitrate is used for the production of potassium nitrate ($KNO3$) also knwon as saltpeter. $KNO3$ is predominately used for the production of gunpowder, as one of its main ingredients [255].
Sodium nitrate $NaNO3$ was purchased from sigma Aldrich, now Merck (product No. 221341) as crystalline powder and used without further purification. The supplier states the molecular weight with 84.99 g/mol and a purity of $\geq$ 99.0 %. The impurities contained are indicated to be $\geq$ 0.005 % [256].

Chapter 4

Preparation of Solutions

The previous Chapters 2 and 3 introduced the properties of proteins, PEG and salts. This Chapter focuses on the preparative procedures to obtain protein, salt and PEG stock solutions as well as the preparation of samples. The standard techniques of a classical wet lab were used, which are prerequisites and are therefore not described any further.

4.1 Protein Stock Solutions

Protein stock solutions were obtained by mixing degassed and Milli-Q-purified water at (20 °C ± 3 °C) with the respective protein powder. This freshly prepared protein solution was filled in an appropriate container, sealed with parafilm and then placed in the refrigerator (4 °C). The solution was given up to two days to ensure the complete dissolution of the protein powder.
The resistivity of the used Milli-Q water is 18.2 MΩ · cm, at a temperature of 25 °C. Degassing was achieved by attaching a vacuum pump to a bottle containing a batch of Milli-Q water. This procedure, which is an additional preparatory step, was carried out to remove any residual dissolved gases such as oxygen to prevent the formation of bubbles which could potentially interfere with further measurements.
Protein stock solutions were prepared to obtain a protein concentration between 200 and 300 mg/ml to ensure working concentrations of 10, 20, 50, 80 and 100 mg/ml in the respective samples (see Chapter 4.4). Afterwards, the protein concentration (c_p) was determined by means of UV/vis absorbance measurements (see Chapter 6.1). Upon storage, the falcon tubes containing a batch of protein stock were sealed with parafilm to decelerate de novo dissolution of gasses and hinder contamination. The protein stock solutions were kept in the refrigerator at 4 °C and only used for up to three weeks.

4.2 Salt Solutions

Based on the molecular weight, the required amount of the respective salts was calculated and then weighed. Then, the appropriate volume (ml) of degassed Milli-Q water was added. Working concentrations were achieved by diluting the required amount of the respective salt stock solution with fresh degassed Milli-Q

water. This was done to, inter alia increase the volume share of salt in a sample, to prevent and minimize systematic errors induced by pipetting. The stock solutions were placed on a bottle roller and gently rolled at low rpm to achieve complete dissolution of the salt crystals. Concentrations of salt stock solutions ranged between 200 mM and 2 M. The salt solutions were sealed with parafilm and stored at RT.
PEG sample preparation required an omnipresence 1 mM of NaN3 to prevent contamination due to bacterial or funghi growth. Therefore, fresh degassed Milli-Q water was admixed with the required amount of NaN3. This NaN3 enriched Milli-Q water was then used for the preparation of NaCl and PEG stock solutions.

4.3 PEG Solutions

The preparation of PEG stock solutions was similar to the previously shown preparation of salt solutions. PEG stock solutions were obtained by weighing an appropriate amount of PEG and adding the respective NaN3 (1 mM) enriched, Milli-Q water in ml, to obtain a 100 (w/V) % solution. This 100 (w/V) % concentrated PEG solution was then gently rolled on a bottle roller utilizing low rpm to ensure the complete dissolution of the PEG. Afterwards, the stock solution was stored in the refrigerator at 4 °C.

4.4 Sample Preparation

The preparation of samples is comparable throughout the different experiments shown within this dissertation. Initially, the target volume or total volume (μl) was set for each series of samples and experiments individually. As an example, samples which were intended to be used for visual inspection of macroscopic phase behavior required a different total volume than samples prepared for Small angle X-ray scattering (SAXS) measurements. Next, the required volume ($^{-}$l) of the respective Milli-Q water (note that PEG samples required omnipresence of 1 mM NaN3 and therefore a different stock solution of Milli-Q) was placed in the appropriate sample container first, followed by adding the respective protein stock and salt solutions. If PEG or more than one salt solution was required, then the salt/PEG which induces the phase behavior was added in the end. The remaining volume was then filled with the appropriate volume of Milli-Q water.
Samples intended to be used for macroscopical inspection (typically 500 μl) were filled in glass vials (1 ml), sealed with parafilm and visually inspected for up to two weeks at RT. Samples which were prone to crystallize, for example BSA with PEG, were kept at RT for up to one month. Due to the addition of NaN3 to these samples, bacterial and or funghi growth can be ruled out.
To investigate the phase behavior microscopically, an appropriate sample volume

(μl) was transferred onto a microscopy slide prepared with a Gene Frame (1×1 cm^2 microscopy frame featuring a thickness of 0.25 mm; purchased from Thermo Scientific, Germany). Subsequently, the prepared slide was sealed with a cover slide and investigated by the optical microscope (Axio Scope.A1, Carl Zeiss AG). Using the (Axio-Cam ICc5, Carl Zeiss AG) camera, attached to the microscope, images were recorded and later processed by the ZEN Lite 2012 and ZEN 2.6 Blue Edition software (see also Chapter 6.3).
Samples for SAXS measurements were filled by use of sterile syringes and needles in quartz glass capillaries with a diameter of 1.5 to 2.0 mm (WJM-Glas/Müller GmbH, Berlin, Germany), sealed with parafilm and subsequently measured. SAXS samples intended to be measured at the P12 beamline (EMBL, DESY, Hamburg) were prepared in reaction tubes, cooled, and transported to the experimental site ($\approx$ 4 °C). In order to perform the measurement, the tubes were placed in the corresponding sample holder and then automatically transferred to the flow cell by use of a sample picking robot.
The samples for DLS measurements were prepared in appropriately sized reaction vessels (ml), according to the above mentioned protocol. Great care was used when preparing these samples, as air bubbles would interfere with the performed measurement. Subsequently, the samples were filtered, using Whatman syringe filters with a pore size of 0.45 μm (Puradisc 13, Global Life Sciences Solutions Operations Uk Ltd.), into quartz glass cuvettes (Pyrex; Corning, Ny, USA) and finally measured. Previously, these cuvettes were properly cleaned with acetone, to remove residual dust particles. It is important, that the applied acetone has had sufficient time to evaporate.

Part III

Methods

Chapter 5

Experimental Scattering Methods

The previous part introduced the essential properties of proteins, PEG, an salts as well as a detailed description of the sample preparation. This part introduces and describes the experimental methods used to study the effective protein-protein interactions.
In the following, the employed scattering techniques and supplementary methods are presented. In addition to the scattering techniques, the various potentials used for potential fitting as part of the data analysis are covered as well.
The described complementary methods (see Chapter 6) were used to control the sample preparation rather than to investigate the effective protein-protein interactions.

5.1 X-ray Scattering

5.1.1 Small Angle X-ray Scattering

Small-angle X-ray scattering (SAXS) was first employed in the 1930s to meet the increasing challenges posed by the analytical investigation of various materials at the nanoscale. Since then, SAXS was continuously improved and underwent significant further development. Moreover, one of the advantages offered by SAXS applications is the reliable yet economically affordable approach to nanostructure analysis. In addition to bulk materials or powders, liquids and solutes are equally suitable for examination by SAXS. Therefore, SAXS qualifies for the analysis of proteins and their effective interactions, present in aqueous solutions [257, 258].
X-rays are essentially scattered by electrons, implying that SAXS is only observable if an electron density inhomogeneity of colloidal size is present in the sample. In the following, solely elastic scattering is covered, as inelastic scattering only occurs to a negligible extent at very small angles [259]. This section introduces the basic concept of two-dimensional SAXS. Further information on the employed experimental setup can be found within the respective result Chapters 7, 8, 9.
In SAXS, one measures and analyzes the intensity of X-ray photons that are elastically scattered by electron density inhomogeneities in the sample [257]. Given the length scale difference of X-ray radiation wavelength λ (Å) to the inhomogeneities of the sample (nm) to the distances between radiation source to sample and sample to detector (m), the incident as well as outgoing photons can be considered

as plane waves. Since we only consider elastic scattering, which does not include change in the X-ray wavelength [258], the absolute values of the incident ($\vec{k_I}$) and outgoing $\vec{k_O}$ wave vectors can be characterized as follows [28, 257, 258, 260–264]:

$$|\vec{k_O}| = |\vec{k_I}| = 2\pi/\lambda. \tag{5.1}$$

The momentum transfer $\vec{Q}$ for elastic scattering (see Figure 5.1) is defined by the following equation:

$$\vec{Q} = \vec{k_O} - \vec{k_I}. \tag{5.2}$$

Thus, the magnitude of the scattering wave vector $\vec{Q}$ is given by

$$Q = |\vec{Q}| = |\vec{k_O} - \vec{k_I}| = \frac{4\pi}{\lambda} \sin\left(\frac{2\theta}{2}\right), \tag{5.3}$$

with 2θ denoting the scattering angle [265]. A graphical representation can be seen in Figure 5.1.
It is common to express the scattered intensity in terms of the differential scattering cross-section ($\mathrm{d}\sigma/\mathrm{d}\Omega$), which is defined as follows:

$$\left(\frac{d\sigma}{d\Omega}\right) = \frac{I_{\mathrm{sec}}}{N_0 \Delta\Omega}. \tag{5.4}$$

N_0 indicates the incident flux density, which is essentially the strength of the incident X-ray beam, or in other words, the photon count per second passing through a unit area. I_{sec} gives the photon count per second collected at the detector, located away from the sample with a solid angle $\Delta\Omega$ [264].
The experimentally measurable intensity I, scattered by the unit volume is defined as follows:

$$I = \frac{1}{V}\frac{d\sigma}{d\Omega} = \frac{\Delta N}{N_0}\frac{1}{d\tau \Delta\Omega} \tag{5.5}$$

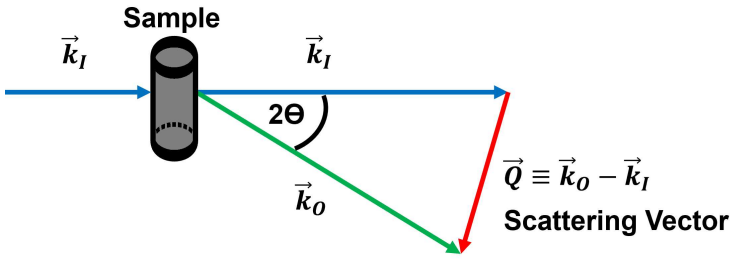

Figure 5.1: *Schematic representation of the scattering geometry. The scattering vector, also known as momentum transfer, is denoted as $\vec{Q}$, $\vec{k_I}$ denotes the incident wave vector, $\vec{k_O}$ the scattered (outgoing) wave vector. 2θ denotes the scattering angle. This Figure is redesigned based on Reference [263].*

with ΔN denoting the elastically scattered part of the X-ray flux in the direction of the solid angle. The sample thickness is given by d and the transmission is denoted τ [260, 263]. The absolute differential scattering cross-section of a sample allows the molecular mass M_w to be determined if additional known information, such as the concentration or chemical properties, are taken into account [258].
For a scatterer j illuminated by X-rays, the scattered intensity $I(Q)$ depends on both, the scattering length b_j and the scattering length density ρ_j. The total scattering density ρ of the sample at the point R can be expressed as a sum over all kinds of atoms (chemical elements), as expressed by the following Equation 5.6 [263].

$$\rho(\vec{R}) = \sum_j \rho_j(\vec{R}) b_j \tag{5.6}$$

In the case of X-rays, the photons interact with all electrons contained in the illuminated sample, and the scattering length b (see Equation 5.7) can be simplified to $b = 0.282 \times 10^{-14}$ m, using the Thompson scattering length [263, 264]:

$$b = \frac{e^2}{(4\pi\epsilon_0 mc^2)}. \tag{5.7}$$

Here, ϵ_0 denotes the permittivity of the free space.
The scattering contrast $\Delta\rho(\vec{r})$ is defined as the difference in scattering length density resulting from the deviation between the solvent ρ_s and the solute $\rho(\vec{r})$ [258–261, 263–265]

$$\Delta\rho(\vec{r}) = \rho(\vec{r}) - \rho_\mathrm{s}. \tag{5.8}$$

The amplitude (A) of the scattered wave at the scattering vector Q is given by

$$A(\vec{Q}) = \int_V \rho(\vec{r}) e^{-i\vec{Q}\vec{r}} \mathrm{d}\vec{r}, \tag{5.9}$$

where the integral is taken over the whole volume of the illuminated sample. This relationship is generally referred to as the Born approximation. The scattered intensity $I(\vec{Q})$ normalized to the illuminated volume V is given by

$$I(\vec{Q}) = \frac{A(\vec{Q})A^*(\vec{Q})}{V} = \frac{1}{V}\int_V \int_V \rho(\vec{r})\rho(\vec{r'}) e^{-i\vec{Q}(\vec{r}-\vec{r'})} \mathrm{d}\vec{r}\,\mathrm{d}\vec{r'} \tag{5.10}$$

with A^* denoting the complex conjugate [257, 258, 260, 261, 263].
The intensity $I_{part}(\vec{Q})$ scattered by a single protein molecule (scatterer) can be written as

$$I_\mathrm{part}(\vec{Q}) = A_\mathrm{part}(\vec{Q}) A^*_\mathrm{part}(\vec{Q}) = V^2_\mathrm{part} P(\vec{Q}), \tag{5.11}$$

where *P(Q)* denotes the scattering form factor.

5.1.2 Form Factor P(Q)

The scattering form factor *P(Q)* of this same molecule is given by the following equation [263]:

$$P(\vec{Q}) = \frac{1}{V_{\text{part}}^2} \int_{V_{\text{part}}} \int_{V_{\text{part}}} \rho(\vec{r})\rho(\vec{r'}) e^{-i\vec{Q}(\vec{r}-\vec{r'})} \mathrm{d}\vec{r}\, \mathrm{d}\vec{r'}. \tag{5.12}$$

Considering the case of a *spherical* scatterer (spherical approximation of a protein molecule shape), the form factor *P(Q)* can be described by the following equation [260, 261, 263],

$$P(Q) = \left(\frac{3[\sin(QR) - QR\cos(QR)]}{(QR)^3} \right)^2 \tag{5.13}$$

with R denoting the radius.
For an *ellipsoid* with a random orientation, the form factor $P(Q)$ is defined as:

$$\begin{gathered} P(Q) \equiv \langle \mid A(Q) \mid^2 \rangle = \int_0^1 \left| \frac{3(\sin u - \cos u)}{u^2} \right|^2 \\ \text{with} \quad u = qb \left((a/b)^2 x^2 + (1-x)^2 \right)^{1/2}. \end{gathered} \tag{5.14}$$

Here a and b denote the radii of the ellipsoid respectively [266]. Exact sizes of the used radii a and b can be found in the corresponding results chapters 7, 8, 9.
The ellipsoidal form factor *P(Q)* (equation 5.14) characterizes the shape of a protein molecule after orientation averaging, thus, describing the global shape of the investigated proteins.
The total scattering intensity $I(Q)$ scattered at a scattering angle of 2θ as a function of Q (see Equation 5.3) can be expressed as follows [261, 263, 266]:

$$I = N_p(\Delta\rho^2)V^2 P(Q)S(Q). \tag{5.15}$$

Here, $S(Q)$ denotes the structure factor, which contains information about the spatial arrangement of individual protein molecules, which depends on the protein interactions [267]. $P(Q)$ denotes the form factor, N_p gives the number of protein molecules within the illuminated volume, V_p denotes the volume of a single protein molecule and the scattering contrast $\Delta\rho$ [261, 263, 266].

5.1.3 Structure Factor S(Q)

The structure factor $S(\vec{Q})$ is given by the following Equation:

$$S(\vec{Q}) = 1 + \frac{N-1}{V} \int_V g(\vec{r}) e^{-i\vec{Q}\vec{r}} \mathrm{d}\vec{r}. \tag{5.16}$$

The pair distribution function $g(\vec{r})$ expresses the probability of encountering a center of any arbitrarily selected particle at a separation $\vec{r}$ from the center of a specified particle. Thus, for N particles in a volume, defined as (N/V), $g(\vec{r})$ is the total quantity of particles to be encountered in the previously defined volume at a separation $\vec{r}$ away from the specified particle. Hence, if the solution is isotropic, the pair distribution function only depends on the absolute value of r. This implies, that the structure factor $S(Q)$ may be averaged over all angular variables and expressed as shown below [258, 259, 263, 264, 267]:

$$S(Q) = 1 + 4\pi \frac{N}{V} \int_0^\infty [g(r) - 1] Q^2 \frac{\sin Qr}{Qr} \mathrm{d}r. \tag{5.17}$$

Here $g(r)$, which now depends only on the distance r between the centers of masses of two protein molecules, is called radial distribution function.

5.1.4 Ornstein Zernicke Equation

According to Equation 5.17, the experimentally measured structure factor S(Q) can be used to determine the radial distribution function g(r). The latter one is defined by the effective interactions between the protein molecules, however, determination of the interaction potential from the radial distribution function is a very complex problem. One of the approaches involves solving of the Ornstein-Zernicke equation [263, 267]

$$h(r_{1,2}) = c(r_{1,2}) + \rho \int d\vec{r}_3 \, c(r_{1,3}) \, h(r_{1,3}), \tag{5.18}$$

where ρ is the density of the protein molecules, $h(r_{1,2}) = g(r_{1,2}) - 1$ is a so-called total correlation function and $c(r_{1,3})$ denotes the direct correlation function, which depends on the pair interaction potential between the molecules. Since we introduced two correlation functions (c and h) instead of the radial distribution function $g(r)$, we still need an additional equation to solve this system. Thus, the "Ornstein-Zernicke" equation requires so-called closure relations 5.19, 5.20 and 5.21 which specify the relation between the direct correlation function $c(r)$ and the potential of interaction $U(r)$.

5.1.5 Closure Relation

In the following the mean spherical approximation (MSA) closure relation (see Equations 5.19 and 5.20) is defined, which is required for the application of both, the screened coulomb and two-Yukawa potential [261, 263, 268].

$$c(r) = -U(r)/k_B T \quad \text{for} \quad r > \sigma \tag{5.19}$$

$$h(r) = -1 \quad \text{for} \quad r < \sigma \tag{5.20}$$

The closure relation developed by Percus and Yevick was applied for the hard sphere and sticky hard spheres potential. The closure relation is defined as follows [263, 269]:

$$c(r) = g(r)[1 - exp(U(r)/k_BT)]. \tag{5.21}$$

5.1.6 Potentials to Model Protein Interactions

Screened Coulomb Potential

The repulsive screened Coulomb (SC) potential was used for protein solutions with trivalent salts featuring an ionic strength smaller than $I < 5$ mM. The definition of the potential is given by Equation 5.22 below.

$$U_{SC}(r) = \begin{cases} \infty & 0 < r < \sigma \\ \frac{\pi\epsilon_0\epsilon\sigma^2\psi_0^2 exp[-\kappa(r-\sigma)]}{r} & r > \sigma \end{cases} \tag{5.22}$$

ε_0 denotes the permittivity of the free space and ε represents the dielectric constant of the solvent, σ denotes the particle diameter and ψ_0 corresponds to the surface potential. The inverse Debye-Hückel screening length is denoted by κ. Additionally, the inter particle spacing is given by r [268, 270, 271]. Utilizing the previously introduced (rescaled) MSA, the structure factor for the SC potential was derived.

Two Yukawa Potential

The two-Yukawa potential (2Y) extends the SC potential. Apart from the repulsive exponential term (K_1), an attractive potential term (K_2) is used as well. By use of the MSA closure relation it is possible to derive $S(Q)$ provided a monodisperse, in this case elliptical, particle system [272].
In this work, the 2Y potential (see Equation 5.23) was used for protein samples admixed with trivalent salt concentrations yielding low ionic strengths within the range of $I < 5$ mM. Here β corresponds to $1/k_BT$ [271, 272].

$$\beta U_{2Y}(r) = \begin{cases} \infty & 0 < r < \sigma \\ -K_1\frac{exp[-Z_1(r-\sigma)]}{(r/\sigma)} - K_2\frac{exp[-Z_2(r-\sigma)]}{(r/\sigma)} & r > \sigma \end{cases} \tag{5.23}$$

Hard Sphere Potential

At ionic strengths ranging from low to moderate, it is possible to consider the surface charge of the proteins as screened. Thus, the overall interaction between the proteins appears to be weak, as the main interaction is facilitated through

excluded volume effects, also known as hard sphere interactions [269, 271]. The hard sphere potential is given by the Equation 5.24 below.

$$U_{HS}(r) = \begin{cases} \infty & \text{for} \quad r < \sigma \\ 0 & \text{for} \quad r \geq \sigma \end{cases} \tag{5.24}$$

In this case σ denotes the particle diameter, whereas r denotes the radius. At moderate ionic strengths, the surface charge of the proteins is sufficiently screened. The overall interparticle interaction is weak, and the protein molecules interact primarily through hard-sphere interactions (excluded volume effect) [266, 271].

Sticky hard Spheres Potential

The sticky hard sphere potential (SHS) is briefly described below. This model requires the Percus-Yevick closure relation. It is a coarse grained model based on the interaction between hard spheres with a hard core, which combines a deep (u_0) and narrow (Δ) attraction potential (square well) at their respective surfaces with an additional short-range attraction. Given the boundaries of the Percus-Yevick closure relation (see Equation 5.21), the Ornstein-Zernike equation can be solved (see Equation 5.18). The sticky hard sphere potential is defined by Equation 5.25 below [266, 271, 273, 274].

$$\beta U(r) = \begin{cases} \infty & r < \sigma = 2R \\ -\beta_0 = \ln\left(\frac{12\tau\Delta}{\sigma+\Delta}\right) & \sigma < r < \sigma + \Delta \\ 0 & r > \sigma + \Delta \end{cases} \tag{5.25}$$

The particle diameter is given by σ, the radius of the particle is denoted as R and the inter particle distance is denoted as r. The stickiness parameter τ is defined as

$$\tau = \frac{1}{12\epsilon} \exp(-U_0/k_B T) \tag{5.26}$$

with ϵ being defined as

$$\epsilon = \frac{\Delta}{(\sigma + \Delta)}. \tag{5.27}$$

The structure factor $S(Q)$ can be determined by use of the Percus-Yevick closure relation (see Equation 5.21), provided the condition of $\Delta \to 0$.

5.1.7 Second Virial Coefficient

The second virial coefficient B_2 is defined as follows:

$$B_2 = 2\pi \int_0^\infty dr\, r^2 \left[1 - \exp(U(r)/k_B T)\right] \tag{5.28}$$

with $U(r)$ representing the pair potential between two particles and r gives the center to center distance between these two particles [196, 273–276]. It is important to note that the second virial coefficient is temperature-dependent due to its definition at infinite dilution, but independent of density or pressure [196].
The second virial coefficient for hard spheres ${B_2}^{HS}$ is defined by the following Equation 5.29 [196].

$$ {B_2}^{HS} = \frac{16\pi R^3}{3} \tag{5.29} $$

If the reduced second virial coefficient B_2/B_2^{HS} is greater than zero, repulsion dominates,

$$ \frac{B_2}{{B_2}^{HS}} > 0(\text{repulsion}) \tag{5.30} $$

whereas in the opposite case

$$ \frac{B_2}{{B_2}^{HS}} < 0(\text{attraction}) \tag{5.31} $$

attraction prevails [196]. Using τ, the reduced second virial coefficient B_2/B_2^{HS} is connected to the SHS potential by the following Equation [276]:

$$ \lim_{\Delta \to 0} \frac{\mathrm{B_2}}{\mathrm{B_2^{HS}}} = 1 - \frac{1}{4\tau}. \tag{5.32} $$

5.1.8 Inverse Intensity Approach

Another approach is to relate the structure factor $S(Q)$ at $Q \to 0$ to the isothermal compressibility χ_T (see Equation 5.33), albeit without applying a potential

$$ S(0) = \rho k_B T \chi_T. \tag{5.33} $$

The osmotic pressure Π for proteins in solution can be expanded by means of the protein number density $\rho = cN_A/M_w$, yielding the following relation [28, 258, 263, 277–280]:

$$ S(0) = k_B T \left(\frac{\partial \Pi}{\partial \rho} \right)^{-1}. \tag{5.34} $$

As an alternative, the osmotic pressure Π can be expanded in terms of the concentration c (see Equation 5.35) [278–280]. Assuming the absence of liquid-liquid phase separation (LLPS), yields $c = c_p \propto \rho$, where ρ denotes the protein number density as defined above.

$$ S(0) = \frac{RT}{M_w} \left(\frac{\partial \Pi}{\partial c} \right)^{-1} \tag{5.35} $$

Here, R denotes the ideal gas constant given in 8.31 $Jmol^{-1}K^{-1}$, thus, yielding the following Equation 5.36

$$\frac{\Pi}{\rho k_B T} = 1 + B_2\rho + ... \tag{5.36}$$

and equation 5.37 respectively [28, 278–280].

$$\frac{\Pi}{cRT} = \frac{1}{M_w} + A_2 c + ... \tag{5.37}$$

Thus, given the condition of $2M_w A_2 c << 1$, the following formalism results in:

$$\frac{1}{S(0)} = 1 + 2M_w A_2 c + ... \tag{5.38}$$

and consequently

$$\frac{1}{S(0)} = 1 + 2B_2\rho + ... \tag{5.39}$$

enabling the virial coefficient (B_2) to be determined. Importantly, the two second virial coefficients A_2 and B_2 are related based on the formalism (Equation 5.40) shown below. Nevertheless, please note that the corresponding units are different.

$$B_2 = A_2 \times \frac{M_w^2}{N_A} \tag{5.40}$$

Considering Equation 5.15 under the condition that the form factor at the origin is given as $P(Q, 0) = 0$, yields the following equation [28, 258, 263, 277–280]:

$$\frac{1}{I(0)} \propto 1 + 2B_2\rho. \tag{5.41}$$

This approach offers the possibility of being applied to both repulsive and attractive conditions without being limited by the constraints imposed by the model.

5.1.9 Synchrotron

First discovered in the 1940s as a secondary reaction in particle accelerators for high-energy physics, synchrotron radiation quickly evolved to become an important and multifunctional scientific instrument. The operating principle of a synchrotron is based on the acceleration of electrons to relativistic speed ($v \approx c$). Upon entry of the storage ring, the electrons have already undergone several accelerations. First, they are accelerated to energies in the range of MeV by use of a linear accelerator. These accelerated electrons are then fed to a booster ring. Here they are accelerated yet another time until they reach energies in the order of GeV; only then the electrons are passed on to the main storage ring. Both,

booster and storage ring force the electrons to describe a circular orbit due to the influence of bending magnets. In the storage ring, the electrons lose energy with each and every orbit, which results from the emission of synchrotron radiation. The energy loss is compensated by use of radio frequency cavities which accelerate the electrons further [281]. Bending magnets not only force the electrons onto a circular orbit, but can also be used for the emission of synchrotron radiation. Linear sections of the storage ring fulfill a series of tasks which range from correction of the beam's trajectory to (re)-focusing of the beam to the emission of synchrotron radiation [281]. By inserting additional magnetic fields to linear sections, which are in this case perpendicularly aligned to the trajectory of the accelerated electrons, it is possible to alter the electron's direction of movement, causing the emittance of synchrotron radiation [281]. In the next generations of synchrotron sources, instead of bending magnets, one uses these specially designed arrays of magnets called wigglers and undulators for the emittance of synchrotron radiation [281]. In the following, we will briefly describe the working principle of an undulator (see Figure 5.2). The shape of the emitted radiation can be described by a narrow cone with γ^{-1} denoting the vertical half-opening angle (see Equation 5.42) [262, 264, 281, 282]. Moreover, the cone is tangential to the electron trajectory and orientated along the flight direction of the electron

$$\gamma^{-1} \approx m_e c^2/\varepsilon_e, \tag{5.42}$$

where ϵ_e is a relativistic energy of an electron. By application of other more convenient units γ is defined as

$$\gamma = 1957 \cdot \epsilon_e \, [GeV] \tag{5.43}$$

[262, 264, 281, 282] yielding $\gamma^{-1} = 0.029°$. Being collimated in such a narrow cone, synchrotron radiation is also very intense. The brightness of modern synchrotron sources is many orders of magnitude higher than that of laboratory X-ray tubes [281]. Undulators are characterized using K, which denotes the so-called magnetic-deflection parameter or in other words the peak magnetic field. In terms of the maximum angular deviation Φ_{max}, K is defined as:

$$\Phi_{max} = K/\gamma. \tag{5.44}$$

Expressing K in terms of the magnetic field B_0 results in

$$K = \frac{eB_0}{mc(2\pi/\lambda_u)} \tag{5.45}$$

with λ_u denoting the spatial periods within the undulator (see Figure 5.2). Compared with the opening angle of the synchrotron radiation, $1/\gamma$, the radiation cone emitted when using an undulator is $1/\sqrt{N\gamma}$ [264, 281, 282].

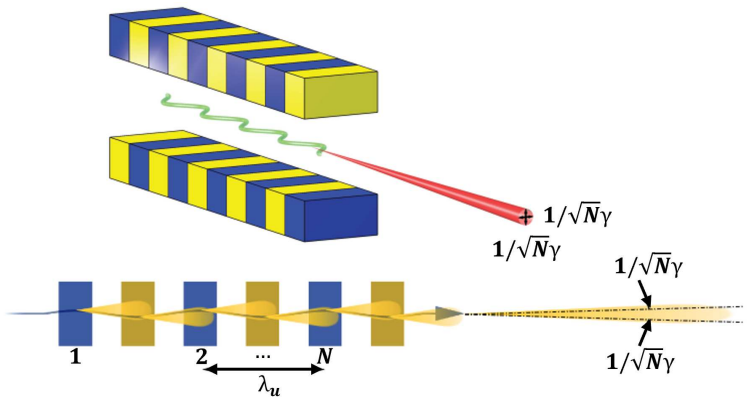

Figure 5.2: *Schematic representation of an undulator, commonly used as an insertion device at synchrotron facilities to obtain X-ray radiation. Two different views are shown for easier visualization: the upper part of the scheme shows a 3D view whilst the lower part shows a topview. This illustration was adapted with changes from Refs [264, 282].*

5.1.10 EMBL SAXS Beamline P12

The SAXS results shown in this doctoral thesis were mostly measured at the P 12 beamline operated by the European Microbiology Laboratory (EMBL) located at the German electron synchrotron, (DESY), which operates the PETRA III storage ring. The most important elements of this beamline are summarized in Figure 5.3.
This beamline, specially equipped for biological samples, is supplied by the low divergence undulator U29. Owing to the double silica crystal Si(111) monochromator, the energy for experiments can be adjusted ranging from 4 up to 20 keV with corresponding wave lengths (λ) ranging from 0.06 to 0.3 nm. However, most commonly a wavelength of 0.124 nm with corresponding energy of 10 keV is applied. Due to the combination of mirrors, slits and collimators, a focused X-ray

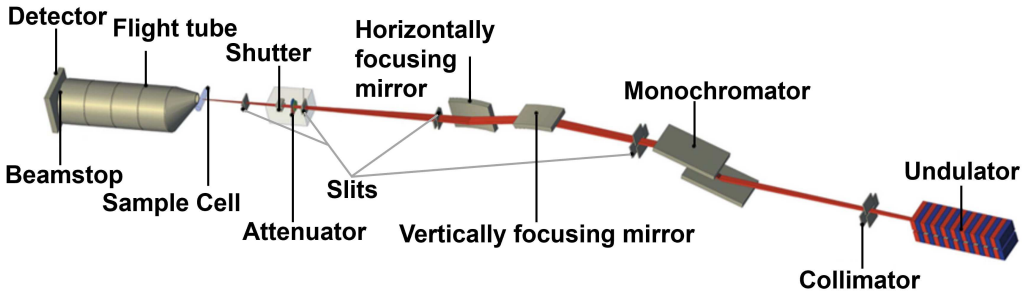

Figure 5.3: *Schematic representation of P-12 beamline operated by the EMBL at the PETRA III storage ring located at DESY. Important components are shown. This illustration was adapted with changes from Ref [283].*

beam of the dimensions $120 \times 200\ \mu m^2$ reaches the sample with a flux of 10^{13} photons per second (s^{-1}). Furthermore, the sample to detector distances can be adjusted to ranges between 1.5 up to 6 m. Most commonly the distance is set to 3.0 - 3.1 m. The total length of the beamline, from the source undulator (U29) to the detector is 83 m Figure 5.3 [283]. Due to the use of two different detectors (Pilatus 6M or Eiger 4M) a resolution from 8 to 10000 Å can be achieved. Sample changing was facilitated by use of the Arinax BioSAXS sample changer for temperatures between 5 up to 60 $^\circ C$ [284].
More precise experimental details on individual measurements are listed in the respective experimental sections of the Results Chapters 7.3.2, 8.5.3 and 9.3.

5.1.11 Xeuss 2.0

Besides synchrotron experiments, the laboratory device Xeuss 2.0 manufactured by XENOCS (France) was used for SAXS measurements as well. The size of the X-ray beam is approximately 1.1×1.5 mm^2. The X-ray beam is generated by a GENIX3D Cu Ultra Low Divergence device [285]. The X-ray beam is monochromotized by a specially developed and coated mirror. The flight tube leading from the X-ray source to the sample chamber is operated under vacuum. The sample chamber on the other hand is operated at atmospheric pressure (atm). Horizontal and vertical positioning of the sample capillaries can be adjusted by use of the respective control motors. The flight tube downstream of the sample chamber towards the detector was evacuated as well. By use of different modules, several sample to detector distances can be facilitated, yielding a Q-range from 0.0042 to 1.42 Å^{-1}. The employed detector is the PILATUS 3R 300K manufactured by DECTRIS [285].

5.1.12 Data analysis

The 2D-SAXS data obtained from different experiments were azimuthally averaged and the resulting intensity profiles of samples and background were further processed. The background measurements ranged from pure water to water and salt to polymer-water-salt mixtures. Depending on the individual sample, the respective background was subtracted in order to evaluate only the scattering contribution of the proteins and thus emphasize the effective interactions occurring among the proteins. Subsequently, the processed data was fitted using Igor Pro and the extension provided by the NIST (Center for Neutron Research) for the versions 6.3 and 9 [271, 286]. The potentials used are described in detail in Chapter 5.1.6. Apart from the model based approach the inverse intensity was assessed, (see Chapter 5.1.8). A calibration to absolute intensity values was not carried out.

The form factor $P(Q)$ that was used to fit the data was calculated based on the script provided by NIST. This script calculates the $P(Q)$ of a sphere based on the data input of an ellipse so that the second virial coefficient of the resulting effective sphere is equal to the second virial coefficient of the ellipse [271]. This was performed to obtain the effective structure factors $S(Q)$ as to be seen in chapter 7.

5.1.13 Structure Determination by X-ray Diffraction

Analogous to SAXS experiments, X-ray crystallography entails the exposure of a sample, in this case a crystalline one, to a collimated X-ray beam followed by the intensity measurements of the scattered photons. Solution scattering is averaged over all orientations of the molecules relative to one another and also to the experimental setup, thus resulting in both: radial symmetry and continuity [287]. On the contrary, X-ray crystallography involves scattering of molecules organized in a crystal lattice resulting in discrete diffraction maxima. Since no radial symmetry prevails, information about specific orientations is preserved, necessitating the rotational repositioning of crystals during data acquisition. In the case of a path difference equal to an integer number of wavelengths with respect to the incident X-rays, the diffracted X-rays constructively interfere and appear as measurable diffraction maxima. Otherwise, the X-rays interfere destructively and thus cannot be observed [287]. The condition at which X-rays interfere constructively, also known as Bragg's law, is

$$2d \sin\theta = n\lambda, \tag{5.46}$$

where d is the distance between a certain set of crystallographic planes. Thus, observing the constructive interference of the scattered X-rays at certain angles (Bragg peaks), one can determine the distances d between the crystallographic planes and, eventually, determine the structure of the crystal, i.e. the lattice parameters, angles of the unit cell and even positions of the atoms (or molecules) within the unit cell. Diffracted radiation at a given wavelength λ requires particular angles of incidence and emission θ to be measured. The number n is referred to as the diffraction order [288].
Mathematically, the same concept can be formulated by writing the structure factor of a crystal as

$$S(h,k,l) = \sum_j f_j \exp[2\pi i(hx_j + ky_j + lz_j)], \tag{5.47}$$

where h, k, l are the Miller indices which uniquely determine a set of parallel crystallographic planes, and x_j, y_j, z_j are the positions of the j-th atom within the unit cell and f_j indicates the resolution-dependent atomic scattering factor [206, 287]. When analyzing crystal structures, the phase is generally lost, as only the intensities derived from the square of the structure factor ($S(h, k, l)$) are measured [287]. Having the position of several atoms identified facilitates phase calculation [206]. Shape and size of a crystalline unit cell is defined by the length of the axes (a, b, c)

and the corresponding angles between them (α, β, γ). The asymmetric unit is defined as the smallest amount of structural information required to reconstruct the entire crystal lattice through symmetries and lattice displacements [287].

5.2 Static Light Scattering (SLS)

To be able to perform static light scattering (SLS) and dynamic light scattering (DLS) measurements, an ALV/CGS-3 goniometer with a digital ALV/LSE-5004 correlator (ALV-GmbH, Langen, Germany) was used, which was operated with the corresponding ALV correlator software V3.0. This setup utilizes a HeNe-Laser with the power of 22 mV and a wavelength $\lambda = 6328\,\text{Å}$. The ALV/CGS-3 device uses a temperature-controlled toluene bath (Haake A10 bath, operated with Haake AC 200 thermostat, Thermo Fisher scientific Inc.).
In static light scattering experiments, the scattering intensity I, averaged over time, depends soley on the scattering contrast K also known as b^2, the concentration c and the osmotic pressure Π. However, this only applies provided the condition that density fluctuations of the solution itself are excluded. Hence, the scattering intensity I can be established as shown in Equation 5.48. k_B denotes the Boltzmann constant and T the temperature [289].

$$I \sim b^2 k_B T \frac{c}{(\frac{\partial \Pi}{\partial c})_{T,N}} \tag{5.48}$$

A quantitative measure for the interaction between solute and solvent was provided by Van´t Hoff [289] (see Equation 5.49 and 5.37)

$$\frac{\partial \Pi}{\partial c} = k_B T \left(\frac{1}{M_w} + 2A_2 c + ... \right). \tag{5.49}$$

Here, the molecular weight is denoted as M_W and the second virial coefficient as A_2. When the incident beam is scattered, it depends on the scattering contrast K, which is the result of the differences between the refractive indices of solvent ($n_{D,0}$) and sample (n_D). Thus, the refractive index is dependent on both, the wavelength of the incident beam as well as the concentration of the investigated sample. Taking into account those two factors, yields the following relation:

$$K = b^2 = \frac{4\pi^2 \; n_{D,0}^2 \left(\frac{\partial n_D}{\partial c}\right)^2}{N_A \lambda^4}. \tag{5.50}$$

The specific refractive index increment is denoted as $(\partial n_D / \partial c)$, the Avogadro number is denoted with N_A and the wavelength is given as λ. The scattered intensity is inversely proportional with to the wavelength of the incident light to the power of four [261, 289–292].
A calibration to absolute scattering intensities can be carried out by measuring of

toluene, a known standard. Toluene has a refractive index comparable to quartz glass ($n = 1.496$ for toluene [289] $n = 1.543$ [293] for quartz glass), which enables a minimalization of reflections between the two interfaces. Using the Rayleigh ratio R_θ, it is possible to define the scattering intensity calibration as follows [261, 263, 289–291]:

$$R_\theta = (I_{\text{sample}} - I_{\text{solvent}}) \frac{I_{\text{standard,absolute}}}{I_{\text{standard}}} \tag{5.51}$$

Here, R_θ is the so-called absolute scattering intensity, which is independent from the experimental setup e.g. scattering volume V or sample to detector distance r, with $I_{\text{standard,absolute}}$ and I_{standard} representing the absolute scattered intensity of the standard, and the intensity of the standard. I_{sample} and I_{solvent} denote the intensity of the sample and the intensity of the solvent respectively.
The absolute intensity R_θ depends on the form factor ($P(Q)$) and can be rewritten as follows:

$$\frac{K_c}{R_\theta} = \frac{1}{M_w P(Q)} + 2A_2 c + \dots . \tag{5.52}$$

When investigating particles which fulfill the condition of (r$< \lambda/20$), $P(Q)$ can be assumed to be unity within the measured Q-range, thus achieving scattering which in turn is independent from the scattering angle (2θ). The resulting Equation gives the inverse intensity K_c/R_θ

$$\frac{K_c}{R_\theta} = \frac{1}{M_w} + 2A_2 c. \tag{5.53}$$

Alternatively, the Intensity R_θ/K_c can be defined as [292]:

$$\frac{R_\theta}{K_c} = M_w P(Q) - 2A_2 \; c \; {M_w}^2 P^2(Q), \tag{5.54}$$

by utilizing an alternative definition of the Rayleigh ratio (see Equation 5.51)

$$R_\theta = \frac{(I_{\text{sample}} - I_{\text{solvent}})\, r^2}{I_0 V}. \tag{5.55}$$

Here, r denotes the distance between the scattering volume and the detector, while V indicates the volume of the scattering solution [289, 292].

5.3 Dynamic Light Scattering (DLS)

In dynamic light scattering (DLS) experiments, information can be obtained from fluctuations in the scattering intensity. In this regard, it is useful to establish the

time correlation function, which is defined by the following formalism [263]:

$$\langle I(Q,t_0)I(Q,t_0+t)\rangle = \lim_{T_M\to\infty}\frac{1}{T_M}\int_0^{T_M} I(Q,t_0)I(Q,t_0+t)\ \mathrm{d}t_0 \tag{5.56}$$

here executed for two cases in which the time delay t is either 0 or ∞. The first case yields [263]:

$$\lim_{t\to 0}\langle I(Q,t_0)I(Q,t_0+t)\rangle = \langle I(Q)^2\rangle. \tag{5.57}$$

the latter one yields:

$$\lim_{t\to\infty}\langle I(Q,t_0)I(Q,t_0+t)\rangle = \langle I(Q)\rangle^2. \tag{5.58}$$

Given short delay times, Equation 5.56 can be reduced to Equation 5.57 whereas longer delay times result in an uncorrelated intensity (see Equation 5.58). By combination of the two Equations (5.57 and 5.58) the following time auto correlation function ($g2(Q,t)$) can be obtained. Here, the $\langle ...\rangle$ specify the time average [263, 289, 294–296].

$$g^2(Q,t) = \frac{\langle I(Q,t_0)I(Q,t_0+t)\rangle}{\langle I(Q,t_0)\rangle^2} \tag{5.59}$$

The Siegert Relation (Equation 5.60) connects the time auto correlation function (Equation 5.59) with the normalized field auto correlation function (Equation 5.61), yielding the following formalism [261]:

$$g^2(Q,t) - 1 = [\beta\, g^1(Q,t)]^2. \tag{5.60}$$

Here β is defined as the coherence factor, which, in addition to the optical alignment and scattering properties of the solute, depends as well on the accuracy of the carried out optical calibration of the instrument. For the DLS measurements shown in this thesis, $\beta \sim 1$ can be assumed.

The normalized field auto correlation function is defined as follows:

$$g^1(Q,t) = \frac{\langle E(Q,t_0)E^*(Q,t_0+t)\rangle}{\langle I(Q)\rangle}. \tag{5.61}$$

with $E(Q,t)$ denoting the amplitude of the electric field of the laser wave [263, 289, 290, 296].
Usually, the decay of the $g2$-function due to dynamics of the scatteres in the system, can be described by an exponential function. For more complex types of dynamics, involving several length scales, one can use the sum of several exponential terms. Based on the assumption of a two-component dynamics, the fast and slow components are specified by the subscript 1 and 2 respectively. In order to approximate the auto correlation function (Equation 5.59), this double exponen-

tial fit function was used. The characteristic relaxation time (τ) can be obtained by the following formalism [297–299]:

$$g2(t) - 1 = \{X_1 \exp[-2(t/\tau_1)] + X_2 \exp[-2(t/\tau_2)]\} \tag{5.62}$$

Assuming that the relaxation time is related to the diffusion of the particles in the solution, one can determine the hydrodynamic radius (r_h), which is linked to the diffusion coefficient (D), via Equation 5.63, developed by Stokes and Einstein [263, 289].

$$D = \frac{k_B T}{6\pi\eta r_h} \tag{5.63}$$

The viscosity is denoted as η. D is connected to the normalized field auto correlation function $g1(Q,t)$ (see Equation 5.61) by the following relation [263, 289, 296]:

$$g1(Q,t) = \exp[-\Gamma t]. \tag{5.64}$$

The decay rate Γ is defined by [263, 289, 294].

$$\Gamma = DQ^2. \tag{5.65}$$

Chapter 6

Complementary Experimental Methods

6.1 Ultraviolet-visible (UV/vis) Spectroscopy of Protein solutions

Ultraviolet-visible (UV/vis) spectroscopy of protein solutions enables a precise determination of the protein concentration by absorbance measurement [300, 301], providing a simple yet efficient approach. The spectrometer measures the ratio between the light intensity I being transmitted through the sample and the incident light intensity I_0. This ratio can then be used to calculate the absorbance A of a given solution [302]:

$$A(\lambda) = \log_{10} \frac{I_0}{I} \tag{6.1}$$

Following the law developed by Beer and Lambert:

$$A(\lambda) = \epsilon \times c \times d, \tag{6.2}$$

the concentration of an absorbing protein in solution is proportional to the total absorption of the solution [303]. Here, the variable ϵ indicates the respective protein specific extinction coefficient (see Table 6.1), c represents the protein concentration in mg/ml and d corresponds to the width of the used cuvette in cm being, proportional to the path length of the monochromatic UV-light passing through the specimen.
The exploitation of an absorption maximum between 279 and 280 nm, caused by aromatic residues of the amino acids tryptophan, tyrosine and phenylalanin contained in the primary structure, enables an accurate concentration determination of the dissolved protein [301, 304].

Table 6.1: *Extinction coefficients of the investigated proteins. The information shown is obtained from Refs. [222, 305, 306].*

Protein	**BLG**	**BSA**	**HSA**	**OVA**
Extinction coefficient $\epsilon_{0.1\ \%}^{279\ \mathbf{nm}}$ **ml/(mg×cm)**	0.961	0.667	0.531	0.700

Owing to inevitable variations associated with mixing, pipetting and sampling, a dilution series (1 : 500, 1 : 250 and 1 : 200) was prepared. In order to prevent and to account for possible dilution errors, a 1 : 10 pre-dilution was initially prepared, which was then used for the aforementioned dilution series. The obtained average concentration value, ultimately defines the protein concentration of the protein stock solution. Importantly, when working with dilutions, the dilution factor requires to be taken into account.
The UV/vis spectroscopy measurements were carried out utilizing the Cary 50 UV/vis spectrometer (Varian Technologies, USA). The setup was operated by use of the software Cary WinUV (Varian Technologies, USA).
The UV/vis spectrometer was also used to determine the transition temperatures of BSA-LaCl3 co-salt systems, which feature the temperature-driven phenomena of lower critical solution temperature behavior (LCST). Therefore, the sample holder of the UV/vis spectrometer was tempered as desired by use of a coupled water bath (Haake A10B and SC 150, Thermo Fisher Scientific, USA). A unique feature of this system is the ability to define a heating ramp, in which the prevailing temperature can be increased, for example by 0.5° C per minute. However, it is also possible to set other desired heating ramps. The water bath was calibrated by use of a thermocouple attached to the sample holder. The UV/vis absorbance measurement was synchronized with the applied heating ramp, yielding a absorbance spectra ranging from 500 nm to 800 nm for every minute. An initial temperature of 12° C and a final temperature of 48° C were set, thus, yielding 72 spectra, which is in accordance with the applied heating ramp. After baseline correction, determined by the absorbance of water, these spectra were summed up to obtain a final curve.

6.2 pH measurements

The pH value is defined as the activity of the hydrogen ion. In this context, the pH value is proportional to the negative decadic logarithm of the hydrogen ion activity [307, 308]:

$$pH = -\log_{10} \alpha_{\mathrm{H}^+} \tag{6.3}$$

The activity α_{H^+} in this case is the effective concentration of the hydrogen ion in the solution [308]

$$pH = -\log_{10} c_{\mathrm{H}^+}. \tag{6.4}$$

Alternatively, hydronium ions ($\mathrm{H3O}^+$) can also be used to determine the pH value [309]:

$$pH = -\log_{10} \mathrm{H3O}^+. \tag{6.5}$$

The pH scale is defined so that a solution is regarded as neutral with a pH value of 7, solutions with a pH value below 7 as acidic and above a pH value of 7 as alkaline [288, 307]. Consequently, an excess of $\mathrm{H3O}^+$ occurs in acidic solutions, whereas an excess of hydroxyl ions (OH^-) is present in alkaline solutions [307].

Prior to pH measurements, a three-point calibration was carried out using pH-adjusted buffer solutions (pH 4, 7 and 10). Typically, a pH sensor consists of two electrodes. In the inner space between the two electrodes resides a buffer filled reservoir with a constant pH value, which is measured by the reference electrode. The working electrode now measures the diffusion of H_3O^+ ions caused by the H_3O^+ gradient between inner and outer layers of the working electrode. Furthermore, the ratio between the reference- and the working electrode is measured so that the H_3O^+ concentration of the solution under investigation can be precisely determined [309].

6.3 Microscopy

The optical microscopy is a well established method for magnified visualization and subsequent recording of small objects or tiny structures. The principle of optical microscopy is based on the refraction of the visible part of light and the resulting magnification of a specimen [310]. By means of microscopy, it is possible to identify different protein phases, such as LLPS, aggregates or protein crystals. Images and videos were captured by the Axio-Cam ICc5 camera, combined with 5×, 10× or 20× magnification, installed on an Axio Scope.A1 microscope (Carl Zeiss AG). The microscope was operated using the ZEN Lite software of 2012 (Carl Zeiss AG). Further experimental details such as sample preparation can be found in chapter 4.4.

Part IV

Results

Chapter 7

Results I: Effective interactions and phase behavior of protein solutions in the presence of hexamine cobalt(III) chloride

This chapter is entirely based on the following Publication:

M. D. Senft, R. Maier, A. Hiremath, F. Zhang, and F. Schreiber, Effective interactions and phase behavior of protein solutions in the presence of hexamine cobalt(III) chloride, The European Physical Journal E 46, 10.1140/epje/s10189-023-00376-6 (2023)

Contribution:	
Research design:	MDS, RM, FZ, FS
Experiments:	MDS, AH
Data analysis and interpretation:	MDS, FZ
Paper Writing:	MDS, FZ, FS
Funding:	FS, FZ

7.1 Abstract

It is well established that deoxyribonucleic acid (DNA) and ribonucleic acid (RNA) exhibit a reentrant condensation (RC) phase behavior in the presence of the trivalent hexamine cobalt (III) cations (Hac) which can be important for their packing and folding. A similar behavior can be observed for negatively charged globular proteins in the presence of trivalent metal cations, such as Y^{3+} or La^{3+}. This phase behavior is mainly driven by charge inversion upon an increasing salt concentration for a fixed protein concentration (c_p). However, as Hac exhibits structural differences compared to other multivalent metal cations, with six ammonia ligands (NH3) covalently bonded to the central cobalt atom, it is not clear that Hac can induce a similar phase behavior for proteins. In this work, we system-

atically investigate whether negatively charged globular proteins β-lactoglobulin (BLG), bovine serum albumin (BSA), human serum albumin (HSA) and ovalbumin (OVA) feature Hac-induced RC. Effective protein-protein interactions were investigated by small-angle X-ray scattering (SAXS). The reduced second virial coefficient (B_2/B_2^{HS}) was obtained as a function of salt concentration. The virial coefficient analysis performed confirms the reentrant interaction (RI) behavior for BLG without actually inducing RC, given the insufficient strengths of the interactions for the latter to occur. In contrast, the strength of attraction for BSA, HSA and OVA are too weak to show RC. Model free analysis of the inverse intensity $1/I(Q \to 0)$ also supports this finding. Looking at different Q-range by employing static (SLS) and dynamic light scattering (DLS) experiments, the presence of RI behavior can be confirmed. The results are further discussed in view of metal cation binding sites in nucleic acids (DNA and RNA), where Hac induced RC phase behavior.

7.2 Introduction

Effective protein-protein interactions determine the phase behavior of proteins in aqueous solutions, including liquid-liquid phase separation (LLPS) and crystallization. Understanding as well as predicting the phase behavior of proteins is therefore not only beneficial for X-ray structural analysis of protein crystals, but also for a more profound understanding of diseases related to the aggregation of proteins [28, 311, 312]. Furthermore, the occurrence of metastable LLPS in protein solutions represents an important mechanism for biological structure formation [25, 26, 28, 31, 311, 313–317]. Diseases such as eye cataract [315, 316], lateral sclerosis [31, 314], sickle cell anemia [25, 26], Alzheimer's disease in line with amyloidosis [31, 313] are related to unwanted protein fiber formation, crystallization, or aggregation.
In aqueous solution, the effective interactions of proteins turn out to be rather complex, as various environmental parameters [312, 317–319] such as the protein concentration, concentration and valence of the salt ions, temperature and pH-value strongly influence their interactions [47]. Moreover, protein-protein interactions are determined by the protein's surface charge pattern or by a modulation of hydrophilic and hydrophobic interactions. In combination with Coulomb interactions, hydrogen bonding, and specific or non-specific salt bridging, this interplay of multiple interactions results in a rich phase behavior of aqueous protein solutions. Further studies, focusing on the modeling of liquid-liquid phase transitions in protein- and colloid-systems, pointed out the relevance of short-ranged attractive forces [190, 196, 275, 320, 321].
Reentrant condensation (RC) is an intriguing phenomenon which occurs in various acidic, globular proteins, given the presence of multivalent metal salts such as YCl_3 [47, 59, 62, 106, 322]. For a fixed protein concentration (c_p) combined with a salt concentration below the value of c^*, or above a second value c^{**}, with

$c^* < c^{**}$, the protein solution appears translucent. If the salt concentration is between c^* and c^{**}, protein condensation occurs, which may include LLPS, aggregation, and protein crystallization [59, 60, 62, 63, 318]. Responsible for the reentrant condensation behavior are both the cation-mediated inversion of the protein charge and the intermittent cation-mediated attraction [107]. Charge reversal and effective attraction induced by multivalent metal ions have been further investigated not only in theoretical studies but also in experiments and simulations [55, 107, 323, 324]. In order to fundamentally understand the origin of the macroscopic phase behavior and the involved interactions, the underlying forces need to be investigated [62].
DNA has been known to condense in aqueous solution in the presence of multivalent cations, such as hexamine cobalt (III) (Hac), for a long time [325]. Due to advancing research in the field of gene therapy, interest in the phenomenon of DNA condensation with multivalent cations increased. The goal of this research field is to develop efficient ways of gene transfer, which requires a simple, effective, and yet reversible method without damaging the DNA in the process [100].
The relatively inert trivalent cation hexamine cobalt (III) features six tightly bound amino groups which inhibits the option of direct coordinate ion bonds between the cobalt and polar groups of the DNA helix [325], therefore fulfilling the above required conditions [100]. In order to enable DNA condensation, approximately three out of four negative charges have to be neutralized by a bound cation [326]. In other words, approximately 90% of the total charges exhibited by DNA have to be neutralized to allow for condensation [327, 328]. DNA neutralization enables and facilitates the compression of DNA as it occurs in the genomes of cells or viruses as well as the deformation of DNA mediated through proteins [326]. When trivalent ions are present in a solution with DNA, the DNA also undergoes RC. It should be emphasized that the driving force for the condensation of DNA is the electrostatic interaction between the cations and the DNA. Furthermore, this leads to attractive, correlated counter-ion fluctuations. Thereby, the counterions also screen Coulombic repulsions between DNA phosphates before the condensation takes place [326, 328]. Apart from DNA condensation, investigations were also performed on RNA [234, 329, 330].
Moreover, Hac proved to be of use in other biological research areas. Hac has been successfully deployed to inhibit an RNA polymerase of West Nile virus in order to investigate the role of magnesium ions, necessary for the catalysis carried out by this RNA polymerase [331]. Furthermore, Hac was used in transformations with *Escherichia coli* to either change the confirmation of the DNA or serve as a counterpart of vitamin B_{12}. Here, it either interferes with the constituents of the vitamin or disrupts its transport system [332]. In addition, Hac has also been proven to possess anti-bacterial and anti-viral effects [233]. The element cobalt (Co) is a standard component of metal alloys [333] which are, among others, used for biomedical implants (e.g. hip prothesis). Expedient wear in combination with corrosion of implants leads to in vivo release of metal ions [334, 335]. This may support unwanted protein aggregation, triggering associated diseases such as lat-

eral sclerosis or Alzheimer´s [336, 337], and may as well trigger metal contact hypersensitivity [337]. When comparing proteins with DNA or conventional colloid suspensions, which are governed by identical charges, it turns out that on the surface positive as well as negative charges are present. These charges are arranged in a rather complex, unevenly distributed pattern, resulting in differences regarding the interactions. Moreover, a DNA molecule can be approximated with a thin extended rod-like shape whereas the proteins examined here feature a globular geometry. In addition, the complex surface charge pattern, together with other kinds of interactions, like hydrophobic interactions or hydration, increase the complexity of the phase behavior for proteins in solution [47, 312, 319]. This work conducts a systematic study of the effective interactions and phase behavior of the proteins BLG, BSA, HSA, and OVA in aqueous solution in the presence of the trivalent salt hexamine cobalt (III) chloride. All mentioned proteins already featured RC behavior induced by several trivalent metal salts [58].
We aim to explore how different concentrations of Hac can tune the effective interactions in these protein solutions and if it is sufficient to induce RC phase behavior. For that, the effective protein-protein interactions were evaluated based on the analysis of the reduced second virial coefficient from SAXS measurements. In addition, SLS and DLS experiments were carried out to explore a different Q-range and to investigate diffusive dynamics. The results are further discussed in view of metal cation binding sites in nucleic acids (DNA and RNA), where Hac induced RC phase behavior.

7.3 Experimental Section

7.3.1 Materials and Sample Preparation

The proteins BLG from bovine milk (product no. L3908, purity of $\geq 90\%$), BSA (product no. A3733, purity of $\geq$ 98%), HSA (product no. A9511, purity of $\geq 97\%$) and OVA from chicken egg white (product no. A5503, purity of $\geq 98\%$) were purchased from Merck and used in the experiments without additional purification. Fundamental biophysiochemical properties of the proteins are summarized in Table 1. Note that the purchased protein β-lactoglobulin (BLG) is a mixture of the two genetic variants A and B, which differ only at two locations within their primary sequence [212]. Moreover, given physiological conditions, BLG features predominantly a dimer configuration [204, 214].
Protein stock solutions were obtained by mixing the required amount of the respective protein stock with deionized and degassed Millipore water (conductivity is 18.2 MΩ cm). The concentration of the protein stock solution was determined by use of a Cary 50 UV/vis spectrophotometer (Varian Technologies) with the appropriate extinction coefficients (see Table 7.1) and the Cary WinUV operating software. The protein solutions were stored in appropriate parafilm-sealed containers to avoid de novo solution of gasses and placed in the fridge at 4 °C [341]. In order

Table 7.1: *Biophysiochemical Properties of BLG, BSA, HSA, and OVA with respective reference.*

Parameters	**BLG**	**BSA**	**HSA**	**OVA**
# amino acid	162 [212]	583 [220]	585 [222]	385 [226]
Molecular weight [kDa]	37 [205]	66.4 [221]	66.44 [222]	45 [225]
pI	5.2 [214]	4.6 [58]	4.7 [222]	4.54 [229]
Charge (pH 7) [e]	-10 [213]	-11 [58]	-9 [58]	-11 [338]
Specific volume [ml/g]	0.750 [339]	0.735 [339]	0.754 [340]	0.745 [306]
Extinction coefficient [ml·mg^{-1} · cm^{-1}]	0.961 [305]	0.667 [305]	0.531 [305]	0.700 [305]

to avoid unwanted bacterial or fungi growth, the protein solutions were used for a maximum of three weeks [342]. Hexamine cobalt (III) chloride ($[Co(NH_3)_6]Cl_3$) powder was purchased from Merck (H7891, for use in transformations, X-ray crystallography), dissolved in deionized and degassed Millipore water and used in the carried out experiments without further purification. This multivalent salt features a molecular weight of 264.48 g/mol and a density of 1.71 g/ml [231]. Systematic deviations arising from variations in protein batches, preparative inaccuracies, and fluctuations in protein and salt stock solutions cannot be ruled out.

7.3.2 Small-Angle X-Ray Scattering

Small-Angle X-ray Scattering (SAXS) experiments were conducted at the P12 beamline of the EMBL, DESY (Hamburg, Germany) [283]. The system employs a highly focused X-ray beam (120 × 200 µm) with an energy of 10 keV, which corresponds to a wavelength of (λ = 1.24 Å). The sample-to-detector distance was set to 3 m. The employed 2M Pilatus (Dectris) detector covered a Q range of 0.002 to 0.45 Å^{-1} [283]. The samples were exchanged by the use of a flow cell. For each sample, 40 exposures of 0.04 s were averaged. Additional SAXS data was collected using the laboratory SAXS instrument Xeuss 2.0 (Xenocs, Grenoble, France) employing a GeniX 3D microfocus X-ray tube consisting of a copper anode, using an X-ray energy of 8.05 keV which corresponds to a wavelength of λ = 1.54 Å. With a sample-to-detector distance of 1666 mm, the employed Pilatus 300K (Dectris) detector covered a Q range of 0.0076 up to 0.344 Å^{-1}. The protein solutions were measured in quartz capillaries with a diameter of 1.5 to 2.0 mm (WJM-Glas Müller GmbH, Berlin, Germany). The acquisition time for each measurement was set to two hours. Each sample preparation was carried out right

before the measurements. The 2D data obtained was azimuthally averaged to yield intensity profiles. Subsequently, the solvent background was measured, treated in a similar manner and finally subtracted from the intensity profiles. Afterward, the background-corrected data was fitted by use of the ellipsoidal sticky hard sphere potential (SHS), originating from Baxter [274], as implemented by the National Institute of Standards and Technology provided add-on for IGOR PRO 6.37 and 9 [286]. The data was analyzed utilizing the same method explained in the references [64, 65]. For a spherical particle of radius R, the SHS is defined as follows:

$$\beta U(r) = \begin{cases} \infty & r < \sigma = 2R \\ -\beta_0 = \ln\left(\frac{12\tau\Delta}{\sigma+\Delta}\right) & \sigma < r < \sigma + \Delta \\ 0 & r > \sigma + \Delta \end{cases} \tag{7.1}$$

Here, β represents $\frac{1}{k_B T}$, τ represents the stickiness parameter, and Δ denotes the width of the square well. The diameter of the hard sphere is denoted by σ, and r denotes the particle spacing. In order to determine the structure factor, a perturbative solution of the Percus-Yevick closure relation was used [273, 274]. In the limit $\Delta \to 0$, the reduced second virial coefficient can be calculated based on

$$\lim_{\Delta \to 0} \frac{\mathrm{B_2}}{\mathrm{B_2^{HS}}} = 1 - \frac{1}{4\tau} \tag{7.2}$$

As shown in equation 7.2 the reduced second virial coefficient is obtained by dividing the second virial coefficient (B_2) by the second virial coefficient for hard spheres ($B_2{}^{HS}$) of radius R given by $\mathrm{B_2^{HS}} = 16\pi\mathrm{R}^3/3$. Simulations and theories have resulted in a universal $\mathrm{B_2/B_2^{HS}}$ value of ≈ -1.56 for the liquid-gas transition in a number of different systems, provided the application of the Percus-Yevick closure relation [106, 198, 275]. Moreover, other potentials such as Screened Coulombic (SC), Two Yukawa (2Y) and hard spheres (HS) were used to fit the SAXS data for different protein systems and different salt concentrations. A detailed description of these potentials can be found in the Supporting Information (see Chapter 7.6). Besides the volume fraction, the axes of the ellipsoids (R_a and R_b) were fixed to R_a 37.6–39.0 Å, R_b 19.5–20.0 Å for BLG, R_a 17.0 Å and R_b 42.0–44.4 Å for BSA. Detailed information on HSA, and OVA, can be found in Table 7.2 in the Supporting Information (see Chapter 7.6). Moreover, the scattering length density (SLD) of the proteins was set to 7.33×10^{-7} [Å^{-2}] for BLG and 7.32×10^{-7} [Å^{-2}] for BSA, HSA, and OVA respectively. The background was set to appropriate values for each curve individually. In order to prevent artificial coupling between the well width Δ and the stickiness parameter τ, Δ was kept at 0.01 σ for all fitted data. Further details on the fitting process and selected potentials for fitting of OVA and HSA SAXS-datasets are shown in the Supporting Information (see Chapter 7.6). We note that B_2 is a simplified way of quantifying the interactions, inter alia, due to the angular average of non-spherical proteins.

7.3.3 Static and Dynamic Light Scattering

Further structural and dynamical information was obtained by dynamic light scattering (DLS) experiments, which were conducted on a pure Hac solution (50 mM), a pure BSA (20 mg/ml) solution and several BSA (20 mg/ml) solutions containing increasing concentrations of Hac (1 to 50 mM) [343]. Prior to the measurements, all samples were filtered using syringe filters (Whatman Puradisc 13; Global Life Sciences Solutions Operations Uk Ltd.) with a 0.45 µm pore size. In this work, an ALV/CGS-3 goniometer with an ALV/LSE-5004 digital correlator (ALV-GmbH, Langen, Germany) operated by the corresponding ALV-Correlator software V 3.0, was used.This instrument utilizes a HeNe-Laser with a wavelength of $\lambda = 6328$ Å as a light source. Quartz glass cuvettes (Pyrex; Corning, Ny, USA) were cleaned with acetone, and after the evaporation of the acetone, filled with the sample solution and subsequently measured. A calibration to absolute scattering intensities was carried out by the use of a toluene measurement, as standard. Using the Rayleigh ratio R_θ the scattering intensity was calibrated using toluene as a standard [289]. The intensity (R_θ/K_c), with K denoting the scattering contrast (Equation 7.3) and c denoting the concentration, can be equated to the inverse of the intensity K_c/R_θ due to the relation of $R_\theta \sim \mathrm{I}_{\mathrm{sample}} - \mathrm{I}_{\mathrm{solvent}}$. Additionally, the measured intensity depends on *P(Q)* of the sample but given the case of small particles ($r < \lambda/20$), $P(Q)$ can be assumed to be unity within the observed Q-range, and therefore the scattering is independent from the scattering angle 2θ [289]. Based on the aforementioned, it is sufficient to perform the measurements only with one angle. In this work, angles between 70 and 90° were used [289].

$$K = \frac{4\pi^2 n^2 \left(\frac{dn}{dK}\right)^2}{N_A \lambda^4} \tag{7.3}$$

Changes in the scattering signal over time are of interest in terms of dynamic information. This can be quantified by the use of the auto correlation function $g_2(t) - 1$ [263, 289, 295].

$$g_2(t) = \frac{\langle I(t_0) I(t_0 - t) \rangle}{\langle I(t_0) \rangle^2} \tag{7.4}$$

Here $\langle ... \rangle$ denotes a time average, the term $I(t_0)$ denotes the scattered intensity at the time t_0 while t denotes the time difference of the correlator. The characteristic relaxation time τ, is obtained by use of the normalized $g_2 - 1$ (Equation 7.5), shown below [299].

$$g_2(t) - 1 = \{A_1 \exp[-2(t/\tau_1)] + A_2 \exp[-2(t/\tau_2)]\} \tag{7.5}$$

Due to the presence of two-component dynamics, the fast and slow components are denoted by subscript 1 and 2 respectively. This double exponential fit function was used to approximate the auto-correlation function (Equation 7.4). All datasets

were fitted utilizing Equation 7.5 to achieve consistency. The fits were carried out by use of MATLAB.

7.4 Results and Discussion

7.4.1 Visual Inspection of the Phase Behavior

First, the phase behavior of various globular proteins was investigated in the presence of Hac at room temperature $(21 \pm 2)\,^{\circ}\mathrm{C}$. The protein concentration was varied between 5 and 100 mg/ml, while the salt concentration was varied between 1 and 50 mM. All examined proteins showed neither crystal growth nor LLPS or aggregation. This is exemplified for 80 mg/ml BLG in Figure 7.1. Owing to the orange color of the dissolved salt, a stronger yellow tint can be seen at higher salt concentrations. Apart from the yellow tint, no opacity or condensates become apparent [47, 58, 59, 62, 65, 169, 266, 344]. A similar assessment for HSA and OVA can be found in the Supporting Information (see Chapter 7.6).

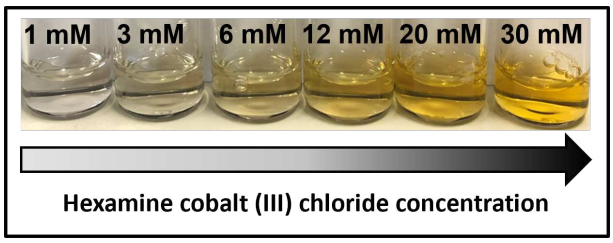

Figure 7.1: *Photograph of BLG with a concentration of* 80 *mg/ml admixed with increasing Hac concentrations (*1 *mM to* 30 *mM, left to right). Due to the orange color of the dissolved salt Hac, an increasing yellow tint can be seen at higher salt concentrations. No aggregation is to be seen.*

To gain further insight, the effective protein-protein interactions of the protein salt solutions were investigated via systematic SAXS measurements. Figure 7.2 shows representative SAXS measurements for 80 mg/ml BSA and 80 mg/ml BLG with increasing Hac concentrations in H_2O (data for OVA and HSA can be found in Figure 7.8 and Figure 7.9, shown in the Chapters 7.6.2 and 7.6.3).
In both protein-salt systems, at low salt concentrations, the net negative charges of the protein molecules dominate the effective protein-protein interactions, as illustrated by a correlation peak at Q 0.06Å^{-1}. An increase in the salt concentration results in an increase in low-Q intensity, which indicates reducing repulsion. Concurrently, the correlation peak fades. As the salt concentration is further increased to 6 mM (for BLG) and 15 mM (for BSA), respectively, attractive interactions dominate the protein salt system. The highest attractive strength is visible at 15 mM salt for BSA and at 12 mM salt for BLG. At higher salt concentrations (20 mM to 50 mM for BSA and 15 mM to 50 mM for BLG), the attractive strength reduces, as indicated by the decreasing low-Q intensities (Figure 7.2 a and b).

This pattern of increasing and subsequent decreasing low-Q intensities as a function of increasing salt concentration resembles to some extent RC phase behavior and is labeled reentrant interaction (RI). Data for HSA and OVA can be found in the Supporting Information (see Chapter 7.6).

Qualitatively, from the provided SAXS profiles, it can be deduced that the above characterized behavior is more pronounced for BLG than it is for the other proteins [63–65, 344]. Previous studies showed that RC is a common phase behavior for BLG, BSA, HSA, and OVA in the presence of either YCl_3, $LaCl_3$, $FeCl_3$ or $AlCl_3$ [58]. Investigations of RC by means of SAXS have shown that RC is associated with an increasing, followed by a decreasing, intensity at low-Q values, given the prerequisite of a constant protein concentration combined with a continuously increasing salt concentration [64, 65]. Additional data sets for 80 mg/ml OVA and HSA, exhibiting a similar but less pronounced behavior are provided in the Chapter 7.6 (see Figures 7.8 and 7.9).

7.4.2 SAXS Characterization of the Effective Interactions

In order to analyze and quantify the effective protein-protein interactions, models employing an ellipsoidal form factor paired with different interaction potentials were fitted to the SAXS data. Figure 7.2 displays SC and SHS model fits for BSA and 2Y followed by SHS model fits for BLG (Figure 7.2 c) with continuously increasing Hac concentrations. Additional fitted SAXS data for the proteins OVA and HSA are included in the Supporting Information (see Chapter 7.6). SC interaction potential fits (BSA) and 2Y interaction potential fits (BLG) were confined to low salt concentrations (0 mM to 5 mM for BSA and 0 to 4 mM for BLG). For these conditions, the electrostatic repulsions prevail, owing to net negative surface charges of the respective dissolved proteins.

In order to describe the attractive potential arising for higher salt concentrations, the SHS combined with an ellipsoidal form factor was used. In agreement with Equation (7.2), the reduced second virial coefficient (B_2/B_2^{HS}) was determined. The results of B_2/B_2^{HS} for BLG and BSA are summarized in Figure 7.3 a, as a function of the salt concentration c_s. Values below $B_2/B_2^{HS} < 0$ represent net attraction, whereas in the opposite case $B_2/B_2^{HS} > 0$, net repulsion prevails.

As to be seen, the curve for BLG is located below the one for BSA, implying higher attractive strengths. BLG features a local minimum around 12 mM with a corresponding B_2/B_2^{HS} value of -1.48, while BSA features a minimum at 15 mM with a corresponding B_2/B_2^{HS} value of 0.033. Hence, it can be deduced that BSA remains within the neutral range at 15 mM Hac, while BLG exhibits a more pronounced attraction. Moreover, these two minima hardly touch the universally predicted B_2/B_2^{HS} values of -1.56 [106] at the critical point, marking the theoretical limits for LLPS. Consequently, a phase transition (with LLPS) is absent. Initially, the values for B_2/B_2^{HS} decrease rapidly until the minimum is reached. Beyond the minimum, the B_2/B_2^{HS} values increase again, but with a less steep slope. This effect may be caused by screening effects of the Cl^- counterions. In-

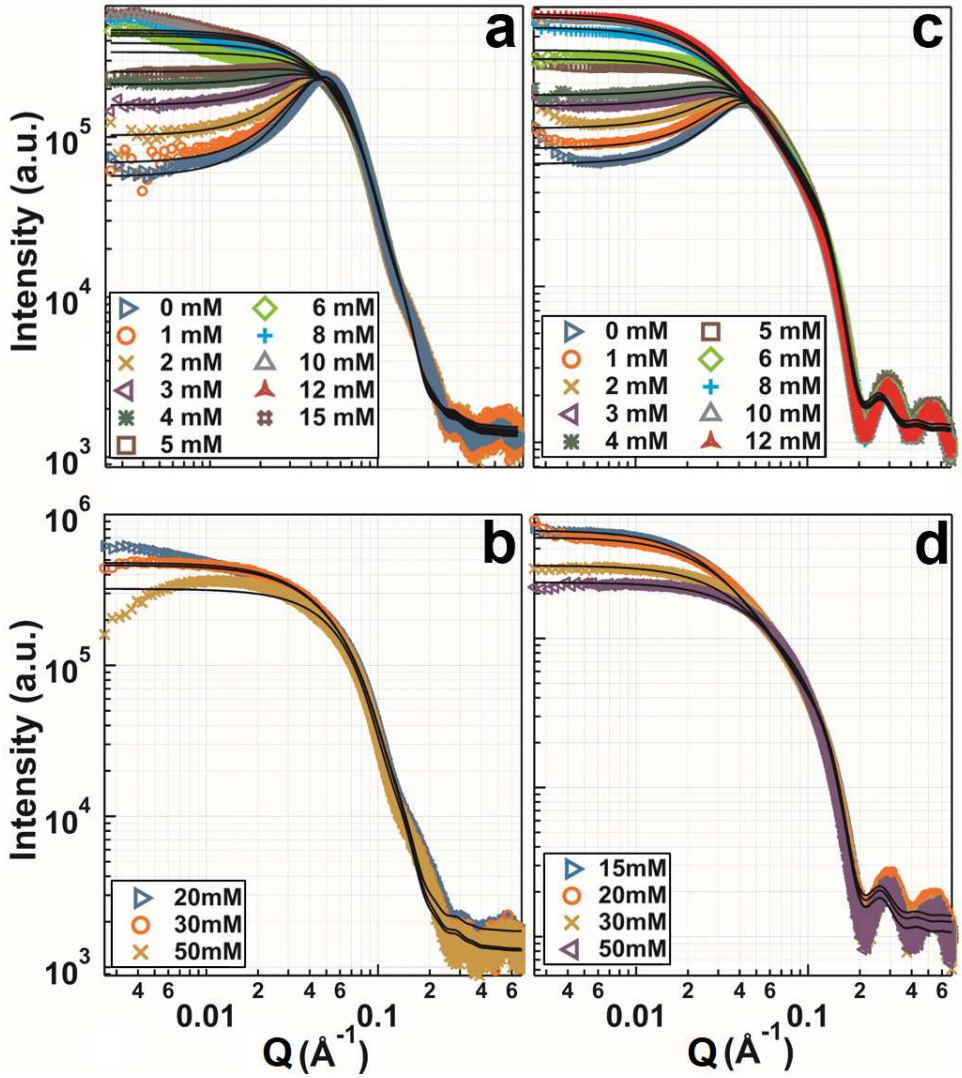

Figure 7.2: *(a, b) SAXS data with model fits (solid lines) for samples in H_2O containing 80 mg/ml BSA with increasing salt concentrations (0 to 50 mM). (c, d) SAXS data with model fits for samples in H_2O containing 80 mg/ml BLG with increasing salt concentrations (0 to 50 mM). The scattering intensity at low-Q increases with increasing salt concentration (a) and (c) and decreases in (b) and (d). In (a), the SC potential was used for 0 to 4 mM salt. The other conditions (5 to 15 mM) were fitted by use of an SHS model. In (c), conditions (0 to 4 mM salt were fitted using a 2Y potential, the other conditions (5 to 12 mM) were fitted using an SHS model. The dashed lines are guides to the eye. Further detailed information on SAXS data analysis is provided in the Chapters 5.1.1, 5.1.12 and 7.6).*

creasing the salt concentration goes along with increasing concentrations of the counterion, which effectively screens the proteins surface charge.

This hypothesis is supported by similar results for divalent cations, which show

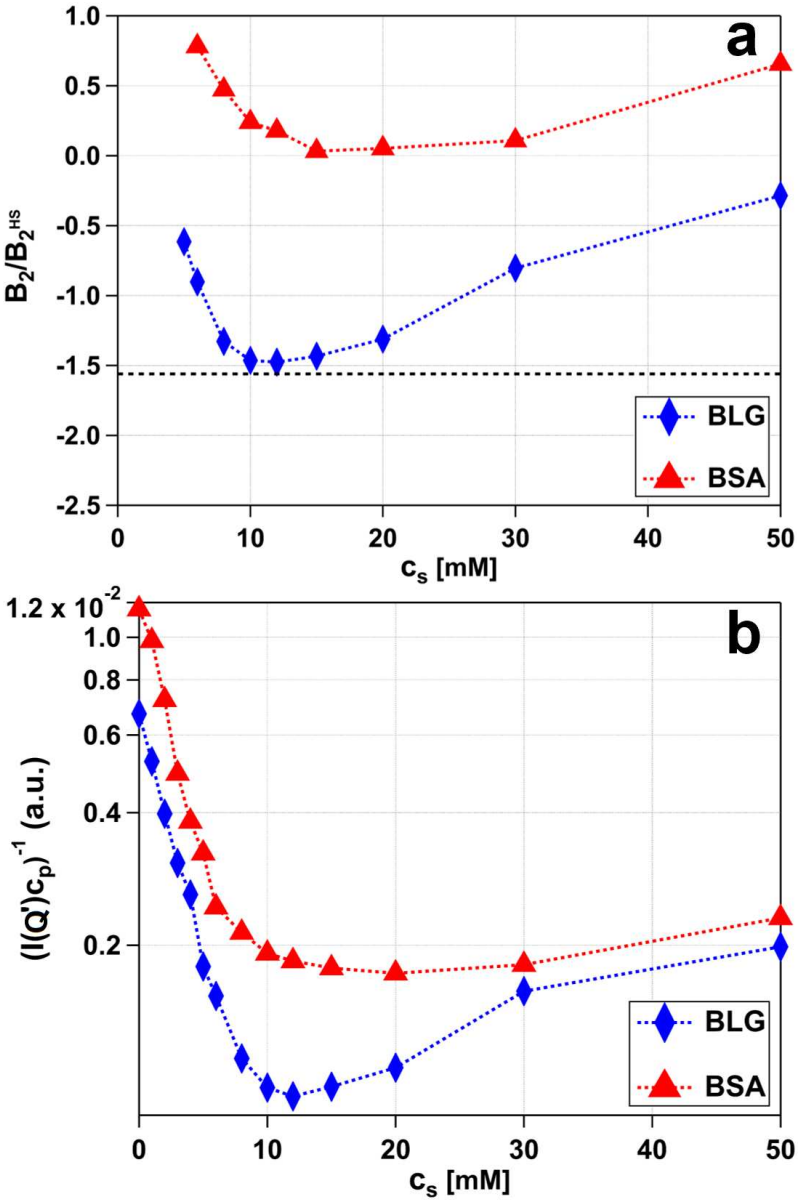

Figure 7.3: *(a) Reduced second virial coefficients and (b) $1/I(Q \to 0)$ behavior of the BLG and BSA samples with c_p 80 mg/ml and varying c_s presented in Figure 7.2. In (a), the black dashed line at -1.56 indicates the suggested and theoretically determined limit of the critical point for the gas-liquid transition (detailed information is provided in the text) [106]. The respective error values of the fits are smaller than the markers used for illustration and are, therefore, not plotted for clarity. (b) The inverse intensities are evaluated at $Q' = 0.03\,\text{Å}^{-1}$, subsequently averaged, and normalized to the molecular weight of the protein monomer.The respective error values are smaller than the markers used for illustration and are, therefore, not plotted for clarity. The dashed lines are guides to the eye. In Chapter 7.6, Figures 7.10, 7.11 and 7.12, show a similar evaluation for the two other proteins OVA and HSA.*

comparable behavior of the interaction potential as a function of cation concentration [323, 324]. A similar evaluation was carried out for the two proteins OVA and HSA. The data can be found in Chapter 7.6.4 (see Figure 7.10). In addition to the above-described model-based analysis (Figure 7.3 a), the scattering at low-Q values (close to 0), namely $1/I(Q \to 0)$, was analyzed as well (Figure 7.3 b). This model-free approach can be applied to repulsive conditions without constraints, unlike the SHS analysis, therefore, allowing to investigate low salt concentrations, too. Importantly, this approach is connected to the reduced second virial coefficient via the following relation [64]:

$$\frac{1}{I(Q \to 0)} \propto \frac{1}{S(Q \to 0)} = 1 + 2B_2\,\rho + ... \tag{7.6}$$

hence, the value of the structure factor near the origin can be expressed by Equation 7.6 which connects the inverse intensity value near the origin to the second virial coefficient [28, 263, 277]. Given the absence of LLPS, the protein concentration is proportional to the protein number density ($c_p \propto \rho$) so the inverse intensity is proportional to the reduced second virial coefficient ($1/I(Q \to 0) \propto B_2/B_2^{HS}$) in this approximation. Therefore, the inverse intensity ($1/I(Q \to 0)$) can be considered as well to describe the effective protein-protein interactions. Moreover, the inverse intensity ($1/I(Q \to 0)$) was normalized to the respective molar protein concentration in [Mol/l].
Overall, the inverse intensity (Figure 7.3 b) follows the trend as indicated by the B_2/B_2^{HS} analysis (Figure 7.3 a) for BLG and BSA respectively. The corresponding error bars of the applied fits are smaller than the symbols used for illustration and are therefore not plotted for clarity. Generally, we assume an uncertainty of 10 % , resulting from sample preparation and data collection. In the Supporting Information (see Chapter 7.6) Figures 7.11 and 7.12, show a similar evaluation for the proteins OVA and HSA.
The effective structure factors *S(Q)* for BSA and BLG, were calculated based on the fitting parameters (Figure 7.2), which were previously converted from oblate ellipsoids to the respective effective radius of a sphere and subsequently depicted in Figure 7.4 [266]. In Figure 7.4 a the evolution of $S_{SC}(Q)$ for BSA (80 mg/ml) for increasing salt concentrations is shown. The structure factor at $Q = 0$ is equal to the normalized osmotic compressibility. A screened Coulombic structure factor of $S_{SC}(0) < 1$ indicates the dominance of the repulsive interaction. The first peak ($\sim 0.06\,\text{Å}^{-1}$) of $S_{SC}(Q)$ represents the correlation between protein molecules in the solution. For increasing salt concentrations, the peak becomes broader and shifts its position towards higher Q values, which suggests a decrease in the correlation length. Furthermore, $S_{SC}(Q \to 0)$ increases with increasing salt concentrations. Therefore, an increase in salt concentration not only decreases the repulsive force, but also weakens the correlation between the protein molecules in the solution. Figure 7.4 c shows the evolution of $S_{2Y}(q)$ for BLG (80 mg/ml) for increasing salt concentrations. Starting from low-Q, the first of

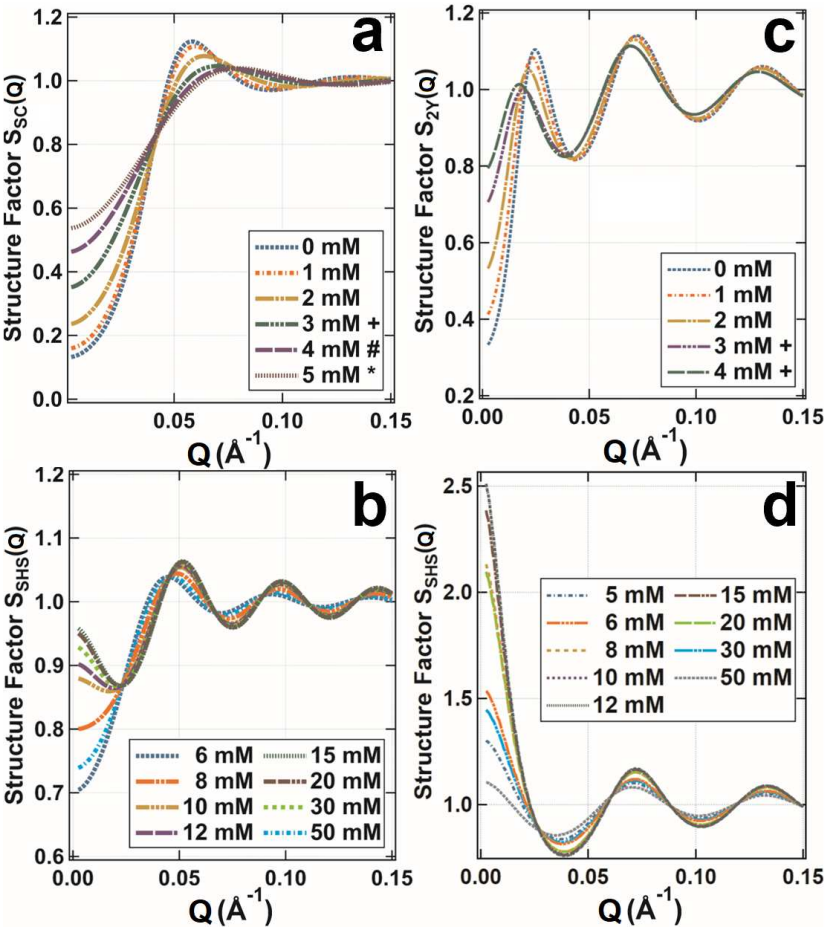

Figure 7.4: *Structure factors calculated from Figure 7.2 as a function of salt concentration. (a, b) show the structure factors for 80 mg/ml BSA while (c, d) show the structure factor for 80 mg/mL BLG. Note that the shown structure factors were calculated using different potentials. Thus, the SC potential was used for Figure (a), while a 2Y potential (further information is given in the Supporting Information; see Chapter 7.6) was used for Figure (c), and an SHS potential was used for Figures (b, c). For all the shown structure factors (a, b, c, d) the respective effective radius of a sphere was used which was previously calculated based on the axes of an oblate ellipsoid, used for SAXS data fitting (see Figure 7.2) [266]. In (a), all conditions were approximated using a particle size of 67.97 Å, exceptions were marked with special characters. Conditions marked with a + were approximated using a particle size of 67.97 Å, conditions marked with a # were approximated using a particle size of 68.75 Å, and conditions marked with a * were approximated using of 69.19 Å. In (c), all conditions were approximated using a particle size of 50.41 Å, exceptions were marked with a + character. The conditions marked with a + were approximated using a particle size of 50.65 Å. In (b), all conditions were approximated using a particle size of 69.83 Å, for (c) a particle size of 51.97 Å was used. For further information, consult the experimental section on SAXS data analysis as well as the Chapter 7.6.*

the two visible peaks ($\sim 0.03\,\text{Å}^{-1}$) represents the correlation of clusters formed whereas the second peak ($\sim 0.07\,\text{Å}^{-1}$) represents the correlation between protein molecules [214, 345]. With increasing salt concentration, the peak shifts towards lower Q values ($\sim 0.02\,\text{Å}^{-1}$), which suggests the formation of small clusters with increasing size. This can be attributed to an increasing particle size, required to properly fit the data (Figure 7.4 c). The second peak ($\sim 0.07\,\text{Å}^{-1}$) represents the particle spacing. Due to the increased particle size induced by an increasing salt concentration, this peak shifts as well to lower Q values indicating enlargement of particle spacing. Furthermore, $S_{2Y}(Q \to 0)$ increases with increasing salt concentration, thus suggesting a decrease in the repulsive force.
In Figure 7.4 d $S_{SHS}(Q \to 0)$ increases up to a salt concentration of 12 mM, indicating a decreasing repulsive force. This finding is in line with the reduced second virial coefficient analysis as well as the $1/I(Q \to 0)$ analysis (Figure 7.3). A further increase in salt yields a decay in $S_{SHS}(Q \to 0)$ suggesting an increasing repulsive force. Again, this observation is in line with the analysis of the reduced second virial coefficient analysis as well as the $1/I(Q \to 0)$ analysis (Figure 7.3). The same is true for BSA with salt concentrations above 5 mM (Figure 7.4 b); the only difference is that the strongest observed attraction is reached at 15 mM salt. For both proteins, the first visible peak, $\sim 0.05\,\text{Å}^{-1}$ for BSA and $\sim 0.07\,\text{Å}^{-1}$ for BLG, increases in height and shifts its position towards higher Q values, indicating higher correlation and a diminishing particle spacing, respectively (Figure 7.4 b, c). A similar analysis was carried out for the proteins OVA and HSA, which can be found in the Supporting Information (see Chapter 7.6, Figures 7.13 and 7.14).

7.4.3 Static and Dynamic Light Scattering Characterization of Diffusion Properties and Interaction

In the following, results obtained by SLS (Figure 7.5) and DLS (Figure 7.6) are discussed. Looking at the SLS analysis (Figure 7.5) of 20 mg/ml BSA with increasing concentrations of Hac (0 to 50 mM), it becomes apparent that the low-Q trend of the scattered intensities is comparable to the trend discussed for the SAXS analysis (see Figure 7.3). With increasing salt concentration, the intensity increases as well. The highest intensity is visible at 12 mM. A further increase in the salt concentration yields a low-Q intensity decrease (Figure 7.5a). This behavior of increasing and decreasing low-Q intensities as a function of continuous increasing salt concentration is labeled RI. Moreover, small clusters with a broad range are visible for 1 mM, for higher salt concentrations (2 to 50 mM) the low-Q intensity increase indicates the formation of bigger aggregates. Despite the presence of aggregates, no turbidity which would indicate a phase transition, was recognizable.
The SLS inverse intensity K_c/R_θ (Figure 7.5b) features a comparable trend to the $1/I(Q \to 0)$ SAXS data shown above (see Figure 7.3 b). The local minima

can be seen at 12 mM salt which is an indicator for attractive conditions. For higher molarities, the intensity increases again, but with a much shallower slope. Again, this effect may be caused by screening effects of the Cl^- counter ion. Nevertheless, differences between $1/I(Q \to 0)$ behavior and the SLS inverse intensity Kc/R_θ are obvious. The most significant difference between the two is seen at low salt concentrations (0 to 3 mM), as the decreasing slope is much steeper for Kc/R_θ. However, the local minimum is within the same range for both measurements. It is

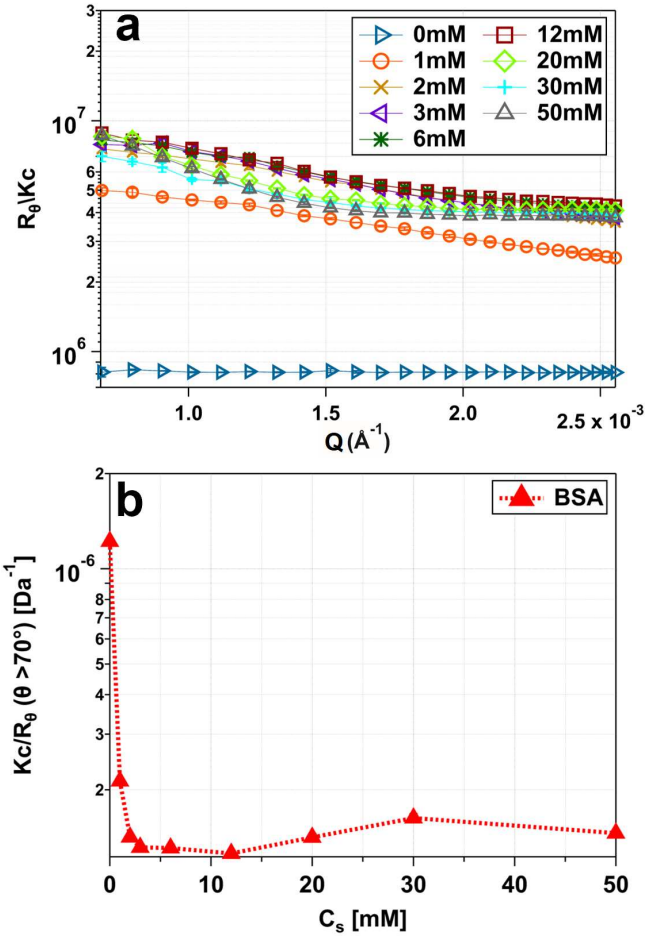

Figure 7.5: *SLS intensity measurements (a) and inverse intensity Kc/R_θ, measured at a scattering angle between 70° and 90° (b). For (a) and (b), the measured samples contain 20 mg/ml BSA with increasing concentrations of Hac (0 mM to 50 mM). The shown lines (solid and dashed) represent guides to the eye. Note that error bars can be smaller than the symbols used for display.*

important to note that the SAXS measurements were made with denser sampling (see Figure 7.3 b). Another deviation is observed at 30 to 50 mM. This difference could occur due to differences in sample preparation or fluctuations. Similar to above, we assume an uncertainty of 10% due to sample preparation and data acquisition. In Figure 7.6 the results for the DLS measurements are presented. The

autocorrelation functions (Figure 7.6 a) of 20 mg/ml BSA with increasing salt concentrations (0 to 50 mM) were fitted (black lines) with a double exponential decay (see Equation 7.5). Based on these fits the fast diffusion coefficient (D1) of the dominant dynamic mode was obtained (see Figure 7.6 b).

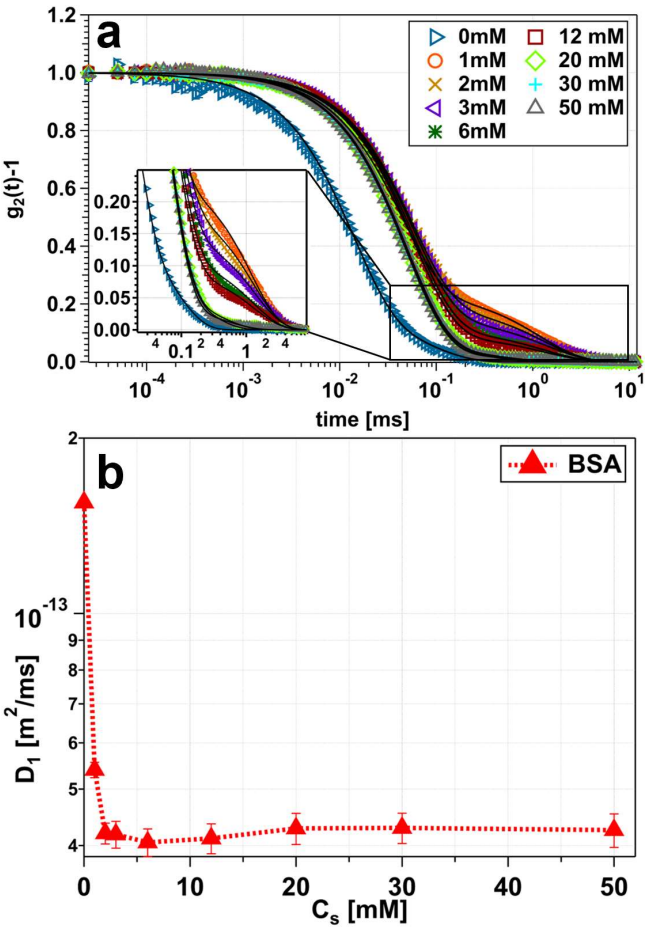

Figure 7.6: *(a) Representative normalized autocorrelation functions (Equation 7.5) as a function of decorrelation time for samples containing 20 mg/ml BSA with increasing concentrations of Hac (0 to 50 mM). The scattering angle was set to $\theta \geq 70°$. The corresponding diffusion coefficient for the first of the two decays is depicted in (b). The dashed lines represent guides to the eye. Note that error bars can be smaller than the symbols used for display.*

However, two decays are visible (Figure 7.6 a), with the most pronounced double-exponential character to be seen for 1 mM Hac. Importantly, the second of the two mentioned decays correspond to a slower particle diffusion, meaning bigger particle sizes. Therefore, this decay can be assigned to aggregation, which is not within the scope of this paper. A general trend of increasing decay times (0 to 1 mM) followed by decreasing decay times (1 to 50 mM) is to be seen (Figure 7.6 a). This trend of increasing and decreasing decay times can be ascribed to

a RI behavior. Looking at the diffusion (Figure 7.6 b), the biggest decrease in the diffusion coefficient (D1) is to be seen within the range from 0 to 3 mM. Increasing the Hac concentration yields a local minimum at 6 mM Hac. Further increase in Hac concentration does not induce significant changes of the diffusion but results in a constant value (20 to 50 mM, Figure 7.6 b). The slower diffusion (decrease in the diffusion constant) indicates dimer and trimer formation, indicating an increasing particle size. Moreover, this is consistent with other data sets presented here (see Figure 7.4). Due to variations in the supplied BLG protein quality, a reliable DLS measurement was not possible and is therefore not shown.

7.4.4 Discussion on the Hac-induced RC Behavior of DNA/RNA and the Absence of RC for BLG, BSA, HSA, and OVA

The results presented above are compared to both: Studies investigating RC of negatively charged globular proteins in the presence of multivalent metal cations and studies examining RC of DNA or RNA in the presence of Hac.
First, looking at the phase behavior of negatively charged globular proteins in solution given the presence of multivalent cations, RC is observed [58]. The process of RC is characterized by a phase diagram featuring a sector consisting of aggregates (Regime II). With continuously increasing salt concentration at a fixed protein concentration, redissolution of the formed aggregates occurs [346]. The proteins BLG, BSA, HSA, and OVA showed RC in the presence of YCl_3, $LaCl_3$, $FeCl_3$, and $AlCl_3$, respectively [58]. The driving force of the RC is ascribed to both, the cation-mediated inversion of protein charge upon binding and the intermittent cation-mediated attraction [107]. Studies investigating RC, utilizing SAXS have shown that RC is associated with an increasing, followed by a decreasing, intensity at low-Q values, given a constant protein concentration combined with a continuously increasing salt concentration. The SHS fits enabling the determination of the reduced second virial coefficients showed a similar behavior [64, 65]. A high intensity at low-Q values (scattering profile) can be interpreted as attractive interaction, since the corresponding reduced second virial coefficient is negative and hence of attractive character. Therefore, the protein-salt system becomes more and more attractive with a maximum at a given salt concentration (highest low-Q intensity in the scattering profiles with a corresponding minimum in the reduced second virial analysis). Typically, the highest attraction is found within the second regime as aggregates or clusters are dominating. The subsequent decrease in low-Q intensity indicates a weakening of the attraction accompanied by an increasing reduced second virial coefficients (transition from Regime II to Regime III) [64, 65]. The investigated protein-Hac systems, however, remained within Regime II (see Figures 7.1 and 7.3). Nevertheless, the course of the scattering profiles and the reduced second virial coefficients are comparable, despite the missing optical phase transition to the second or third regime, respectively.

Therefore, it can be assumed that the observed attraction is not sufficiently strong to induce the transition to the second regime.
Considering ion-induced protein interactions with regard to the different cation radii, it can be seen that the strength of attraction decreases with increasing cation radius [344]. Similar observations were made for HSA in the presence of different lanthanoid cations [347]. Hac features a 420 pm ion radius, whereas the ion radii of $Ho3^+$ or $Y3^+$ are 4.6 times smaller. The ion radius for $La3^+$ is four times smaller compared to Hac [348]. A possible explanation for the decreasing ion-induced protein attractions with increasing ion radius could be that for small ion radii, the charge of the ion is concentrated near the protein binding site [344]. The results of the investigated proteins in the presence of Hac are in line with other studies [344, 347], since Hac, being the largest cation among those listed, evokes the least attraction. Hence, the ionic radius is one parameter influencing the ion-protein interaction.
However, structural differences between Hac and the listed cations have to be considered as well (see Figure 7.7 a). Hac features six covalently bonded ammonia ligands ($NH3$) arranged octahedrally around the central cobalt atom that do not exchange with the solvent, yielding a kinetically stable complex in aqueous solution (see Figure 7.7 a) [233, 234, 330]. This structural difference may also contribute to weaker ion-protein interactions, due to the fact that the charge of the ion may not be concentrated near the possible protein binding site.
Yet, Hac induces reentrant condensation of DNA and RNA, as demonstrated by several studies [100, 325–328, 330]. However, Hac does not induce RC of negatively charged globular proteins as demonstrated by the experiments depicted here. The structural differences between DNA, RNA and proteins are of importance: proteins feature a complex surface pattern due to inhomogeneously distributed positive and negative charges. In addition, the binding sites feature different geometries resulting in few, but strong binding sites for interactions with multivalent cations [322]. In contrast, nucleic acids feature a more homogenous charge pattern. Typically, the prevalence of the phosphate backbone is responsible for the overall negative charge distribution [322]. Given these structural differences, the reason for RC in DNA and its absence in globular negatively charged proteins might be due to different cation binding or bridging mechanisms. Considering the mechanism of ion-activated attractive patches, solvent-exposed carboxyl side chains of negatively charged globular proteins located at the protein surface form coordinative bonds with multivalent metal ions such as Y^{3+}. This process is characterized by an activation and subsequent occupation of a protein patch. Every protein features only a limited number of patches on its surface. Only if an activated patch interacts with a non-activated (unoccupied) patch of a second protein, an ionic bridge, which connects the two protein molecules, can be established (see Figure 7.7 b) [107]. Therefore, a continuously increasing salt concentration increases the number of occupied patches, accompanied by an increasing number of ion salt bridges formed. Experimentally, the ionic bridge formation can be monitored by

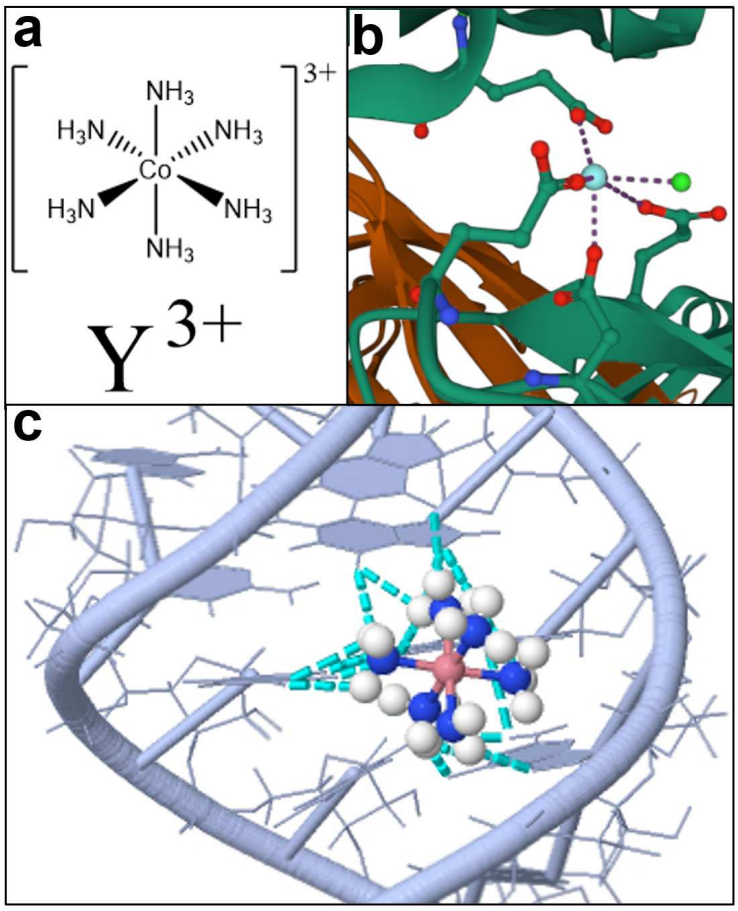

Figure 7.7: *(a) Comparison of the two Lewis formulas of the hexamine cobalt (III) cation (top; a) and of yttrium cation (bottom; a). In both cases, the chloride counterions of were omitted to provide a simpler representation. (b) Ionic Y3+ bridging between two BLG monomers. The schematic was obtained by use of PDB entry 3PH5, [349] and the Mol* Viewer software [350]. (c) Schematic illustration of the P5b stem-loop group I intron ribozyme with the Hac binding sites highlighted. The central cobalt atom is shown in dark pink, while its ammonia ligands (NH_3) are highlighted in blue (N) and white (H). The dashed cyan lines represent the established hydrogen bonds. The six ammonia ligands form hydrogen bonds with O6 and N7 of the three guanines (the right strand of the shown helix) and O4 of the two uracils (U13 and U14) located on the opposite (left) strand. The schematic was obtained using JSmol software [351] with PDB entry 1AJF [234].*

the charge inversion of the protein molecule [107]. For BLG in the presence of Y^{3+}, the ion-activated attractive patch model is in good agreement as shown by crystal structure analysis. In this case, the four bound Y^{3+} ions contribute significantly to the bridging contacts of the unit cell (see Figure 7.7 b) [59, 349]. A different situation can be seen for HSA in the presence of Y^{3+}. The majority of

contacts are formed by protein–protein interactions, whereby the influence of the multivalent cation is noticeably weaker [60].
In comparison to the above, differences can be seen for the ion-induced DNA condensation. When modeling DNA condensation, given the assumption that the negative charge is solely compensated by Hac cations, the DNA "wraps" around the ion [326].
Additionally, the Hac molecule is kinetically stable, which implies that its six ammonia ligands are not replaced with the solvent. This feature allows the formation of hydrogen bonds between the six ammonia ligands and nucleic acids, with Hac being a so-called hydrogen donor (attributed to the present 18 hydrogen atoms). The major groove of DNA represents a typical yet specific binding site for Hac, as other possible binding sites are less frequently targeted. In the presence of a sufficiently high Hac concentration, the form of DNA is altered [329, 330] from B-DNA (right-handed helices, "average" DNA confirmation reported by Watson and Crick) to either A-DNA (slightly different confirmation but also right-handed helices) or Z-DNA (different DNA confirmation featuring left-handed helices) [330, 352]. Interestingly, the shape of Z-DNA offers a good fit of the Hac complex and allows the formation of five hydrogen bonds together with O6 guanine, N7 guanine and the present oxygen atoms of the phosphate backbone. In comparison, B-DNA does not offer these characteristics [330]. A-DNA features an easily accessible large major and a less pronounced minor groove compared to B-DNA. Within this major groove of A-DNA, two adjacent negatively charged phosphate backbones can be neutralized by the trivalent Hac cation, which may be the reason for the favoring of A-DNA [330]. Looking at an nuclear magnetic resonance study of the P5b stem-loop of the group I intron ribozyme RNA (see Figure 7.7 c) [234] the exact binding of the Hac-complex was elucidated. The major groove features not only a negatively charged surface but also several acceptors for hydrogen bond formation with the Hac ion [234]. The hydrogen bonds are formed between the Hac complex and O6 as well as N7 of the three guanines (G7, G6, and G5) and the O4 of the two uracil nucleobases (U13 and U14; see Figure 7.7 c) [234]. A similar behavior was found for NMR studies with group II intron Sc.aI5γ [329]. Here, the three determined Hac binding sites featured similar conditions of additional stabilization due to hydrogen bonds [329]. Therefore, these results suggests that the binding of Hac requires not only negative charges, but multiple hydrogen bonds to induce condensation. These requirements are fulfilled for DNA or RNA but are not met in the case of globular proteins.

7.5 Conclusion

The comparison of several multivalent cations with Hac shows that Hac features by far the largest cation radius (420 pm). This is in line with an observed decreasing ion-induced protein interaction strength with increasing cation radius. Furthermore, the obtained reduced second virial coefficient analysis shows that

none of the protein-Hac systems investigated induces strong enough attraction, resulting in the absence of LLPS due to insufficient attractions. This was also confirmed by SLS and DLS measurements, which indicate cluster formation and oligomerization (formation of dimers/trimers), but neither phase transition nor LLPS was observed. Another possible aspect contributing to the RI behavior of globular negatively charged proteins (BLG, BSA, HSA, and OVA) in the presence of Hac could be the low charge density of Hac. This might occur due to widely distributed charges that act as single counterions, resulting in nonspecific binding of Hac which is sufficient to induce RI but insufficient to induce RC. Moreover, differences in the binding mechanism of multivalent metal ions to proteins and Hac to RNA/DNA become apparent. While the multivalent cations interact with the solvent-exposed carboxyl side chains of negatively charged globular proteins (e.g., BLG with Y^{3+}), the Hac cation features additional hydrogen bonds when binding to a DNA groove. Therefore, the binding of the Hac cation to DNA is not only specific, but requires a precise fit, negative charges, and atoms to form hydrogen bonds with. This leads to the assumption that Hac mostly binds through hydrogen bonding. So far, however, all crystal structures of negatively charged proteins in the presence of multivalent cations resolved by our group indicate that the binding mechanism is of electrostatic nature, implying that net negatively charged residues complex the cation [59–61]. Hence, hydrogen bonding of Hac with the globular, net negatively charged proteins may occur. This is in turn supported by the herein presented experiments, such as the formation of clusters, confirmed by SLS and DLS and, the weak RI confirmed by SAXS. Therefore, this could be an explanation for the presence of RI and absence of the RC in the investigated protein-Hac systems.

7.6 Supporting Information

This Chapter is based on the Supporting Information of the publictaion:

M. D. Senft, R. Maier, A. Hiremath, F. Zhang, and F. Schreiber, Effective interactions and phase behavior of protein solutions in the presence of hexamine cobalt(III) chloride, The European Physical Journal E 46, 10.1140/epje/s10189-023-00376-6 (2023).

To avoid repetition, parts of the Supporting Information, dealing with SAXS theory, as well as the respective potentials used for fitting and the model free inverse Intensity approach $1/I(Q \to 0) \propto 1/S(Q) = \rho k_B T \chi_T$, are integrated in Chapter 5.1.

The original version of the Supporting Information should not be withheld, and can be accessed free of charge following the link below:
`https://link.springer.com/article/10.1140/epje/s10189-023-00376-6`
last checked 21.10.2024, 17:02.

7.6.1 Additional information on the used Parameters for SAXS Data Analysis and Fitting

In the following, the two Tables 7.2 and 7.3 summarize important parameters used for the SAXS data analysis and potential fitting. Table 7.2 gives an overview about the potentials used to obtain information about effective protein interactions for HSA as well as OVA protein solutions. Table 7.3 lists all the investigated proteins with the respective corresponding calculated scattering length densities (SLD's).

Table 7.2: *Particle sizes used (in Å) subdivided according to protein and the used potential for approximation. The particles were assumed to be elliptical.*

Potential	**Protein**	**Axis (a)** [Å]	**Axis (b)** [Å]
SC	OVA	44.20	20.20
HS	OVA	53.60	19.82
SHS	OVA	57.00	19.82
SC	HSA	18.00	42.50
SHS	HSA	18.00	42.50

Table 7.3: *Calculated scattering length density ($Å^{-2}$) listed together with the corresponding proteins.*

Protein	**Calculated scattering length density** [$Å^{-2}$]
BLG	7.33×10^{-7}
BSA	7.32×10^{-7}
OVA	7.32×10^{-7}
HSA	7.32×10^{-7}

Moreover, one important input parameter required, to fit the potentials to the SAXS data is the protein volume fraction ϕ. The protein volume fraction ϕ can be calculated for any given protein concentration $c_p = m_p/V_s$ according to the following equation [214]:

$$\phi = \frac{c_p}{1 + c_p \times \nu} \times \nu. \tag{7.7}$$

Here, c_p represents the protein concentration (g/ml), the protein mass is given by m_p and V_s denotes the volume of added water. ν corresponds to the specific volume (ml/g) of the respective protein. Based on Equation 7.7, the respective protein volume fractions ϕ were calculated for fitting the SAXS data obtained.

7.6.2 Fitted SAXS Data of Ovalbumin

The effective protein-protein interactions of the protein-salt solutions were investigated by use of systematic SAXS measurements. Figure 7.8 shows the representative SAXS measurements for 80 mg/ml OVA with increasing Hac concentrations (mM) in H_2O. Given low salt concentrations (0 to 4 mM), the net negative charges of the protein molecules dominate the effective protein-protein interactions, as illustrated by the correlation peak $Q = 0.06Å^{-1}$. An increase in the salt concentration results in an increasing low Q intensity, which indicates reducing repulsion, while concurrently, the correlation peak fades out (4 mM). As the salt concentration is increased further, the highest attraction becomes apparent at 30 mM salt. Any further increase of the salt concentration reduces the attractive strength. This is indicated by the decreasing low Q intensity at 50 mM salt (Figure 7.8 b). For Ovalbumin at low salt concentrations (0 to 4 mM) the SC, for intermediate salt concentrations (5 to 8 mM) the HS and for high salt concentrations (10 to 50 mM) the SHS interaction potential was used (see solid black lines in Figure 7.8). According to table 7.2, the elliptical axes had to be adjusted for the approximation of the data using different potentials. One reason for this behavior could be dimerization of the Ovalbumin monomers.

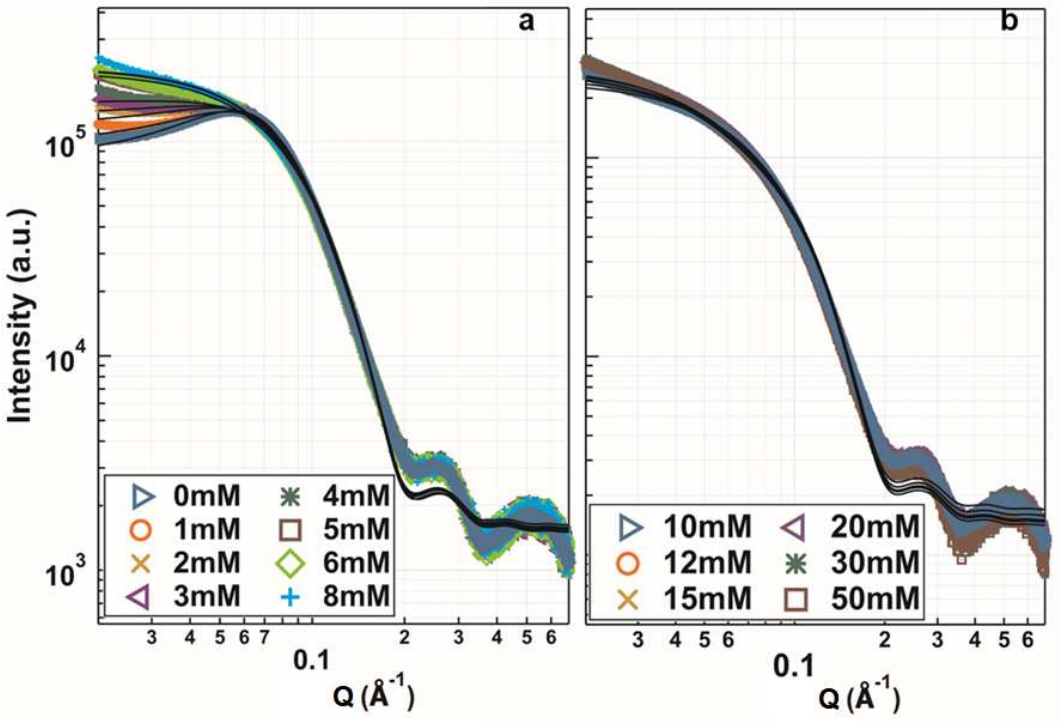

Figure 7.8: *(a, b) SAXS data with model fits (solid black line) for samples in H_2O containing* 80 *mg/ml OVA with increasing salt concentrations (*0 *to* 50 *mM). The scattering intensity at low q increases with increasing salt concentration (a) and decreases in (b). In (a), for low ionic strengths (*0 *to* 4 *mM) the SC potential was used. For intermediate ionic strengths, (*5 *to* 8 *mM) the HS potential was consulted. The other remaining conditions (*10 *to* 50 *mM) were fitted by use of the SHS potential (b). The respective error values are smaller than the markers used for illustration and are therefore not plotted for clarity.*

7.6.3 Fitted SAXS data of Human Serum Albumin

A similar evaluation of the SAXS data on the protein HSA with increasing salt concentrations of Hac was carried out. Figure 7.9 shows the representative SAXS measurements for 80 mg/ml HSA with increasing Hac concentrations (mM) in H_2O. Given low salt concentrations (0 to 5 mM), the net negative charges of the protein molecules dominate the effective protein-protein interactions, as illustrated by a correlation peak, visible at $Q = 0.06\text{Å}^{-1}$. Increasing the salt concentration further, results in a vanished correlation peak. The highest low Q intensity is visible at 8 mM. Increasing the salt concentration further results in a discontinuous decrease in low Q intensity. Discontinuous, because the low Q intensity for 12 mM salt is below the low Q intensities for 10, 15 and 20 mM salt. For HSA, at low salt concentrations (0 to 5 mM) the SC, for higher salt concentrations (6 to 30 mM) the SHS interaction potential was used (see solid black lines in Figure 7.9). The elliptical axes were fixed to the values given in Table 7.2.

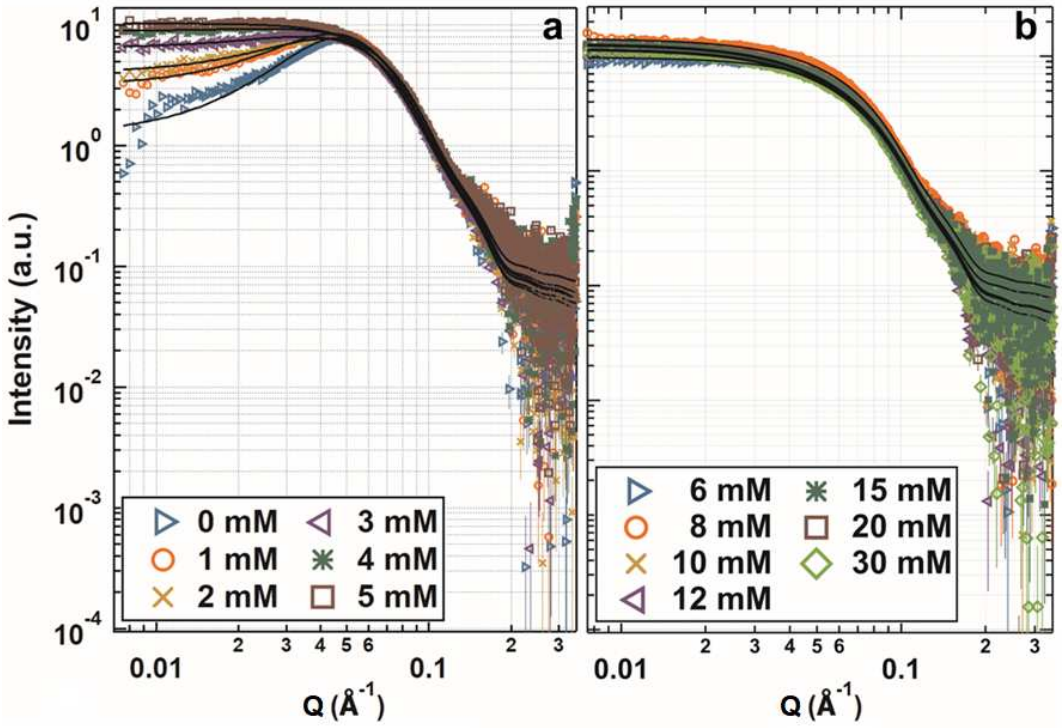

Figure 7.9: *(a, b) Laboratory SAXS data with model fits (solid black line) for samples in H2O containing 80 mg/ml HSA with increasing salt concentrations (0 to 30 mM). The scattering intensity at low Q increases with increasing salt concentration (a) and decreases in (b). In (a), for low ionic strengths (0 to 5 mM) the SC potential was used. The other remaining conditions (10 to 30 mM) were fitted by use of the SHS potential (b). Note that the data from the laboratory SAXS device features a different Q-range. The laboratory SAXS device settings can be found in the Experimental section of the Manuscript see Chapter 7.3.2. Error bars are indicated by vertical lines.*

7.6.4 Second Virial Coefficient Analysis of Ovalbumin and Human Serum Albumin

In Figure 7.10, the calculated second virial coefficient (B_2/B_2^{HS}) for the SAXS measurements of 80 mg/ml OVA and HSA in the presence of Hac are shown. For OVA (red triangles, Figure 7.10) it can be seen that from 10 mM on the second virial coefficient decreases rapidly. The minimum is reached at 30 mM salt. Taken together, the OVA Hac system remains repellent as the reduced second virial coefficient is greater than zero ($B_2/B_2^{HS} > 0$).
In the case of HSA (blue diamonds, Figure 7.10), starting from a low salt concentration (6 mM), the second virial coefficient decreases with increasing salt concentration.Increasing the salt concentration up to 10 mM results in weakening of the repulsions. At 10 mM a secondary minimum can be seen. Increasing the

salt concentration up to 12 mM results in an increase of the reduced second virial coefficient. The primary minimum is visible at 15 mM salt. Further increase in salt concentration leads to an increased repulsion. Overall, the investigated HSA Hac system remains repellent as indicated by the second virial coefficient ($B_2/B_2^{HS} > 0$).

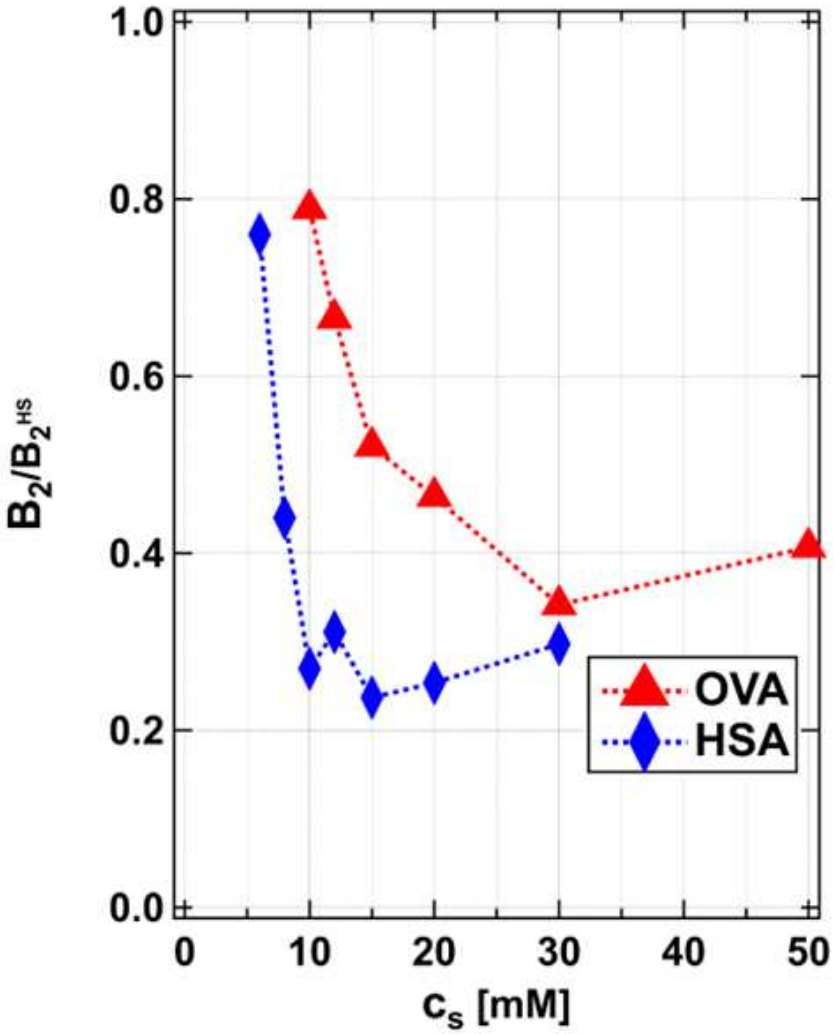

Figure 7.10: *Reduced second virial coefficient behavior of the investigated OVA and HSA samples with a c_p of 80 mg/ml and varying c_s (mM), based on the SHS potential fits presented in Figure 7.8 and 7.9. The respective error values are smaller than the markers used for illustration and are therefore not plotted for clarity. The dashed lines are guides to the eye.*

7.6.5 Inverse Intensity Analysis of Ovalbumin

In Figure 7.11 the $1/I(Q \to 0)$ trend for 80 mg/ml OVA admixed with increasing concentrations of Hac is shown. The inverse intensity follows the same trend as indicated by the reduced second virial coefficient analysis (see Figure 7.10), with the highest attractiveness present at a concentration of 30 mM salt.

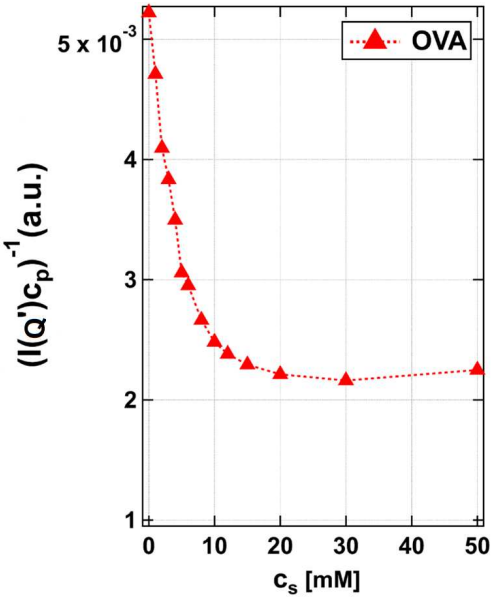

Figure 7.11: *$1/I(Q \to 0)$ behavior of the investigated OVA samples with c_p 80 mg/ml and varying c_s (0 to 50 mM Hac). The inverse intensities at $Q' = 0.03\,\text{Å}^{-1}$ are normalized to the molecular weight of the protein monomer. The error values are smaller than the markers used for illustration and are therefore not plotted for clarity. The dashed lines are guides to the eye.*

7.6.6 Inverse Intensity Analysis of Human Serum Albumin

Looking at the fits from Figure 7.9, it can be seen that these describe the data only partially well. Deviations are visible at the intermediate (0.04 to $0.06\,\text{Å}^{-1}$) and high Q (0.2 to $0.3\,\text{Å}^{-1}$) regions. From this it can be deduced that there are possible discrepancies between the virial coefficient analysis, which implies a model-based fitting of the data, and the model free $1/I(Q \to 0)$ analysis (see Figure 7.12). Note that the intensities for OVA (Figure 7.11) are different, due to the different devices used. Therefore, the intensity is given in arbitrary units (a.u.).

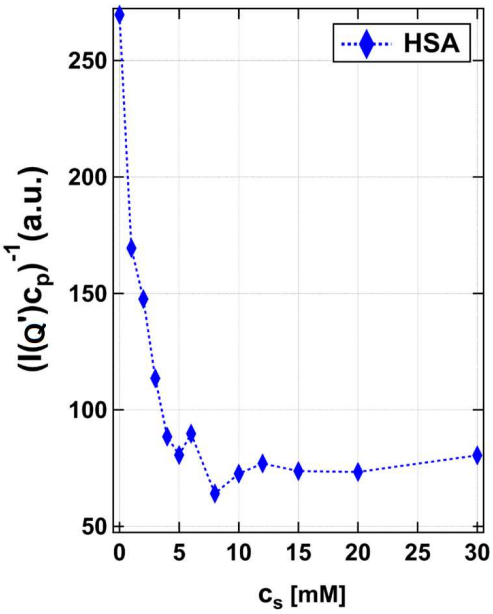

Figure 7.12: *$1/I(Q \to 0)$ behavior of the investigated HSA samples with c_p 80 mg/ml and varying c_s (0 to 30 mM Hac). The inverse intensities at $Q' = 0.03\,\text{Å}^{-1}$ are normalized to the molecular weight of the protein monomer. The respective error values are smaller than the markers used for illustration and are therefore not plotted for clarity. The dashed lines are guides to the eye. Note that the data from the laboratory SAXS device features a different Q-range. The laboratory SAXS device settings can be found in the Experimental section of the Manuscript see Chapter 7.3.2.*

7.6.7 S(Q) Data on Ovalbumin

Figure 7.13 shows the *S(Q)* for 80 mg/ml OVA with increasing Hac concentrations based on the fits provided in Figure 7.8. The effective structure factors *S(Q)* were calculated based on the fitting parameters (see Table 7.2 and 7.3), which were previously converted from oblate ellipsoids to the respective effective radius of a sphere and subsequently depicted in Figure 7.13. A structure factor of $S_{SC}(0) < 1$ (see Figure 7.13 a) indicates the dominance of repulsive interaction. The first peak ($\sim 0.075\,\text{Å}^{-1}$) of $S(Q)_{SC}$ represents the correlation between a pair of protein molecules in the solution. For increasing salt concentrations, the peak becomes broader and shifts its position towards higher Q values, suggesting a decreasing correlation length. As to be seen in Table 7.2, the particle diameter was increased at intermediate and high ionic strengths (see Figure 7.13 b and c). The peak position shifted to lower Q values ($\sim 0.05\,\text{Å}^{-1}$; see Figure 7.13 b). Looking at the $S(Q)_{\text{SHS}}$, the first visible peak, ($\sim 0.05\,\text{Å}^{-1}$), increases in height and shifts its position towards higher Q values, which is an indication for a higher correlation and a diminishing particle spacing (Figure 7.13 c).

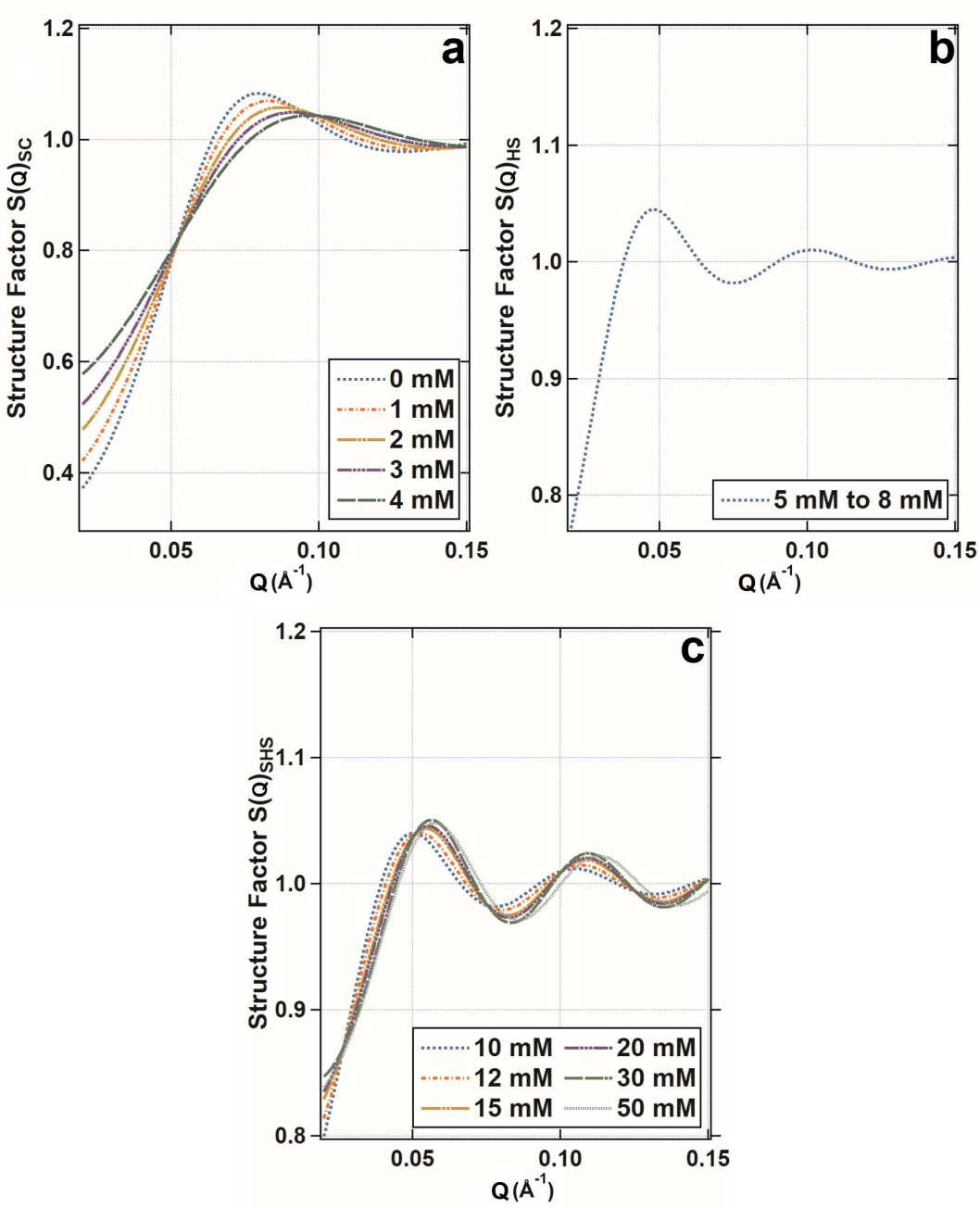

Figure 7.13: *Structure factors calculated from Figure 7.8, as a function of the salt concentration. (a, b, and c) present the structure factors for* 80 *mg/ml OVA. Note that the shown structure factors were calculated using different potentials. Thus, the SC potential was used for figure (a), while a HS potential was used for figure (b) and an SHS potential was used for figure (c). In (a), all conditions were approximated using a particle size of* 55.33 Å*, in (b) all conditions were approximated using a particle size of* 60.18 Å*. In (c), all conditions were approximated using a particle size of* 62.04 Å*. Note, that for all the shown structure factors (a, b, c and d) the respective effective radius of a sphere was used which was previously calculated based on the oblate ellipsoidal axes, used for SAXS data fitting [266].*

7.6.8 S(Q) Data on HSA

Figure 7.14 shows the *S(Q)* for 80 mg/ml HSA with increasing Hac concentrations based on the fits provided in Figure 7.9. A structure factor of S_{SC} (0) < 1 (see Figure 7.14 a) indicates the dominance of repulsive interaction. The first peak (~ 0.06 Å^{-1}) of $S_{SC}(Q)$ represents the correlation between a pair of protein molecules in the solution. For increasing salt concentrations, the peak becomes broader and shifts its position towards higher Q values, suggesting a decreasing correlation length. As Table 7.2 shows, the particle diameter was increased towards higher ionic strengths. Looking at the $S(Q)_{SHS}$, the peak position shifted to lower Q values (~ 0.05 Å^{-1}), and increases in height and shifts its position towards higher Q values, which is an indication for a higher correlation and a diminishing particle spacing (Figure 7.14 b).

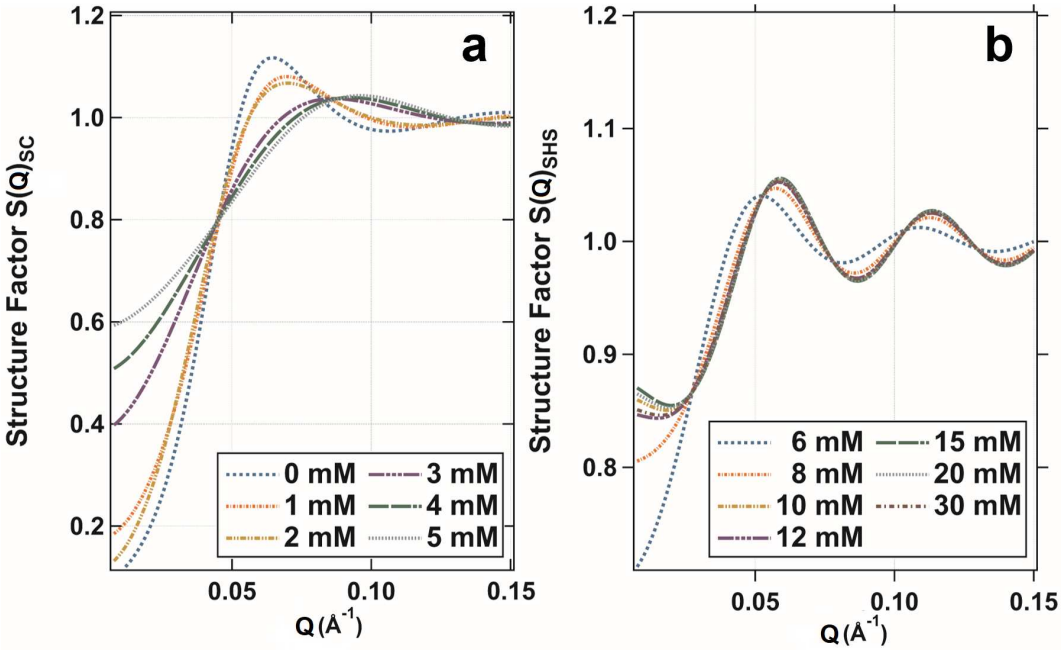

Figure 7.14: *Structure factors calculated from Figure 7.9 as a function of salt concentration. (a and b) show the structure factors for* 80 *mg/ml HSA. Note that the shown structure factors were calculated using different potentials. Thus, the SC potential was used for figure (a), while an ESHS potential was used for figure (b). In (a), all conditions were approximated using a particle size of* 68.06 Å*, in (b) all conditions were approximated using a particle size of* 68.06 Å*. Note, that for all the shown structure factors (a, b, c and d) the respective effective radius of a sphere was used which was previously calculated based on the oblate ellipsoidal axes, used for SAXS data fitting [266].*

Chapter 8

Results II: The Role of Specific and Nonspecific Interactions in Crystallization Behavior of BSA and HSA Protein Solutions

This chapter is entirely based on the following Publication:

Maximilian D. Senft, G. Zocher, S. Retzbach, R. Maier, A. Hiremath, F. Zhang, T. Stehle and F. Schreiber, Role of Specific and Nonspecific Interactions in the Crystallization Behavior of BSA and HSA Protein Solutions, Crystal Growth & Design, 25(8), 2418-2429, 10.1021/acs.cdg.4c01535 (2024).

Contribution:	
Research design:	MDS, FZ, GZ, FS, RM
Experiments:	MDS, SR, GZ, RM, AH
Data analysis and interpretation:	MDS, FZ, GZ
Paper Writing:	MDS, GZ, FZ, FS, TS, RM, SR
Funding:	FS, TS, FZ, GZ

8.1 Abstract

The crystallization conditions of proteins are sensitive to the prevailing interactions. Even the two similar proteins, bovine and human serum albumin (BSA and HSA), exhibit different crystallization conditions despite their comparable function, biophysical properties, shape, and size ($\approx$ 60 kDa and a 75.8 % sequence identity). In this work, we provide a comparison of specific and nonspecific interactions regarding the crystallization behavior of BSA and HSA. The results of the analysis of crystal packing interfaces indicate that HSA uses a relatively larger part of its surface area to establish crystal contacts compared to its bovine counterpart. Likewise, HSA utilizes more of its residues for crystal contact formation, offering a broader range of options to establish attractive interactions. Phase diagrams of the BSA-PEG and HSA-PEG systems were established in order to

gain more precise insights into the nonspecific depletion interactions. It turns out that BSA crystallizes predominantly via depletion interactions, whereas HSA does not. Subsequent systematic small-angle scattering (SAXS) measurements of the two systems in combination with quantitative modeling provide insights into the induced effective interactions, allowing for a better understanding of the two protein-PEG systems. The results obtained were compared to the previously established reentrant condensation (RC) phase behavior of BSA and HSA. The RC phase behavior is caused by the specific interaction of proteins with added multivalent cations. In this case, HSA crystallizes, but BSA does not. This comparison emphasizes the different roles of specific and nonspecific interactions for the crystallization behavior of BSA and HSA.

8.2 Introduction

Understanding the effective interactions of proteins requires sound knowledge of the basic thermodynamic properties of the protein solution, ranging from concentration to solvent properties. Solvent properties include pH value, ionic strength, and the properties of the additives. [170, 353, 354] The resulting effective interactions between protein molecules can be tuned by the addition of salts, polymers, [57, 148, 354] or small organic molecules, [354] thus influencing the phase behavior. Protein phase diagrams enable predictions, [355] contributing to the study of protein condensation-related [356–359] and crystallization-related diseases. [360–364]

Previous work on bovine serum albumin (BSA) and human serum albumin (HSA) in the presence of trivalent metal salts such as YCl_3 or $CeCl_3$ showed that both proteins feature a rich and diverse phase behavior. [59, 60, 365] Moreover, the results showed that HSA crystallized reliably under the experimental conditions used, whereas BSA did not. [365] This approach exploits specific interactions [107] to induce the rich phase behavior of the two proteins and the crystallization of HSA. [60, 365]. This different crystallization behavior is particularly interesting, as both proteins share numerous similarities and perform similar tasks in their respective mammalian species. Mammalian serum albumin is not only responsible for the binding and transportation of small molecules, such as fatty acids or amino acids, but also for physiological functions, including the maintenance of the pH value and the osmotic pressure of the blood plasma [217, 218, 222]. Apart from that, they share a comparable size and 75.8 % sequence identity. [167] Despite these similarities, upon examination of the physiochemical properties, which are summarized in Table 8.1, subtle differences are apparent as well and are frequently not sufficiently taken into account. The industrial production of BSA is cheaper and more convenient than its homologous human counterpart, which is why BSA is often examined as a reference for globular proteins, and the results are thus assigned to HSA. [366] Further analogies, characteristics, and differences of the two proteins BSA and HSA are discussed in detail in ref [365].

Taking these subtle differences into account, aqueous BSA and HSA protein solutions were exposed to the nonspecific, polymer-induced depletion interaction to elucidate the role of specific and nonspecific interactions in phase and crystallization behavior. In a colloidal context, HSA and BSA exhibit a globular structure combined with a net negatively charged surface at neutral pH. [58] In order to describe the present system, proteins are interpreted as spheres that exhibit (essentially) hard-sphere interactions. Synthetic polymers, on the other hand, are regarded as penetrable hard spheres that do not interact with each other. Each protein is surrounded by a depletion layer. Once two depletion layers overlap, a previously inaccessible volume becomes available for the polymer chains, causing an entropy gain. The overlap of depletion layers entails that no polymer can remain nor enter this area, yielding an attractive force pushing the proteins together. [48, 152] This attractive force results exclusively from repulsive interactions originating from the entropic effect. [48, 151, 154, 367] Yet, two distinct cases result from the size differences between proteins and polymers, referred to as the protein limit [157, 368, 369] and colloid limit. [151, 154, 367] In the colloid limit, the polymer chains are smaller than or similar in size to the proteins, whereas the protein limit describes the opposite case. [151, 154, 157, 367–369] Apart from depletion interactions, a direct interaction between polymers and proteins is postulated. [370, 371] Even though polyether [372] PEG is regarded as an unbranched, nonionic, nonadsorbing polymer ($H(OCH_2CH_2)nOH$), [237] interactions between polymers and proteins via hydrogen bond formation cannot be ruled out. [373] This results in interactions that are more complicated than those exclusively responsible for depletion.

In this work, we investigated the depletion-induced effects of polymer PEG on the phase behavior of proteins BSA and HSA. In addition to the macroscopic phase behavior, systematic small-angle X-ray scattering (SAXS) experiments within the colloidal limit while exceeding the overlap concentration of the polymer (c^*) provide further insight into the effective interactions. Fitting the SAXS data with a sticky hard-sphere potential allows for the characterization of the prevailing effective interactions. The results obtained, which are attributable to nonspecific depletion effects, were compared with the reentrant condensation (RC) [47] phase behavior induced by specifically acting metal cations. [107] It was shown that YCl_3 and $CeCl_3$ induce RC phase behavior for both proteins, while crystallization only occurred for HSA. [59, 60, 365] However, if the effect is changed from specific interactions (metal cations) to nonspecific interactions (PEG-induced depletion), only BSA crystals form. The unit cell parameters of BSA crystals were determined by X-ray diffraction analysis. A comparison of the crystal structure with the literature [167, 168] was not only limited to BSA but also extended to HSA. By sophisticated purification and labor-intensive protocols, HSA crystallization was reported to occur in the presence of PEG. [218, 374] Analyzing these crystal structures offers new insights into effective protein-protein interactions and their tunability by selecting specific or nonspecific interactions. The experimental results underline the importance of the chosen crystallization strategy, as the subtle

differences between the two similar proteins, BSA and HSA, are not negligible.

8.3 Results

8.3.1 Phase Behavior of BSA and HSA in the Presence of PEG

Initially, experimental phase diagrams for both proteins, BSA (Fig. 8.1 (a)) and HSA (Fig. 8.1 (b)), in the presence of 100 mM NaCl with increasing (w/V) % ratios of PEG (0–45 (w/V) %) at RT ($21 \pm 1\,^{\circ}$C) were established by macroscopic inspection combined with microscopy. The protein concentration was varied between 20, 50, 80 and 100 mg/ml. Both proteins feature a rich phase behavior, which includes liquid-liquid phase separation (LLPS), aggregation, and, for BSA, crystallization (see Fig. 8.1 (a, b), respectively). Due to the admixing of 100 mM of NaCl, the charges of the globular, negatively charged proteins BSA and HSA are screened. The solutions appeared macroscopically clear upon visual inspection (see Fig. 8.1 (c) for BSA and Fig. 8.1 (d) for HSA). Further increase of the PEG concentration ((w/V) %) resulted in a visually opaque solution. This transition from clear to opaque is named t^* and highlighted by a magenta line for the two respective plots (see Fig. 8.1 (a) for BSA and Fig. 8.1 (b) for HSA).
In addition to the visual inspection, microscopic images were taken to support the macroscopic observations (see panels (a)–(c) in Fig. 8.2 for BSA and panels (d)–(f) in Fig. 8.2 for HSA). Analysis of both phase diagrams revealed that both proteins feature a comparable t^* transition, where lower protein amounts require higher concentrations of PEG to derive the system in a turbid state. For BSA at 20 mg/ml, this occurs at 33 (w/V) % PEG, for 20 mg/ml HSA, it occurs at 30 (w/V) % PEG. At 100 mg/ml, both proteins feature a similar t^* transition point at 25 (w/V) % PEG. For both proteins LLPS occurs just above the t^* transition. Noteworthy, more LLPS conditions were found for HSA, resulting in a larger area of the phase diagram being occupied by LLPS compared to BSA (see the grayish area in Figs. 8.1 (a, b)). Generally, lower concentrations of the respective protein require higher PEG concentrations to induce LLPS.
Above the LLPS threshold (at very high PEG concentrations), aggregate formation is found for both proteins. However, the phase behavior of BSA differs significantly from that of HSA due to crystal formation (see Fig. 8.1 (a) green diamonds and Fig. 8.2 microscopic image (c)). Notably, crystallization was observed under additional conditions (data not shown). A comparison of the HSA phase diagram with the BSA phase diagram shows a shift in LLPS toward higher PEG concentrations ((w/V) %) for BSA, while the phase boundary t^* is also slightly shifted upward. This indicates stronger attractions in HSA than in BSA solutions under the same conditions, particularly below or at the transition t^* (see Fig. 8.5).

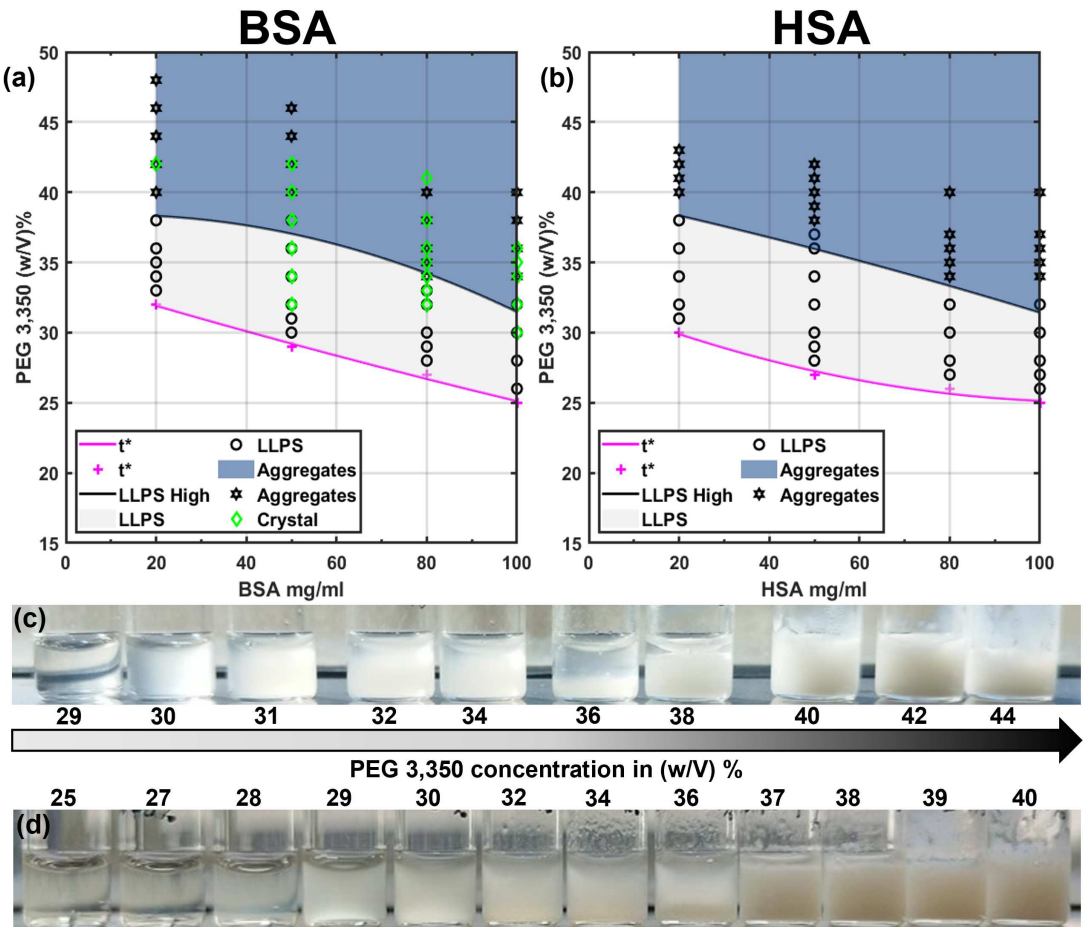

Figure 8.1: *Phase behavior of BSA (a) and HSA (b) at protein concentrations of* 20, 50, 80 *and* 100 *mg/ml, in the presence of* 100 *mM NaCl, with increasing amounts of (w/V) % of PEG* M_w3350. *The phase transition t* is highlighted by a magenta line. LLPS is to be observed within the grayish shaded area. Black solid lines show the respective LLPS border. Aggregates are observed within the blue-shaded area. For BSA (a) green diamonds marked crystal formation. Black stars and black circles show the investigated samples featuring aggregates and LLPS, respectively (a, b). In (c), a photograph shows the visual inspection of BSA at a concentration of* 50 *mg/ml, admixed with increasing (w/V) % of PEG (from* 29 *to* 44 *(w/V) %), arranged from left to right. In (d) a photograph shows the visual inspection of HSA with a concentration of* 50 *mg/ml, admixed with increasing (w/V) % of PEG (from* 25 *to* 40 *(w/V) %), also arranged from left to right.*

Visual inspection was performed immediately after sample preparation. The samples were prepared in one set, i.e., one protein concentration (e.g., 50 mg/ml) with increasing PEG 3350 concentrations at a constant level of 100 mM NaCl. Visual inspection images (see Figure 8.1 (c),(d)) were taken immediately after sample preparation (within a minute to hour time scale). Microscopy images (see Figure 8.2 (a–f)) were acquired after sample preparation (within 1 or 2 days).

However, microscopy images of BSA protein crystals (see Figure 8.2 (c)) were taken after growth. BSA crystallization was observed after incubating for a few days (up to 7 days). Further incubation of crystalline samples (from 7 days up to a month) promoted crystal growth but did not necessarily enhance the growth of quality crystals. It was observed that after a long enough period of time (individual for each crystalline sample), the crystals appeared enlarged and submerged in a translucent liquid.
Incubation beyond 2 days enhanced aggregate sedimentation and promoted the formation of a dense white sludge buildup at the bottom of the reaction vail for samples featuring LLPS and aggregates. The small liquid phase above this dense white sludge remained clear and translucent.

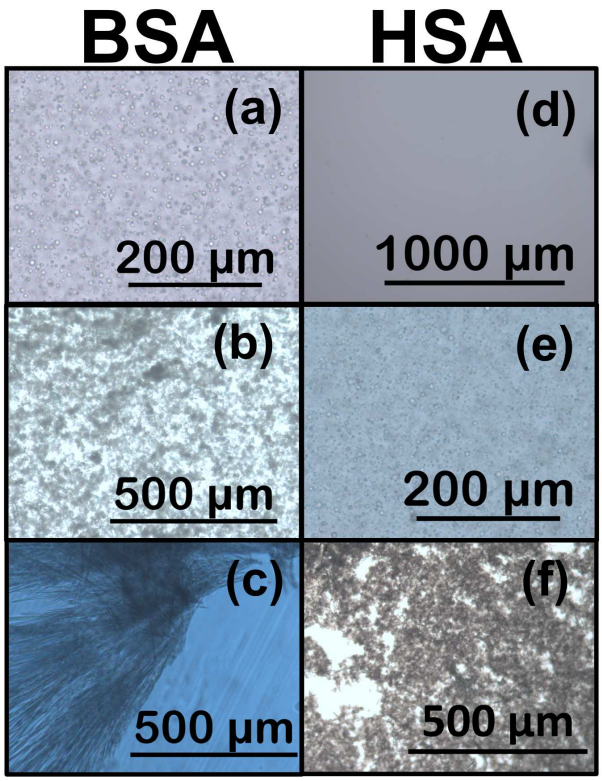

Figure 8.2: *Microscopic examination of (a–c) BSA and (d–f) HSA. All microscopic images share a protein concentration of* 50 *mg/ml mixed with* 100 *mM NaCl. Panel (a) shows a snapshot of LLPS for BSA at* 30 *(w/V) % PEG. Representative snapshots of (b) BSA aggregation at* 40 *(w/V) % PEG, (c) BSA crystal at* 34 *(w/V) % PEG, (d) below t* for HSA at* 26 *(w/V) % PEG, (e) LLPS for HSA at* 32 *(w/V) % PEG, and (f) HSA aggregation at* 41 *(w/V) % PEG.*

8.3.2 Size Ratio q and the Colloidal Limit

To ensure the applicability of the depletion effect, the length scales of the polymer solutions, which were changed by increasing or decreasing the polymer concentration ((w/V) %), had to be assessed to capture the interaction between the proteins. Given a dilute system, the radius of gyration (Eq. 8.1) of the polymer provides an estimate of the applicable length scales [160]

$$R_{g,PEG} = 0.0215\, M_w{}^{(0.583\pm0.031)} \tag{8.1}$$

where M_w denotes the average molecular weight. Due to shrinkage of the PEG polymer chain with increasing concentration, [162] the radius of gyration needs to be adjusted according to Eq. 8.2. [161]

$$R_{G,PEG} = R_{g,PEG}(c_{PEG}/c^*_{PEG})^{-1/8} \tag{8.2}$$

Upon reaching the overlap concentration c^* of the polymer, the solution is referred to as semidilute. [158] At c^*, the polymer chains start to overlap, forming an entangled polymer mesh. [164] In case of PEG 3350, c^* can be found at 10 (w/V) %. [68] Here, the radius of gyration inadequately describes the applicable length scales. Therefore, the length scale has to be adjusted to the polymer mesh size ζ_b. [160, 166] This mesh size can be calculated using Eq. 8.3 [161].

$$\zeta_b \approx R_{G,PEG,}(c_{PEG}/c^*_{PEG})^{-3/4}. \tag{8.3}$$

Based on this formula (Eqs. 8.1, 8.2, 8.3), the size ratio q (Eq. 8.4) [368] for both BSA and HSA proteins at 50 and 100 mg/ml in the presence of 100 mM NaCl with increasing PEG (w/V) % can be obtained (see Fig.8.3).

$$q = \frac{2\,\zeta_b}{\sigma} \tag{8.4}$$

Here, the diameter of the respective protein is denoted by σ. This size ratio q allows the classification of the colloid polymer solutions into different categories. If the size ratio $q < 1$ is applicable, this is referred to as the colloidal limit, whereas in the opposite case $q > 1$ is classified as the protein limit. [48, 157, 158, 368] The experiments shown in this work are within the colloidal limit (see Fig. 8.3). In addition to a size ratio of $q < 1$, the requirement of $q < 0.3$ was met for most conditions, which allows for an area of coexistence between a colloidal crystal and liquid (strictly for $q < 0.3$) as well as for some form of gas-liquid coexistence ($q > 0.3$) within the phase diagram [48, 157, 368, 375–377]. Based on the formalism shown above, the size ratio q is the largest around the overlap concentration c^*. The experiments reported here are in the q range from $q \approx 0.55$ to $q \approx 0.2$. The black dashed line in Fig.8.3 indicates the aforementioned condition of $q < 0.3$, above which gas-liquid type coexistence can be found. This agrees with the experimentally determined phase diagram (see Fig. 8.1 (a),(c)).

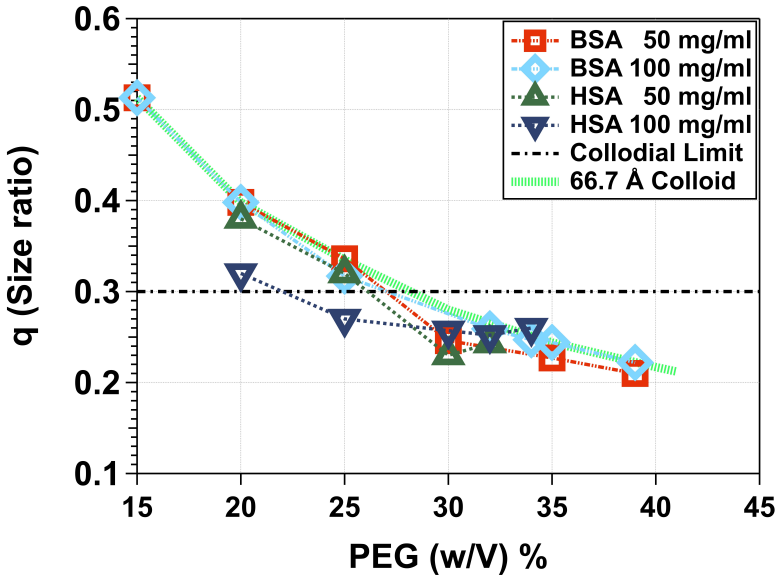

Figure 8.3: *Calculated size ratio (q) for* 50 *and* 100 *mg/ml BSA and HSA in the presence of 100 mM NaCl for different PEG concentrations ((w/V) %). The black dashed line indicates the theoretically determined collodial limit. The green line serves as a guide to the eye and indicates the size ratio for a colloid with a diameter σ of* 66.7 Å*. Besides, lines serve guides to the eye.*

On the other hand, below this line, crystal formation and coexistence of colloidal crystal and liquid is possible. It was found that the crystallization conditions for BSA are in agreement with this experimentally and theoretically determined limit (see also Fig. 8.1 (a) and 8.2 (c)) for the reported experiments. Therefore, the rich phase behavior observed here can be described as a consequence of the depletion effect.

8.3.3 Depletion-Induced Effective Protein-Protein Interactions

In order to obtain further information about the effective protein-protein interactions upon the addition of PEG 3350 M_w, systematic SAXS measurements were performed. The obtained results for protein concentrations of 50 and 100 mg/ml BSA and HSA admixed with 100 mM NaCl are summarized in Fig.8.4. At low PEG concentrations, all SAXS curves share a common feature: with increasing PEG concentration, the intensity at low Q increases. This initial increase can be equated to a reduction of repulsion. A further increase in the PEG concentration yields in attraction, with the low Q intensity reaching its maximum. For 50 mg/ml BSA and HSA, the maximum can be observed at 30 (w/V) % PEG (see Fig. 8.4 (a),(c)). For 100 mg/ml BSA and HSA, the maximum is visible at 25 (w/V) % PEG (see Fig. 8.4 (b),(d)).

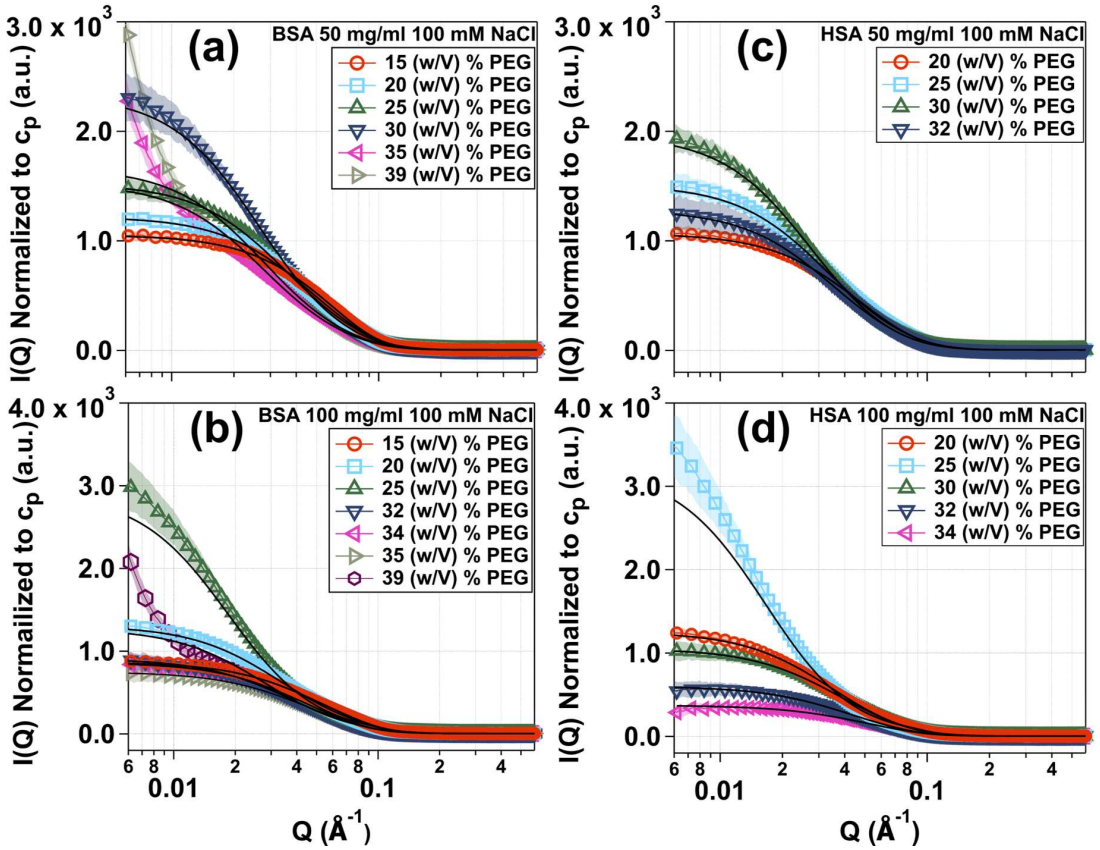

Figure 8.4: *SAXS data for 50 mg/ml (a, c) and 100 mg/ml (b, d) BSA/HSA in the presence of 100 mM NaCl. Data are background-corrected and normalized to the respective protein concentration (c_p). Due to phase separation and aggregation, the SAXS measurements were performed on the dilute phase of the respective samples. In order to ensure comparability, the resulting SAXS intensity profiles were normalized to the original protein concentration using a control sample. Further details on the normalization to the protein concentration c_p can be found in the Experimental Section 8.5. Throughout, the PEG concentration (w/V) % varies from 15 up to 39 %. SHS model fits are featured as solid black line. For readability, only every fifth data point is shown. Besides the black line (SHS model fit), lines serve as guides for the eye. Notice that the error bars are represented as opaque shadows with the corresponding color.*

Further increase in the PEG concentration yields LLPS, (see Fig. 8.1 (a),(b)) and leads to a low Q decrease (see Fig. 8.4). Curves for 50 mg/ml BSA with 35 and 39 (w/V) % PEG (see Fig. 8.4 (a)) and 100 mg/ml BSA with 39 (w/V) % PEG (see Fig. 8.4 (b)) feature a different shape for low and intermediate Q, compared to the other curves of their respective sample sets. This behavior can be traced back to BSA condensate/aggregate formation. An ellipsoidal form factor combined with a SHS model (solid black lines) was applied as a model to fit the data. Based on these fits, B_2/B_2^{HS} values were extracted, which allow for quantifying these

aforementioned observations. B_2/B_2^{HS} values can be termed an intermolecular measure of interactions. The prefixes of the B_2/B_2^{HS} values indicate the type of interaction; i.e., values greater than zero indicate net repulsion, whereas values less than zero indicate net attraction. All investigated samples Fig. 8.5, regardless of the protein system (BSA or HSA) feature an initial B_2/B_2^{HS} value around ± 0.0 indicating neutral to attractive intermolecular interactions. With increasing PEG concentration (w/V) %, the B_2/B_2^{HS} curves decrease linearly before reaching a common B_2/B_2^{HS} value of ≈ -1.5 at 25 (w/V) % PEG.

At a concentration of 25 (w/V) % PEG, the value of B_2/B_2^{HS} is lower for HSA than for BSA. This is consistent with the phase diagrams (see Fig. 8.1 (a),(b)) and indicates stronger attractive forces in HSA than in BSA solutions under the same conditions (25 (w/V) % PEG). However, a further increase in the PEG (w/V) % concentration leads to a reversal of this effect, which is reflected in lower B_2/B_2^{HS} values for BSA compared to HSA (see Fig. 8.5 (a)).

Beyond 25 (w/V) %, the curves for HSA 50 and 100 mg/ml HSA likewise decrease linearly, albeit with a less pronounced slope. The same tendency can be seen for 100 mg/ml BSA. Only the curve for 50 mg/ml BSA is different. This curve decreases linearly up to 35 (w/V) % PEG. Above 35 (w/V) % PEG, the slope changes and becomes steeper before reaching its minima at $= -3.5$ B_2/B_2^{HS}. The B_2/B_2^{HS} curves are in good agreement with the experimentally obtained phase diagrams (see Fig. 8.1 (a),(b)). A deeper analysis of the collected data (Figs. 8.1, 8.3 and 8.4) indicates that the observed crystallization conditions of BSA occur in the predicted q range of $q < 0.3$, which allows the coexistence of colloidal crystal and colloidal liquid. This behavior is in accordance with the literature. [48, 157, 368, 375–377]

Similarly, the occurrence of crystals can be characterized by a window of B_2/B_2^{HS} values: $-10 \lesssim B_2/B_2^{HS} \lesssim -1$, [195–197] which is well consistent with the data shown here.

Moreover, a model-free analysis of the inverse intensity $1/(I(Q')$ normalized to $c_p \to 0$ of the scattering at low Q values ($Q' = 0.0064\,\text{Å}^{-1}$), close to the origin, was performed (Fig. 8.5 (b)). Unlike the model-based SHS analysis, this method does not require attractive conditions within the system. This approach is connected to the reduced second virial coefficient shown by the following relation. [28, 263, 277]

$$\frac{1}{I(Q \to 0)} \propto \frac{1}{S(Q \to 0)} = 1 + 2B_2\,\rho + ... \tag{8.5}$$

If LLPS is absent, the protein concentration c_p can be expressed to be proportional to the number density ρ, ($c_p \propto \rho$), so the inverse intensity ($1/I(Q \to 0)$ is proportional to the reduced second virial coefficient. Due to the occurrence of LLPS, c_p varies between the measured dilute, and the dense phase, leading to the differences that are to be seen when comparing B_2 with $1/I(Q \to 0)$.

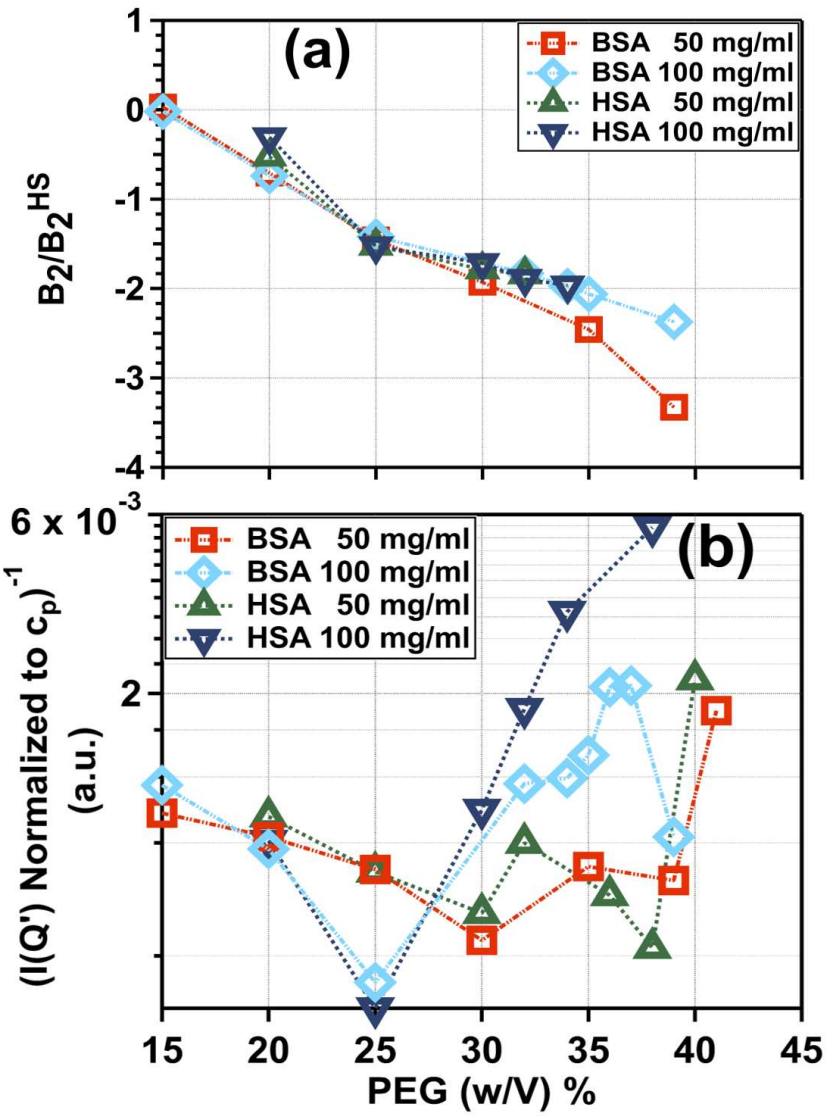

Figure 8.5: *(a) Reduced second virial coefficients and (b) $1/(I(Q')$ normalized to $c_p \rightarrow 0)$ behavior of BSA and HSA for 50 and 100 mg/ml in th presence of 100 mM NaCl as a function of PEG (w/V) % concentration. (b) Due to phase separation and aggregation, the SAXS measurements were performed with the dilute phase of the respective samples. In order to ensure comparability, the resulting SAXS intensity profiles were normalized to the original protein concentration using a control sample. Further details on the normalization to the protein concentration c_p can be found in the Experimental Section 8.5. For BSA (50 mg/ml) with 35 (w/V) % and 40 (w/V) % of PEG and HSA (100 mg/ml) with 39 (w/V) % PEG, the respective fits (see Fig. 8.4) were used to extract the inverse intensities (further details are to be found in the text). The inverse intensity was evaluated at $Q' = 0.0064\,\text{Å}^{-1}$. The dashed lines in (a, b) serve as guides for the eye. The respective error values are smaller than the used markers and are not plotted for readability.*

Importantly, for the matching dilute and dense phase, the same reduced values of the second virial coefficient can be obtained as a result of phase equilibrium. [64, 196, 275] The results presented for the protein interactions are in agreement with the macroscopic observations (see Figs. 8.1 and 8.5). All samples feature LLPS and show an initial decrease in the inverse intensity followed by an increase after reaching the respective minima. This behavior is in accordance with the second virial coefficient analysis. Looking at the inverse intensity, two different minima are observed. Curves for 100 mg/ml BSA and HSA feature a minima at 25 (w/V) % PEG, whereas for curves of 50 mg/ml BSA and HSA this minima occurs at higher PEG concentrations (30 (w/V) %). Increasing the PEG concentration further results in an LLPS, perceived as an inverse intensity increase. Due to the low Q increase at 50 mg/ml BSA with 35 and 39 (w/V) % PEG and 100 mg/ml BSA with 39 (w/V) % PEG induced by BSA aggregation/condensation, the corresponding SHS model fit was used for the inverse intensity (see Fig. 8.4 (a),(b) and Fig. 8.5 (b)). The fit does not consider aggregation, yielding a curve following a pattern similar to one without aggregation. Note that generally we assume an uncertainty of 10 % for the SAXS results presented here, which arise from preparatory inaccuracies and data collection.
In order to elucidate the differences between nonspecific and specific interactions with regard to the crystallization behavior of BSA and HSA, the results obtained on nonspecific interactions are compared to those of previous studies on BSA and HSA in the presence of trivalent metal salts. Examining BSA and HSA in the presence of trivalent salts yields a rich and diverse phase diagram, comparable to that observed in the depletion interaction (see Fig. 8.1). It is known that trivalent salts induce reentrant condensation (RC) phase behavior in HSA and BSA solutions [47, 59, 60, 62, 322, 365]. The rich and diverse phase diagram of RC not only contains aggregates but also LLPS or crystallization [47, 56, 58, 60, 107, 318, 365]. Initially, the protein molecules possess a net negative surface charge and repel each other [47, 55, 59, 62, 169, 318]. In addition, the long-range electrostatic repulsion stabilizes the protein molecules and the solution appears clear [47]. Upon addition of multivalent salts, the net negative surface charges of the protein molecules are neutralized. Crossing the first critical salt concentration, the solution turns opaque and aggregates, LLPS or crystallization can be observed. Increasing the salt concentration further yields a charge inversion and the formally net negatively charged proteins become positive. Upon crossing the second critical salt concentration, the protein salt solution turns clear again, as now the protein molecules repel each other. [47, 57–59, 148, 169, 318] Thus, a further increase of the salt concentration, exceeding the second critical salt concentration, enhances the net positive surface charge, and therefore further enhances the repulsion [47, 55, 59, 62, 169, 318]. This experimentally observed behavior corresponds to the physical description of the patchy particle model. [107, 109] Previous works by Maier *et al.* [60, 365] reveal, that the addition of $CeCl_3$ triggers RC phase behavior for both protein systems. For the tested conditions, only the HSA system exhibited crystallization, whereas BSA did not.

A comparison of the obtained B_2/B_2^{HS} values of BSA and HSA in the presence of 100 mM NaCl and PEG with B_2/B_2^{HS} values for BSA and HSA in the presence of CeCl3 measured by Maier *et. al* [365] reveals that both systems feature similarly low second virial coefficient values (see Fig. 8.6). Since HSA and BSA exhibit RC phase behavior in the presence of CeCl3, this behavior is also reflected in the virial coefficient analysis. At sufficiently high concentrations of salt (c_{salt}), a steep increase in the B_2/B_2^{HS} values is observed, reflecting the RC behavior (see Fig. 8.6 (a)). Generally, B_2/B_2^{HS} values can be used as a guideline to predict protein crystallization. [195, 198] Investigation on protein crystallization showed that virial coefficient values (B_2/B_2^{HS}) within a range of $-10 \lesssim B_2/B_2^{HS} \lesssim -1$, feature a suitable level of attraction between the individual protein molecules for crystallization to occur. [195–197] In addition, ideal growth conditions for crystals were found at two locations in the phase diagram: near but above the critical point or slightly below the critical point. In the first case, density fluctuations are in favor of crystallization, enhancing the nucleation rate, whereas in the second case, the growth of a crystal is facilitated by a two step process. [190, 198]
Interestingly, only HSA crystallized in the presence of CeCl3 provided the investigated conditions despite sufficiently low (attractive) B_2/B_2^{HS} values (see Fig. 8.6 (a)). [195–197, 365]

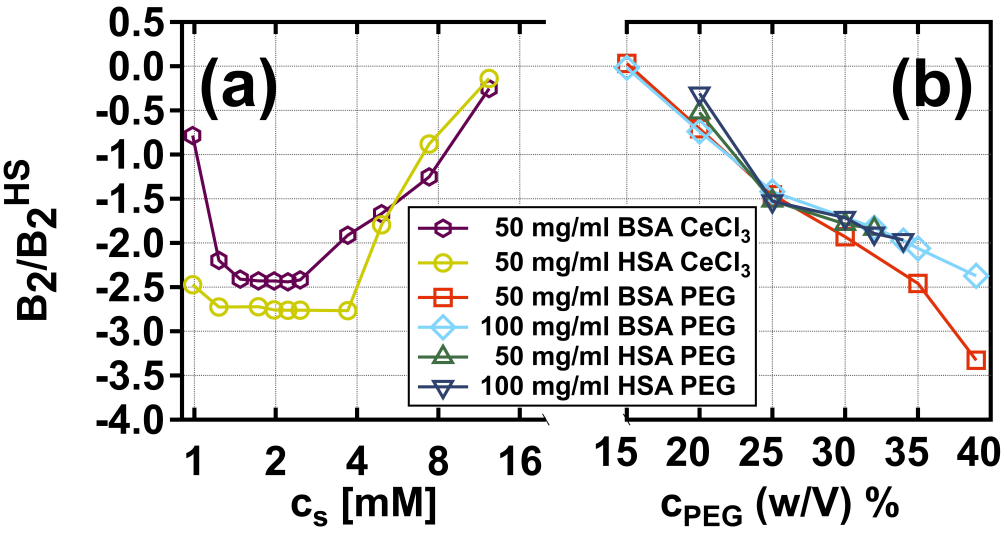

Figure 8.6: *Comparison of B_2/B_2^{HS} values for HSA and BSA in the presence of CeCl3 (data were taken from ref [365]) with (b) B_2/B_2^{HS} values of BSA and HSA admixed with PEG. Please note that two separate X-axes are provided. The left X-axis indicates the CeCl3 concentration (c_s mM) in logarithmic scale to the base of two (log). The right-hand side X-axis indicates the PEG concentration (c_{PEG} (w/V) %)) on a linear scale.*

The measurements on the BSA-and HSA-PEG systems showed that provided the conditions investigated, only BSA was able to crystallize, again, despite the sufficiently low (attractive) B_2/B_2^{HS} values (see Fig. 8.6 (b)). [195–197]
Moreover, the obtained crystals from the HSA-trivalent salt system (e.g., $CeCl_3$ or YCl_3) exhibit the $P2_12_12_1$ space group. [60, 365] The BSA crystals, on the other hand, crystallize in a $C2$ space group. Despite their similarities, small differences require different crystallization strategies, taking into account the experimental conditions used in each study. The X-ray diffraction analysis of BSA crystals and the analysis of the BSA and HSA crystal surfaces is described below.

8.3.4 Discussion on the Different Crystallization Behaviors in the Presence of PEG and Multivalent Salts

The following section addresses both the similarities and differences between BSA and HSA and derives key mechanisms that could trigger the different bulk (crystallization) behaviors of BSA and HSA.
X-ray structure analysis showed that BSA crystals observed in this study are isomorphous to the BSA structure reported by Majorek *et al.* [168] with unit cell parameters of $a = 220.1\,\text{Å}$, $b = 44.8\,\text{Å}$, $c = 144.4\,\text{Å}$, and $\beta = 114.2\,°$ crystallized in space group C2. Model coordinates were not further refined, as the crystal packing is already reported. Next, we compared the crystallographic protein interfaces of BSA and HSA. Both proteins show a sequence identity of 75.6 % and adopt a similar protein fold, although their N-terminal domain (residues $1 - 150$ for BSA) differ significantly. The C-terminal amino acids (residues $151 - 500$ for BSA) showed a Cα rmsd of 2.26 Å over 344 aligned residues. It is noteworthy that the combined total mean buried surface area of BSA is substantially lower than that of HSA, with values of 1190 and $1960\,\text{Å}^2$, respectively. However, a reliable statistical analysis is hampered by the limited number of BSA structures deposited with the protein data bank. A randomly picked data set for HSA that we have prepared to avoid user-introduced data bias based on our preselection of reported HSA structures resulted in a comparable total buried surface area of $1890\,\text{Å}^2$ and showed that HSA has in general utilized a larger surface area for crystal contact formation (see Table 8.2 in the Supporting Info 8.6). We mapped all interface areas of the proteins on the surface. Although the pattern of amino acids contributing to crystal contacts looks comparable, HSA utilizes a larger number of residues for crystal contact formation, which indicates a larger number of potential attraction sites for HSA (see Fig. 8.7).
A histogram plot showing the relative frequency of an amino acid to be part of an interface also indicates that HSA utilizes a broader number of residues to take part in protein-protein contact formation (SI Figure 5). A similar conclusion can be made by grouping the interface residues by their number of contacts and plotting their normalized frequency (by the total number of interactions) of the data set (SI Figure 6).

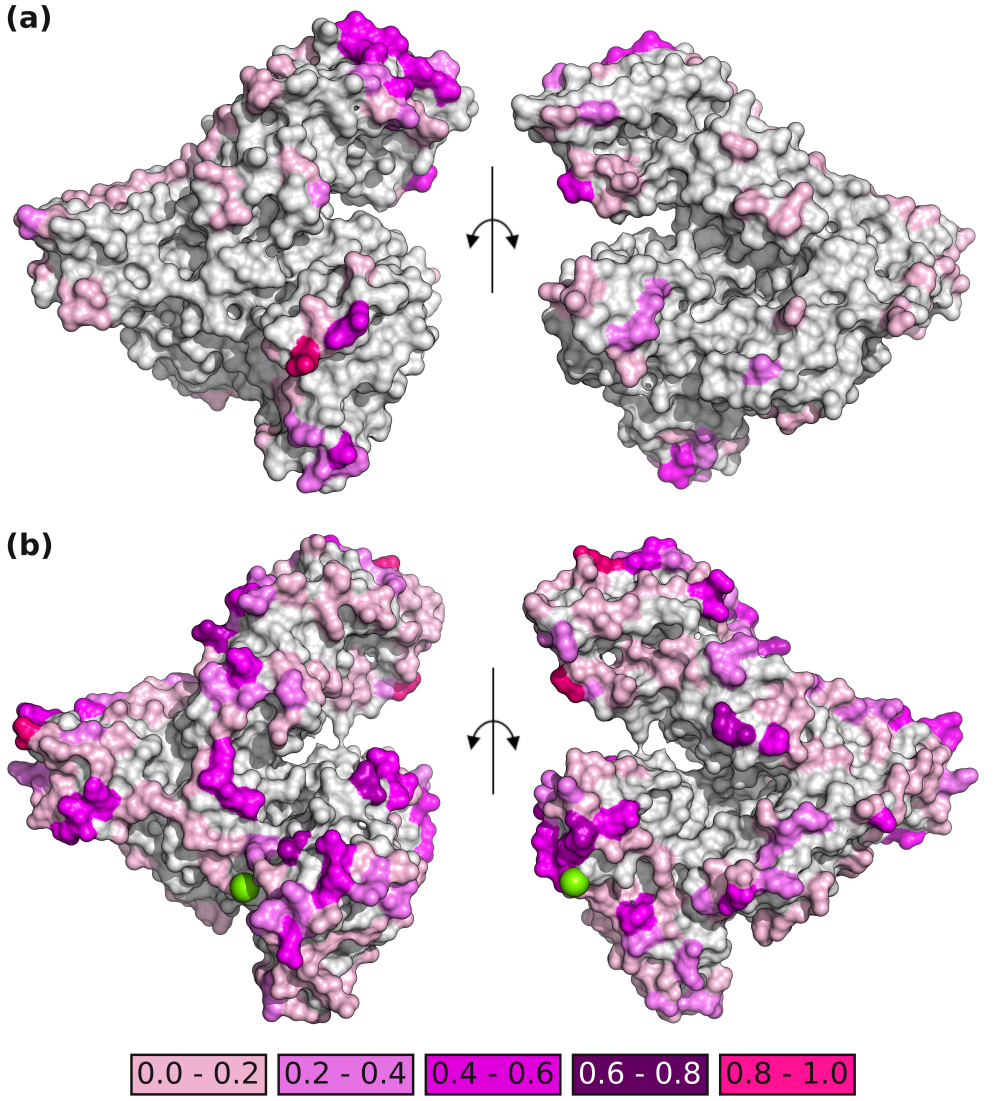

Figure 8.7: *Crystal contact areas of BSA (a) and HSA (b). The proteins are shown from both sides in similar orientations. The front view is shown on the left, and the back view is shown on the right of each panel (180 °). Green spheres indicate the positions of Y^{3+} ions in PDB entry 7A9C. Amino acids involved in crystal contact formation are colored in different shades of violet to pink based on their individual relative weighted surface area from minor impact (light violet) to crucial residues (hot pink). The weighted surface area is calculated by the summation of all crystal contact area contributions of an individual residue over interfaces in all pdb entries of the chosen data set. A cut-off value of 20 $Å^2$ is applied, and residues below this cutoff value are neglected from the calculation. A detailed analysis that takes different cut-off values into account can be found in Supporting Information 8.6 (SI Figure 8.10 and 8.11). The individual summed per residue surface area is then divided by the largest individual per residue surface area to obtain an individual (per residue) relative weighted surface area that is not dependent on the number of all investigated contact interfaces.*

This shows that HSA residues possess a wider spread in the number of contacts compared to the BSA data set.
Next, we compared if BSA is in general capable of establishing a comparable yttrium ion (Y^{3+})-mediated packing as observed for HSA by building a hypothetical BSA-Y^{3+} lattice similar to pdb entry 7A9C. [60] Both protomers possess a theoretical pI of 5.6 and therefore seem to be capable of forming similar coulombic interactions with positively charged ions. We found that BSA lacks at least one glutamate residue (in BSA A367) that would be essential to form a comparable chelating Y^{3+} complex bridging two HSA protomers, as reported for pdb entry 7A9C. [60] In addition, the formation of salt bridges requires a structural match (recognition) between two protein surfaces and therefore exhibits a strong orientation dependence. [46] This does not, however, exclude a potential complex formation with yttrium ions at a discrete position of a negatively charged patch on the BSA surface.

8.4 Conclusion

In this work, the behavior of the two proteins BSA and HSA in the presence of the polymer PEG 3350 M_w and 100 mM NaCl was investigated. For both protein-PEG systems (BSA and HSA), phase diagrams were established. Both systems featured rich and diverse phase behavior (see Figure 8.1). However, provided the applied experimental conditions, only the BSA-PEG-salt system featured crystallization, whereas the HSA-PEG-salt system did not. The space group of the BSA crystals was determined by X-ray diffraction analysis. The results confirmed that the space group found corresponds to previously published C2 space group of BSA [167, 168]. Based on the ratio of polymer to colloid size q, it was determined that the colloid limit $q < 1$ applies. This calculated size ratio allows the experimental phase behavior to be compared with those obtained from colloid-polymer theory within the framework of depletion interactions. Results revealed an agreement between the theoretical and experimental phase diagrams, [86] suggesting that the phase behavior can be attributed to simple depletion interactions. Furthermore, it cannot be ruled out that apart from the depletion effect, other interactions or effects interfere and trigger the observed phase behavior. These could include hydration effects, hydrophobic interactions, or even dispersion forces. However, the protein-polymer solutions do not form aggregates in the following three cases: absence of the polymer (PEG 33350 M_w) and salt (100 mM NaCl), presence of salt and absence of the polymer, [57, 266, 378] and presence of the polymer and absence of salt. [379] This suggests that the observed phase behavior can be attributed to depletion interaction. In order to maintain this reasoning, it is necessary to consider the structure of the colloids from a coarse-grained perspective, which allows us to describe the proteins as hard spheres. Given the absence of salt and polymers, BSA and HSA solutions are stable up to high concentrations, which indicates for only minor interactions.

In addition to the phase behavior, SAXS measurements were conducted in order to further quantify the protein-PEG-salt systems by means of second virial coefficient analysis (B_2/B_2^{HS}). It was shown that with increasing PEG concentration B_2/B_2^{HS} decreases; thus, both systems increase their attractiveness. Additionally, both systems feature B_2/B_2^{HS} values corresponding to $-10 \lesssim B_2/B_2^{HS} \lesssim -1$. [195–197] This clearly indicates that both protein-polymer-salt-systems feature low enough B_2/B_2^{HS} values for crystallization. However, as mentioned above, crystallization was observed only for the BSA-PEG salt-system. Moreover, the obtained B_2/B_2^{HS} values were compared to B_2/B_2^{HS} for BSA- and HSA-$CeCl_3$-salt systems recorded by Maier *et. al* [365] (see Figure 8.6). Interestingly, for BSA and HSA with $CeCl_3$, similarly low B_2/B_2^{HS} values were recorded, indicating that both BSA and HSA could potentially form crystals. However, utilizing $CeCl_3$, only the HSA system showed crystallization.
Next, a crystal surface analysis of HSA and BSA revealed that HSA utilizes a greater number of solvent exposed-amino acids for intermolecular protein-protein interactions, eventually resulting in crystal formation. This agrees with the large number of reported crystal structures in the protein database where 118 HSA entries are reported to form at least 13 different crystal packings. In contrast, eight BSA entries are found in the protein data bank, all crystallized in an isomorphous crystal packing of space group C2. Although the sequence similarity of approximately 76 % and a comparable isoelectric point of 5.6 for both proteins suggest a closely related phase behavior, their crystallization properties are fundamentally different. This is also demonstrated by their different behavior with respect to Y^{3+} ions. Although HSA is capable to form cation-mediated intermolecular protein-protein interfaces via positively charged Y^{3+} ions, a comparable behavior is not observed for BSA, as the crucial acidic residues are either not found at the HSA-specific positions or adopt conformation that would not allow for a comparable chelating effect. This clearly indicates that phase behavior of a protein is not directly accessible by the phase diagram of closely related proteins, as minor changes in the surface landscape render it necessary to determine the phase diagram for every protein candidate individually.

8.5 Experimental

8.5.1 Materials and Sample Preparation

Proteins BSA (A3733, purity of $\leq 98\,\%$) and HSA (A9511, purity of $\leq 97\,\%$), sodium azide (NaN_3) (S8032-25G), and poly(ethylene glycol) powder (PEG, $H(OCH_2CH_2)nOH$, average size of M_n3350, 202444-250G) were purchased from Sigma-Aldrich, now Merck, and used in the executed experiments without further purification. Similarly, sodium chloride NaCl was purchased from Merck and, without further purification, used in the experiments. In order to prevent any contamination caused by unwanted bacterial or fungi growth, 1 mM NaN_3 was

added to deionized and degassed Millipore water (a conductivity of 18.2 MΩ cm). This Millipore water was then used to prepare stock solutions by dissolving the required amounts of protein powder, NaCl or PEG. The stock solutions were prepared at room temperature ((RT) 21 ± 1 °C).
After preparation, the protein stock solutions were immediately incubated for at least 24 h at 4 °C to ensure dissolution of the protein powder. The concentration of the protein stock solution was determined by a Cray 50 UV-vis spectrophotometer (Varian Technologies) with the appropriate extinction coefficients (see Table 1) and the Cary WinUV operating software. The absorbance was measured at 280 nm. The protein solutions were stored at 4 °C in air impermeable containers to avoid the re-dissolution of gases [341]. Moreover, the protein solutions were used exclusively for a total duration of 3 weeks [380]. The PEG stock solution was prepared using a weight-to volume-ratio (w/V) % of 100 % (1 g PEG to 1 ml of Millipore water). The PEG solution and the salt solution were stored at RT. All samples were obtained by mixing the required amount of the previously prepared Millipore water, protein stock solution, PEG stock solution, and NaCl stock solution. The prepared samples showed a pH value well above the pI of the respective protein, measured with a pH meter from Mettler Toledo (Germany). Investigation of the samples was carried out at RT. Systematic deviations arising from variations in protein batches, preparative inaccuracies, and fluctuations in protein and other stock solutions cannot be ruled out.

8.5.2 BSA and HSA Phase Behavior determination

Visual inspection was performed to determine the phase diagrams for BSA and HSA (Fig. 8.1) in the presence of PEG and NaCl. According to this, a sample series with four different protein concentrations (20, 50, 80 and 100 mg/ml) accompanied by 100 mM NaCl and increasing PEG concentrations (w/V %) were prepared for BSA and HSA, respectively. To avoid confusion, t^* is defined as the transition border from a clear sample to a turbid one, as to be seen in Fig. 8.1.
Besides inspection by the eye, an optical microscope (Axio Scope.A1, Carl Zeiss AG) was used for a more precise optical investigation of the samples. Images were recorded by a camera (AxioCam ICc5, Carl Zeiss AG) operated with the software ZEN Lite 2012. Microscopy samples were collected from the respective previously prepared phase diagram sample series. This involved dispensing 25 µl of the sample onto a Gene Frame, (1 × 1 cm) with a thickness of 0.25 mm (Thermo Scientific^{TM}, Germany). Afterward, the Gene Frame was covered with a coverslip. In order to investigate crystallization, appropriate samples (in tubes or microscopy slides) were stored and observed over a longer period of time ranging from 7 days (microscopy slide) up to one month (tubes).

Table 8.1: *Important physiochemical properties of BSA and HSA*

	BSA	**HSA**
# amino acid	583 [220]	585 [222]
molecular weight [kDa]	66.4 - 67 [221, 381]	66.4 - 69 [222, 223]
pI (pH 7)	4.6 [58]	4.7 [222]
specific volume [ml/g]	0.735 [339]	0.754 [340]
ellipsoid R(a) [Å]	17	18
ellipsoid R(b) [Å]	42.00 - 55.00	45.00 - 56.17
extinction coefficient $[\mathrm{ml} \times \mathrm{mg}^{-1} \times \mathrm{cm}^{-1}]$	0.667 [305]	0.531 [305]

8.5.3 SAXS and Data Analysis

In small-angle X-ray scattering (SAXS) experiments dealing with suspended particles in solution, the measured intensity profile *I(Q)* can be described as a function of the momentum transfer Q:

$$I(Q) \propto n_p \Delta\rho^2 V_p^2 \langle P(Q) \rangle S(Q), \tag{8.6}$$

this relation is given for mono-disperse and spherical particles. The number density of the dissolved particles is given by n_p, while the $\Delta\rho$ denotes the cross-sectional scattering difference between the particle and the solvent. V_p represents the volume of the particle. The momentum transfer is defined as $Q = (4\pi/\lambda)\sin(2\theta/2)$. Here, λ denotes the wavelength and $2\,\theta$ denotes the scattering angle. The shape and size of the scattered particle averaged over the spatial orientation are given by form factor $\langle P(Q) \rangle$. $S(Q)$ denotes the structural factor, describing the spatial arrangement of the particles, which is governed by the interaction potential. From this, it can be deduced that the structural factor $S(Q)$ describes the effect of positional correlations [263, 382].
SAXS data was collected at the P12 beamline of the EMBL (DESY, Hamburg, Germany). The measurement setup utilizes a focused X-ray beam ($120 \times 200\,\mu\mathrm{m}$) with an energy of 10 keV and a corresponding wavelength of $\lambda = 1.24$ Å. The sample-to-detector distance was set to 3.1 m. A Q range of 0.002-0.45$\mathrm{Å}^{-1}$ was covered by a 2M Pilatus (Dectris) detector. Prior to the measurement, the samples were carefully centrifuged, and subsequently, the supernatant was measured. Each sample was illuminated for 30 exposures, with a duration of 0.095 s each. Exchanging of samples was realized by use of a flow cell. The intensity profiles were obtained by azimuthal averaging of the collected 2 D data sets. Averaging of each data set was performed only after a manual check for consistency. Inconsistent exposures due to, e.g., air bubbles in the flow cell were sorted out. Unlike its behavior in neutron scattering experiments, PEG has an almost identical X-ray scattering cross section per unit volume to H_2O, allowing the polymer salt

mixture to be considered as background [383]. The background measurements were treated likewise and then subtracted from the sample profiles. By subtraction of the defined background, SAXS scattering curves (Fig. 8.4) were obtained, containing solely the contribution from the proteins. The avreaged background measurements used for subtraction are given in the Supporting Information 8.6 (SI Fig. 8.9).
Data analysis was performed using an IGOR PRO 9 add-on provided by the National Institute of Standards and Technology (NIST)[286]. The background-corrected data sets were fitted using the sticky hard-sphere potential (SHS) [274], utilizing an ellipsoidal form factor. A similar pipeline for SAXS data processing can be found in the refs [64, 65, 384]. The SHS potential for a spherical particle of radius R, is defined in Equation 8.7.

$$\beta U(r) = \begin{cases} \infty & r < \sigma = 2R \\ -\beta_0 = \ln\left(\frac{12\tau\Delta}{\sigma+\Delta}\right) & \sigma < r < \sigma + \Delta \\ 0 & r > \sigma + \Delta, \end{cases} \tag{8.7}$$

Here, β indicates the inverse of the thermal energy, $1/k_BT$. τ indicates the stickiness parameter, Δ indicates the width of the square well, and σ indicates the diameter of the hard sphere. Based on the perturbative solution of the Percus-Yevick closure relation, the structure factor was calculated [273, 274]. Equation 8.8 shows the calculation for the reduced second virial coefficient within the limitation of $\Delta \to 0$.

$$\lim_{\Delta \to 0} \frac{\mathrm{B}_2}{\mathrm{B}_2^{\mathrm{HS}}} = 1 - \frac{1}{4\tau} \tag{8.8}$$

To obtain the reduced second virial coefficient, we divide the second virial coefficient (B_2) with the second virial coefficient for hard spheres ($\mathrm{B}_2^{\mathrm{HS}}$) of radius R. This relation is given by $\mathrm{B}_2^{\mathrm{HS}} = 16\pi\mathrm{R}^3/3$. Combining the results from simulations and theories has led to a universal $\mathrm{B}_2/\mathrm{B}_2^{\mathrm{HS}}$ value of ≈ -1.5 for the liquid-gas transition in a multitude of different systems, provided that the Percus-Yevick closure relation being applied [198, 275].
The protein concentration within the supernatant (dilute phase) was determined by averaging ten intensity values at high $Q \approx 0.4\,\mathrm{\AA}^{-1}$ of a non-phase separated (control) sample at 50, and 100 mg/ml. Similarly, these intensity values were taken from each sample individually. The protein concentration was calculated by dividing the intensity value of the non-phase separated respective control by the intensity value of the sample, followed by multiplying the result by 100. The protein concentration (mg/ml) values thus obtained were then used to calculate the protein volume fraction. This correction was necessary because only the supernatant was measurable due to phase separation and aggregation, thus ensuring comparability.
Besides the volume fraction, the axes of the ellipsoids were fixed to values shown

in Table 8.1. Moreover, the scattering length density (SLD) of the proteins was set to $7.32 \times 10^{-7}\,\text{Å}^{-2}$. The background was set to appropriate values for each curve individually. In order to prevent artificial coupling between the well width Δ and the stickiness parameter τ, Δ was kept at $0.01\,\sigma$ for all fitted data.

8.5.4 BSA Crystal Analysis and Packing Comparison of HSA with BSA

BSA crystals were analyzed by single crystal X-ray diffraction experiments. Therefore, single crystals of the suspension were extracted. To cryoprotect the crystals, the supernatant of the suspension was supplemented with glycerol (26 w/V %). BSA crystals were transferred in the cryo solution, rapidly washed, mounted into a loop and flash-frozen in liquid nitrogen before data collection at beamline X06SA (swiss light source, Villigen, Switzerland). Although several crystals were tested, the diffraction quality was limited, with the best diffracting crystals yielding a high resolution of approx. 3.5 Å. This was sufficient to unequivocally determine the crystal packing using XDS [385]. The protein crystallized in space group C2 with unit cell parameters of $a = 220.1$ Å, $b = 44.8$ Å, $c = 144.4$ Å, and $\beta = 114.2\,°$. A comparison of all BSA structures deposited to the protein data bank revealed a similar crystal packing with cell parameters of $a = 215.66$ Å, $b = 45.10$ Å, $c = 142.41$ Å, and $\beta = 114.0\,°$ as reported by Majorek *et al.,* [168] and therefore yield to the decision to not further refine the resulting structure but to focus on a detailed interface analysis of available BSA and HSA structures. As a consequence, we searched the protein data bank for structures of human serum albumin and bovine serum albumin, yielding 113 entries for HSA and eight entries for BSA. For BSA, all annotated structure resulted from isomorphous crystal packing of space group C2 with unit cell parameters very close to $a = 215.7$ Å, $b = 45.1$ Å, $c = 142.4$ Å, and $\beta = 114.0\,°$. Our packing analysis of HSA excluded all structures where HSA was determined either by Cryo-EM or NMR and those in which HSA was complexed with a proteinogenic interaction partner, resulting in a data set of 97 HSA structures. Next, we sorted the entries by the reported crystallographic space group and assessed their isomorphism based on the unit cell parameters, yielding a data set separated into 14 groups. Out of this data set, we picked ten structures that used either PEG molecules or phosphate/salt conditions for the crystallization experiment and analyzed the crystal packing interfaces using EPPIC [386]. As the selection is user biased, we decided to include a second analysis, utilizing the same data set but randomly picked ten structures, chosing a single member per group from the 14 groups and avoid duplicate entries. For further analysis, we annotated the size of each crystallographic interface, the amino acids contributing to a crystallographic interface, and the frequency of each amino acid's contribution to packing. In addition, we performed a surface area-based analysis, investigating the individual contribution of a residue to a crystallographic contact by calculating its surface area using PDBePISA. [387]

Moreover, we performed the same analysis based on the frequency with which a residue was found in an interface. We performed the same analysis for all data sets, including the data set chosen based on the crystallization conditions and the randomized data set, and compared the data to the available data for BSA. We generated surface representations of BSA and HSA using PYMOL (The PyMOL Molecular Graphics System, Version 3.0 Schrödinger, LLC.) and colored the amino acids contributing to interface formation based on how often these residues are reported in an interface area (see Figure 8.7).

8.6 Supporting Information

This Chapter is based on the Supporting Information of the publictaion:

Maximilian D. Senft, G. Zocher, S. Retzbach, R. Maier, A. Hiremath, F. Zhang, T. Stehle and F. Schreiber, Role of Specific and Nonspecific Interactions in the Crystallization Behavior of BSA and HSA Protein Solutions, Crystal Growth & Design, 25(8), 2418-2429, 10.1021/acs.cdg.4c01535 (2024).

The original version of the Supporting Information should not be withheld, and can be accessed free of charge following the link below:
`https://pubs.acs.org/doi/10.1021/acs.cgd.4c01535#_i24`
last checked 30.07.2025, 11:05

8.6.1 Visual inspection of samples for the Phase diagrams of Figure 8.1 (a) and (b)

Enlarged image of the two exemplary sample sets (8.8 BSA (a) and HSA (b)) used for visual determination of t^* borders for the phase diagrams (see Fig. 8.1 in the manuscript). The images shown here correspond to Fig. 8.1 (c) and (d) of the manuscript. For both images (a) and (b) the protein concentration ((a) BSA and (b) HSA) was fixed to 50 mg/ml while the PEG 3350 concentrations increased from left to right. Both samples were additionally admixed with 100 mM NaCl.

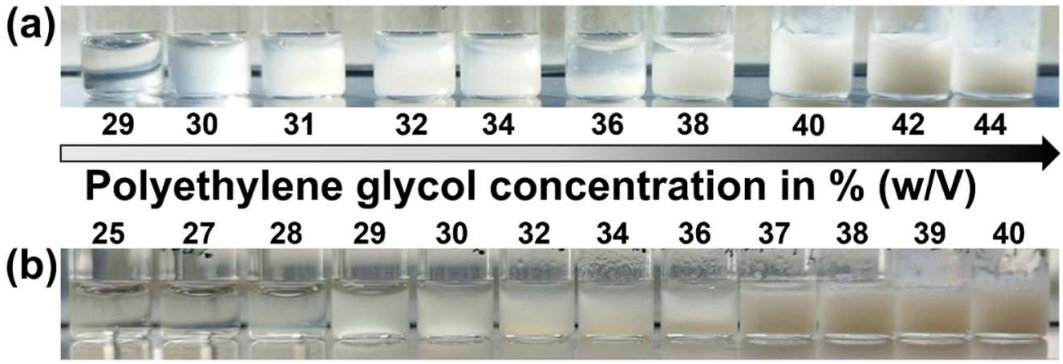

Figure 8.8: *Images from samples used for the visual inspection of BSA with a concentration of 50 mg/ml admixed with increasing (w/V) % of PEG (from 29 to 44 (w/V) %) and 100 mM NaCl are shown from left to right (a). In (b) a photograph of visual inspection for HSA with a concentration of 50 mg/ml admixed with increasing (w/V) % of PEG (from 25 to 40 (w/V) %) and 100 mM NaCl are shown from left to right.*

8.6.2 SAXS background measurements

Averaged background measurements for Milli-Q water mixed with 100 mM NaCl and increasing concentrations of PEG 3350 (10 to 45 (w/V) %). The Background measurements were treated similar to the recorded protein data sets. More precise Information on data acquisition and treatment is to be found in the Experimental part of the manuscript. In addition, a sample (BSA 100 mg/ml with 100 mM NaCl and 15 PEG (w/V) %) is shown before correction, to illustrate the differences in magnitude between sample and background. Please note that this plot is provided in a double logarithmic format.

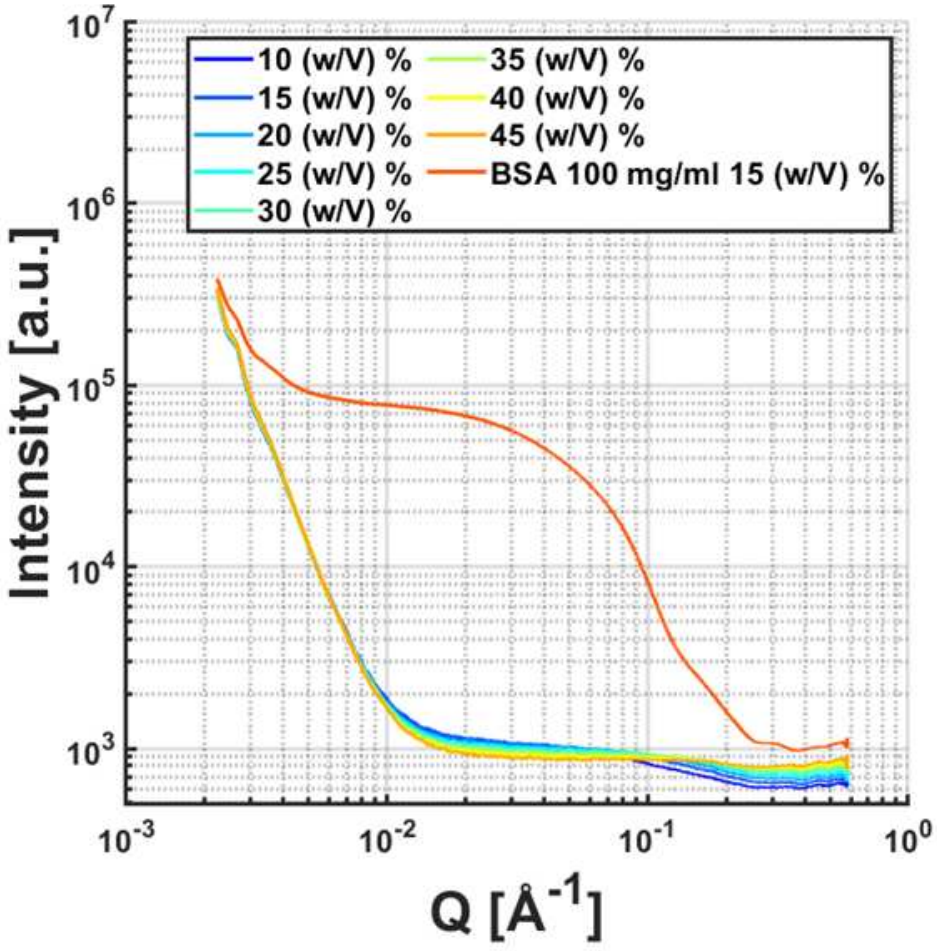

Figure 8.9: *Scattering backgrounds for 100 mM NaCl with increasing concentrations of PEG (w/V) % dissolved in Milli-Q H_2O. The provided background scattering curves were treated similar to the scattering data provided in the manuscript. Highlighted in orange is an uncorrected sample of BSA 100 mg/ml with 100 mM NaCl and 15 (w/V) % PEG to illustrate the differences in magnitude between background and the uncorrected sample. Please note that this plot is in a double logarithmic scale.*

Table 8.2: *Interface surface analysis of HSA and BSA structures deposited to the protein data bank. Interface calculation of the annotated pdb-entries was performed by PDBePISA. [387] The BSA crystal contact analysis is limited by the low amount of BSA structures deposited so far. For HSA, two data sets were generated out of the* 137 *available HSA crystal structures. One data set (ten non-redundant members) is based on a preselection where PEG was used to crystallize the protein. A second data set uses ten randomly picked pdb-entries that are not part of the preselection.*

PDB-entry	**# of interfaces**	**Total surface area [Å^2] per protomer**
BSA		
3V03	10	910
4F5S	13	1476
Mean values	**11.5**	**1193**
HSA-selected		
7DJN	12	2511
7VR0	5	2616
6M4R	12	2601
6M5D	3	1873
1AO6	6	1327
1BM0	7	1379
1E78	7	871
2I2Z	5	2179
3CX9	5	2123
7OV6	8	2117
Mean values	**7**	**1959**
HSA-random		
1E7G	5	1763
8EW4	5	3099
2BXE	7	840
4EMX	10	1379
7EEK	8	2255
3A73	5	2489
7FFS	7	970
3SQI	8	1866
6M5D	3	1873
Mean values	**5.8**	**1887**
HSA-Y^{3+}		
7A9C		1751
		+ 2 Yttrium bridging interfaces

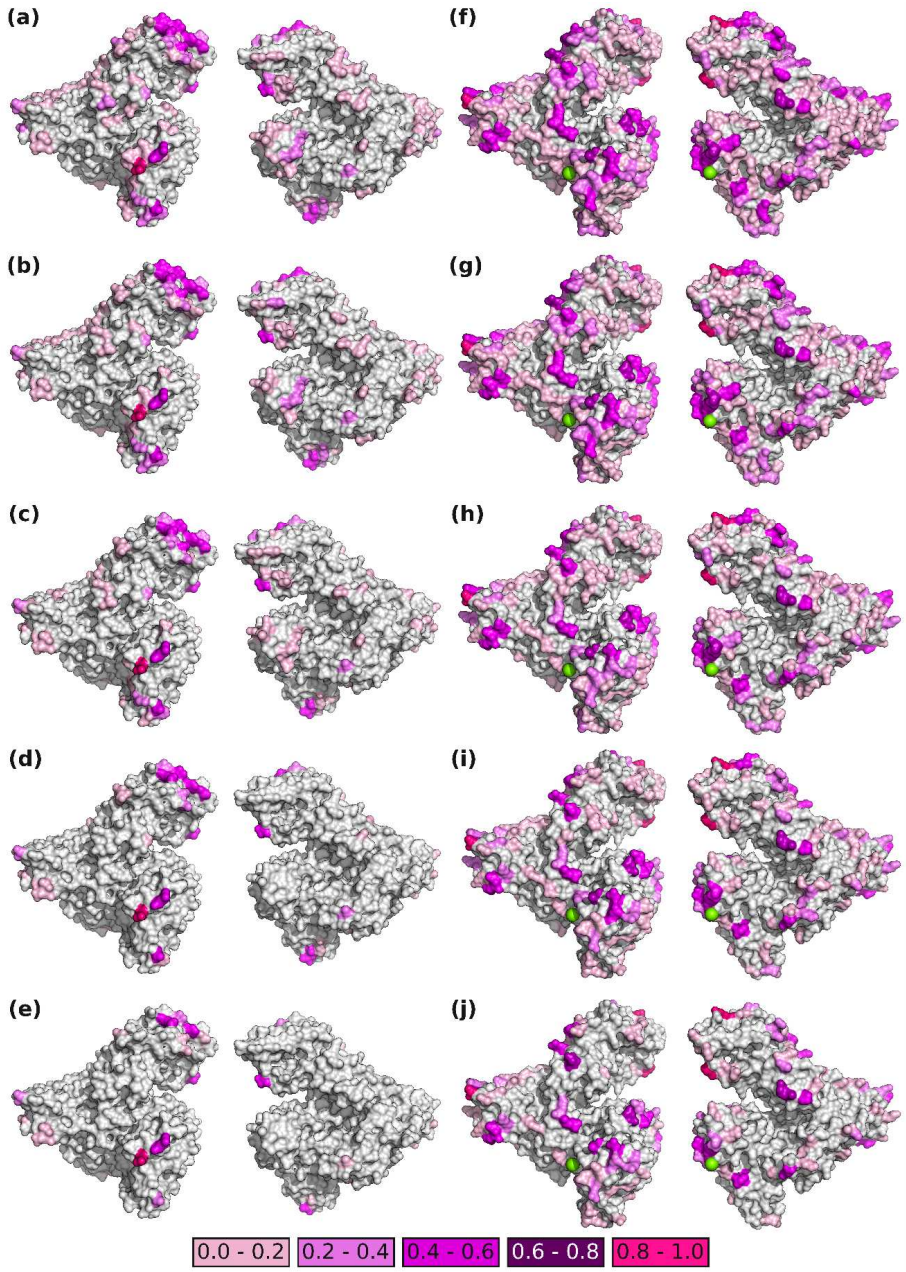

Figure 8.10: *Crystal contact analysis of BSA (left, panels a-e) and HSA (right, f-j) as surface representation in two orientations. Front view left and back view right are shown. Amino acids are colored* ***by a weighted surface contribution****. The calculation uses the interface analysis of PDBePISA. [387] The resulting xml-files from the contact analysis were processed by an in-house script. The buried surface area of each amino acid is summed up if it is above a certain threshold (a+f: above 10 Å^2, b+g: above 20 Å^2, c+h: above 30 Å^2, d+i, above 40 Å^2, e+j: above 50 Å^2) and divided by the buried surface area of the amino acid possessing the largest positional buried surface area of either BSA or HSA to obtain a relative positional buried surface area (rpbsa) for each individual surface amino acid. This procedure avoids effects on different numbers of interfaces of BSA and HSA. The amino acids are than colored based on their rpbsa from light gray (not involved in contact formations) to pink (80-100 % rpbsa) as depicted by the color scheme in the figure.*

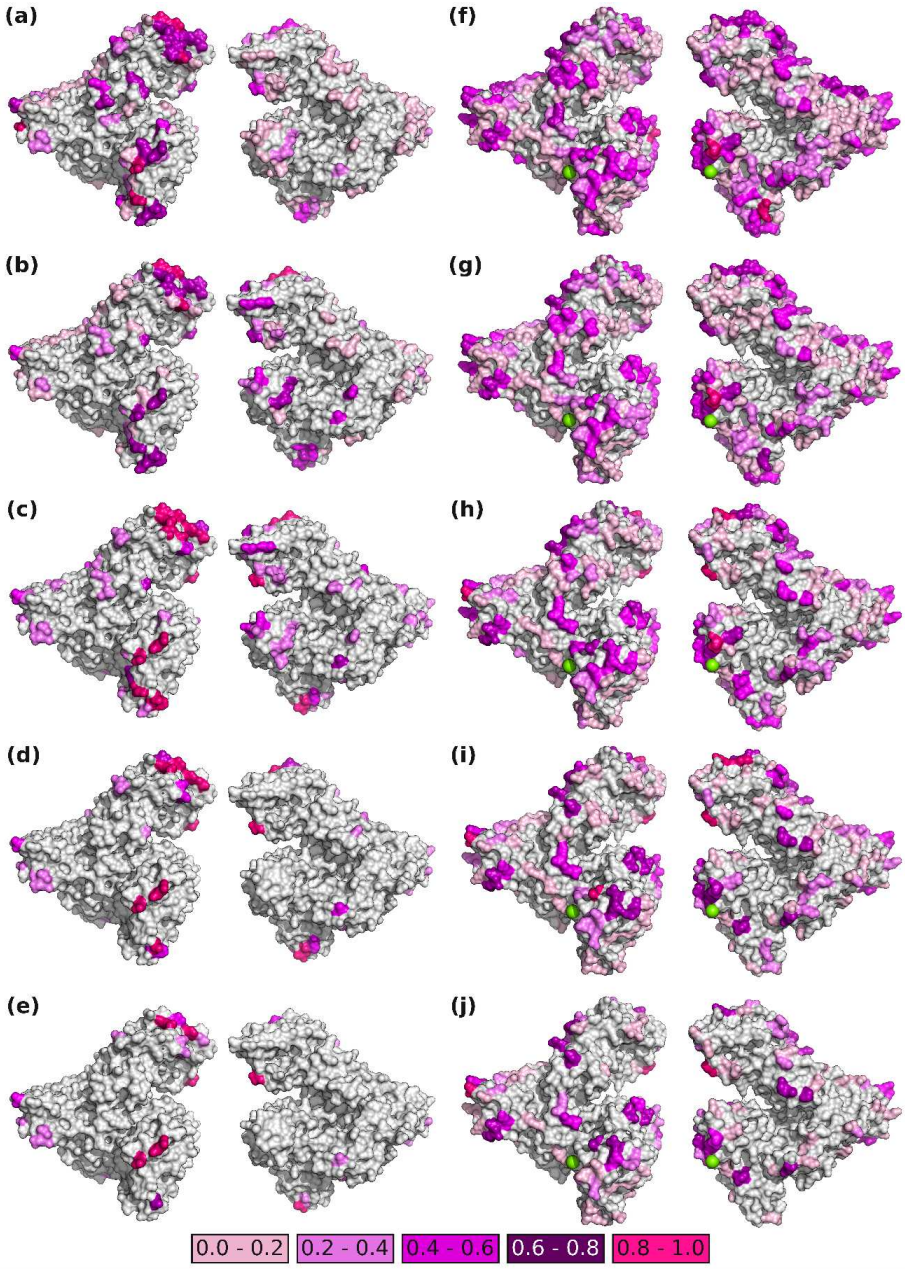

Figure 8.11: *Crystal contact analysis of BSA (left, panels a-e) and HSA (right, f-j) as surface representation in two orientations. Front view left and back view right are shown. Amino acids are colored* ***by their frequency of appearance in crystal contacts****. The calculation uses the interface analysis of PDBePISA. [387] The resulting xml-files from the contact analysis were processed by an in-house script. An amino acid is counted if the amino acid contributes to an interface above a certain threshold (a+f: above 10 Å^2, b+g: above 20 Å^2, c+h: above 30 Å^2, d+i, above 40 Å^2, e+j: above 50 Å^2). The frequency of each amino acid is divided by the maximum individual frequency of either BSA or HSA to obtain a relative individual frequency (rif) for each amino acid. This procedure reduces effects on different numbers of interfaces of BSA and HSA. The amino acids are than colored based on their rif from light gray (not involved in contact formations) to pink (80-100 % rif) as depicted by the color scheme in the figure.*

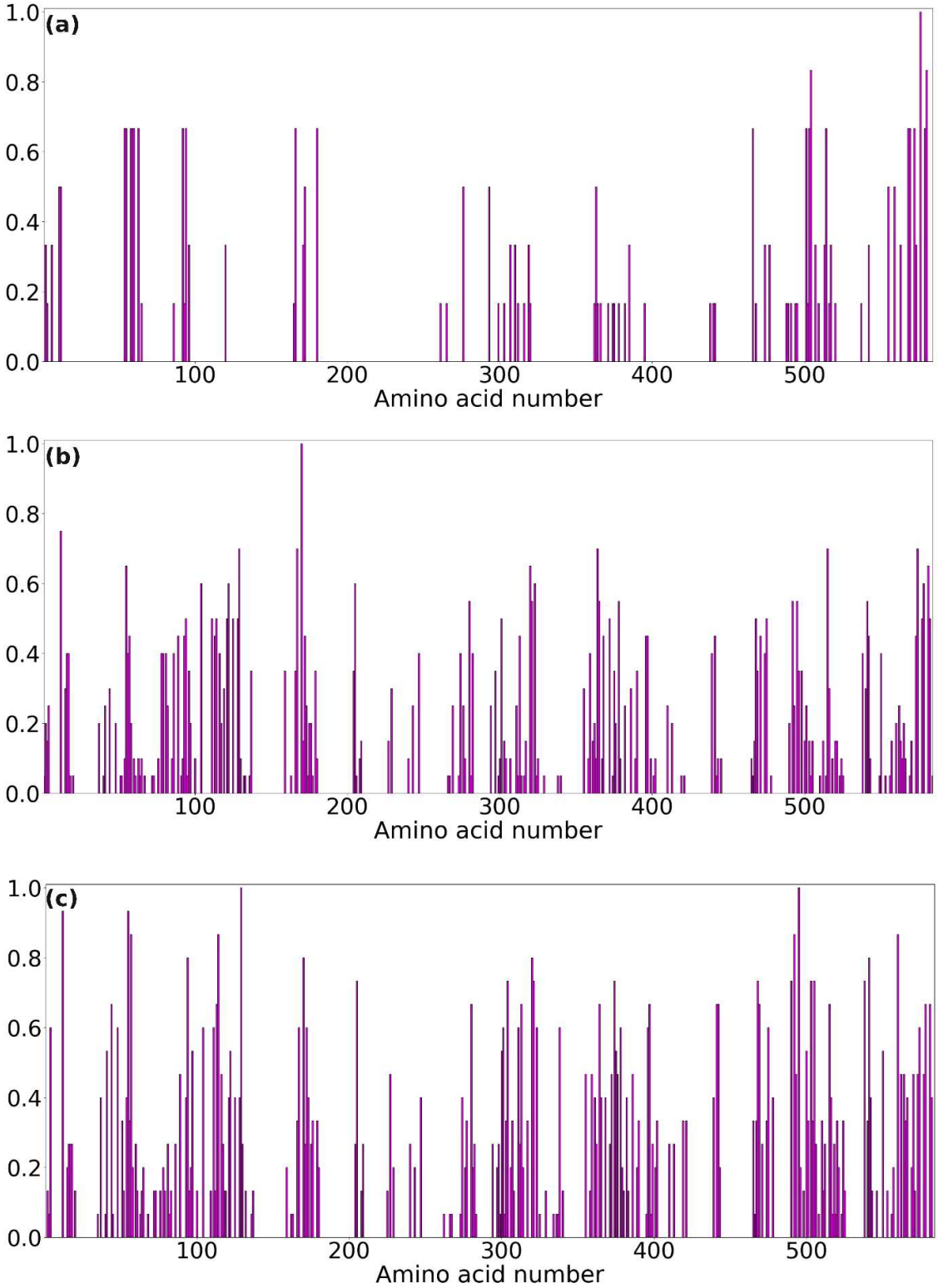

Figure 8.12: *Histogram plot of BSA (a) compared to HSA pre-selcetion (b) and HSA random selection (c) data sets. The relative frequency of an amino acid is plotted against the sequence. Residues with rif equals to zero are not involved in crystal contact formation.*

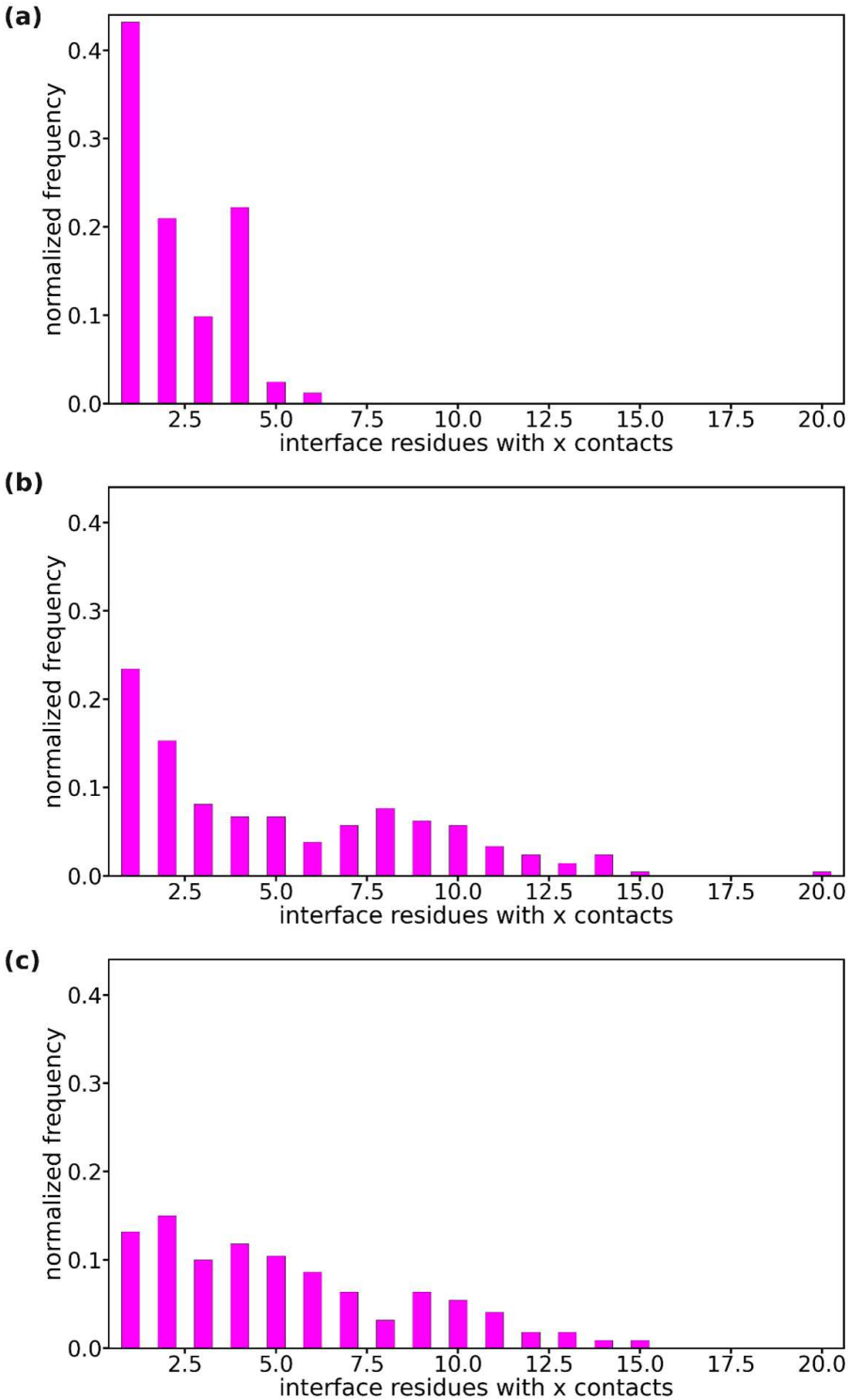

Figure 8.13: *The interface residues are grouped by their number of contacts within all interfaces of the data set and plotted against the normalized frequency of data set BSA (a), data set HSA random (b) and data set HSA preselected (c). The normalized frequency is obtained from each data set by summation of all interface contacts and normalizing the frequency to this value. More generally, the diagram shows how many residues were found from low to high degree interactions within the data set. The data presented here suffers from the low amount of data available for BSA structures.*

Chapter 9

Results III: Specific Co-Ion Effects of Globular Protein Solutions with Trivalent Salts

The following chapter summarizes the progress made on the topic of *Specific Co-Ion Effects of Globular Protein Solutions with Trivalent Salts*. As this Manuscript provides a consolidated overview of this topic, data from previous theses are included and quoted at the appropriate places. A list of the respective contributions is to be found in the table below.

Maximilian D. Senft, Lukas Lang, Ismail S. Muhammad, Michal K. Braun, Fajun Zhang and Frank Schreiber

Contribution:	
Research design:	MDS, FZ, FS
Experiments:	MDS and LL, MKB, ISM
Data analysis and interpretation:	MDS, FZ, LL, MKB
Writing:	MDS, FZ, LL, MKB
Funding:	FS, FZ

9.1 Abstract

This work investigates the effective interactions of dissolved bovine serum albumin (BSA) protein solutions tuned with LaCl3 and different sodium co-salts (Na_2SO_4, NaCl, NaBr, $NaNO_3$ and NaSCN), numerated in the Hofmeister series. These BSA LaCl3 co-salt systems can undergo liquid liquid phase separation (LLPS) and feature a lower critical solution temperature (LCST) behavior. This is demonstrated by use of temperature controlled UV/vis cloud point measurements. Based on these measurements, the co-salts exert an influence on the transition temperatures of the respective systems in accordance to an inverse Hofmeister series. Moreover, the transition temperatures for the different BSA LaCl3 co-salt systems can be described by a Langmuir isotherm like function. In addition to the UV/vis measurements, phase diagrams were recorded as a function of the different concentrations of LaCl3 and co-salt (mM), showing a rich phase behavior. To quantify the effective interactions between the BSA proteins more precisely, SAXS

measurements were carried out. The model-based analysis by means of sticky hard spheres using an ellipsoidal form factor ($P(Q)$) provides a second virial coefficient analysis. This type of analysis serves as an indicator of whether the predominant interactions of the proteins are of a repulsive or attractive nature. To quantify the predominant interactions, an inverse intensity analysis was carried out which is independent of a concrete model. These SAXS measurements were added to capture a complete picture based on the provided phase diagrams.

9.2 Introduction

Gaining knowledge about protein phase behavior is a key aspect of research dedicated to proteins. This gained knowledge enables the targeted manipulation and control, necessary for the formulation of antibody based drugs, and also to understand diseases related to protein condensation. An understanding of proteins' phase transition provides important insights regarding protein crystallization pathways. Therefore, a major focus of protein research is concentrated on the study of liquid-liquid phase separation (LLPS), not least because of a number of contributions to various diseases related to protein condensation, such as cataract or sickle cell anemia [25, 26, 28, 315, 316, 388]. During LLPS, a protein solution separate into a dense and a diluted phase. The metastability of LLPS can also play an important role in the nucleation of protein solutions [28, 190, 311].
In an aqueous solution of the globular, net-negatively charged protein bovine serum albumin (BSA), the addition of the trivalent salt LaCl3 causes reentrant condensation (RC) [64, 65, 344]. RC means, that an initially clear BSA solution with a fixed protein concentration (c_p) will turn opaque upon the systematic addition of salt (LaCl3). Two salt concentrations (c_s) t^* and t^{**} have to be introduced: if the salt concentration is lower ($<$) than t^*, the protein solution appears clear (Regime I). If the salt concentration exceeds ($>$) t^* but fulfills the condition of beeing lower ($<$) than t^{**}, the protein solution is opaque due to protein condensation, but possibly also due to simultaneous occurrence of protein aggregates or even LLPS (Regime II). If the salt concentration is $> t^{**}$, the protein solution appears clear again (Regime III) [64, 65, 344].
This behavior, known as RC, can be explained by charge inversion, whereby in Regime II the net surface charges of the proteins are shielded by the trivalent La^{3+} cation [55]. Therefore, the net (BSA) protein surface charges are either slightly negative or almost neutral (close to the t^* border but in Regime I), neutral to slightly positive (deep within Regime II), almost positive (close to the t^{**} border but in Regime II) and positive (in Regime III), thus favoring the previously enumerated effects [55, 107].
By preparing a BSA solution (e.g. c_p 80 mg/ml) close to the t^*, but within Regime II, whilst admixing it with different sodium salts (e.g. Na_2SO_4, NaCl, NaBr, $NaNO_3$ or NaSCN) of the Hofmeister series, these BSA-LaCl3 co-salt systems can undergo LLPS when increasing the temperature, and therefore feature

a lower critical solution temperature (LCST). Consequently, the substances contained in such a mixture are miscible for all possible compositions, provided that the temperature remains below a specific transition temperature. This contrasts the familiar behavior of upper critical solution temperature (UCST) [62, 389]. This classical UCST behavior can be found, for different aqueous protein solutions like β-lactoglobulin [59], crystallin [388], or lysozyme [317, 390, 391].
Apart form cations in the BSA co-salt mixture (La^{3+}, Na^{+}), the present anions (e.g. Cl^{-} or $NO3^{-}$) do also exert a significant effect on the properties of the BSA-protein solution, especially on the solubility [129, 392, 393].
The Hofmeister series [112] organizes the anions in a sequence ranging from *cosmotorpe* to *chaotrope*. *Cosmotrope* anions like $SO_4{}^{2-}$ reduce the solubility of proteins (commonly known as salting-out effect), whereas *chaotrope* anions like SCN^{-} increase the solubility of proteins (known as salting-in effect) [116, 124, 394]. The Hofmeister series reads as follows [112]:
$\mathbf{SO_4{}^{2-} > HPO_4{}^{2-} > CH_3CO_2{}^{-} > HCO_3{}^{-} > Cl^{-} > Br^{-} > NO_3{}^{-} > ClO_3{}^{-} > I^{-} > SCN^{-}}$,
with *cosmortope* anions featuring a greater charge density compared to the more *chaotrope* anions [395]. The concept of the Hofmeister series is derived from the structure "forming" (cosmotropic) and structure "breaking" (chaotropic) characteristics of the investigated ions in aqueous solutions. Cosmotropic ions interact stronger with water. The water molecules accumulating around the ions are considered to be "structured", when compared to the remainder of the water. Chaotropic ions, on the other hand, "break" the structure of the surrounding water molecules and thus exert a weaker interaction with the water molecules [116, 119, 120, 394]. However, the disturbance of the water caused by the addition of salt does not adequately explain the Hofmeister effect, as the hydrogen bonding network of water remains intact beyond the first hydration shell of the ions [396].
Beside proteins [116, 129], polymers [145, 392] and elastin like poly peptides [393, 397, 398] demonstrated to have a similar LCST behavior, emerging from the anions of the Hofmeister series.
Despite the considerable progress being made by the incorporation of dispersion forces and hydration, the molecular basis of the Hofmeister series, thus the specific ionic effects, are yet to be unraveled. Derived from the Jones-Dole viscosity coefficient, better known as the enthalpy of hydration, the law of matching water affinities emerged. This law describes the development of ion pairs from chaotropic and cosmotropic ions as a function of their hydration enthalpy with a higher propensity for pair formation if the respective hydration enthalpies match or are approximately of equal magnitude. If this model is now deployed to proteins in solution, chaotropic or cosmotropic side chain residues are obtained based on the predominant charge, functional group, their respective hydration enthalpy and resemblance to cosmotopic or chaotropic ions. [119, 120, 123, 124].

However, this theory is not free of criticism, as it disregards interactions between ions and neutral protein binding sites present on the protein surface [399, 400]. Owing to the limited inclusion of protein surfaces, or rather their interfacial surfaces in terms of their dielectric constants whilst neglecting the smeared surface charge, the prediction made based on the law of matching water affinities appears to be inverted [124]. From a qualitative point of view, the effects of the Hofmeister series can, however, be adequately represented with simplified electrolyte models, provided that appropriate attention is devoted to the present dispersion forces [57]. In this work we systematically analyzed the LCST behavior of the BSA $LaCl_3$ co-salt solutions. Therefore, the phase diagrams were established for two different sodium salts of the Hofmeister series (NaCl and $NaNO_3$). By use of temperature controlled UV/vis measurements the LLPS transition temperatures for the investigated protein (BSA $LaCl_3$) co-salt (Na_2SO_4, NaCl, NaBr, $NaNO_3$ and NaSCN) systems were determined. The use of the Langmuir isotherm gives an estimate of the transition temperature data of these systems, indicating a saturation phenomenon. To complement the collected data, SAXS measurements were carried out to quantify the effective interactions amongst the protein molecules. To obtain a measure for the effective interactions, the reduced second virial coefficent (B_2/B_2^{HS}) as well as the inverse intensity analysis ($1/I(Q \to 0)$) were selected and subsequently evaluated.

9.3 Experimental Section

The protein BSA (A7906), the inorganic halide $LaCl_3$ (product No. 449830) as well as the sodium based co-salts Na_2SO_4, NaCl, NaBr, $NaNO_3$ and NaSCN with the respective product numbers (product No. 239313, 450014, 310506, 221341 and 467871) were purchased from Sigma Aldrich, (Merck) and used in the experiments without additional purification or treatment.
The protein stock solutions were prepared by mixing the protein powder with deionized and degassed Millipore water (conductivity of 18.2 MΩ cm). These protein solutions were then measured using a Cary 50 UV/vis spectrometer operating with the Cary WinUV software (both devices originate from Varian Technologies, USA) together with the corresponding extinction coefficient for BSA ($0.667\,\mathrm{ml} \cdot \mathrm{mg}^{-1} \cdot \mathrm{cm}^{-1}$) [305] to determine their concentration.
Initially, the phase diagrams for the BSA $LaCl_3$ co-salt systems (NaCl and $NaNO_3$) were established. This was done by visual inspection of different samples with a constant BSA concentration of 80 mg/ml, while the $LaCl_3$ concentration as well as the co-salt concentration were gradually increased from 0 to 100 mM. In order to determine the LLPS borders more precisely, the optical microscope Axio Scope.A1 (Carl Zeiss AG, DE) was used. Therefore, samples which were prone to undergo LLPS were transferred onto a microscopy slide, covered with a cover slip and subsequently investigated. Images were taken in appropriate time intervals by use of the AxioCam ICc5 (Carl Zeiss AG, DE) which was operated with the

software ZEN Lite 2012 (Carl Zeiss AG, DE). The obtained images were revised using the same software as well as the ZEN 2.6 blue software (Carl Zeiss AG, DE).
In order to investigate the LCST behavior of 80 mg/ml BSA solutions admixed with 10 mM $LaCl_3$ and with increasing concentrations (0.1 mM up to 1 M) of sodium co-salts, enumerated by the Hofmeister series, the UV/vis spectrometer was modified by use of a temperature controlled water bath (Haake A10B and SC 150, Thermo Fisher Scientific, USA).
The samples were prepared using the previously produced protein and salt stock solutions at 12° C (±2° C). Subsequently, the prepared samples were centrifuged for 2 minutes utilizing $6860 \times g$, in order to remove aggregates that could interfere with the measurement. Upon installation of the sample, the pre-cooled water bath (12° C) was heated up to 48° C applying a heating ramp (0.5° C/min). Calibration of the temperature controlled water bath was done prior to the measurements by measuring the temperature of a UV/vis cuvette filled with Milli-Q water utilizing a thermocouple. The measured temperature was compared to the temperature of the water bath and adjusted accordingly in the event of deviations.
The absorption between 500 and 800 nm was recorded every minute, in synch with the applied heating ramp. The 20 mM sample of NaSCN was treated differently, as this sample already showed slight turbidity at ≈ 12° C. To account for this, the temperature controlled UV/vis measurement was started a 8° C. The LCST behavior was determined using the major peak, which is only visible when the first derivative of the integrated absorption is plotted against the temperature.
For the investigation of the effective protein-protein interactions, the BSA $LaCl_3$ co-salt systems were analyzed using small angle X-ray scattering SAXS. The data was recorded at P-12 beamline, which is operated by the European Molecular Biology Laboratory (EMBL) and located at the German Electron Synchrotron (DESY). The applied setup involved a 10 keV highly focused X-ray beam (10^{13} photons per second) with the corresponding wavelength of $\lambda = 1.24\,\text{Å}^{-1}$. The dimensions of the beam were adjusted to a diameter of $120 \times 200\ \mu m^2$ (full width at half maximum). For all the carried out measurements, the sample to detector distance was set to 3.1 m, yielding a Q-range of 0.003 to $0.7\,\text{Å}^{-1}$. Collection of the data was facilitated by use of a 2 M Pilatus (Dectris) detector, placed at the end of the evacuated flight tube [283]. Samples were prepared in advance and shipped in chilled and appropriate containers to the EMBL facilities in Hamburg, Germany. Loading and exchange of samples was done by use of a flow cell. The exposure time was set to 0.004 s with each sample being illuminated for a total of 40 times. The data obtained was first averaged azimuthally to obtain intensity profiles. The intensity profiles were then background corrected. The correction of the obtained data sets was performed by subtracting the corresponding salt solutions $LaCl_3$ (10 mM) combined with the respective co-salt (NaCl and $NaNO_3$) concentrations 5 to 500 mM. This background correction of the data sets was done utilizing a MATLAB software.

These background-corrected intensity profiles were then fitted by use of the IGOR PRO 9 software together with the National Institute of Standards and Technology (NIST) provided add-on [286]. To fit the data, a sticky hard spheres potential (SHS) as developed by Baxter [274] was used combined with an ellipsoidal form factor $P(Q)$. The elliptical axes R_a and R_b were adjusted to 17 Å and 55 Å respectively.
The SHS potential, which represents a modification [273] of the square well potential [401], is characterized by a hard sphere repulsion, for a spherical particle of radius R, at a constant short-range attraction over a given distance Δ from the particle surface. Provided the Percus-Yevick closure relation [273, 274], the SHS interaction potential is given by

$$\beta U(r) = \begin{cases} \infty & r < \sigma = 2R \\ -\beta_0 = \ln\left(\frac{12\tau\Delta}{\sigma+\Delta}\right) & \sigma < r < \sigma + \Delta \\ 0 & r > \sigma + \Delta \end{cases} \tag{9.1}$$

with r denoting the particle spacing, whilst σ denotes the diameter of the hard spheres. Normalization to thermal energy is denoted as $\beta = \frac{1}{k_B T}$. The stickiness parameter is given as τ and the width of the square well is denoted as Δ. Considering the limit $\Delta \to 0$, this implies a limited range of attraction, causing the hard spheres to adhere only upon direct contact. Utilizing this limit gives

$$\lim_{\Delta \to 0} \frac{\mathrm{B}_2}{\mathrm{B}_2^{\mathrm{HS}}} = 1 - \frac{1}{4\tau}, \tag{9.2}$$

connecting the stickiness parameter τ to the reduced second virial coefficient. Here $\mathrm{B}_2^{\mathrm{HS}} = 16\pi \mathrm{R}^3/3$ represents the second virial coefficient for hard spheres of radius R.
The second virial coefficient is given by

$$B_2 = 2\pi \int_0^\infty dr\, r^2 \left[1 - \exp(U(r)/k_B T)\right] \tag{9.3}$$

whereby this is a simple yet efficient approach to quantify the prevailing effective interactions. A negative value indicates attractive interactions whereas a positive values indicates repulsive interactions [106]. However, the second virial coefficient must be treated with caution, as it only represents a simplified approach for determining the existing effective interactions owing to the performed angular averaging of the anisotropic proteins. The scattering length density was set to 7.32×10^{-7} [Å^{-2}]. The background level was adjusted individually for each data set. For all data, Δ (the width of the square well) was kept at $0.01\,\sigma$.

9.4 Results and Discussion

In order to gain a better understanding of the BSA-LaCl3 co-salt systems, phase diagrams for both co-salts NaCl (Figure 9.1 a) and NaNO3 (Figure 9.1 b) at RT ($20 \pm 3\,^{\circ}\mathrm{C}$) were established. Therefore, the BSA concentration was fixed to 80 mg/ml, whilst the respective co-salt concentrations were varied between 1 and 100 mM. Both systems feature two transition concentrations t^* (highlighted by blue diamonds) and t^{**} (highlighted by magenta crosses) which enclose an LLPS area (highlighted by black squares). The blue t^* line identifies the transition from a clear to an opaque solution, while the magenta t^{**} line identifies the transition from an opaque to a clear solution.
With increasing LaCl3 concentrations, the LLPS area expands towards higher co-salt concentrations. This expansion towards higher co-salt concentrations is more pronounced for the NaNO3 system (see Figure 9.1 b), compared to the NaCl system (see Figure 9.1 a). Taking a closer look at the LLPS area in the phase diagram, a few differences can be seen. LLPS begins in the NaNO3 system (Figure 9.1 b) at 10 mM LaCl3 and 11 mM NaNO3, whereas this co-salt concentration is yet insufficient to cause LLPS in the NaCl system (Figure 9.1 a). In the NaCl co-salt system, LLPS only starts at 15 mM LaCl3 and 20 mM NaCl. Continuing, the lower LLPS limit is quite similar for both systems. In the NaNO3 system (Figure 9.1 b), it shows a slight increase towards higher NaNO3 concentrations and slightly higher LaCl3 concentrations ($\approx$ 1 to 2 mM). For the NaCl system (Figure 9.1 a) at 20 mM NaCl, a slightly higher concentration of LaCl3 is required to drive the system towards LLPS. This downward shift is possibly caused by experimental deviations. Towards higher NaCl concentrations, the LaCl3 concentration remains around 15 mM. The upper LLPS boundary runs almost linear in the NaNO3 system (Figure 9.1 b). It starts at 19 mM LaCl3 with 10 mM NaNO3 and ends at 63 mM LaCl3 with 100 mM NaNO3. In the case of NaCl (Figure 9.1 a), this linear increase is also recognizable, but not as pronounced. Here, the upper LLPS limit starts at 20 mM LaCl3 with 20 mM NaCl and ends at 35 mM LaCl3 with 100 mM NaCl. Moreover, the t^{**} transition for the BSA LaCl3 NaCl co-salt system has a less pronounced slope compared to the t^{**} transition for the NaNO3 system (see Figure 9.1 a and b). The t^* transition on the other hand, runs more or less similar for both diagrams (see Figure 9.1).
Following the phase diagrams, the LCST behavior of the BSA-LaCl3 co-salt systems was investigated. Therefore, the transition temperatures of the different systems (BSA with 10 mM LaCl3 and varying co-salt concentrations) were monitored, whilst simultaneously measuring the UV/vis absorbance between 500 and 800 nm. The received absorbance curves were summed and subsequently plotted against the temperature. By fitting a ninth degree polynomial function to the received data, the first derivative was obtained. Using this derivative, the obtained major peak of this derivative was used to determine the transition temperature (see Figure 9.2). The results for all samples are summarized in Figure 9.3.

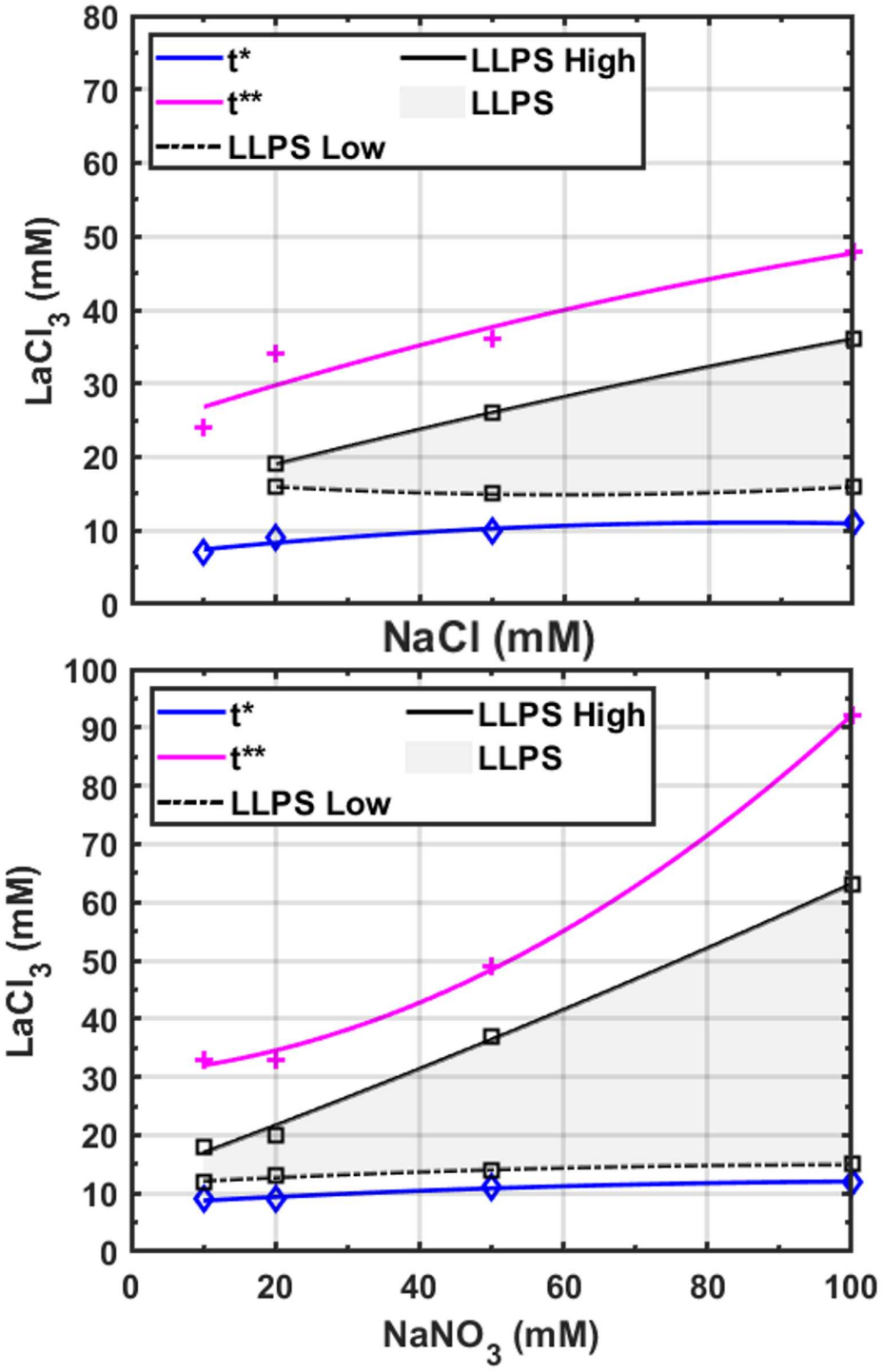

Figure 9.1: *Phase diagrams for 80 mg/ml BSA with 10 mM LaCl3 admixed with the co-salts NaCl (a) and NaNO3 (b) at RT (20 °C ± 3 ∘C). The displayed lines used to indicate t*, t** and LLPS are guides to the eye. Note that the co-salt concentrations for NaCl and NaNO3 do start at 10 mM. Lower concentrations were not considered. The data for this figure was adapted from reference [402].*

It is important to note, that a control sample which does not contain any co-salt is shown as well (see Figure 9.3). The plotted error bars represent the full width half maximum obtained by the first derivative of the cumulative absorbance curves. Looking at the overall picture, all the BSA-LaCl3 co-salt systems investigated show the same trend towards a reduction in the transition temperature (change of turbidity from an initially clear to an opaque solution), albeit to varying degrees. Apart from Na_2SO_4 (3.5 mM), the biggest deviation in the transition temperature can be seen at 20 mM co-salt concentration (Figure 9.3). A further increase in the co-salt concentration leads to an increase in the transition temperature far above the initial transition temperature, determined without additional co-salt. The initial transition temperature for the BSA-LaCl3 system without additional co-salts was measured at a temperature of 37.9 ° C (see Figure 9.3). From the observed transition temperatures for the different BSA-LaCl3 co-salt systems, it can be deduced that the more chaotropic the ions are, the greater the reduction of the transition temperature, yielding an inverse Hofmeister series: $\mathbf{SO_4^{2-}}$ $6.92 \pm 1°\,\mathbf{C} \leq \mathbf{Cl^-}$ $7.14 \pm 1°\,\mathbf{C} < \mathbf{Br^-}$ $13.22 \pm 0.8°\,\mathbf{C} < \mathbf{NO_3^-}$ $17.9 \pm 1.1°\,\mathbf{C} < \mathbf{SCN^-}$ $25.56 \pm 4°\,\mathbf{C}$,
with emphasize on the difference in the obtained respective transition temperatures.

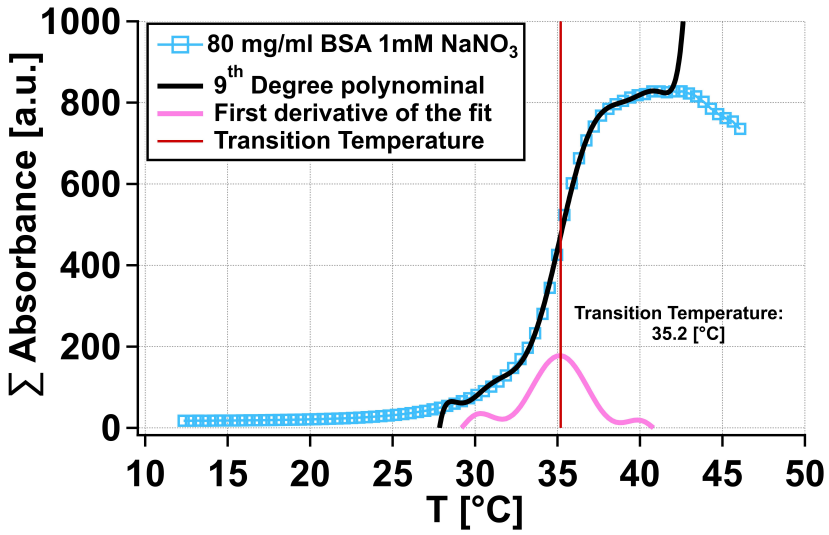

Figure 9.2: *Representation for visualizing the UV/vis based transition temperature analysis performed. Exemplary, the procedure is shown for the sample 80 mg/ml BSA with 10 mM LaCl3 mixed with 1 mM NaNO3. The light blue squares show the summed absorbance values between 500-800 nm for increasing temperatures (12 °C to 48 °C). Note that only every second data point is displayed, and the light blue line is a guide to the eye. The black line indicates the polynomial fit (9^{th} degree). The derivative of the fit is shown in magenta. The transition temperature (35.2 °C) was determined based on the peak of the derivative (red line). The data and the corresponding fits were adapted from reference [403].*

At first, the ion-specific effects of the Hofmeister series were attributed to the ions' ability to affect the structure of water [116, 124, 393]. However, it was then shown that the occurring hydrogen bonds between the individual water molecules were not altered beyond the first hydration shell surrounding the dissolved ions [396]. It was demonstrated that cosmotropic anions were able to polarize water molecules engaged in hydrogen bonding to the macromolecule, thus attenuating the hydrogen bonds between water molecules and the macromolecule. Chaotropic anions on the other hand affect the hydrophobic hydration of nonpolar side chains by alternating the surface tension at the macromolecule-water interface [393]. Thus, the chloride anion (Cl^-) is an exception as it is known to increase the surface tension [129].
Previous studies investigating the Hofmeister series on lysozyme at low salt concentrations showed that chaotropic anions increase the cloud point transition temperature due to ion pairing. Upon reaching a maximum transition temperature, the temperature then decreased again owing to a reduction of the interfacial tension. The chloride ion (Cl^-) was an exception to this behavior as the observed transition temperature rose due to strong ion pairing. However, even at higher salt concentrations the transition temperature continued to rise owing to an increase of the interfacial tension. These experiments revealed that an inverse Hofmeister series can be observed for protein salt systems [127, 129].
Nevertheless, BSA systems involving multivalent salts (e.g. $LaCl_3$, $HoCl_3$ or YCl_3) were characterized to possess a LCST behavior [144, 149] contrary to the observed UCST behavior of lysozyme [129]. Therefore, as the data indicate (Figure 9.3), a reduction of the cloud point temperature is to be expected.
Beyond ion pairing of charged groups on the surface of macromolecules, uncharged polar groups were also targeted as binding sites for anions [404, 405]. The combination of these different competing effects yields a complex yet multifaceted behavior of proteins when exposed to dissolved salts.
To further elucidate and possibly quantify the observed behavior of the BSA-$LaCl_3$ co-salt systems, a Langmuir type of binding was assumed to occur between the dissolved anions and the proteins surface. Here, the anions are thought to act similar to an ideal gas, which adsorbs on to an idealized protein surface having unambiguous yet limited number of binding sites [116, 124, 129].
Therefore, the data obtained was approximated by use of Equation 9.4, which contains besides the Langmuir binding isotherm, an additional linear term c. The equation reads as follows:

$$T = T_0 + c[M] + \frac{B_{max}[M]e^{-b[M]}}{K_d + [M]e^{-b[M]}}, \tag{9.4}$$

with T_0 indicating the cloud point temperature of the BSA-$LaCl_3$ mixture (from clear to turbid) in pure water, without the addition of the respective sodium based co-salts.

Furthermore, the term c represents a linear contribution to the temperature trend obtained and correlates with the increase in surface tension of the anions. M indicates the respective molar concentration of the salt. By deploying the term $e^{-b[M]}$, the charge neutralization due to anion binding is taken into account. The terms B_{max} and K_d indicate the affinity of the anions to the protein surface as well as their effectiveness in changing the obtained transition temperature of the respective BSA-LaCl3 co-salt systems [116, 124, 129].
The fits (dashed lines) to the obtained data (NaCl circles, NaNO3 triangles) are shown in Figure 9.4. Subtraction of the linear term $(T_0 + c[M])$, yields Langmuir binding isotherms with appearance similar to a saturation curve although with different slopes and terminal values.

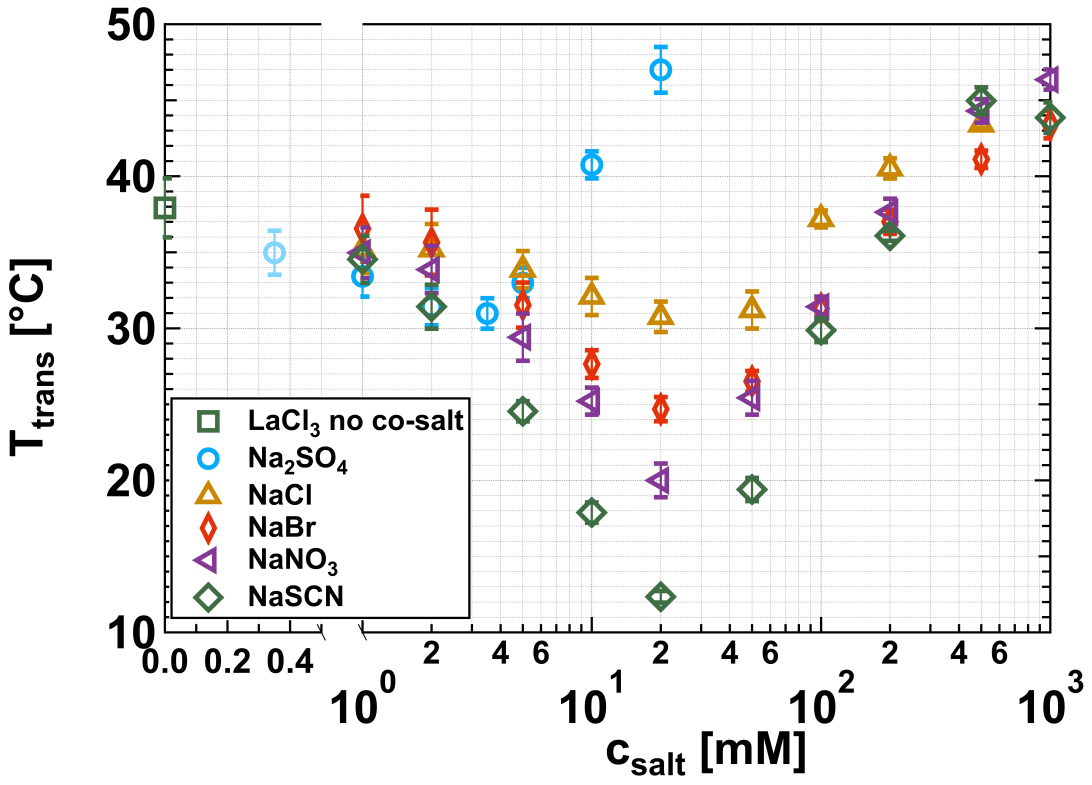

Figure 9.3: *UV/vis determined transition temperatures for* 80 *mg/ml BSA solutions with* 10 *mM LaCl3 admixed with different co-salts (NaCl, NaNO3, Na2SO4, NaBr and NaSCN). The used co-salt concentrations range from* 0.35 *mM to* 1 *M. The co-salt concentrations (mM) are displayed in a split axes format. The left co-salt concentration axis is in linear scale (*0 *to* 0.5 *mM). The right co-salt concentration axis is in logarithmic scale (*1 *mM to* 1 *M). The transition temperature (Y-axis) is shown in a linear format. The data for this figure was adapted from reference [403].*

Based on the fitting of Langmuir shaped binding isotherms, the B_{max} values were obtained, which can be regarded as a measure to quantify the effectiveness of an anion to pair with the protein's surface. In other words, this value indicates the maximum decrease in cloud point temperature (° C) upon full ion pairing between the anions and the charges on the protein's surface. Comparing the obtained B_{max} values (see Table 9.1) with the observed UV/vis transition temperature data (see P. 144 and corresponding Figure 9.3), this yields similar trends of comparable magnitude. The more chaotropic anion ($NO3^-$) reduces the cloud point temperature more than the Cl^- anion. Hence, the $NO3^-$ anion exhibits a stronger affinity to the protein's surface than the Cl^- anion. This observation points to the intermediate result that the reduction of the cloud point is stronger, as the chaortopic character of the anion is increased.
Recalling the experimentally ascertained law of matching water affinities [119, 120, 123, 124], which assesses the formation of ion pairs on the basis of hydration enthalpies ($-\Delta H^0$) and charge (see Chapter 9.2) reflects the above-mentioned trend of decreasing cloud point temperature coinciding with increasing chaotropic character of the anions (see Table 9.1). Fundamental in this regard, however, is the fact that weakly hydrated anions display a more pronounced affinity to the surface of the protein molecules [116, 123, 129]. Concomitantly, this observation is corroborated by the specific ionic surface tension ($d\gamma/dc_i$) in aqueous solution (see Table 9.1). This metric is indicative of a change in surface tension in an aqueous solution upon administration of an electrolyte concentration (mM).

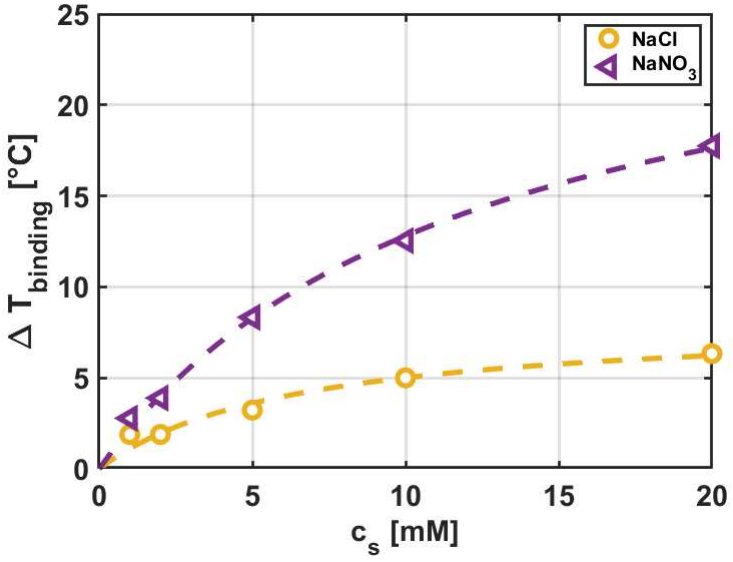

Figure 9.4: *Langmuir isotherms, fitted to* 80 *mg/ml BSA samples admixed with* 10 *mM LaCl3 for increasing co-salt concentrations (mM) of NaCl and NaNO3. The fitted Langmuir isotherms are shown as dashed lines in the respective color of the co-salt. The data and the corresponding fits were adapted from reference [403].*

A different picture emerges at higher salt concentrations beyond a concentration of 20 mM (3.5 mM for Na_2SO_4), as the cloud point temperature transitions from a decrease to an increase (see Figure 9.3). In this regard, studies on RC of HSA admixed with YCl_3 and increasing concentrations of the co-salt NaCl revealed an increase of the two concentrations t^* and t^{**} separating Regime I from Regime II and Regime II from Regime III respectively. As a result, the entire phase diagram has gradually moved to higher YCl_3 concentrations [54].

Table 9.1: *Comparison of B_{max} values to ion specific properties for the salts NaCl and $NaNO_3$. The data for this table was adapted from [403].*

co-salt	$\mathbf{B_{max}}$ $(^\circ\mathbf{C})$	$-\mathbf{\Delta H^0}$[**kJ/mole**] [406]	$\mathbf{d\gamma/dc_i}$ [$\mathbf{mN/m \cdot M}$] [407]
NaCl	6.07	381	1.73
$NaNO_3$	18.48	314	1.21

The addition of the monovalent salt NaCl is suspected to alternate the binding equilibrium of the multivalent salt YCl_3 to the surface of the HSA protein, thus resulting in an increase of the t^* transition concentration, provided a fixed protein concentration [54]. Transferring and applying this result now to the BSA $LaCl_3$ co-salt systems indicates that the t^* boundary is elevated, hence, the overall interactions appear to be attenuated in favor of an increasing cloud point transition temperature. Focusing now on the transition from Regime II to Regime III, the change in t^{**}, which is associated with an increasing NaCl concentration, is due to a reduction in repulsion triggered by screening of charges [54].
Moving on from the UV/vis experiments, the focus will now be on the SAXS experiments that were conducted. The SAXS measurements were performed to obtain a better understanding of the effective protein interactions. Azimuthally averaged intensity profiles were appropriately background corrected and subsequently approximated by use of a sticky hard spheres (SHS) potential [274] which employs an ellipsoidal form factor $P(Q)$ (for further information consult Chapter 9.3 and 5.1.1). The obtained results for 80 mg/ml BSA admixed with 10 mM $LaCl_3$ and varying concentrations (5 to 500 mM) of either NaCl or $NaNO_3$ at 20 ± 2°C are depicted in Figure 9.5 a and b respectively. In Figure 9.5, the SHS fits to the data are shown as solid black lines. The B_2/B_2^{HS} values obtained from the fit of the data are shown in Figure 9.6 a. The analysis of the inverse intensity at low-Q ($1/I(Q' \to 0)$) is shown in Figure 9.6 b.
Looking at the obtained SAXS curves, it becomes apparent that with increasing co-salt concentrations, the low-Q intensities decrease. This initial intensity decrease can be equated to a gradually emerging repulsion which increases as the co-salt concentration (mM) increases (see Figure 9.5). This increasing repulsion is reflected in the obtained B_2/B_2^{HS} analysis (see Figure 9.6 a). Nevertheless, the effective interactions are initially attractive and then transition to repulsive interactions for higher co-salt concentrations (see Figure 9.6 a).

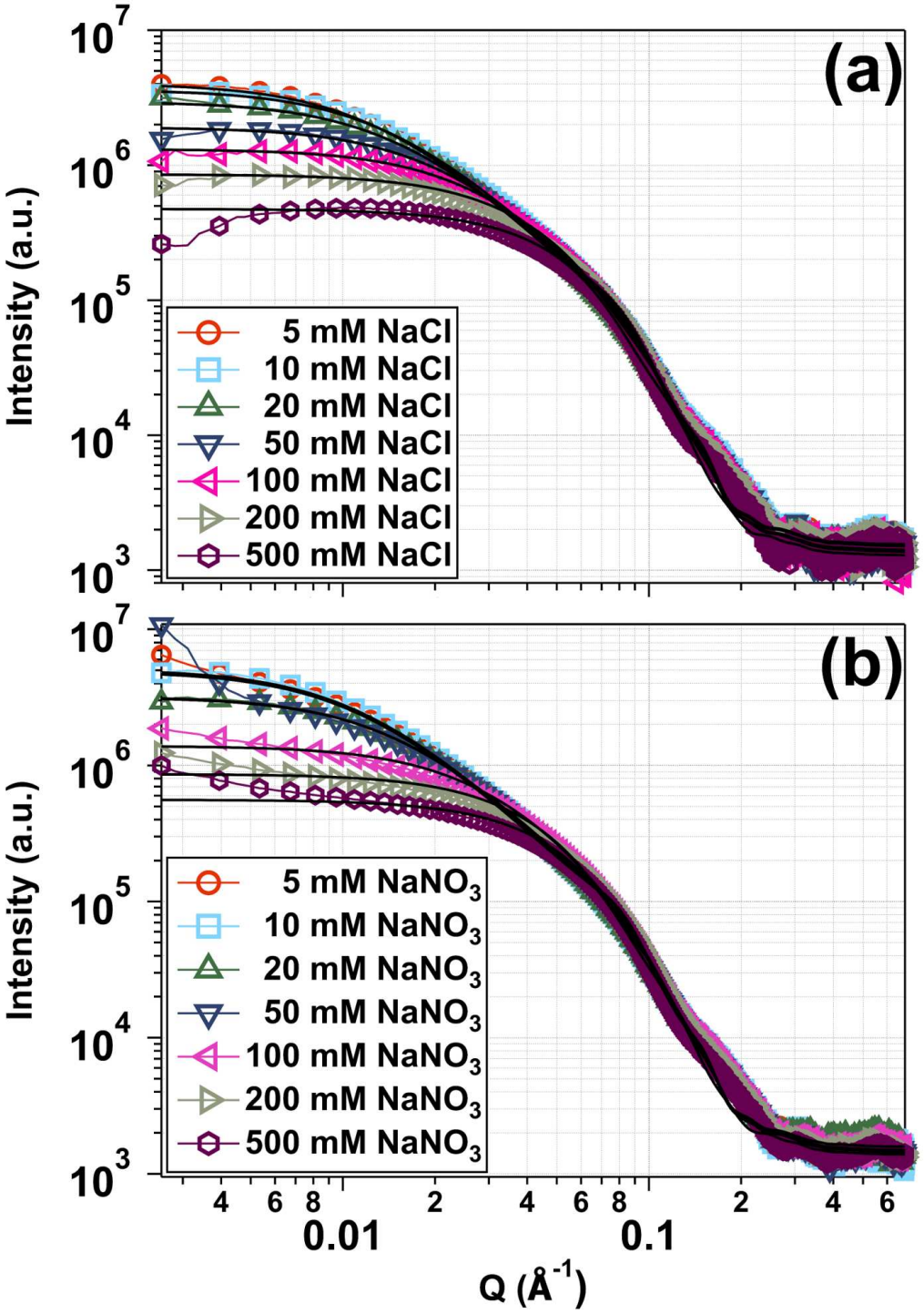

Figure 9.5: *(a, b) SAXS data with SHS model fits (solid lines) for aqueous samples, containing* 80 *mg/ml BSA admixed with* 10 *mM LaCl3 with increasing co-salt concentrations* 5 *to* 500 *mM, measured at* $20 \pm 2°C$*. In (a) NaCl was used as a co-salt, whereas (b) shows the obtained data using NaNO3 as a co-salt. For clarity, only every fifth data point is displayed. The graph is shown in a double logarithmic format.*

At intermediate Q-values ($Q \approx 0.4\,\text{Å}^{-1}$), the scattering curves overlap and decrease further with increasing Q-values until they level off at approximately the same intensity (a.u.). This shows across all measured samples, that the protein concentration is accurately adjusted to 80 mg/ml and has no major fluctuations. In general, the overall shape of the scattering curves appears to be the same for all samples measured. However, small differences can still be recognized. For example, an over correction of the data is particularly evident at higher NaCl concentrations (50 to 500 mM). This can be recognized by the fact that the curve initially rises at low-Q values, eventually remains constant and then decreases within the intermediate Q-range superimposed with the other scattering curves (see Figure 9.5 a). A different picture emerges for the scattering curves of NaNO3. Here, aggregate formation is evident at 5, 50, 100 to 500 mM co-salt concentration. This can be identified by an initially different gradient at low-Q values. The gradient then changes and the curves in question resemble the global shape again (see Figure 9.5). These mentioned difficulties certainly influence the fit of the ellipsoid SHS potential and therefore the obtained B_2/B_2^{HS} values, which will be discussed in the following.

As to be seen in Figure 9.6, the B_2/B_2^{HS} curve for NaCl resembles a sigmoidal shape whilst the curve for NaNO3 deviates more from this shape. Initially, at low co-salt concentrations the B_2/B_2^{HS} values indicate for attractive effective interactions amongst the BSA protein molecules. Then the B_2/B_2^{HS} values gradually increase with higher co-salt concentrations and transition from a negative B_2/B_2^{HS} value to a positive B_2/B_2^{HS} value at approximately 150 mM for NaNO3 and 200 mM for NaCl. These co-salt concentrations mark the turnover from attractive to repulsive interactions for both NaCl and NaNO3. Interestingly, the B_2/B_2^{HS} curve of NaNO3 is quite similar to that of NaCl given lower concentrations, but shows an anomaly at 50 mM. Here, the B_2/B_2^{HS} value of NaNO3 remains constant between 20 and 50 mM. Moreover, the B_2/B_2^{HS} curve of NaNO3 runs below the one of NaCl for low concentrations (between 5 to 50 mM). At higher concentrations it is the other way around. However, the final B_2/B_2^{HS} value at 500 mM is comparable for both systems, yet the B_2/B_2^{HS} value for NaCl is higher than that of NaNO3.

As to be seen in Figure 9.6 a, the obtained B_2/B_2^{HS} values between 5 and 20 mM (for NaCl) and between 5 and 50 mM (for NaNO3), respectively, are below the predicted B_2/B_2^{HS} value of -1.56 (see Table 9.2), which marks the theoretical limit for LLPS at the critical point [106].

To complement these results, an inverse intensity analysis is performed, which is referred to below as $1/I(Q' \to 0)$ and does not require the approximation of a model to the obtained scattering data (see Figure 9.6). Here Q' denotes the value of $Q = 0.0134\,\text{Å}^{-1}$, used for this analysis.

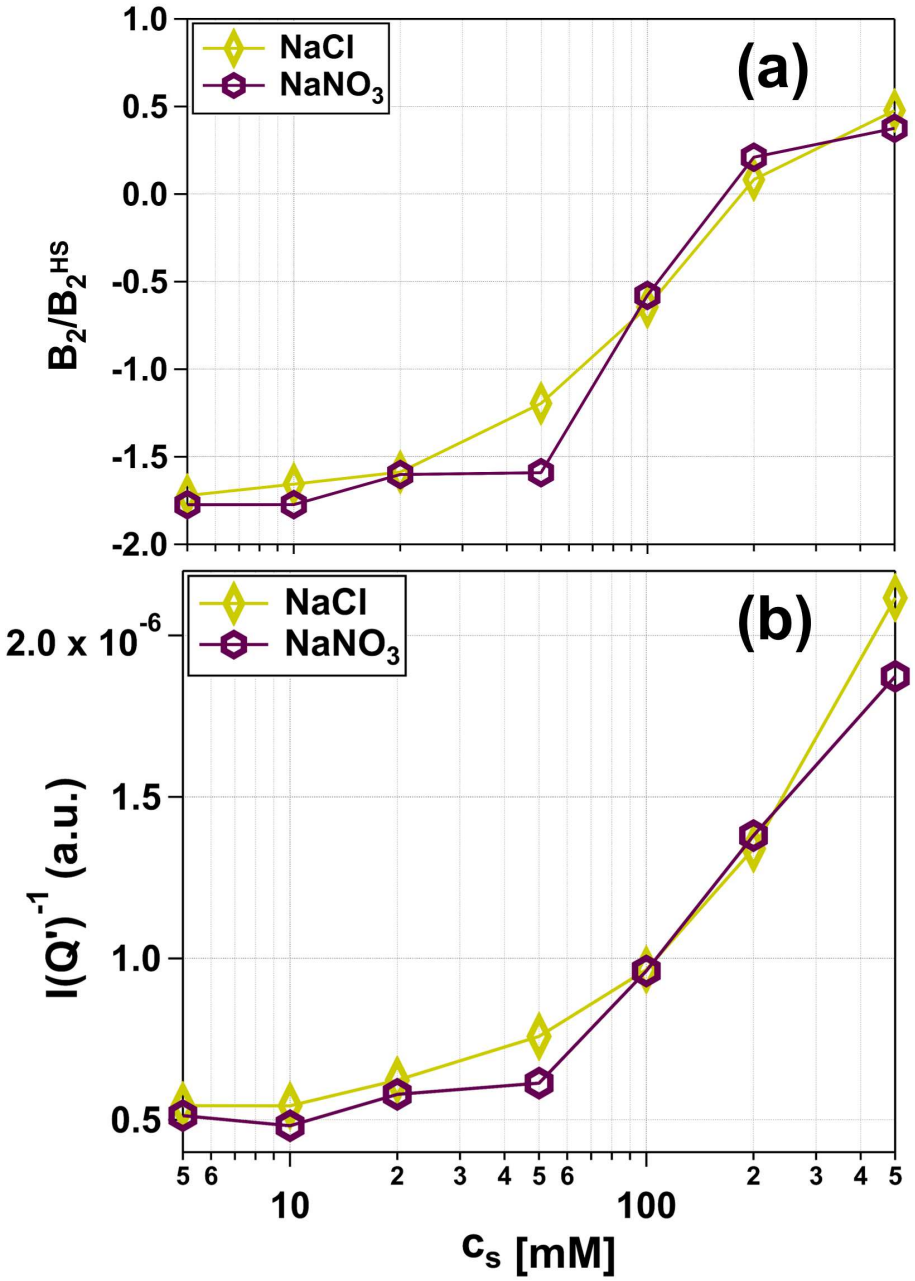

Figure 9.6: *(a) Reduced second virial coefficients (B_2/B_2^{HS}) and $1/I(Q' \to 0)$ (inverse intensity) behavior (b) for samples containing 80 mg/ml BSA admixed with 10 mM LaCl3 and varying co-salt concentrations c_s (mM) of NaCl (yellow) and NaNO3 (purple). Here Q' corresponds to a value of $0.0134\,\text{Å}^{-1}$. Note that the co-salt concentrations are displayed in a logarithmic format. On the contrary, the axis indicating the reduced second virial coefficients (a) and the axis indicating the inverse intensities (b) are displayed in a linear scale. The respective error values are smaller than the markers and are not plotted for clarity. The lines connecting the respective markers are guides to the eye.*

This approach can be described by the following equation:

$$\frac{1}{I(Q' \to 0)} \propto \frac{1}{S(Q \to 0)} = 1 + 2B_2\,\rho + ..., \tag{9.5}$$

thus, connecting $1/I(Q' \to 0)$ to the inverse of the structure factor near the origin $1/S(Q \to 0)$ with the second virial coefficent B_2 [28, 263, 277]. Further details on this approach can be found in Chapter 5.1.8. The $1/I(Q' \to 0)$ curves for NaCl and NaNO3 exhibit the form of an exponential function, unlike the sigmoidal one obtained when analyzing B_2/B_2^{HS}. Nevertheless, NaNO3 also shows minor deviations in the curve progression, which are comparable to the ones found in the sigmoidal curve for B_2/B_2^{HS} (see Figure 9.6 a and b). Initially, the $1/I(Q' \to 0)$ values decrease from 5 to 10 mM for NaNO3, which indicates phase separation accompanied by aggregate formation upon further increase of the co-salt concentration. Beyond this minimum at 10 mM NaNO3, the curve increases step wise, with comparable values for 20 and 50 mM, before the curve continues to increase in an exponential function type of shape.
Connecting the results from UV/vis measurements with those from SAXS experiments does not provide a clear and consistent outcome. Based on the phase diagrams (see Figure 9.1) and the UV/vis measurements (see Figure 9.3), it would be expected that a similar behavior can be seen in the SAXS data. This would imply that the effective interactions initially become stronger (more attractive) with increasing co-salt concentration, up to about 20 mM. However, the SAXS data do not reflect this type of behavior (see Table 9.2 and Figures 9.5 and 9.6). Increasing the co-salt concentration further would yield more and more repulsive interactions. In accordance with an inverse Hofmeister series, it would be expected that the effective interactions are stronger for NaNO3 than for NaCl. Thus, the latter case is confirmed by the SAXS data, even if the difference is quite small compared to the differences observed in the cloud point temperatures measured in UV/vis experiments. Table 9.2 summarizes this discrepancy between UV/vis and SAXS data quite well. The strongest reduction in cloud point measurements was observed at 20 mM co-salt concentration with a reduction of $\approx 7 \pm 1\,°C$ and $\approx 18 \pm 1.1\,°C$ for NaCl and NaNO3 respectively. However, the SAXS data do not reflect this type of behavior (see Table 9.2 and Figures 9.5 and 9.6). At 20 mM, the SAXS analysis resulted in a second virial coefficient of ≈ -1.6, which is within the theoretical limit for LLPS [106], i.e. the sample is still located within regime II. Yet the lowest value of the second viral coefficient is found at 5 mM co-salt concentration with ≈ -1.7. Here, the reduction of the cloud point temperature is less pronounced with $\approx 4 \pm 1.22\,°C$ (NaCl) and $\approx 8.5 \pm 1.55\,°C$ (NaNO3), corresponding to a difference of approximately 4 °C for NaCl and 12 °C for NaNO3 when compared to the 20 mM values (see Table 9.2).

Table 9.2: *Comparison of the transition temperature values for samples containing 80 mg/ml BSA with 10 mM LaCl3 and a co-salt (either NaCl or NaNO3) concentration of 20 mM (UV/vis) with the corresponding second virial coefficient values (SAXS). The additional columns on the right indicate the lowest obtained second virial coefficient values, the matching co-salt concentration (mM) and the matching transition temperatures. The UV/vis data was adapted from [403].*

co-salt	**[mM]**	$\mathbf{T_{trans}}\,[^\circ\,\mathbf{C}]$	B_2	**[mM]**	$\mathbf{T_{trans}}\,[^\circ\,\mathbf{C}]$	B_2
NaCl	**20**	31 ± 1	-1.58	**5**	33.9 ± 1.22	-1.72
NaNO3	**20**	20 ± 0.8	-1.60	**5**	29.4 ± 1.55	-1.77

Furthermore, an influence of the La^{3+} cations on the previously elaborated effects can be ruled out. This can be deduced from an earlier study which conducted investigations on BSA-LaCl3 as well as BSA-La(NO3)3 systems, revealing a significant difference in phase behavior between the two salts [65]. The observed difference could ultimately be attributed to a stronger affinity of $NO3^-$ to the protein surface compared to Cl^- anions, causing an increased attraction between the protein-cation complexes. Simultaneously, the binding of La^{3+} cations to the proteins surface was not impaired by Cl^- and $NO3^-$ anions [65].

9.5 Conclusion and Outlook

Nevertheless, the SAXS results show a certain tendency to support the reduction in cloud point temperature shown by the UV/vis measurements. As expected and also discussed in detail, the co-salt NaNO3 shows stronger effective interactions than the co-salt NaCl, thus confirming the inversion of the Hofmeister series for the investigated systems. However, the SAXS results obtained should not be exaggerated. The discrepancy shown between the reduction in cloud point temperature at 20 mM and the values of the second virial coefficient are ambiguous. A similar mismatch between second virial coefficient and cloud point reduction is evident at a co-salt concentration of 5 mM (see Table 9.2).
The increase of cloud point temperature at higher co-salt cocnentrations i.e. beyond 20 mM is thus reflected in the SAXS data (see Figures 9.5 and 9.6). The results obtained from UV/vis cloud point temperature measurements yielded a pronounced reduction upon addition of different sodium based co-salts of the Hofmeister series ($Na2SO4$, NaCl, NaBr, NaNO3 and NaSCN) to a BSA (80 mg/ml) LaCl3 (10 mM) system. Adding these co-salts reduced the cloud point temperature in every system without exception. The lowest temperature i.e. the strongest reduction was to be found at a co-salt concentration of 20 mM co-salt. At higher co-salt concentrations, the cloud point temperature increases again. It turned out that the chaotropic salts cause a greater reduction in the cloud point temperature than the cosmotropic salts.

This indicated that the reduction in cloud point temperature follows an inverse order of the Hofmeister series: $\mathbf{SO_4}^{\mathbf{2-}} \leq \mathbf{Cl}^- < \mathbf{Br}^- < \mathbf{NO_3}^- < \mathbf{SCN}^-$. In the case of low salt concentrations, the anions bind to the protein surface with specific affinity, thus changing the effective interactions among them. Upon exceeding a critical co-salt concentration, the effective interactions gradually increase in repulsiveness, owing to a shift of the t^* border to higher salt concentrations. As a result, the BSA LaCl3 co-salt system is forced out of regime II into regime I.
Due to the ambiguous results, further experiments are advised. Therefore, additional and systematic SAXS experiments would aid to gain more profound insights to the effective interactions induced by co-salt addition to the BSA LaCL3 system. Similarly, to the conducted SAXS experiments, the co-salts NaNO3 and NaCl should be represented. However, NaSCN induced the strongest reduction of the BSA LaCl3 system and should be included in the investigations. In line with the systematic approach, preparation and experiment should be executed within a reasonable temperature frame. Here, it would be ideal to measure at 10 °C and monitor the changes in effective interactions owing to co-salt addition, eliminating influence induced by temperature. With these three co-salts, the Hofmeister series is adequately represented, which would suggest a qualitative statement. Temperature controlled SAXS experiments would also yield interesting data, as then the cloud point reduction over a span of 36 °C, as observed by UV/vis, could be reproduced. However, highly focused X-ray beams as to be found at synchrotron facilities yield non-negligible radiation damage to the sample [408–410]. This could be reduced if several different spots on a sample are measured. Applying a temperature ramp of 0.5 °C would require plenty of samples and/or an excessive measurement time despite the work around of having multiple spots available. Similarly, adjusting the heating ramp to a much steeper increase would also yield disbalances of the sample thermal equilibrium or would yield unwanted aggregation of the protein [410]. Moreover, it is advisable to include additional background measurements in order to be able to subtract these from the measured data. Importantly, these circumstances should be considered in future measurements.
All in all, systematic SAXS measurements of the BSA LaCl3 system with the three different co-salts NaCl, NaNO3 and NaSCN at 10 °C are advised.

Part V

Conclusion and Outlook

Chapter 10

Conclusion

The following chapter summarizes the most important results of the research discussed in this thesis. The subsequent Chapter 11 provides an outlook on future research projects.

The aim of this work was to gain a deeper understanding of the role of specific and non-specific effective interactions of proteins in solution caused by the use of different additives, such as salts or polymer. In this case, the term salt has a broader definition, as both cations and anions were subject to the research presented here. Changing the salt or polymer concentration offers a simple yet efficient way to tune the phase behavior of proteins. The predictive interactions were determined by potential fits to SAXS measurements, which were used to evaluate the reduced osmotic second virial coefficient B_2/B_2^{HS}. This coefficient serves as a measure to quantify the protein-protein interactions. Negative B_2/B_2^{HS} values are indicative for attraction whereas positive values indicate repulsion.

Chapter 7 of Part IV investigates the behavior of the globular, negatively charged proteins β-lactoglobulin (BLG), bovine serum albumin (BSA), human serum albumin (HSA) and ovalbumin (OVA) in the presence of the trivalent salt hexamine cobalt (III) chloride ($[Co(NH3)6]Cl3$). The trivalent hexamine cobalt (III) cation (Hac) differs from other trivalent cations due to its six covalently bonded octahedrally arranged $NH3$ groups. Prior to this thesis, it has been reported that trivalent salts such as $YCl3$ or $LaCl3$ induce reentrant condensation (RC) phase behavior of these proteins. Similarly, Hac was reported to induce RC phase behavior of deoxyribonucleic acid (DNA) and ribonucleic acid (RNA). RC phase behavior is characterized by a neutralization of the protein's surface charge followed by a charge reversal. Three different regimes (I, II, III) emerge, with regime II (medium salt concentration) beeing characterized by an opaque and turbid appearance due to protein clustering and aggregation. In addition, this regime is sometimes associated with liquid-liquid phase separation (LLPS). Within regime I, the salt concentration is insufficient (low) to induce a phase transition, the proteins repel each other (net negative surface charge), and the solution appears clear. In regime III (high salt concentration) the cations not only screen the protein's surface charge but invert it, yielding a macroscopically clear solution. The proteins repel each other due to same sign (positive) charges (see Figure 1.5).

RC phase behavior of proteins in small angle X-ray scattering (SAXS) experiments is characterized by an increasing intensity at low Q values, followed by decreasing intensity within the same Q-range, provided that the protein concentration

remains constant whereas the salt concentration is increased continuously. The results show that Hac is unable to induce both; a phase transition and RC phase behavior for all proteins studied. However, a new phenomenon called reentrant interaction (RI) was found for BLG. RI shows a similar behavior in SAXS experiments (see Figure 7.2) but lacks sufficiently low reduced second virial coefficient values (see Figure 7.3), which would be necessary for a phase transition to occur. Importantly, a phase transition would be coupled to a transition from regime I to regime II, which would be indicative for RC behavior. Static light scattering (SLS) and dynamic light scattering (DLS) measurements support RI behavior of BLG (see Figures 7.5 and 7.6). Considering the cation radius of Hac in comparison to other cations such as Y^{3+} or La^{3+}, it becomes apparent that the ion radius of Hac is about four times larger. Thus, the absence of a phase transition and ultimately RC phase behavior for the Hac-BLG protein system is consistent with the observation that with an increasing ion radius the strength of the ion-protein interaction decreases. Visually, no phase transition could be observed either. The solution appeared clear at all times apart from a yellow discoloration which intensified with increasing salt concentrations. This change of color can be ascribed to the orange color of the salt (see Figure 7.1). Comparing the interaction of BLG with YCl3 and Hac with DNA/RNA reveals an interesting difference. It has been reported that the solvent exposed carboxyl side chain of BLG interacts with the Y^{3+} cations whereas Hac establishes additional hydrogen bonds when interacting with DNA/RNA (see Figure 7.7).
However, weak interactions between Hac and protein might still occur, as confirmed by SLS and DLS measurements (see Figures 7.6 and 7.5), but the observed oligomers (dimers/trimers) are not big enough to visually opacify the solution, nor to promote a phase transition.
The subsequent results Chapter 8 investigated the behavior of BSA and HSA in the presence of different polethylene glycol (PEG) concentrations w/V% and 100 mM NaCl. The two proteins BSA and HSA are similar counterparts from two different mammalian species. However, despite their similar size, shape, function and sequence identity ($\approx$ 76 %), their slight differences result in completely different crystallization behaviors. This different crystallization behavior was investigated in the work presented here.
A previous study by Maier et al. [365] showed, that both proteins exhibit RC phase behavior in the presence of CeCl3. In addition, SAXS measurements revealed comparably low reduced second osmotic virial coefficient values B_2/B_2^{HS} for both proteins (see Figure 8.6 a). B_2/B_2^{HS} values serve as a measure to capture and quantify the attraction between the dissolved protein molecules. In accordance with the literature, it has been established, that a crystallization window is to be found in close proximity to the metastable critical point of LLPS. Typically a range from $-10 < B_2/B_2^{HS} < -1$ is ascribed to this crystallization slot. Despite the sufficiently low B_2/B_2^{HS} values, only the HSA-CeCl3 system showed crystallization, whereas the BSA-CeCl3 system did not.

Switching the interactions from specific (salt CeCl3) to non-specific (polymer) inverts the crystallization behavior; BSA crystallizes whereas HSA does not. Comparably to the study conducted by Maier et al. [365], SAXS experiments revealed that both proteins feature similarly low B_2/B_2^{HS} values (see Figure 8.6). Again, the obtained B_2/B_2^{HS} values for both systems correspond to the aforementioned crystallization range, however, only the BSA-PEG system crystallized whereas the HSA-PEG system did not (see Figure 8.2 c and Figure 8.1). Single crystal X-ray diffraction confirmed a C_2 space group in accordance to a previously reported BSA structure of Majorek et al.. The conducted systematic analysis of the crystal surfaces for BSA and HSA crystals clearly indicates that, compared to its bovine counterpart, HSA utilizes a relatively larger fraction of its surface for the formation of crystal contacts. In addition, HSA utilizes more of its residues and thus offers a broader spectrum of possibilities to establish attractive interactions (see table 8.2). BSA on the other hand, predominately crystallizes via non-specific depletion interactions whereas HSA does not. The results obtained indicate that the two proteins require different crystallization strategies despite their similarities.

The provided phase diagrams for both proteins in the presence of PEG $3,350$ and 100 mM NaCl support this finding (see Figure 8.1). Interestingly, the observed phase behavior can be ascribed to the depletion effect. By use of SAXS measurements, a size ratio of $q \approx 0.3$ could be determined (see Figure 8.3). In accordance to literature, a q value of ≈ 0.3 indicates for the colloidal limit to be applied. Moreover, the observed phase behavior is in line with colloid-polymer theory in the picture of the depletion interaction. Results revealed an agreement between the theoretical and experimental phase diagrams suggesting that the phase behavior can be attributed to simple interactions such as depletion interactions.

In Chapter 9 the effects of the monovalent salts Na2SO4, NaCl, NaBr, NaNO3 and NaSCN on the BSA-LaCl3 system are investigated. The phase diagrams for the two BSA-LaCl3 co-salt systems (NaCl or NaNO3) are provided in Figure 9.1. In order to obtain these phase diagrams not only the co-salt concentrations were altered but also the LaCl3 concentrations.

Adding various co-salts (Na2SO4, NaCl, NaBr, NaNO3 and NaSCN), whose anions belong to the Hofmeister series, to this BSA-LaCl3 system not only shows LLPS (see Figure 9.1), but also a lower critical solution temperature (LCST) behavior.

The list of anions developed by Hofmeister arranges the anions in an order ranging from *cosmotrope* to *chaotrope*. Cosmotropic anions like $SO_4{}^{2-}$ reduce the solubility of proteins, whereas chaotropic anions such as SCN^- increase the solubility of proteins. A complete enumeration of the Hofmeister series for anions is to be found in Chapter 9.2.

LCST describes the occurrence of LLPS induced by an increase in temperature. Consequently, the substances contained in such a mixture are miscible as long as the temperature remains below a certain transition temperature. UV/vis cloud

point measurements showed, that the anions exert a significant influence on the transition temperature, following an inverse Hofmeister series (see Figure 9.3). This implies that the stronger the chaotropic character of an anion, the more the transition temperature decreases. This finding is supported by the provided Langmuir fits to the obtained UV/vis cloud point measurements (see Figure 9.4). Moreover, this finding is in accordance with the law of matching water affinities. This law describes the ion pair formation for chaotropic and cosmotropic ions on the basis of their respective hydration enthalpies. Therefore, the tendency to form pairs is greater if the hydration enthalpies are more or less equal. If this concept is transferred to proteins in solution, chaotropic or cosmotropic side chain residues are obtained on the surface of the proteins. It turns out that weakly hydrated (chaotropic) anions have a greater affinity to the surface of the proteins (see table 9.1).
Prior to this thesis M K. Braun et al. [65] reported, that LaCl3 induces RC phase behavior in BSA solutions. Based on this information, samples for SAXS measurement were kept within regime II by adjusting the LaCl3 concentration to precisely 10 mM and only the co-salt concentration was altered. Moreover, the measurements were carried out at RT. Although the results of the SAXS measurements (see Figure 9.5) are ambiguous, they support the observation, that the anion $NO3^-$ induces stronger effective interactions compared to the chloride anion (Cl^-). The ambiguity arises because the obtained B_2/B_2^{HS} values (see Figure 9.6) do not coincide with the observed cloud point measurements (see Figure 9.3). Essentially, the B_2/B_2^{HS} values are expected to be the lowest (attractive) exactly at that co-salt concentration at which the UV/vis cloud point measurements determined the lowest temperature of the LCST behavior (see Figure 9.3). However, the B_2/B_2^{HS} values indicate, that a significantly lower salt concentration is much more attractive. Increasing the co-salt concentration further decreases attraction and increases repulsion (see Figure 9.6). Therefore, further temperature controlled SAXS measurements are advised. This is discussed in more detail in the following Chapter 11.
All in all, the aim of this work was to contribute to a comprehensive understanding of the effective interactions of proteins. Relevant protein-protein, protein-salt and protein-polymer interaction behaviors were investigated and characterized. The scientific results presented show, that not only the charge is decisive for the interaction of cations with proteins, but also the size and, in the case of Hac, the ability to establish hydrogen bonds. Furthermore, BLG revealed a new effect of RI. The investigation of BSA and HSA in the presence of the polymer PEG showed that BSA requires non-specific interactions for crystal formation. HSA, on the other hand, is more diverse and utilizes more of its residues and thus offers a broader spectrum of possibilities to establish attractive interactions, which are often of a specific nature. The investigation of BSA-LaCl3 under the influence of co-salts shows that not only cations but also anions have a significant influence on the behavior of proteins. Different concentrations of co-salts reduce the LCST to different degrees thereby following an inverted Hofmeister series for anions.

Chapter 11

Outlook

Although various scientific questions have been answered by the work presented in this thesis, others remain open. This section summarizes open questions and provides an outlook on possible future research projects.

As already described in Chapter 7, the hexamine cobalt(III) cation has six covalently bound ammonia ligands (NH_3), which are arranged octahedrally around the central cobalt atom. These covalent bound NH_3 groups appear to be fundamental for the interaction of Hac with DNA and RNA, as previously discussed [329]. For the interaction of Hac with proteins, these NH_3 groups may hinder a co-ordination type of interaction. This aceptor-donor type of interaction was previously discussed on the basis of BLG interaction with Y^{3+} [59, 349]. Therefore, conducting similar experiments with a Hac derivative e.g. a trivalent cobalt salt with only five bound NH_3 groups could help to understand this behavior. One of the possible derivatives could be the pentaaminaquacobalt(III) ion ($Co[(NH_3)_5(H_2O)]^{3+}$), which, however, has to be produced experimentally. Apart from this, there is only a limited number of alternatives, most if not all hydrolyze to divalent cations when dissolved in water. Apart from cobalt (Co) other elements such as Ru, Rh or Ir are reported to form comparable complexes [255], however close attention has to be devoted to the ion radii as it has been reported that an increase in the ion radius is accompanied by a reduction in attraction [344].

The work presented on the role of specific and non-specific interactions in the crystallization behavior of BSA and HSA protein solutions clearly shows the differences in the crystallization strategies (see Chapter 8). HSA crystallizes when sufficient concentrations (mM) of $CeCl_3$ are added, while BSA does not (Maier et al. [365]). The HSA crystallization mediated by $CeCl_3$ is due to specific interactions in accordance with the donor-acceptor principle. BSA, on the other hand, crystallizes in the presence of PEG supplemented with 100 mM NaCl, which is due to the non-specific depletion effect. Under these experimental conditions, HSA does not crystallize.

These results provide a starting point for further research on crystallization and kinetics. In particular, whether the observed BSA crystallization occurs in a one-step or two-step process. In addition, the BSA crystals did not always grow into large single crystals, but occasionally into small needle-like crystals. However, the reproducibility of these needle-like crystals proved to be complicated due to unpredictable appearance. The characterization and identification of the precise and exact conditions of these needle-like crystals require extensive experimental

investigations, which are not within the scope of this work. Nevertheless, the information shown in this work could help to further constrain the conditions required for needle-like crystal growth in order to complement the BSA-PEG NaCl phase diagram.
Several SAXS measurements contained Bragg reflections which originated from these needle-like BSA crystals. Yet again, the reproducibility hindered progress on this matter. Approximating the Bragg reflections with the GSAS-II software suggested a potential new space group for BSA. These results could not be reproduced and require extensive further experiments. Further research could therefore focus on the kinetics and the characterization of these needle-like BSA crystals in more detail.
Continuing, the investigated BSA/HSA protein-PEG NaCl systems could be interesting for X-ray photon correlation spectroscopy (XPCS) measurements. XPCS could provide further insights to the diffusion behavior and provide new insights on the LLPS behavior as well.
Another interesting addition to this work would be to change the solvent from H_2O to D_2O. This change in solvent is expected to alter the phase behavior, even if only slightly. Moreover, this change of solvent would enable small angle neutron scattering experiments (SANS), which could help to characterize this system even further. Unlike X-rays, neutrons are scattered by the atomic nucleus and not by the electrons, which is why the information obtained is different and contributes to a better understanding.
Chapter 9 reports on the progress on the specific co-Ion effects of globular protein solutions with trivalent Salts (BSALaCl3 admixed with co-salts). Due to the ambiguous results arising from the disagreement between UV/Vis cloud point measurements and the results of the SAXS analysis, a recommendation for additional SAXS measurements is therefore already included in Chapter 9.5. The ambiguity arises from the fact that the reduction in cloud point temperatures (UV/vis measurements) does not correspond to the B_2/B_2^{HS} values obtained from the approximation of the SAXS data obtained by the SHS potential. Hence, additional SAXS measurements either at 10 °C or temperature controlled, with a comparable temperature range to the conducted UV/vis measurements are advised. In addition, the salt NaSCN should be represented in future SAXS measurements, as it induced the strongest reduction of the LCST.
Apart from further SAXS measurements, a solvent exchange from H_2O to D_2O could yield interesting new data. This exchange in solvent would allow not only to compare the phase diagrams but also for SANS measurements. SANS measurements could provide data regarding the hydration of the protein and the influence on the hydration exerted by the co-ions. This idea is related to the law of matching water affinities, which is argued on the basis of changes in hydration enthalpy and has been used to explain the experimentally observed decrease in transition temperatures. The different scattering methods could provide new, otherwise hidden information that could contribute to the further characterization of the BSA-LaCl3 co-salt system.

Taken together, this work shows that proteins are highly complex molecules which react very sensitively to their ambient medium. Even the smallest changes in various physio-chemical values such as pH, charge, temperature or even pressure exert major effects and influence their phase behaviour. Therefore, the understanding of protein phase behaviour is important especially in a medical context. For example, unwanted aggregation or crystallization represent a clinical condition. In order to treat diseases, therapeutics such as vaccines, which involve functional proteins in solution, are required to be stable in order to exert the desired curing effect accordingly. Stability of the protein solution can thus be influenced by addition of salts or other additives. The proteins investigated here can therefore be regarded as models that not only allow the knowledge acquired to be expanded, but also to be transferred to more complicated and complex proteins.

List of Own Publications

The following enumeration contains various publications [A]-[G], produced during the course of this dissertation. The fundamental publications comprising this thesis are highlighted by [A]-[B]

[A] M. D. Senft, G. Zocher, S. Retzbach, A. Hiremath, R. Maier, F. Zhang, T. Stehle, and F. Schreiber. The Role of Specific and Non-Specific Interactions in Crystallization Behavior of BSA and HSA Protein Solutions. *Submitted to Crystal Growth & Design* (2024).

[B] M. D. Senft, R. Maier, A. Hiremath, F. Zhang, and F. Schreiber. Effective interactions and phase behavior of protein solutions in the presence of hexamine cobalt(III) chloride. *EPJE* 46, 119 (2023).

[C] A .Girelli, M. Bin, M. Filianina, M. Dargasz, N. D. Anthuparambil, J. Möllner, A. Zozulya, I. Andronis, S. Timmermann, S. Berkowicz, S. Retzbach, M. Reiser, A.M. Raza, M. Kowalski, M.S. Akhundzadeh, J. Schrage, C.H. Woo, M. D. Senft, L.F. Reichart, A. Leonau, P.P. Rajaiah, W. Chèvremont, T. Seydel, J. Hallmann, A. Rodriguez-Fernandez, J-E. Pudell, F. Brausse, U. Boesenberg, J. Wrigley, M. Youssef, W. Lu, W. Jo, R. Shayduk, A. Madsen, F. Lehmkühler, M. Paulus, F. Zhang, F. Schreiber, C. Gutt and F. Perakis. Coherent X-rays reveal anomalous molecular diffusion and cage effects in crowded protein solutions. *tbp* (2024).

[D] N. D. Anthuparambil, S. Timmermann, M. Dargasz, S. Retzbach, M. D. Senft, N. Begam, A. Raguslkaya, M. Paulus, F. Zhang, F. Westermaier, M. Sprung, F. Schreiber, and C. Gutt. Salt induced slowdown of kinetics and dynamics during thermal gelation of egg-yolk *J. Chem. Phys.* 161, 055102 (2024).

[E] S. Timmermann, N. D. Anthuparambil, A. Girelli, N. Begam, M. Kowalski, S. Retzbach, M. D. Senft, M. S. Akhundzadeh, H.- F.Poggemann, M. Moron, A. Hiremath, D. Gutmüller, M. Dargasz, Ö. Öztürk, M. Paulus, F. Westermaier, M. Sprung, A. Raguslkaya, F. Zhang, F. Schreiber, and C. Gutt. Cluster-X-ray driven and intrinsic dynamics in protein gels. *Sci. Rep*, 13, 11048, (2023).

[**F**] N. D. Anthuparambil, A. Girelli,S. Timmermann, M. Kowalski, M. S. Akhundzadeh, S. Retzbach, M. D. Senft, M. Dargasz, D. Gutmüller, A. Hiremath, M. Moron, Ö. Öztürk, H.- F.Poggemann, A. Raguslkaya, N. Begam, A. Tosson, M. Paulus, F. Westermaier, F. Zhang, M. Sprung, F. Schreiber, and C. Gutt. Exploring non-equilibrium processes and spatio-temporal scaling laws in heated egg yolk using coherent X-rays. *Nat. Comm.* 14, 5580 (2023).

[**G**] N. Begam, S. Timmermann, A. Raguslkaya, A. Girelli, M. D. Senft, S. Retzbach, N. D. Anthuparambil, M. S. Akhundzadeh, M. Kowalski, M. Reiser, F. Westermaier, M. Sprung, F. Zhang, C. Gutt, and F. Schreiber. Effects of temperature and ionic strength on the microscopic structure and dynamics of egg white gels, *J. Chem. Phys.* 158, 074903 (2023).

Acknowledgement

Gratitude is not only the greatest of all virtues, but also the mother of all others.
-Marcus Tullius Cicero-

I want to dedicate the following lines to all the people who have accompanied and supported me throughout the period of this doctoral thesis.
First and foremost, I would like to thank my two supervisors, Prof. Dr. Dr. hc Frank Schreiber and PD. Dr. Fajun Zhang, for offering me the opportunity to pursue a doctorate. Thank you for the trust you have placed in me, for your constant support, for all the fruitful discussions we have had and the knowledge you have imparted. I am equally grateful to you for allowing me the freedom to evolve and develop, and that I could always rely on your guidance. Thanks to your efforts, I was able to participate in various SAXS and XPCS large scale experiments which cannot be taken for granted. Thank you for your inventiveness and your words of encouragement when things did not go according to plan.
Next, I would like to thank my examination board, consisting of the written examiners PD. Dr. Fajun Zhang and Prof. Dr. Monika Fleischer as well as the the oral examiners Prof. Dr. Dr. hc. Frank Schreiber and Prof. Dr. Thilo Stehle.
I would also like to express my thank to Dr. Alexander Gerlach for his technical support, his efforts in maintaining the scientific equipment I used and his continuous IT support. The Moneta cloud service, which you helped to create, is a great asset and has proven itself to be a valuable tool more than once.
Thanks to the technical support from Bernd Hofferberth, many problems were solved within a short period of time and clever solutions were found to ensure smooth operation of the measurment devices.
I would like to thank Dr. Georg Zocher for our joint collaboration. Thank you for the interesting insights and great discussions.
Furthermore, I would like to thank my friend Dr. Ivan Zahluznyy, who helped me with words and deeds and always had an open ear for me. Your lectures on X-ray scattering techniques in an experimental context were extremely helpful and contributed a considerable amount to my understanding of this complex subject. Our trip to Scotland was a lot of fun and I am glad we shared this memory.
I would like to thank my friends Paul Zimmermann and Anton Pylypenko for our great time we regularly spent together at the gym after work. Doing sports with you guys really helped me to wind down, clear my head and made working on my thesis more enjoyable.
At this point I would like to thank my friend Ingrid Dax for encouraging me to start the process of writing this thesis earlier than I had anticipated. Our regular thesis writing sessions were much appreciated and helped a lot.

A special thanks belongs to Sebastian Retzbach, Dr. Sonja Timmermann, Ross Ewan Cater, Sebastian Schwartzkopf, Dr. Furio Surfaro, Hadra-Sioux Banks-Machado, Dr. Ekaterina Kneschaurek, Niels Scheffczyk, and Paul Zimmermann who proof read this thesis and provided exceptional suggestions to improve not only the writing but also the chain of arguments.
I would also like to express may thanks to the research group members and former group members for the many conversations, discussions and coffee rounds that made every day a little sweeter. Thank you Dr. Ralph Maier, Dr. Anita Girelli, Dr. Nafisa Begam, Dr. Anastasia Ragulskaya, Dr. Furio Surfaro, Hadra-Sioux Banks-Machado, Dr. Dmitry Lapkin, Dr. Elena Chulanova, Sebastian Retzbach, Niels Scheffczyk , Dr. Lena Merten, Dr. Ekaterina Kneschaurek, Dr. Frederik Unger, Dr. Julian Hausch, Dr. Ingrid Dax, Constantin Völter, Leonard Simeonov, Sebastian Schwartzkopff, Paul Zimmermann, Anton Pylypenko, and Ross Ewan Carter.
Special thanks of course belongs to the "Rüdigers", Michelle Dragasz, Marvin Kowalski, Dr. Sonja Timmermann and Sebastian Retzbach. Thank you for the many great moments we were able to experience together at shared beam times. Thanks to you, it was always a great pleasure. I will never forget our really unusual script names for our measurements, which are probably unique at DESY.
I would also like to express my gratitude to all my friends, who were always helping and encouraging. Thank you for the continuous support.

I would like to thank my girlfriend Dr. Sonja Timmermann for her constant support throughout the work of this thesis.
Last but not least I would like to thank my parents Susanne and Ulrich Senft, and my sister Isa Senft for their support throughout the years which helped me to pursue this doctorate.

List of acronyms

A-DNA Right-Handed Helices Desoxyribonucleic Acid

AO Asakura Osawa

a.u. Arbitrary Unit

B-DNA Average Right-Handed Helices Desoxyribonucleic Acid

BLG β-lactoglobulin

BSA Bovine serum albumin

CL Colloidal Limit

CNT Classical Nucleation Theory

DESY Deutsches Elektronen-Synchrotron

DLS Dynamic Light Scattering

DLVO Derjaguin-Landau-Verwey-Overbeek

DNA Desoxyribonucleic Acid

EMBL European Molecular Biology Laboratory

EPPIC Evolutionary Protein-Protein Interface Classifier

Hac Hexamin Cobalt(III)chloride

HS Hard Sphere Potential

HSA Human serum albumin

LCST Lower Critical Solution Temperature

LLPS Liquid-Liquid Phase Separation

MSA Mean Spherical Approximation

NIST National Institute of Standards and Technology

OVA Ovalbumin

PDB Protein Database

PEG Polyethylene gylcol

PETRA Positron-Elektron-Tandem-Ring-Anlage

pH pH

pI Isoelectric Point

RC Reentrant Condensation

RI Reentrant Interaction

RNA Ribonucleic Acid

SARS Severe Acute Respiratory Syndrome

SAXS Small angle X-ray scattering

SC Screened Coulomb Potenital

SHS Sticky Hard Spheres Potential

SLD Scattering Length Density

SLS Static Light Scattering

UCST Upper Critical Solution Temperature

UV/vis Ultraviolet-visible Spectroscopy

vdW van der Waals

XDS X-ray Detector Software

2Y Two-Yukawa Potential

Z-DNA Left-Handed Helices Desoxyribonucleic Acid

Bibliography

[1] K. Van Holde, C. Johnson, and P. S. Ho, *Principles of physical biochemistry*, 2 ed., Pearson, Upper Saddle River, NJ, 2005 (en).

[2] F. Bezanilla, *Voltage-gated ion channels*, Biological Membrane Ion Channels: Dynamics, Structure, and Applications (2007), 81–118.

[3] S. J. Benkovic and S. Hammes-Schiffer, *A perspective on enzyme catalysis*, Science **301** (2003), 1196–1202.

[4] E. Perozo, D. M. Cortes, P. Sompornpisut, A. Kloda, and B. Martinac, *Open channel structure of mscl and the gating mechanism of mechanosensitive channels*, Nature **418** (2002), 942–948.

[5] A. Ciccia and S. J. Elledge, *The DNA damage response: making it safe to play with knives*, Molecular Cell **40** (2010), 179–204.

[6] S. R. Hertzler, J. C. Lieblein-Boff, M. Weiler, and C. Allgeier, *Plant proteins: assessing their nutritional quality and effects on health and physical function*, Nutrients **12** (2020), 3704.

[7] E. Arentson-Lantz, S. Clairmont, D. Paddon-Jones, A. Tremblay, and R. Elango, *Protein: A nutrient in focus*, Applied Physiology, Nutrition, and Metabolism **40** (2015), 755–761.

[8] S. Assenza and R. Mezzenga, *Soft condensed matter physics of foods and macronutrients*, Nature Reviews Physics **1** (2019), 551–566.

[9] C. M. Dobson, *Protein folding and misfolding*, Nature **426** (2003), 884–890.

[10] K. Maruyama, *Connectin/titin, giant elastic protein of muscle*, The FASEB Journal **11** (1997), 341–345.

[11] J. A. Marsh and S. A. Teichmann, *Structure, dynamics, assembly, and evolution of protein complexes*, Annual Review of Biochemistry **84** (2015), 551–575.

[12] T. Walzthoeni, A. Leitner, F. Stengel, and R. Aebersold, *Mass spectrometry supported determination of protein complex structure*, Current Opinion in Structural Biology **23** (2013), 252–260.

[13] J. Janin, R. P. Bahadur, and P. Chakrabarti, *Protein–protein interaction and quaternary structure*, Quarterly Reviews of biophysics **41** (2008), 133–180.

[14] C. C. Malbon, *G proteins in development*, Nature Reviews Molecular cell biology **6** (2005), 689–701.

[15] A. Illanes et al., *Enzyme biocatalysis*, Principles and Applications. Editorial Springer-Verlag New York Inc., United States (2008), 1–56.

[16] T. D. Pollard and J. A. Cooper, *Actin, a central player in cell shape and movement*, Science **326** (2009), 1208–1212.

[17] M. Vendruscolo, J. Zurdo, C. E. MacPhee, and C. M. Dobson, *Protein folding and misfolding: a paradigm of self–assembly and regulation in complex biological systems*, Philosophical Transactions of the Royal Society of London. Series A: Mathematical, Physical and Engineering Sciences **361** (2003), 1205–1222.

[18] R. Thibault, L. Genton, and C. Pichard, *Body composition: why, when and for who?*, Clinical Nutrition **31** (2012), 435–447.

[19] The UniProt Consortium, *Uniprot knowledgebase*, 2024, `https://www.uniprot.org/uniprotkb`; last checked 22.07.2024, 15:11.

[20] K. E. Goodwill, M. G. Tennant, and R. C. Stevens, *High-throughput x-ray crystallography for structure-based drug design*, Drug Discovery Today **6** (2001), 113–118.

[21] A. Jen and H. P. Merkle, *Diamonds in the rough: protein crystals from a formulation perspective*, Pharmaceutical Research **18** (2001), 1483–1488.

[22] S. K. Basu, C. P. Govardhan, C. W. Jung, and A. L. Margolin, *Protein crystals for the delivery of biopharmaceuticals*, Expert Opinion on Biological Therapy **4** (2004), 301–317.

[23] R. Giegé, *A historical perspective on protein crystallization from 1840 to the present day*, The FEBS Journal **280** (2013), 6456–6497.

[24] S. Pu and K. Hadinoto, *Continuous crystallization as a downstream processing step of pharmaceutical proteins: A review*, Chemical Engineering Research and Design **160** (2020), 89–104.

[25] O. Galkin, K. Chen, R. L. Nagel, R. E. Hirsch, and P. G. Vekilov, *Liquid-liquid separation in solutions of normal and sickle cell hemoglobin*, Proceedings of the National Academy of Sciences of the United States of America **99** (2002), 8479–8483.

[26] M. Da Fonseca, H. S. Oueis, and P. S. Casamassimo, *Sickle cell anemia: a review for the pediatric dentist*, Pediatric Dentistry **29** (2007), 159–169.

[27] T. N. Williams and S. L. Thein, *Sickle cell anemia and its phenotypes*, Annual Review of Genomics and Human Genetics **19** (2018), 113–147.

[28] J. D. Gunton, A. Shiryayev, and D. L. Pagan, *Protein condensation: Kinetic pathways to crystallization and disease*, 1. paperback ed. ed., Cambridge Univ. Press, New York, NY, 2014.

[29] A. P. Minton, *The effect of time-dependent macromolecular crowding on the kinetics of protein aggregation: a simple model for the onset of age-related neurodegenerative disease*, Frontiers in Physics **2** (2014), 48.

[30] A. Aguzzi and T. O'connor, *Protein aggregation diseases: pathogenicity and therapeutic perspectives*, Nature Reviews Drug Discovery **9** (2010), 237–248.

[31] C. A. Ross and M. A. Poirier, *Protein aggregation and neurodegenerative disease*, Nature medicine **10** (2004), S10–7.

[32] A. Green, *Cerebrospinal fluid brain-derived proteins in the diagnosis of alzheimer's disease and creutzfeldt–jakob disease*, Neuropathology and Applied Neurobiology **28** (2002), 427–440.

[33] A. Kakio, S.-i. Nishimoto, K. Yanagisawa, Y. Kozutsumi, and K. Matsuzaki, *Cholesterol-dependent formation of GM1 ganglioside-bound amyloid β-protein, an endogenous seed for Alzheimer amyloid*, Journal of Biological Chemistry **276** (2001), 24985–24990.

[34] F. Cardoso, *Huntington disease and other choreas*, Neurologic Clinics **27** (2009), 719–736.

[35] J. P. Doye, A. A. Louis, and M. Vendruscolo, *Inhibition of protein crystallization by evolutionary negative design*, Physical Biology **1** (2004), P9.

[36] J. Cui, F. Li, and Z.-L. Shi, *Origin and evolution of pathogenic coronaviruses*, Nature Reviews Microbiology **17** (2019), 181–192.

[37] P. Sarzi-Puttini, V. Giorgi, S. Sirotti, D. Marotto, S. Ardizzone, G. Rizzardini, S. Antinori, and M. Galli, *Covid-19, cytokines and immunosuppression: what can we learn from severe acute respiratory syndrome?*, Clinical and Experimental Rheumatology **38** (2020), 337–342.

[38] B. Ju, Q. Zhang, J. Ge, R. Wang, J. Sun, X. Ge, J. Yu, S. Shan, B. Zhou, S. Song, et al., *Human neutralizing antibodies elicited by sars-cov-2 infection*, Nature **584** (2020), 115–119.

[39] C. O. Barnes, C. A. Jette, M. E. Abernathy, K.-M. A. Dam, S. R. Esswein, H. B. Gristick, A. G. Malyutin, N. G. Sharaf, K. E. Huey-Tubman, Y. E. Lee, et al., *Sars-cov-2 neutralizing antibody structures inform therapeutic strategies*, Nature **588** (2020), 682–687.

[40] J. Ge, R. Wang, B. Ju, Q. Zhang, J. Sun, P. Chen, S. Zhang, Y. Tian, S. Shan, L. Cheng, et al., *Antibody neutralization of sars-cov-2 through ace2 receptor mimicry*, Nature Communications **12** (2021), 250.

[41] H. Gruell, K. Vanshylla, T. Weber, C. O. Barnes, C. Kreer, and F. Klein, *Antibody-mediated neutralization of sars-cov-2*, Immunity **55** (2022), 925–944.

[42] L. Zhang, D. Lin, X. Sun, U. Curth, C. Drosten, L. Sauerhering, S. Becker, K. Rox, and R. Hilgenfeld, *Crystal structure of sars-cov-2 main protease provides a basis for design of improved α-ketoamide inhibitors*, Science **368** (2020), 409–412.

[43] J. Lee, C. Kenward, L. J. Worrall, M. Vuckovic, F. Gentile, A.-T. Ton, M. Ng, A. Cherkasov, N. C. Strynadka, and M. Paetzel, *X-ray crystallographic characterization of the sars-cov-2 main protease polyprotein cleavage sites essential for viral processing and maturation*, Nature Communications **13** (2022), 5196.

[44] C. N. Nanev, *Kinetics and intimate mechanism of protein crystal nucleation*, Progress in Crystal Growth and Characterization of Materials **59** (2013), 133–169.

[45] M. Bermudez, J. Mortier, C. Rakers, D. Sydow, and G. Wolber, *More than a look into a crystal ball: Protein structure elucidation guided by molecular dynamics simulations*, Drug Discovery Today **21** (2016), 1799–1805.

[46] D. Fusco and P. Charbonneau, *Soft matter perspective on protein crystal assembly*, Colloids and Surfaces B: Biointerfaces **137** (2016), 22–31.

[47] F. Zhang, M. W. A. Skoda, R. M. J. Jacobs, S. Zorn, R. A. Martin, C. M. Martin, G. F. Clark, S. Weggler, A. Hildebrandt, O. Kohlbacher, and F. Schreiber, *Reentrant condensation of proteins in solution induced by multivalent counterions*, Physical Review Letters **101** (2008), 148101.

[48] H. N. Lekkerkerker, R. Tuinier, and M. Vis, *Colloids and the depletion interaction*, Springer International Publishing, 2011.

[49] H. N. W. Lekkerkerker, R. Tuinier, and M. Vis, *Colloids and the depletion interaction*, 2 ed., Springer International Publishing, Cham, Switzerland, 2024.

[50] P. L. Privalov, *Cold denaturation of protein*, Critical Reviews in Biochemistry and Molecular Biology **25** (1990), 281–306.

[51] L. C. Antonino, R. A. Kautz, T. Nakano, R. O. Fox, and A. L. Fink, *Cold denaturation and 2 H_2O stabilization of a staphylococcal nuclease mutant*, Proceedings of the National Academy of Sciences **88** (1991), 7715–7718.

[52] M. R. Krebs, K. R. Domike, and A. M. Donald, *Protein aggregation: more than just fibrils*, Biochemical Society Transactions **37** (2009), 682–686.

[53] K. L. Moreau and J. A. King, *Protein misfolding and aggregation in cataract disease and prospects for prevention*, Trends in Molecular Medicine **18** (2012), 273–282.

[54] E. Jordan, F. Roosen-Runge, S. Leibfarth, F. Zhang, M. Sztucki, A. Hildebrandt, O. Kohlbacher, and F. Schreiber, *Competing salt effects on phase behavior of protein solutions: Tailoring of protein interaction by the binding of multivalent ions and charge screening*, The Journal of Physical Chemistry B **118** (2014), 11365–11374.

[55] F. Roosen-Runge, B. S. Heck, F. Zhang, O. Kohlbacher, and F. Schreiber, *Interplay of pH and binding of multivalent metal ions: charge inversion and reentrant condensation in protein solutions*, The Journal of Physical Chemistry B **117** (2013), 5777–5787.

[56] F. Zhang, F. Roosen-Runge, A. Sauter, M. Wolf, R. M. Jacobs, and F. Schreiber, *Reentrant condensation, liquid–liquid phase separation and crystallization in protein solutions induced by multivalent metal ions*, Pure and Applied Chemistry **86** (2014), 191–202.

[57] F. Zhang, F. Roosen-Runge, M. W. A. Skoda, R. M. J. Jacobs, M. Wolf, P. Callow, H. Frielinghaus, V. Pipich, S. Prévost, and F. Schreiber, *Hydration and interactions in protein solutions containing concentrated electrolytes studied by small-angle scattering*, Physical Chemistry Chemical Physics **14** (2012), 2483.

[58] F. Zhang, S. Weggler, M. J. Ziller, L. Ianeselli, B. S. Heck, A. Hildebrandt, O. Kohlbacher, M. W. Skoda, R. M. Jacobs, and F. Schreiber, *Universality of protein reentrant condensation in solution induced by multivalent metal ions*, Proteins: Structure, Function, and Bioinformatics **78** (2010), 3450–3457.

[59] F. Zhang, G. Zocher, A. Sauter, T. Stehle, and F. Schreiber, *Novel approach to controlled protein crystallization through ligandation of yttrium cations*, Journal of Applied Crystallography **44** (2011), 755–762.

[60] R. Maier, G. Zocher, A. Sauter, S. Da Vela, O. Matsarskaia, R. Schweins, M. Sztucki, F. Zhang, T. Stehle, and F. Schreiber, *Protein crystallization in the presence of a metastable liquid–liquid phase separation*, Crystal Growth & Design **20** (2020), 7951–7962.

[61] A. Sauter, M. Oelker, G. Zocher, F. Zhang, T. Stehle, and F. Schreiber, *Nonclassical pathways of protein crystallization in the presence of multivalent metal ions*, Crystal Growth & Design **14** (2014), 6357–6366.

[62] O. Matsarskaia, M. K. Braun, F. Roosen-Runge, M. Wolf, F. Zhang, R. Roth, and F. Schreiber, *Cation-induced hydration effects cause lower critical solution temperature behavior in protein solutions*, The Journal of Physical Chemistry B **120** (2016), 7731–7736.

[63] M. R. Fries, D. Stopper, M. K. Braun, A. Hinderhofer, F. Zhang, R. M. J. Jacobs, M. W. A. Skoda, H. Hansen-Goos, R. Roth, and F. Schreiber, *Multivalent-ion-activated protein adsorption reflecting bulk reentrant behavior*, Physical Review Letters **119** (2017), 228001.

[64] M. K. Braun, A. Sauter, O. Matsarskaia, M. Wolf, F. Roosen-Runge, M. Sztucki, R. Roth, F. Zhang, and F. Schreiber, *Reentrant Phase Behavior in Protein Solutions Induced by Multivalent Salts: Strong Effect of Anions Cl^- Versus NO_3*, The Journal of Physical Chemistry B **122** (2018), 11978–11985.

[65] M. K. Braun, M. Wolf, O. Matsarskaia, S. Da Vela, F. Roosen-Runge, M. Sztucki, R. Roth, F. Zhang, and F. Schreiber, *Strong isotope effects on effective interactions and phase behavior in protein solutions in the presence of multivalent ions*, The Journal of Physical Chemistry B **121** (2017), 1731–1739.

[66] A. Sauter, F. Roosen-Runge, F. Zhang, G. Lotze, R. M. Jacobs, and F. Schreiber, *Real-time observation of nonclassical protein crystallization kinetics*, Journal of the American Chemical Society **137** (2015), 1485–1491.

[67] R. Maier, B. Sohmen, S. Da Vela, O. Matsarskaia, C. Beck, R. Schweins, T. Seydel, F. Zhang, and F. Schreiber, *Protein crystallization from a preordered metastable intermediate phase followed by real-time small-angle neutron scattering*, Crystal Growth & Design **21** (2021), 6971–6980.

[68] D. Vivarès, L. Belloni, A. Tardieu, and F. Bonneté, *Catching the PEG-induced attractive interaction between proteins*, The European Physical Journal E **9** (2002), 15–25.

[69] O. Galkin and P. G. Vekilov, *Control of protein crystal nucleation around the metastable liquid–liquid phase boundary*, Proceedings of the National Academy of Sciences **97** (2000), 6277–6281.

[70] A. I. Jion, L.-T. Goh, and S. K. Oh, *Crystallization of IgG1 by mapping its liquid–liquid phase separation curves*, Biotechnology and Bioengineering **95** (2006), 911–918.

[71] M. Lemanowicz, A. Mielańczyk, T. Walica, M. Kotek, and A. Gierczycki, *Application of polymers as a tool in crystallization—a review*, Polymers **13** (2021), 2695.

[72] C. J. Roberts, T. K. Das, and E. Sahin, *Predicting solution aggregation rates for therapeutic proteins: approaches and challenges*, International Journal of Pharmaceutics **418** (2011), 318–333.

[73] A. S. Raut and D. S. Kalonia, *Pharmaceutical perspective on opalescence and liquid–liquid phase separation in protein solutions*, Molecular Pharmaceutics **13** (2016), 1431–1444.

[74] B. D. Mason, J. Zhang-van Enk, L. Zhang, R. L. Remmele, and J. Zhang, *Liquid-liquid phase separation of a monoclonal antibody and nonmonotonic influence of hofmeister anions*, Biophysical Journal **99** (2010), 3792–3800.

[75] P. Papon, J. Leblond, and P. H. E. Meijer, *The physics of phase transitions*, Advanced Texts in Physics, Springer, Berlin, Germany, 2002.

[76] S. Z. Cheng, *Phase transitions in polymers: The role of metastable states*, Elsevier, Amsterdam, 2008.

[77] P. Atkins and J. D. Paula, *Atkins' physical chemistry*, 9 ed., OUP Oxford, New York, London, 2010.

[78] A. Heintz, *Thermodynamik - Grundlagen und Anwendungen*, Springer-Verlag, Berlin Heidelberg New York, 2017.

[79] *Basiswissen physikalische chemie*.

[80] B. Linder, *Thermodynamics and introductory statistical mechanics*, John Wiley & Sons, 2004.

[81] U. Müller, *Chemie*, 11 ed., Thieme, Stuttgart, Germany, mar 2014 (de).

[82] H. Kuhn, H.-D. Forsterling, and D. H. Waldeck, *Principles of physical chemistry*, 2 ed., Wiley-Blackwell, Hoboken, NJ, feb 2009.

[83] P. Richet, *The physical basis of thermodynamics*, 2001 ed., Kluwer Academic/Plenum, New York, NY, aug 2001.

[84] I. Teraoka, *Statistical thermodynamics*, John Wiley & Sons, Nashville, TN, apr 2019.

[85] R. A. Jones, *Soft condensed matter*, vol. 6, Oxford University Press, 2002.

[86] V. J. Anderson and H. N. Lekkerkerker, *Insights into phase transition kinetics from colloid science*, Nature **416** (2002), 811–815.

[87] G. Foffi, G. D. McCullagh, A. Lawlor, E. Zaccarelli, K. A. Dawson, F. Sciortino, P. Tartaglia, D. Pini, and G. Stell, *Phase equilibria and glass transition in colloidal systems with short-ranged attractive interactions: application to protein crystallization*, Physical Review E **65** (2002), 031407.

[88] J. B. Rowe, R. A. Cancel, T. D. Evangelous, R. P. Flynn, S. Pechenov, J. A. Subramony, J. Zhang, and Y. Wang, *Metastability gap in the phase diagram of monoclonal igg antibody*, Biophysical Journal **113** (2017), 1750–1756.

[89] D. L. Nelson and M. M. Cox, *Lehninger principles of biochemistry*, 6 ed., W.H. Freeman, New York, NY, nov 2012 (en).

[90] R. Glaser, *Biophysics: An introduction*, Springer Berlin Heidelberg, 2012.

[91] F. Zhang, M. K. Feustel, M. W. Skoda, R. M. Jacobs, F. Roosen-Runge, T. Seydel, M. Sztucki, and F. Schreiber, *Effective interactions in protein solutions with and without clustering*, Physica A: Statistical Mechanics and its Applications **650** (2024), 129995.

[92] T. Markovich, D. Andelman, and R. Podgornik, *Charged membranes: Poisson–Boltzmann theory, the dlvo paradigm, and beyond*, Handbook of lipid membranes, CRC Press, 2021, pp. 99–128.

[93] D. Leckband and J. Israelachvili, *Intermolecular forces in biology*, Quarterly Reviews of Biophysics **34** (2001), 105–267.

[94] J. N. Israelachvili, *14 - electrostatic forces between surfaces in liquids*, Intermolecular and Surface Forces (Third Edition) (J. N. Israelachvili, ed.), Academic Press, Boston, third edition ed., 2011, pp. 291–340.

[95] M. Boström, D. Williams, and B. Ninham, *Specific ion effects: why DLVO theory fails for biology and colloid systems*, Physical Review Letters **87** (2001), 168103.

[96] D. N. Petsev and P. G. Vekilov, *Evidence for non-dlvo hydration interactions in solutions of the protein apoferritin*, Physical Review Letters **84** (2000), 1339.

[97] A. K. Arora, B. Tata, A. Sood, and R. Kesavamoorthy, *Reentrant phase transition in charged colloidal suspensions*, Physical Review Letters **60** (1988), 2438.

[98] J. Yamanaka, H. Yoshida, T. Koga, N. Ise, and T. Hashimoto, *Reentrant order-disorder transition in ionic colloidal dispersions by varying particle charge density*, Langmuir **15** (1999), 4198–4202.

[99] H. Versmold, *A. K. Arora and B. V. R. Tata: Ordering and Phase Transitions in Charged Colloids, Complex Fluids and Fluid Microstructures Series, VCH, ISBN 0-471-18630-9, DM 185,-*, Berichte der Bunsengesellschaft für physikalische Chemie **102** (1998), 288–288.

[100] T. T. Nguyen, I. Rouzina, and B. I. Shklovskii, *Reentrant condensation of DNA induced by multivalent counterions*, The Journal of Chemical Physics **112** (2000), 2562–2568.

[101] T. T. Nguyen and B. I. Shklovskii, *Complexation of DNA with positive spheres: phase diagram of charge inversion and reentrant condensation*, The Journal of Chemical Physics **115** (2001), 7298–7308.

[102] V. A. Bloomfield, *DNA condensation*, Current Opinion in Structural Biology **6** (1996), 334–341.

[103] P.-Y. Hsiao, *Overcharging, charge inversion, and reentrant condensation: Using highly charged polyelectrolytes in tetravalent salt solutions as an example of study*, The Journal of Physical Chemistry B **112** (2008), 7347–7350.

[104] P. K. Jha, J. W. Zwanikken, and M. O. De La Cruz, *Understanding swollen–collapsed and re-entrant transitions in polyelectrolyte nanogels by a modified donnan theory*, Soft Matter **8** (2012), 9519–9522.

[105] L. Valencia, E. M. Nomena, S. Monti, W. Rosas-Arbelaez, A. P. Mathew, S. Kumar, and K. P. Velikov, *Multivalent ion-induced re-entrant transition of carboxylated cellulose nanofibrils and its influence on nanomaterials' properties*, Nanoscale **12** (2020), 15652–15662.

[106] M. Wolf, F. Roosen-Runge, F. Zhang, R. Roth, M. W. Skoda, R. M. Jacobs, M. Sztucki, and F. Schreiber, *Effective interactions in protein–salt solutions approaching liquid–liquid phase separation*, Journal of Molecular Liquids **200** (2014), 20–27.

[107] F. Roosen-Runge, F. Zhang, F. Schreiber, and R. Roth, *Ion-activated attractive patches as a mechanism for controlled protein interactions*, Scientific Reports **4** (2014), 7016.

[108] F. Zhang, R. Roth, M. Wolf, F. Roosen-Runge, M. W. Skoda, R. M. Jacobs, M. Stzucki, and F. Schreiber, *Charge-controlled metastable liquid–liquid phase separation in protein solutions as a universal pathway towards crystallization*, Soft Matter **8** (2012), 1313–1316.

[109] F. Surfaro, F. Zhang, F. Schreiber, and R. Roth, *The ion-activated attractive patchy particle model and its application to the liquid–vapor phase transitions*, The Journal of Chemical Physics **161** (2024).

[110] J. R. Espinosa, J. A. Joseph, I. Sanchez-Burgos, A. Garaizar, D. Frenkel, and R. Collepardo-Guevara, *Liquid network connectivity regulates the stability and composition of biomolecular condensates with many components*, Proceedings of the National Academy of Sciences **117** (2020), 13238–13247.

[111] H. Liu, S. K. Kumar, and F. Sciortino, *Vapor-liquid coexistence of patchy models: Relevance to protein phase behavior*, The Journal of Chemical Physics **127** (2007).

[112] F. Hofmeister, *Zur Lehre von der Wirkung der Salze*, Archiv für experimentelle Pathologie und Pharmakologie **24** (1888), 247–260.

[113] Y. Zhang and P. S. Cremer, *Chemistry of Hofmeister anions and osmolytes*, Annual Review of Physical Chemistry **61** (2010), 63–83.

[114] X. He and A. G. Ewing, *Hofmeister series: From aqueous solution of biomolecules to single cells and nanovesicles*, ChemBioChem **24** (2023), e202200694.

[115] Y. Zhang and P. S. Cremer, *Interactions between macromolecules and ions: the hofmeister series*, Current Opinion in Chemical Biology **10** (2006), 658–663.

[116] H. I. Okur, J. Hladílková, K. B. Rembert, Y. Cho, J. Heyda, J. Dzubiella, P. S. Cremer, and P. Jungwirth, *Beyond the Hofmeister series: Ion-specific effects on proteins and their biological functions*, The Journal of Physical Chemistry B **121** (2017), 1997–2014.

[117] V. Mazzini and V. S. Craig, *What is the fundamental ion-specific series for anions and cations? Ion specificity in standard partial molar volumes of electrolytes and electrostriction in water and non-aqueous solvents*, Chemical Science **8** (2017), 7052–7065.

[118] K. P. Gregory, G. R. Elliott, H. Robertson, A. Kumar, E. J. Wanless, G. B. Webber, V. S. Craig, G. G. Andersson, and A. J. Page, *Understanding specific ion effects and the Hofmeister series*, Physical Chemistry Chemical Physics **24** (2022), 12682–12718.

[119] K. D. Collins, *Charge density-dependent strength of hydration and biological structure*, Biophysical Journal **72** (1997), 65–76.

[120] K. D. Collins, *Ions from the Hofmeister series and osmolytes: effects on proteins in solution and in the crystallization process*, Methods **34** (2004), 300–311.

[121] P. Jungwirth and B. Winter, *Ions at aqueous interfaces: From water surface to hydrated proteins*, Annual Review of Physical Chemistry **59** (2008), 343–366.

[122] K. D. Collins, *Ion hydration: Implications for cellular function, polyelectrolytes, and protein crystallization*, Biophysical Chemistry **119** (2006), 271–281.

[123] K. D. Collins, *The behavior of ions in water is controlled by their water affinity*, Quarterly Reviews of Biophysics **52** (2019), e11.

[124] A. Salis and B. W. Ninham, *Models and mechanisms of hofmeister effects in electrolyte solutions, and colloid and protein systems revisited*, Chemical Society Reviews **43** (2014), 7358–7377.

[125] J. M. Fox, K. Kang, W. Sherman, A. Héroux, G. M. Sastry, M. Baghbanzadeh, M. R. Lockett, and G. M. Whitesides, *Interactions between Hofmeister anions and the binding pocket of a protein*, Journal of the American Chemical Society **137** (2015), 3859–3866.

[126] N. Schwierz, D. Horinek, and R. R. Netz, *Reversed anionic Hofmeister series: the interplay of surface charge and surface polarity*, Langmuir **26** (2010), 7370–7379.

[127] N. Schwierz, D. Horinek, U. Sivan, and R. R. Netz, *Reversed Hofmeister series—The rule rather than the exception*, Current Opinion in Colloid & Interface Science **23** (2016), 10–18.

[128] M. Bončina, J. Reščič, and V. Vlachy, *Solubility of lysozyme in polyethylene glycol-electrolyte mixtures: the depletion interaction and ion-specific effects*, Biophysical Journal **95** (2008), 1285–1294.

[129] Y. Zhang and P. S. Cremer, *The inverse and direct Hofmeister series for lysozyme*, Proceedings of the National Academy of Sciences **106** (2009), 15249–15253.

[130] S. Finet, F. Skouri-Panet, M. Casselyn, F. Bonnete, and A. Tardieu, *The Hofmeister effect as seen by SAXS in protein solutions*, Current Opinion in Colloid & Interface Science **9** (2004), 112–116.

[131] M. Boström, F. W. Tavares, S. Finet, F. Skouri-Panet, A. Tardieu, and B. Ninham, *Why forces between proteins follow different Hofmeister series for pH above and below pI*, Biophysical Chemistry **117** (2005), 217–224.

[132] S. Da Vela, C. Exner, R. S. Schäufele, J. Möller, Z. Fu, F. Zhang, and F. Schreiber, *Arrested and temporarily arrested states in a protein–polymer mixture studied by USAXS and VSANS*, Soft Matter **13** (2017), 8756–8765.

[133] F. Cardinaux, T. Gibaud, A. Stradner, and P. Schurtenberger, *Interplay between spinodal decomposition and glass formation in proteins exhibiting short-range attractions*, Physical Review Letters **99** (2007), 118301.

[134] N. Shimada, M. Nakayama, A. Kano, and A. Maruyama, *Design of ucst polymers for chilling capture of proteins*, Biomacromolecules **14** (2013), 1452–1457.

[135] E. Karjalainen, V. Aseyev, and H. Tenhu, *Counterion-induced UCST for polycations*, Macromolecules **47** (2014), 7581–7587.

[136] Y. Kotsuchibashi, *Recent advances in multi-temperature-responsive polymeric materials*, Polymer Journal **52** (2020), 681–689.

[137] M. Le, W. Huang, K.-F. Chen, C. Lin, L. Cai, H. Zhang, and Y.-G. Jia, *Upper critical solution temperature polymeric drug carriers*, Chemical Engineering Journal **432** (2022), 134354.

[138] H. G. Schild and D. A. Tirrell, *Microcalorimetric detection of lower critical solution temperatures in aqueous polymer solutions*, Journal of Physical Chemistry **94** (1990), 4352–4356.

[139] A. M. Kisselev and E. Manias, *Phase behavior of temperature-responsive polymers with tunable LCST: An equation-of-state approach*, Fluid Phase Equilibria **261** (2007), 69–78.

[140] G. Pasparakis and C. Tsitsilianis, *Lcst polymers: Thermoresponsive nanostructured assemblies towards bioapplications*, Polymer **211** (2020), 123146.

[141] H. Nuhn and H.-A. Klok, *Secondary structure formation and LCST behavior of short elastin-like peptides*, Biomacromolecules **9** (2008), 2755–2763.

[142] N. K. Li, F. G. Quiroz, C. K. Hall, A. Chilkoti, and Y. G. Yingling, *Molecular description of the LCST behavior of an elastin-like polypeptide*, Biomacromolecules **15** (2014), 3522–3530.

[143] T. I. Morozova, N. A. García, O. Matsarskaia, F. Roosen-Runge, and J.-L. Barrat, *Structural and dynamical properties of elastin-like peptides near their lower critical solution temperature*, Biomacromolecules **24** (2023), 1912–1923.

[144] O. Matsarskaia, S. Da Vela, A. Mariani, Z. Fu, F. Zhang, and F. Schreiber, *Phase-separation kinetics in protein–salt mixtures with compositionally tuned interactions*, The Journal of Physical Chemistry B **123** (2019), 1913–1919.

[145] T. López-León, J. L. Ortega-Vinuesa, D. Bastos-González, and A. Elaissari, *Thermally sensitive reversible microgels formed by poly (N-Isopropylacrylamide) charged chains: A Hofmeister effect study*, Journal of Colloid and Interface Science **426** (2014), 300–307.

[146] G. Wu, S.-C. Chen, Q. Zhan, and Y.-Z. Wang, *Well-defined amphiphilic biodegradable comb-like graft copolymers: Their unique architecture-determined LCST and UCST thermoresponsivity*, Macromolecules **44** (2011), 999–1008.

[147] E. Clark and J. Lipson, *LCST and UCST behavior in polymer solutions and blends*, Polymer **53** (2012), 536–545.

[148] F. Zhang, *Nonclassical nucleation pathways in protein crystallization*, Journal of Physics: Condensed Matter **29** (2017), 443002.

[149] N. Begam, O. Matsarskaia, M. Sztucki, F. Zhang, and F. Schreiber, *Unification of lower and upper critical solution temperature phase behavior of globular protein solutions in the presence of multivalent cations*, Soft Matter **16** (2020), 2128–2134.

[150] F. Oosawa and S. Asakura, *Surface tension of high-polymer solutions*, The Journal of Chemical Physics **22** (1954), 1255–1255.

[151] S. Asakura and F. Oosawa, *Interaction between particles suspended in solutions of macromolecules*, Journal of Polymer Science **33** (1958), 183–192.

[152] R. Hunter, *Foundations of colloid science*, Oxford University Press, 2001.

[153] R. Tuinier, J. Rieger, and C. de Kruif, *Depletion-induced phase separation in colloid–polymer mixtures*, Advances in Colloid and Interface Science **103** (2003), 1–31.

[154] A. Vrij, *Polymers at interfaces and the interactions in colloidal dispersions*, Pure and Applied Chemistry **48** (1976), 471–483.

[155] T. Cosgrove (ed.), *Colloid science*, 2 ed., Wiley-Blackwell, Chichester, England, mar 2010.

[156] S. Ramakrishnan, M. Fuchs, K. S. Schweizer, and C. F. Zukoski, *Entropy driven phase transitions in colloid–polymer suspensions: Tests of depletion theories*, The Journal of Chemical Physics **116** (2002), 2201–2212.

[157] K. J. Mutch, J. S. van Duijneveldt, J. Eastoe, I. Grillo, and R. K. Heenan, *Small-angle neutron scattering study of microemulsion-polymer mixtures in the protein limit*, Langmuir **24** (2008), 3053–3060.

[158] P.-G. De Gennes, *Scaling concepts in polymer physics*, Cornell University Press, 1979.

[159] D. Marzi, B. Capone, J. Marakis, M. C. Merola, D. Truzzolillo, L. Cipelletti, F. Moingeon, M. Gauthier, D. Vlassopoulos, C. N. Likos, et al., *Depletion, melting and reentrant solidification in mixtures of soft and hard colloids*, Soft Matter **11** (2015), 8296–8312.

[160] K. Devanand and J. Selser, *Asymptotic behavior and long-range interactions in aqueous solutions of poly (ethylene oxide)*, Macromolecules **24** (1991), 5943–5947.

[161] I. Teraoka, *Polymer solutions. An introduction to physical properties. New York: Wiley & Sons*, Inc. Publication (2002).

[162] P. A. Gurnev, C. B. Stanley, M. A. Aksoyoglu, K. Hong, V. A. Parsegian, and S. M. Bezrukov, *Poly(ethylene glycol)s in semidilute regime: Radius of gyration in the bulk and partitioning into a nanopore*, Macromolecules **50** (2017), 2477–2483.

[163] F. Zosel, A. Soranno, K. J. Buholzer, D. Nettels, and B. Schuler, *Depletion interactions modulate the binding between disordered proteins in crowded environments*, Proceedings of the National Academy of Sciences **117** (2020), 13480–13489.

[164] Y. Mao, M. Cates, and H. Lekkerkerker, *Depletion force in colloidal systems*, Physica A: Statistical Mechanics and its Applications **222** (1995), 10–24.

[165] M. Fuchs and K. S. Schweizer, *Structure of colloid-polymer suspensions*, Journal of Physics: Condensed Matter **14** (2002), R239.

[166] W. Poon, P. Pusey, and H. Lekkerkerker, *Colloids in suspense*, Physics World **9** (1996), 27.

[167] A. Bujacz, *Structures of bovine, equine and leporine serum albumin*, Acta crystallographica. Section D, Biological crystallography **68** (2012), 1278–1289.

[168] K. A. Majorek, P. J. Porebski, A. Dayal, M. D. Zimmerman, K. Jablonska, A. J. Stewart, M. Chruszcz, and W. Minor, *Structural and immunologic characterization of bovine, horse, and rabbit serum albumins*, Molecular Immunology **52** (2012), 174–182.

[169] F. Zhang, F. Roosen-Runge, A. Sauter, R. Roth, M. W. A. Skoda, R. M. J. Jacobs, M. Sztucki, and F. Schreiber, *The role of cluster formation and metastable liquid—liquid phase separation in protein crystallization*, Faraday Discussions **159** (2012), 313.

[170] A. McPherson and J. A. Gavira, *Introduction to protein crystallization*, Acta Crystallographica Section F: Structural Biology Communications **70** (2014), 2–20.

[171] A. Ducruix and R. Giegé, *Crystallization of nucleic acids and proteins: A practical approach*, OUP Oxford, oct 1999.

[172] S. Durbin and G. Feher, *Protein crystallization*, Annual Review of Physical Chemistry **47** (1996), 171–204.

[173] G. Nicolis and D. Maes (eds.), *Kinetics and thermodynamics of multistep nucleation and self-assembly in nanoscale materials*, Advances in Chemical Physics, John Wiley & Sons, Nashville, TN, may 2012.

[174] R. Hilfiker and M. von Raumer (eds.), *Polymorphism in the pharmaceutical industry*, 1 ed., Blackwell Verlag, Berlin, Germany, feb 2019.

[175] M. Volmer and A. Weber, *Keimbildung in übersättigten Gebilden*, Zeitschrift für Physikalische Chemie **119U** (1926), 277–301.

[176] R. Becker and W. Döring, *Kinetische Behandlung der Keimbildung in übersättigten Dämpfen*, Annalen der Physik **416** (1935), 719–752.

[177] J. Frenkel, *A general theory of heterophase fluctuations and pretransition phenomena*, The Journal of Chemical Physics **7** (1939), 538–547.

[178] S.-T. Yau and P. G. Vekilov, *Direct observation of nucleus structure and nucleation pathways in apoferritin crystallization*, Journal of the American Chemical Society **123** (2001), 1080–1089.

[179] M. Sleutel, J. Lutsko, A. E. Van Driessche, M. A. Durán-Olivencia, and D. Maes, *Observing classical nucleation theory at work by monitoring phase transitions with molecular precision*, Nature Communications **5** (2014), 5598.

[180] P. Ohodnicki Jr, D. Laughlin, M. McHenry, and M. Widom, *Application of classical nucleation theory to phase selection and composition of nucleated nanocrystals during crystallization of Co-rich (Co, Fe)-based amorphous precursors*, Acta Materialia **58** (2010), 4804–4813.

[181] J. Guo and S. J. Severtson, *Application of classical nucleation theory to characterize the influence of carboxylate-containing additives on $CaCO_3$ nucleation at high temperature, pH, and ionic strength*, Industrial & Engineering Chemistry Research **42** (2003), 3480–3486.

[182] D. Erdemir, A. Y. Lee, and A. S. Myerson, *Nucleation of crystals from solution: classical and two-step models*, Accounts of Chemical Research **42** (2009), 621–629.

[183] N. M. Dixit and C. F. Zukoski, *Competition between crystallization and gelation: a local description*, Physical Review E **67** (2003), 061501.

[184] J. M. Garcıa-Ruiz, *Nucleation of protein crystals*, Journal of Structural Biology **142** (2003), 22–31.

[185] J. De Yoreo, *A perspective on multistep pathways of nucleation*, Crystallization via Nonclassical Pathways Volume 1: Nucleation, Assembly, Observation & Application, ACS Publications, 2020, pp. 1–17.

[186] C. N. Nanev, *Advancements (and challenges) in the study of protein crystal nucleation and growth; thermodynamic and kinetic explanations and comparison with small-molecule crystallization*, Progress in Crystal Growth and Characterization of Materials **66** (2020), 100484.

[187] P. G. Vekilov, *Nucleation*, Crystal growth & design **10** (2010), 5007–5019.

[188] C. Li, Z. Liu, E. C. Goonetilleke, and X. Huang, *Temperature-dependent kinetic pathways of heterogeneous ice nucleation competing between classical and nonclassical nucleation*, Nature Communications **12** (2021), 4954.

[189] R. P. Sear, *The non-classical nucleation of crystals: microscopic mechanisms and applications to molecular crystals, ice and calcium carbonate*, International Materials Reviews **57** (2012), 328–356.

[190] P. R. ten Wolde and D. Frenkel, *Enhancement of protein crystal nucleation by critical density fluctuations*, Science (New York, N.Y.) **277** (1997), 1975–1978.

[191] J. S. Du, Y. Bae, and J. J. De Yoreo, *Non-classical crystallization in soft and organic materials*, Nature Reviews Materials **9** (2024), 229–248.

[192] D. Gebauer and H. Cölfen, *Prenucleation clusters and non-classical nucleation*, Nano Today **6** (2011), 564–584.

[193] P. G. Vekilov, *The two-step mechanism of nucleation of crystals in solution*, Nanoscale **2** (2010), 2346–2357.

[194] P. G. Vekilov and M. A. Vorontsova, *Nucleation precursors in protein crystallization*, Acta Crystallographica Section F Structural Biology Communications **70** (2014), 271–282.

[195] A. George and W. W. Wilson, *Predicting protein crystallization from a dilute solution property*, Acta Crystallographica Section D: Biological Crystallography **50** (1994), 361–365.

[196] F. Platten, J. Hansen, D. Wagner, and S. U. Egelhaaf, *Second virial coefficient as determined from protein phase behavior*, The Journal of Physical Chemistry Letters **7** (2016), 4008–4014.

[197] L. Hentschel, J. Hansen, S. U. Egelhaaf, and F. Platten, *The crystallization enthalpy and entropy of protein solutions: microcalorimetry, van't Hoff determination and linearized poisson–boltzmann model of tetragonal lysozyme crystals*, Physical Chemistry Chemical Physics **23** (2021), 2686–2696.

[198] G. A. Vliegenthart and H. N. W. Lekkerkerker, *Predicting the gas–liquid critical point from the second virial coefficient*, The Journal of Chemical Physics **112** (2000), 5364–5369.

[199] S. Whitelam, *Control of pathways and yields of protein crystallization through the interplay of nonspecific and specific attractions*, Physical Review Letters **105** (2010), 088102.

[200] A. Sauter, F. Roosen-Runge, F. Zhang, G. Lotze, A. Feoktystov, R. M. Jacobs, and F. Schreiber, *On the question of two-step nucleation in protein crystallization*, Faraday Discussions **179** (2015), 41–58.

[201] V. N. Uversky, *Proteins without unique 3d structures: Biotechnological applications of intrinsically unstable/disordered proteins*, Biotechnology Journal **10** (2015), 356–366.

[202] A. Andreeva, D. Howorth, C. Chothia, E. Kulesha, and A. G. Murzin, *SCOP2 prototype: a new approach to protein structure mining*, Nucleic Acids Research **42** (2014), D310–D314.

[203] D. R. Flower, *The lipocalin protein family: structure and function*, Biochemical Journal **318** (1996), 1–14.

[204] Z. Naqvi, E. Ahmad, R. H. Khan, and M. Saleemuddin, *Non-native states of bovine beta-lactoglobulin induced by acetonitrile: pH-dependent unfolding of the two genetic variants a and b*, Cell Biochemistry and Biophysics **66** (2013), 175–185.

[205] S. Pervaiz and K. Brew, *Homology of beta-lactoglobulin, serum retinol-binding protein, and protein hc*, Science (New York, N.Y.) **228** (1985), 335–337.

[206] L. Sawyer, G. Kontopidis, and S.-Y. Wu, *β-lactoglobulin–a three-dimensional perspective*, International Journal of Food Science & Technology **34** (1999), 409–418.

[207] S. Brownlow, J. H. M. Cabral, R. Cooper, D. R. Flower, S. J. Yewdall, I. Polikarpov, A. C. North, and L. Sawyer, *Bovine β-lactoglobulin at* 1.8Å *resolution—still an enigmatic lipocalin*, Structure **5** (1997), 481–495.

[208] G. Kontopidis, C. Holt, and L. Sawyer, *Invited review: β-lactoglobulin: binding properties, structure, and function*, Journal of Dairy Science **87** (2004), 785–796.

[209] S. Le Maux, S. Bouhallab, L. Giblin, A. Brodkorb, and T. Croguennec, *Bovine β-lactoglobulin/fatty acid complexes: binding, structural, and biological properties*, Dairy Science & Technology **94** (2014), 409–426.

[210] M. D. Pérez and M. Calvo, *Interaction of β-lactoglobulin with retinol and fatty acids and its role as a possible biological function for this protein: a review*, Journal of Dairy Science **78** (1995), 978–988.

[211] Q. Wang, J. C. Allen, and H. E. Swaisgood, *Binding of vitamin D and cholesterol to β-lactoglobulin*, Journal of Dairy Science **80** (1997), 1054–1059.

[212] M. Verheul, J. S. Pedersen, S. P. F. M. Roefs, and K. G. de Kruif, *Association behavior of native β-lactoglobulin*, Biopolymers (1999), 11–20.

[213] U. M. Elofsson, M. A. Paulsson, and T. Arnebrant, *Adsorption of β-lactoglobulin A and B in relation to self-association: Effect of concentration and pH*, Langmuir **13** (1997), 1695–1700.

[214] M. K. Braun, M. Grimaldo, F. Roosen-Runge, I. Hoffmann, O. Czakkel, M. Sztucki, F. Zhang, F. Schreiber, and T. Seydel, *Crowding-controlled cluster size in concentrated aqueous protein solutions: Structure, self- and collective diffusion*, The Journal of Physical Chemistry Letters **8** (2017), 2590–2596.

[215] S. Curry, H. Mandelkow, P. Brick, and N. Franks, *Crystal structure of human serum albumin complexed with fatty acid reveals an asymmetric distribution of binding sites*, Nature Structural Biology **5** (1998), 827–835.

[216] J. Figge, T. Rossing, and V. Fencl, *The role of serum proteins in acid-base equilibria.*, The Journal of Laboratory and Clinical Medicine **117** (1991), 453–467.

[217] L. R. Barbosa, M. G. Ortore, F. Spinozzi, P. Mariani, S. Bernstorff, and R. Itri, *The importance of protein-protein interactions on the pH-induced conformational changes of bovine serum albumin: a small-angle X-ray scattering study*, Biophysical Journal **98** (2010), 147–157.

[218] S. Sugio, A. Kashima, S. Mochizuki, M. Noda, and K. Kobayashi, *Crystal structure of human serum albumin at 2.5 Å resolution*, Protein Engineering **12** (1999), 439–446.

[219] D. C. Carter and J. X. Ho, *Structure of serum albumin*, Advances in Protein Chemistry **45** (1994), 153–203.

[220] M. Yang, C. Dutta, and A. Tiwari, *Disulfide-bond scrambling promotes amorphous aggregates in lysozyme and bovine serum albumin*, The Journal of Physical Chemistry B **119** (2015), 3969–3981.

[221] K. Hirayama, S. Akashi, M. Furuya, and K.-i. Fukuhara, *Rapid confirmation and revision of the primary structure of bovine serum albumin by ESIMS and Frit-FAB LC/MS*, Biochemical and Biophysical Research Communications **173** (1990), 639–646.

[222] T. Peters, *All about albumin: Biochemistry, genetics, and medical applications*, Academic Press, 1996.

[223] M. Dockal, D. C. Carter, and F. Ruker, *Conformational transitions of the three recombinant domains of human serum albumin depending on pH*, Journal of Biological Chemistry **275** (2000), 3042–3050.

[224] J. A. Huntington and P. E. Stein, *Structure and properties of ovalbumin*, Journal of Chromatography B: Biomedical Sciences and Applications **756** (2001), 189–198.

[225] G. Martos, P. Contreras, E. Molina, and R. López-Fandiño, *Egg white ovalbumin digestion mimicking physiological conditions*, Journal of Agricultural and Food Chemistry **58** (2010), 5640–5648.

[226] A. D. Nisbet, R. H. Saundry, A. J. Moir, L. A. Fothergill, and J. E. Fothergill, *The complete amino-acid sequence of hen ovalbumin*, European Journal of Biochemistry **115** (1981), 335–345.

[227] L. McReynolds, B. W. O'Malley, A. D. Nisbet, J. E. Fothergill, D. Givol, S. Fields, M. Robertson, and G. G. Brownlee, *Sequence of chicken ovalbumin mRNA*, Nature **273** (1978), 723–728.

[228] S. L. C. Woo, W. G. Beattie, J. F. Catterall, A. Dugaiczyk, R. Staden, G. G. Brownlee, and B. W. O'Malley, *Complete nucleotide sequence of the chicken chromosomal ovalbumin gene and its biological significance*, Biochemistry **20** (1981), 6437–6446.

[229] J. A. Beeley, S. M. Stevenson, and J. G. Beeley, *Polyacrylamide gel isoelectric focusing of proteins: Determination of isoelectric points using an antimony electrode*, Biochimica et Biophysica Acta (BBA) - Protein Structure **285** (1972), 293–300.

[230] M. Yamasaki, Y. Arii, B. Mikami, and M. Hirose, *Loop-inserted and thermostabilized structure of P1-p1 cleaved ovalbumin mutant R339T*, Journal of Molecular Biology **315** (2002), 113–120.

[231] Merck KGaA, *Hexammin-cobalt(iii)-chlorid*, `https://www.sigmaaldrich.com/DE/de/product/sigma/h7891`; last checked 25.02.2024, 15:55.

[232] W. C. Fernelius, *Inorganic syntheses, volume 2*, vol. 2, John Wiley & Sons, 2009.

[233] E. L. Chang, C. Simmers, and D. A. Knight, *Cobalt complexes as antiviral and antibacterial agents*, Pharmaceuticals (Basel, Switzerland) **3** (2010), 1711–1728.

[234] J. S. Kieft and I. Tinoco, *Solution structure of a metal-binding site in the major groove of RNA complexed with cobalt (III) hexammine*, Structure **5** (1997), 713–721.

[235] A. A. D'souza and R. Shegokar, *Polyethylene glycol (peg): a versatile polymer for pharmaceutical applications*, Expert Ppinion on Drug Delivery **13** (2016), 1257–1275.

[236] P. Bohn and M. A. Meier, *Uniform poly (ethylene glycol): a comparative study*, Polymer Journal **52** (2020), 165–178.

[237] J. Maxfield and I. Shepherd, *Conformation of poly (ethylene oxide) in the solid state, melt and solution measured by Raman scattering*, Polymer **16** (1975), 505–509.

[238] Merck KGaA, *Poly(ethylenglykol) 3,350, powder*, `https://www.sigmaaldrich.com/DE/de/product/aldrich/202444`; last checked 25.02.2024, 16:00.

[239] J. R. Boyce, *The paradox of value, directed technical change, and the relative abundance of the chemical elements*, Resource and Energy Economics **58** (2019), 101114.

[240] Internetchemie ChemLin, *Lanthan(III)-chlorid Stoffdaten und Eigenschaften*, `https://www.internetchemie.info/substanz/Lanthan(III)-chlorid.php.`; last checked 23.02.2024, 11:29; last modification 28.04.2020.

[241] J. Yang, Q. Liu, S. Wu, Q. Xi, and Y. Cai, *Effects of lanthanum chloride on glutamate level, intracellular calcium concentration and caspases expression in the rat hippocampus*, Biometals **26** (2013), 43–59.

[242] Merck KGaA, *Lanthan(iii)-chlorid*, `https://www.sigmaaldrich.com/DE/de/product/aldrich/449830`; last checked 23.02.2024, 11:26.

[243] S. R. Feldman, *Sodium chloride*, Kirk-Othmer Encyclopedia of Chemical Technology (2000), 1–27.

[244] P. Van Rooyen and J. Boeyens, *Sodium thiocyanate*, Acta Crystallographica Section B: Structural Crystallography and Crystal Chemistry **31** (1975), 2933–2934.

[245] A. L. Schwan, *Sodium thiocyanate*, Encyclopedia of Reagents for Organic Synthesis (2001).

[246] Merck KGaA, *Sodium thiocyanate*, `https://www.sigmaaldrich.com/DE/de/product/aldrich/467871`; last checked 25.02.2024, 19:16.

[247] D. E. Garrett, *Sodium sulfate: handbook of deposits, processing, & use*, Elsevier, 2001.

[248] D. S. Kostick, *Sodium sulfate*, US Geological Survey Minerals Yearbook (2013), 150–151.

[249] Merck KGaA, *Sodium sulfate*, `https://www.sigmaaldrich.com/DE/de/product/sigald/239313`; last checked 25.02.2024, 22:02.

[250] R. Chandler, M. Jamshad, J. Yule, A. Robinson, F. Alam, K. A. Dunne, N. Nabi, I. Henderson, and D. Huber, *Genetic screen suggests an alternative mechanism for azide-mediated inhibition of seca*, bioRxiv (2017), 173039.

[251] J. Tat, K. Heskett, S. Satomi, R. B. Pilz, B. A. Golomb, and G. R. Boss, *Sodium azide poisoning: a narrative review*, Clinical Toxicology **59** (2021), 683–697.

[252] Merck KGaA, *Sodium azide*, `https://www.sigmaaldrich.com/DE/de/product/sial/s8032`; last checked 26.02.2024, 12:06.

[253] B. Oelkers, *Natriumbromid*, Oct 2022, `https://roempp.thieme.de/lexicon/RD-14-00364`; last checked 17.06.2024, 13.58.

[254] Merck KGaA, *Sodium bromid*, `https://www.sigmaaldrich.com/DE/de/product/sigald/310506`; last checked 17.06.2024, 13:19.

[255] A. F. Holleman, E. Wiberg, and N. Wiberg, *Lehrbuch der anorganischen Chemie*, 102 ed., Walter de Gruyter, Berlin, 2007.

[256] Merck KGaA, *Sodium nitrate*, `https://www.sigmaaldrich.com/DE/de/product/sigald/221341`; last checked 17.06.2024, 13:40.

[257] B. B. He, *Two-dimensional x-ray diffraction*, Wiley, June 2018.

[258] D. I. Svergun, M. H. Koch, P. A. Timmins, and R. P. May, *Small angle x-ray and neutron scattering from solutions of biological macromolecules*, vol. 19, OUP Oxford, 2013.

[259] O. Glatter and O. Kratky (eds.), *Small angle x-ray scattering*, Academic Press, San Diego, CA, mar 1982 (en).

[260] E. M. Anitas, *Small-angle scattering (neutrons, x-rays, light) from complex systems: Fractal and multifractal models for interpretation of experimental data*, Springer International Publishing, 2019.

[261] R. Borsali and R. Pecora, *Soft-matter characterization*, Springer Science & Business Media, 2008.

[262] D. Sivia, *Elementary scattering theory: For x-ray and neutron users*, OUP Oxford, 2011.

[263] P. Linder and T. Zemb, *Neutrons, x-rays, and light: Scattering methods applied to soft condensed matter*, 1 ed., Delta Series-Elsevier, 2002.

[264] J. Als-Nielsen and D. McMorrow, *Elements of modern X-ray physics*, John Wiley & Sons, 2011.

[265] L. Feigin, D. I. Svergun, et al., *Structure analysis by small-angle x-ray and neutron scattering*, vol. 1, Springer, 1987.

[266] F. Zhang, M. W. A. Skoda, R. M. J. Jacobs, R. A. Martin, C. M. Martin, and F. Schreiber, *Protein interactions studied by SAXS: effect of ionic strength and protein concentration for BSA in aqueous solutions*, The Journal of Physical Chemistry B **111** (2007), 251–259.

[267] G. Nägele, *The physics of colloidal soft matter*, Centre of Excellence for Advanced Materials and Structures Warsaw, 2004.

[268] J.-P. Hansen and J. B. Hayter, *A rescaled MSA structure factor for dilute charged colloidal dispersions*, Molecular Physics **46** (1982), 651–656.

[269] J. K. Percus and G. J. Yevick, *Analysis of classical statistical mechanics by means of collective coordinates*, Physical Review **110** (1958), 1–13.

[270] J. B. Hayter and J. Penfold, *An analytic structure factor for macroion solutions*, Molecular Physics **42** (1981), 109–118.

[271] National Institute of Standarts and Technology, *SANS model function documentation*, 2010, `https://www.nist.gov/system/files/documents/2021/03/10/SANS_Model_Docs_v4.10.pdf`; last checked 08.04.2024, 11:57.

[272] Y. Liu, W.-R. Chen, and S.-H. Chen, *Cluster formation in two-Yukawa fluids*, The Journal of Chemical Physics **122** (2005).

[273] S. V. G. Menon, C. Manohar, and K. S. Rao, *A new interpretation of the sticky hard sphere model*, The Journal of Chemical Physics **95** (1991), 9186–9190.

[274] R. J. Baxter, *Percus–Yevick equation for hard spheres with surface adhesion*, The Journal of Chemical Physics **49** (1968), 2770–2774.

[275] M. G. Noro and D. Frenkel, *Extended corresponding-states behavior for particles with variable range attractions*, The Journal of Chemical Physics **113** (2000), 2941–2944.

[276] N. Kern and D. Frenkel, *Fluid–fluid coexistence in colloidal systems with short-ranged strongly directional attraction*, The Journal of Chemical Physics **118** (2003), 9882–9889.

[277] J.-P. Hansen and I. R. McDonald, *Theory of simple liquids: with applications to soft matter*, 3 ed., Academic press, Elsevier, 2006.

[278] F. Bonnete and D. Vivares, *Interest of the normalized second virial coefficient and interaction potentials for crystallizing large macromolecules*, Acta Crystallographica Section D: Biological Crystallography **58** (2002), 1571–1575.

[279] F. Bonneté, S. Finet, and A. Tardieu, *Second virial coefficient: variations with lysozyme crystallization conditions*, Journal of Crystal Growth **196** (1999), 403–414.

[280] D. I. Svergun and M. H. J. Koch, *Small-angle scattering studies of biological macromolecules in solution*, Reports on Progress in Physics **66** (2003), 1735–1782.

[281] S. Mobilio, F. Boscherini, C. Meneghini, et al., *Synchrotron radiation*, Springer, 2016.

[282] P. Willmott, *An introduction to synchrotron radiation: Techniques and applications*, Wiley, mar 2019.

[283] C. E. Blanchet, A. Spilotros, F. Schwemmer, M. A. Graewert, A. Kikhney, C. M. Jeffries, D. Franke, D. Mark, R. Zengerle, F. Cipriani, S. Fiedler, M. Roessle, and D. I. Svergun, *Versatile sample environments and automation for biological solution X-ray scattering experiments at the P12 beamline (PETRA III, DESY)*, Journal of Applied crystallography **48** (2015), 431–443.

[284] European Molecular Biology Laboratory, *Technical characteristics of beamline P12*, 2021, `https://www.embl-hamburg.de/biosaxs/p12/characteristics.html`; last checked 16.04.2024, 12:07.

[285] XENOCS SAS, *Xeuss 2.0 operation manual*, 2015.

[286] S. R. Kline, *Reduction and analysis of SANS and USANS data using IGOR Pro*, Journal of Applied Crystallography **39** (2006), 895–900.

[287] C. D. Putnam, M. Hammel, G. L. Hura, and J. A. Tainer, *X-ray solution scattering (SAXS) combined with crystallography and computation: defining accurate macromolecular structures, conformations and assemblies in solution*, Quarterly Reviews of Biophysics **40** (2007), 191–285.

[288] C. E. Mortimer, U. Müller, and J. Beck (eds.), *Chemie*, 11 ed., Thieme, Stuttgart, Germany, 2014.

[289] W. Schärtl, *Light scattering from polymer solutions and nanoparticle dispersions*, 1. ed. ed., Springer Berlin, Berlin, 2007.

[290] P. C. Hiemenz and T. P. Lodge, *Polymer chemistry*, CRC press, 2007.

[291] K. Onuma, A. Oyane, K. Tsutsui, K. Tanaka, G. Treboux, N. Kanzaki, and A. Ito, *Precipitation kinetics of hydroxyapatite revealed by the continuous-angle laser light-scattering technique*, The Journal of Physical Chemistry B **104** (2000), 10563–10568.

[292] A. M. Striegel, *Stepan Podzimek: Light scattering, size exclusion chromatography and asymmetric flow field flow fractionation. Powerful tools for the characterization of polymers, proteins and nanoparticles*, Analytical and Bioanalytical Chemistry **402** (2012), 1857–1858.

[293] G. Ghosh, *Dispersion-equation coefficients for the refractive index and birefringence of calcite and quartz crystals*, Optics Communications **163** (1999), 95–102.

[294] S. Falke and C. Betzel, *Dynamic light scattering (DLS)*, 173–193, Springer International Publishing, Cham, 2019, pp. 173–193.

[295] B. J. Berne and R. Pecora, *Dynamic light scattering: With applications to chemistry, biology and physics*, Dover Publications, Mineola, 2013.

[296] J. Stetefeld, S. A. McKenna, and T. R. Patel, *Dynamic light scattering: a practical guide and applications in biomedical sciences*, Biophysical Reviews **8** (2016), 409–427.

[297] N. Begam, S. Da Vela, O. Matsarskaia, M. K. Braun, A. Mariani, F. Zhang, and F. Schreiber, *Packing and dynamics of a protein solution approaching the jammed state*, Soft Matter **16** (2020), 7751–7759.

[298] M. Shibayama and T. Norisuye, *Gel formation analyses by dynamic light scattering*, Bulletin of the Chemical Society of Japan **75** (2002), 641–659.

[299] S. K. Sinha, Z. Jiang, and L. B. Lurio, *X-ray photon correlation spectroscopy studies of surfaces and thin films*, Advanced Materials (Deerfield Beach, Fla.) **26** (2014), 7764–7785.

[300] H. Förster, *UV/vis spectroscopy*, Characterization I (H. G. Karge and J. Weitkamp, eds.), Springer Berlin Heidelberg, 2004, pp. 337–426.

[301] C. M. Stoscheck, *[6] quantitation of protein*, Guide to Protein Purification (M. P. Deutscher, ed.), Methods in Enzymology, vol. 182, Academic Press, 1990, pp. 50–68.

[302] J. Verhoeven, *Glossary of terms used in photochemistry (IUPAC Recommendations 1996)*, Pure and Applied Chemistry **68** (1996), 2223–2286.

[303] Beer, *Bestimmung der Absorption des rothen Lichts in farbigen Flüssigkeiten*, Annalen der Physik **162** (1852), 78–88.

[304] D. Nelson and M. Cox, *Lehninger principles of biochemistry*, W. H. Freeman, 2017.

[305] R. L. Lundblad and F. Macdonald, *Handbook of biochemistry and molecular biology*, CRC Press, 2018.

[306] Jorge Babul and Earle Stellwagen, *Measurement of protein concentration with interferences optics*, Analytical Biochemistry **28** (1969), 216–221.

[307] C. Westcott, *pH Measurements*, Elsevier Science, 2012.

[308] S. Karastogianni, S. Girousi, and S. Sotiropoulos, *ph: Principles and measurement*, Encyclopedia of Food and Health **4** (2016), 333–338.

[309] M. Toledo, *A guide to pH measurement: theory and practice of laboratory pH applications*, Manual for pH-meter (2016).

[310] D. Lawlor, *Introduction to light microscopy: tips and tricks for beginners*, Springer, 2019.

[311] P. G. Vekilov, *Dense liquid precursor for the nucleation of ordered solid phases from solution*, Crystal Growth & Design **4** (2004), 671–685.

[312] Roberto Piazza, *Interactions and phase transitions in protein solutions*, Current Opinion in Colloid & Interface Science **5** (2000), 38–43.

[313] J. Ghiso and B. Frangione, *Amyloidosis and Alzheimer's disease*, Advanced Drug Delivery Reviews **54** (2002), 1539–1551.

[314] A. Patel, H. O. Lee, L. Jawerth, S. Maharana, M. Jahnel, M. Y. Hein, S. Stoynov, J. Mahamid, S. Saha, T. M. Franzmann, A. Pozniakovski, I. Poser, N. Maghelli, L. A. Royer, M. Weigert, E. W. Myers, S. Grill, D. Drechsel, A. A. Hyman, and S. Alberti, *A Liquid-to-Solid Phase Transition of the ALS Protein FUS Accelerated by Disease Mutation*, Cell **162** (2015), 1066–1077.

[315] Y. Wang, A. Lomakin, J. J. McManus, O. Ogun, and G. B. Benedek, *Phase behavior of mixtures of human lens proteins gamma d and beta b1*, Proceedings of the National Academy of Sciences of the United States of America **107** (2010), 13282–13287.

[316] R. J. Siezen, M. R. Fisch, C. Slingsby, and G. B. Benedek, *Opacification of gamma-crystallin solutions from calf lens in relation to cold cataract formation*, Proceedings of the National Academy of Sciences of the United States of America **82** (1985), 1701–1705.

[317] M. Muschol and F. Rosenberger, *Liquid–liquid phase separation in supersaturated lysozyme solutions and associated precipitate formation/crystallization*, The Journal of Chemical Physics **107** (1997), 1953–1962.

[318] D. Soraruf, F. Roosen-Runge, M. Grimaldo, F. Zanini, R. Schweins, T. Seydel, F. Zhang, R. Roth, M. Oettel, and F. Schreiber, *Protein cluster formation in aqueous solution in the presence of multivalent metal ions–a light scattering study*, Soft Matter **10** (2014), 894–902.

[319] R. Piazza, *Protein interactions and association: an open challenge for colloid science*, Current Opinion in Colloid & Interface Science **8** (2004), 515–522.

[320] J. Hansen, F. Platten, D. Wagner, and S. U. Egelhaaf, *Tuning protein-protein interactions using cosolvents: specific effects of ionic and non-ionic additives on protein phase behavior*, Physical Chemistry Chemical Physics : PCCP **18** (2016), 10270–10280.

[321] M. H. J. Hagen and D. Frenkel, *Determination of phase diagrams for the hard–core attractive Yukawa system*, The Journal of Chemical Physics **101** (1994), 4093–4097.

[322] O. Matsarskaia, F. Roosen-Runge, and F. Schreiber, *Multivalent ions and biomolecules: Attempting a comprehensive perspective*, ChemPhysChem **21** (2020), 1742–1767.

[323] R. Akiyama and R. Sakata, *An integral equation study of reentrant behavior in attractive interactions between like-charged macroions immersed in an electrolyte solution*, Journal of the Physical Society of Japan **80** (2011), 123602.

[324] S. Fujihara and R. Akiyama, *Attractive interaction between macroanions mediated by multivalent cations in biological fluids*, Journal of Molecular Liquids **200** (2014), 89–94.

[325] J. Widom and R. L. Baldwin, *Cation-induced toroidal condensation of DNA*, Journal of Molecular Biology **144** (1980), 431–453.

[326] B. A. Todd and D. C. Rau, *Interplay of ion binding and attraction in DNA condensed by multivalent cations*, Nucleic Acids Research **36** (2008), 501–510.

[327] J. Pelta, F. Livolant, and J. L. Sikorav, *Dna aggregation induced by polyamines and cobalthexamine*, The Journal of Biological Chemistry **271** (1996), 5656–5662.

[328] H. Deng and V. A. Bloomfield, *Structural effects of cobalt-amine compounds on DNA condensation*, Biophysical Journal **77** (1999), 1556–1561.

[329] D. Donghi, M. Pechlaner, C. Finazzo, B. Knobloch, and R. K. O. Sigel, *The structural stabilization of the κ three-way junction by Mg(II) represents the first step in the folding of a group II intron*, Nucleic Acids Research **41** (2013), 2489–2504.

[330] M. Rowinska-Zyrek, M. Skilandat, and R. K. O. Sigel, *Hexaamminecobalt (III) - Probing Metal Ion Binding Sites in Nucleic Acids by NMR Spectroscopy*, Zeitschrift für anorganische und allgemeine Chemie **639** (2013), 1313–1320.

[331] I. Bougie and M. Bisaillon, *Metal ion-binding studies highlight important differences between flaviviral RNA polymerases*, Biochimica et Biophysica Acta **1794** (2009), 50–60.

[332] D. Hanahan, *Studies on transformation of escherichia coli with plasmids*, Journal of Molecular Biology **166** (1983), 557–580.

[333] P.-J. Cunat, *Alloying elements in stainless steel and other chromium-containing alloys*, Euro Inox **2004** (2004), 1–24.

[334] Y. S. Hedberg and I. Odnevall Wallinder, *Metal release from stainless steel in biological environments: A review*, Biointerphases **11** (2016).

[335] I. Milošev, *From in vitro to retrieval studies of orthopedic implants*, CORROSION **73** (2017), 1496–1509.

[336] Y. S. Hedberg, M. Pettersson, S. Pradhan, I. Odnevall Wallinder, M. W. Rutland, and C. Persson, *Can Cobalt(II) and Chromium(III) Ions Released from Joint Prostheses Influence the Friction Coefficient?*, ACS Biomaterials Science & Engineering **1** (2015), 617–620.

[337] J. K. Chen and J. P. Thyssen, *Metal allergy: from dermatitis to implant and device failure*, Springer, 2018.

[338] L. Ianeselli, F. Zhang, M. W. A. Skoda, R. M. J. Jacobs, R. A. Martin, S. Callow, S. Prévost, and F. Schreiber, *Protein-protein interactions in ovalbumin solutions studied by small-angle scattering: effect of ionic strength and the chemical nature of cations*, The Journal of Physical Chemistry B **114** (2010), 3776–3783.

[339] J. C. Lee and S. N. Timasheff, *Partial specific volumes and interactions with solvent components of proteins in guanidine hydrochloride*, Biochemistry **13** (1974), 257–265.

[340] T. Hianik, S. Poniková, J. Bágel'ová, and M. Antalík, *Specific volume and compressibility of human serum albumin–polyanion complexes*, Bioorganic & Medicinal Chemistry Letters **16** (2006), 274–279.

[341] X. H. Zhang, X. D. Zhang, S. T. Lou, Z. X. Zhang, J. L. Sun, and J. Hu, *Degassing and temperature effects on the formation of nanobubbles at the mica/water interface*, Langmuir **20** (2004), 3813–3815.

[342] J. M. Mirtallo, K. Caryer, P. J. Schneider, L. Ayers, and P. J. Fabri, *Growth of bacteria and fungi in parenteral nutrition solutions containing albumin*, American Journal of Health-System Pharmacy **38** (1981), 1907–1910.

[343] Y. Li, V. Lubchenko, and P. G. Vekilov, *The use of dynamic light scattering and Brownian microscopy to characterize protein aggregation*, The Review of Scientific Instruments **82** (2011), 053106.

[344] O. Matsarskaia, F. Roosen-Runge, G. Lotze, J. Möller, A. Mariani, F. Zhang, and F. Schreiber, *Tuning phase transitions of aqueous protein solutions by multivalent cations*, Physical Chemistry Chemical Physics : PCCP **20** (2018), 27214–27225.

[345] Y. Liu, L. Porcar, J. Chen, W.-R. Chen, P. Falus, A. Faraone, E. Fratini, K. Hong, and P. Baglioni, *Lysozyme protein solution with an intermediate range order structure*, The Journal of Physical Chemistry B **115** (2011), 7238–7247.

[346] V. Lobaskin and K. Qamhieh, *Effective macroion charge and stability of highly asymmetric electrolytes at various salt conditions*, The Journal of Physical Chemistry B **107** (2003), 8022–8029.

[347] K. Schomäcker, D. Mocker, R. Münze, and G.-J. Beyer, *Stabilities of lanthanide-protein complexes*, International Journal of Radiation Applications and Instrumentation. Part A. Applied Radiation and Isotopes **39** (1988), 261–264.

[348] Y. Marcus, *Ion properties*, Dekker, New York, 1997.

[349] F. Zhang, G. Zocher, A. Sauter, T. Stehle, and F. Schreiber, *Novel approach to controlled protein crystallization through ligandation of yttrium cations*, Applied Crystallography **44** (2011), 755–762.

[350] D. Sehnal, S. Bittrich, M. Deshpande, R. Svobodová, K. Berka, V. Bazgier, S. Velankar, S. K. Burley, J. Koča, and A. S. Rose, *Mol* viewer: modern web app for 3d visualization and analysis of large biomolecular structures*, Nucleic Acids Research **49** (2021), W431–W437.

[351] R. M. Hanson, J. Prilusky, Z. Renjian, T. Nakane, and J. L. Sussman, *JSmol and the Next-Generation Web-Based Representation of 3D Molecular Structure as Applied to Proteopedia*, Israel Journal of Chemistry **53** (2013), 207–216.

[352] D. W. Ussery, *DNA Structure: A-, B-and Z-DNA Helix Families*, Encyclopedia of Life Sciences **1** (2002), e003122.

[353] N. Asherie, *Protein crystallization and phase diagrams*, Methods **34** (2004), 266–272.

[354] A. McPherson, *Crystallization of biological micromolecules*, Cold Spring Harbor Laboratory Press, New York, NY, dec 1998.

[355] S. Alberti, A. Gladfelter, and T. Mittag, *Considerations and challenges in studying liquid-liquid phase separation and biomolecular condensates*, Cell **176** (2019), 419–434.

[356] A. Kakio, S.-i. Nishimoto, K. Yanagisawa, Y. Kozutsumi, and K. Matsuzaki, *Cholesterol-dependent formation of gm1 ganglioside-bound amyloid β-protein, an endogenous seed for alzheimer amyloid*, Journal of Biological Chemistry **276** (2001), 24985–24990.

[357] S. I. Cohen, S. Linse, L. M. Luheshi, E. Hellstrand, D. A. White, L. Rajah, D. E. Otzen, M. Vendruscolo, C. M. Dobson, and T. P. Knowles, *Proliferation of amyloid-β42 aggregates occurs through a secondary nucleation mechanism*, Proceedings of the National Academy of Sciences **110** (2013), 9758–9763.

[358] A. G. Larson, D. Elnatan, M. M. Keenen, M. J. Trnka, J. B. Johnston, A. L. Burlingame, D. A. Agard, S. Redding, and G. J. Narlikar, *Liquid droplet formation by HP1α suggests a role for phase separation in heterochromatin*, Nature **547** (2017), 236–240.

[359] S. Kilic, A. Lezaja, M. Gatti, E. Bianco, J. Michelena, R. Imhof, and M. Altmeyer, *Phase separation of 53 BP 1 determines liquid-like behavior of DNA repair compartments*, The EMBO Journal **38** (2019), e101379.

[360] K. R. Acharya and S. J. Ackerman, *Eosinophil granule proteins: form and function*, Journal of Biological Chemistry **289** (2014), 17406–17415.

[361] C. Liu, B. Yan, S. Qi, Y. Zhang, L. Zhang, and C. Wang, *Predictive significance of Charcot–Leyden crystals for eosinophilic chronic rhinosinusitis with nasal polyps*, American Journal of Rhinology & Allergy **33** (2019), 671–680.

[362] P. F. Weller, *Eosinophilia*, Journal of Allergy and Clinical Immunology **73** (1984), 1–10.

[363] B. P. Davis and M. E. Rothenberg, *Eosinophils and cancer*, Cancer Immunology Research **2** (2014), 1–8.

[364] A. Pande, J. Pande, N. Asherie, A. Lomakin, O. Ogun, J. King, and G. B. Benedek, *Crystal cataracts: human genetic cataract caused by protein crystallization*, Proceedings of the National Academy of Sciences **98** (2001), 6116–6120.

[365] R. Maier, M. R. Fries, C. Buchholz, F. Zhang, and F. Schreiber, *Human versus bovine serum albumin: a subtle difference in hydrophobicity leads to large differences in bulk and interface behavior*, Crystal Growth & Design **21** (2021), 5451–5459.

[366] A. Bujacz, K. Zielinski, and B. Sekula, *Structural studies of bovine, equine, and leporine serum albumin complexes with naproxen*, Proteins: Structure, Function, and Bioinformatics **82** (2014), 2199–2208.

[367] S. Asakura and F. Oosawa, *On interaction between two bodies immersed in a solution of macromolecules*, The Journal of Chemical Physics **22** (1954), 1255–1256.

[368] K. J. Mutch, J. S. van Duijneveldt, and J. Eastoe, *Colloid–polymer mixtures in the protein limit*, Soft Matter **3** (2007), 155–167.

[369] P. G. Bolhuis, E. J. Meijer, and A. A. Louis, *Colloid-polymer mixtures in the protein limit*, Physical Review Letters **90** (2003), 068304.

[370] T. Arakawa and S. N. Timasheff, *Mechanism of polyethylene glycol interaction with proteins*, Biochemistry **24** (1985), 6756–6762.

[371] J. Israelachvili, *The different faces of poly (ethylene glycol)*, Proceedings of the National Academy of Sciences **94** (1997), 8378–8379.

[372] J. M. Harris, *Poly (ethylene glycol) chemistry: biotechnical and biomedical applications*, Springer Science & Business Media, 1992.

[373] P. Chanphai, L. Bekale, S. Sanyakamdhorn, D. Agudelo, and H.-A. Tajmir-Riahi, *Effect of synthetic polymers on polymer–protein interaction*, Polymer **55** (2014), 572–582.

[374] P. A. Zunszain, J. Ghuman, T. Komatsu, E. Tsuchida, and S. Curry, *Crystal structural analysis of human serum albumin complexed with hemin and fatty acid*, BMC Structural biology **3** (2003), 1–9.

[375] W. C. Poon, J. S. Selfe, M. B. Robertson, S. M. Ilett, A. D. Pirie, and P. N. Pusey, *An experimental study of a model colloid-polymer mixture*, Journal de Physique II **3** (1993), 1075–1086.

[376] F. L. Calderon, J. Bibette, and J. Biais, *Experimental phase diagrams of polymer and colloid mixtures*, Europhysics Letters (EPL) **23** (1993), 653–659.

[377] H. N. Lekkerkerker, W. C.-K. Poon, P. N. Pusey, A. Stroobants, and P. B. Warren, *Phase behaviour of colloid + polymer mixtures*, Europhysics Letters (EPL) **20** (1992), 559–564.

[378] G. Pellicane and M. Cavero, *Theoretical study of interactions of BSA protein in a NaCl aqueous solution*, The Journal of Chemical Physics **138** (2013).

[379] J.-J. Lai, H.-Y. Yan, Y. Liu, and Y. Huang, *Effects of PEG molecular weight on its interaction with albumin*, Chinese Journal of Polymer Science **33** (2015), 1373–1379.

[380] J. M. Mirtallo, K. Caryer, P. J. Schneider, L. Ayers, and P. J. Fabri, *Growth of bacteria and fungi in parenteral nutrition solutions containing albumin*, American Journal of Hospital Pharmacy **38** (1981), 1907–1910.

[381] B. Jachimska, M. Wasilewska, and Z. Adamczyk, *Characterization of globular protein solutions by dynamic light scattering, electrophoretic mobility, and viscosity measurements*, Langmuir **24** (2008), 6866–6872.

[382] J. S. Pedersen, *Analysis of small-angle scattering data from colloids and polymer solutions: modeling and least-squares fitting*, Advances in Colloid and Interface Science **70** (1997), 171–210.

[383] P. Thiyagarajan, D. Chaiko, and R. Hjelm Jr, *A neutron scattering study of poly (ethylene glycol) in electrolyte solutions*, Macromolecules **28** (1995), 7730–7736.

[384] M. D. Senft, R. Maier, A. Hiremath, F. Zhang, and F. Schreiber, *Effective interactions and phase behavior of protein solutions in the presence of hexamine cobalt(III) chloride*, The European Physical Journal E **46** (2023), 119.

[385] W. Kabsch, *XDS*, Acta Crystallographica Section D: Biological Crystallography **66** (2010), 125–132.

[386] S. Bliven, A. Lafita, A. Parker, G. Capitani, and J. M. Duarte, *Automated evaluation of quaternary structures from protein crystals*, PLOS computational biology **14** (2018), e1006104.

[387] E. Krissinel and K. Henrick, *Inference of macromolecular assemblies from crystalline state*, Journal of molecular biology **372** (2007), 774–797.

[388] G. B. Benedek, *Cataract as a protein condensation disease: the proctor lecture.*, Investigative Ophthalmology & Visual Science **38** (1997), 1911–1921.

[389] P. Atkins and J. De Paula, *Elements of physical chemistry*, 5 ed., Oxford University Press, London, England, jan 2009.

[390] J. Möller, S. Grobelny, J. Schulze, S. Bieder, A. Steffen, M. Erlkamp, M. Paulus, M. Tolan, and R. Winter, *Reentrant liquid-liquid phase separation in protein solutions at elevated hydrostatic pressures*, Physical Review Letters **112** (2014), 028101.

[391] C. Gögelein, D. Wagner, F. Cardinaux, G. Nägele, and S. U. Egelhaaf, *Effect of glycerol and dimethyl sulfoxide on the phase behavior of lysozyme: Theory and experiments*, The Journal of Chemical Physics **136** (2012).

[392] Y. Zhang, S. Furyk, D. E. Bergbreiter, and P. S. Cremer, *Specific ion effects on the water solubility of macromolecules: PNIPAM and the Hofmeister series*, Journal of the American Chemical Society **127** (2005), 14505–14510, PMID: 16218647.

[393] Y. Cho, Y. Zhang, T. Christensen, L. B. Sagle, A. Chilkoti, and P. S. Cremer, *Effects of Hofmeister anions on the phase transition temperature of elastin-like polypeptides*, The Journal of Physical Chemistry B **112** (2008), 13765–13771.

[394] R. L. Baldwin, *How Hofmeister ion interactions affect protein stability*, Biophysical Journal **71** (1996), 2056–2063.

[395] J. W. Bye and R. J. Falconer, *Thermal stability of lysozyme as a function of ion concentration: A reappraisal of the relationship between the Hofmeister series and protein stability*, Protein Science **22** (2013), 1563–1570.

[396] A. W. Omta, M. F. Kropman, S. Woutersen, and H. J. Bakker, *Negligible effect of ions on the hydrogen-bond structure in liquid water*, Science **301** (2003), 347–349.

[397] M. Manno, A. Emanuele, V. Martorana, P. San Biagio, D. Bulone, M. Palma-Vittorelli, D. McPherson, J. Xu, T. Parker, and D. Urry, *Interaction of processes on different length scales in a bioelastomer capable of performing energy conversion*, Biopolymers: Original Research on Biomolecules **59** (2001), 51–64.

[398] A. Ribeiro, F. J. Arias, J. Reguera, M. Alonso, and J. C. Rodríguez-Cabello, *Influence of the amino-acid sequence on the inverse temperature transition of elastin-like polymers*, Biophysical Journal **97** (2009), 312–320.

[399] M. Lund, L. Vrbka, and P. Jungwirth, *Specific ion binding to nonpolar surface patches of proteins*, Journal of the American Chemical Society **130** (2008), 11582–11583.

[400] L. Medda, C. Carucci, D. F. Parsons, B. W. Ninham, M. Monduzzi, and A. Salis, *Specific cation effects on hemoglobin aggregation below and at physiological salt concentration*, Langmuir **29** (2013), 15350–15358.

[401] R. Sharma and K. Sharma, *The structure factor and the transport properties of dense fluids having molecules with square well potential, a possible generalization*, Physica A: Statistical Mechanics and its Applications **89** (1977), 213–218.

[402] I. S. Muhammad, *Co-salt effects on the phase behavior of protein solutions in the presence of trivalent salt*, Master's thesis, Institut für Angewandte Physik, Eberhard Karls Universität Tübingen, 2023.

[403] L. Lang, *Effect of anions on the phase behavior of protein solutions in the presence of mulivalent salts*, Bachelor's thesis, Institut für Angewandte Physik, Eberhard Karls Universität Tübingen, 2018.

[404] H. I. Okur, J. Kherb, and P. S. Cremer, *Cations bind only weakly to amides in aqueous solutions*, Journal of the American Chemical Society **135** (2013), 5062–5067.

[405] K. B. Rembert, J. Paterová, J. Heyda, C. Hilty, P. Jungwirth, and P. S. Cremer, *Molecular mechanisms of ion-specific effects on proteins*, Journal of the American Chemical Society **134** (2012), 10039–10046.

[406] D. W. Smith, *Ionic hydration enthalpies*, Journal of Chemical Education **54** (1977), 540.

[407] L. M. Pegram and M. T. Record, *Hofmeister salt effects on surface tension arise from partitioning of anions and cations between bulk water and the air-water interface*, The Journal of Physical Chemistry B **111** (2007), 5411–5417.

[408] J. B. Hopkins and R. E. Thorne, *Quantifying radiation damage in biomolecular small-angle x-ray scattering*, Journal of Applied Crystallography **49** (2016), 880–890.

[409] E. F. Garman and M. Weik, *X-ray radiation damage to biological macromolecules: further insights*, Journal of Synchrotron Radiation **24** (2017), 1–6.

[410] L. Young, E. T. Nienhuis, D. Koulentianos, G. Doumy, A. M. March, S. H. Southworth, S. B. Clark, T. M. Orlando, J. A. LaVerne, and C. I. Pearce, *Photon-in/photon-out x-ray free-electron laser studies of radiolysis*, Applied Sciences **11** (2021), 701.